Spread-Spectrum Techniques For Environmentally-Friendly Underwater Acoustic Communications

Benjamin Sherlock

School of Electrical and Electronic Engineering
Newcastle University

This thesis is submitted for the degree of
Doctor of Philosophy

July 2017

Abstract

Anthropogenic underwater noise has been shown to have a negative impact on marine life. Acoustic data transmissions have also been shown to cause behavioural responses in marine mammals. A promising approach to address these issues is through reducing the power of acoustic data transmissions. Firstly, limiting the maximum acoustic transmit power to a safe limit that causes no injury, and secondly, reducing the radius of the discomfort zone whilst maximising the receivable range. The discomfort zone is dependent on the signal design as well as the signal power. To achieve these aims requires a signal and receiver design capable of synchronisation and data reception at low-received-SNR, down to around -15 dB, with Doppler effects. These requirements lead to very high-ratio spread-spectrum signaling with efficient modulation to maximise data rate, which necessitates effective Doppler correction in the receiver structure.

This thesis examines the state-of-the-art in this area and investigates the design, development and implementation of a suitable signal and receiver structure, with experimental validation in a variety of real-world channels. Data signals are designed around m-ary orthogonal signaling based on bandlimited carrierless PN sequences to create an M-ary Orthogonal Code Keying (M-OCK) modulation scheme. Synchronisation signal structures combining the energy of multiple unique PN symbols are shown to outperform single PN sequences of the same bandwidth and duration in channels with low SNR and significant Doppler effects.

Signals and receiver structures are shown to be capable of reliable communications with band of 8 kHz to 16 kHz and transmit power limited to less than 170.8 dB re 1 µPa @ 1 m, or 1 W of acoustic power, over ranges of 10 km in sea trials, with low-received-SNR below -10 dB, at data rates of up to 140.69 bit/s. Channel recordings with AWGN demonstrated limits of signal and receiver performance of BER 10^{-3} at -14 dB for 35.63 bit/s, and -8.5 dB for 106.92 bit/s. Piloted study of multipath exploitation showed this performance could be improved to -10.5 dB for 106.92 bit/s by combining the energy of two arrival paths.

Doppler compensation techniques are explored with experimental validation showing synchronisation and data demodulation at velocities over ranges of ±2.7 m/s.

Non-binary low density parity check (LDPC) error correction coding with M-OCK signals is investigated showing improved performance over Reed-Solomon (RS) coding of equivalent code rate in simulations and experiments in real underwater channels.

The receiver structures are implemented on an Android mobile device with experiments showing live real-time synchronisation and data demodulation of signals transmitted through an underwater channel.

To The Tempest

Softly whispering
Messages of importance;
Whales swim undisturbed.

Acknowledgements

There are a number of people and organisations to acknowledge and thank for the existence of this thesis.

Firstly, my thanks to Jeff Neasham, my primary PhD supervisor, for the inspiration, for the conversations, and for generally enabling this project to happen. Thanks also to Charalampos Tsimenidis, my secondary supervisor, for providing another valuable perspective on the research and writing.

I also owe thanks to members of the SEA Lab team, past and present. Jeff Neasham, Gerry Goodfellow, Dave Graham, Hengda Ding and Lindsay Smith. For the collegial working culture, open sharing of knowledge and experience, and stepping up to assist each other in field trials. Research such as that contained herein cannot happen without such people.

Thanks to Neil Armstrong and his crew aboard the RV Princess Royal (School of Marine Science and Technology) for enabling the Sea Trials to take place.

Thanks to Matthew Simms and his team at Royal Quays Marina for enabling the various Marina Trials to take place.

For support throughout the programme, I also wish to thank various groups within the School of EEE. The school office staff, the IT staff, the mechanical workshop staff and the electronic workshop staff. All of whom enabled the smooth continuation of the research project.

The research in this thesis was funded by the UK Engineering and Physical Sciences Research Council (EPSRC) through a PhD Doctoral Training Account (DTA).

The investigation on the use of non-binary LDPC with M-OCK was made possible through the contributions of Zhen Mei and Martin Johnston at Newcastle University. Encoded packets were generated by Zhen Mei to the author's specifications, and the source code for the original log-FFT-QSPA decoder was provided by Martin Johnston.

Special thanks to the friends who encouraged me to take on the PhD project and keep going. Barbara Sturm. Dave Cooper. Swati Gola. Asif Shah. Dave Bullock. Vicky Forster. John Fry.

Thanks to my family who have supported me as always. Elizabeth, Katy, Vicki and Sam.

And finally, thanks especially to my wife, Rosalind Miranda Beaumont, who has shared in the emotional rollercoaster associated with undertaking a PhD.

Table of contents

List of figures

List of tables

Nomenclature

Roman Symbols

B	Bandwidth
BT_s	Bandwidth-Symbol Time Product
C	Channel Capacity
E_b/N_0	Energy per bit to Noise spectral density ratio
E_s/N_0	Energy per symbol to Noise spectral density ratio
F_s	Sample Frequency
P	Power
PG_s	Processing Gain per Symbol
T	Time
T_s	Symbol Time Period
dB	Decibel

Acronyms / Abbreviations

ACCOBAMS	Agreement on the Conservation of Cetaceans in the Black Sea Mediterranean Sea and Contiguous Atlantic Area
AGC	Automatic Gain Control
ASCOBANS	Agreement on the Conservation of Small Cetaceans of the Baltic, North East Atlantic, Irish and North Seas
AWGN	Additive White Gaussian Noise
BER	Bit Error Rate

BOK	Binary Orthogonal Keying
BRS	Behavioural Response Study
CSS	Chirp Spread Spectrum
DSSS	Direct-Sequence Spread Spectrum
DVB-T	Digital Video Broadcasting - Terrestrial
EM	Electromagnetic
FEC	Forward Error Correction
FHSS	Frequency Hopping Spread Spectrum
FPGA	Field Programmable Gate Array
HFM	Hyperbolic Frequency Modulation
ISI	Inter-Symbol Interference
LDPC	Low Density Parity Check Code
LFM	Linear Frequency Modulation
LFSR	Linear Feedback Shift Register
LPD	Low Probability of Detection
LPI	Low Probability of Interception
M-OCK	M-ary Orthogonal Code Keying
M-OS	M-ary Orthogonal Signaling
M-QAM	M-ary Quadrature Amplitude Modulation
M-Sequence	Maximal Length Sequence
NDK	Native Development Kit
NOAA	National Oceanic and Atmospheric Administration
NRDC	National Resources Defense Council
NRZ Level	Non-Return-To-Zero Level
OFDM	Orthogonal Frequency-Division Multiplexing

PAPR	Peak to Average Power Ratio
PN	Pseudorandom Noise
ppt	Parts per thousand
PRBS	Pseudorandom Binary Sequences
RS	Reed-Solomon Code
SBC	Single-Board Computer
SDAM	Software Defined Acoustic Modem
SDK	Software Development Kit
SEL	Sound Exposure Level
SL	Source Level
SPL	Sound Pressure Level
UUV	Unmanned Underwater Vehicle
UWSN	Underwater Wireless Sensor Network

Chapter 1

Introduction

Earth's oceans cover more than two thirds of the surface of the planet and are home to a wide variety of marine life, yet according to NOAA over 95% of the world under the seas remains undiscovered. As technology progresses, distributed networks of battery-powered subsea sensors and fleets of autonomous underwater vehicles (AUV) allows us to discover, measure and learn so much more of the underwater world. All of this data needs to be returned to land- or ship-based computers for processing but installing wired networks is not always feasible, so underwater acoustic communication becomes the most suitable method of long range data transfer when comparing with other wireless methods.

Regulation for underwater acoustic transmission power and frequency bands has not yet advanced to the same degree as that for terrestrial radio communications. This has led to increasing interference between underwater acoustic systems as well as impacting negatively on marine life. If the goal is to be achieved of long-term underwater acoustic network infrastructure for communication and/or navigation, the industry needs to do this in a way that does not create an environmental problem.

A promising approach to address the issues raised above is through reducing the power of acoustic transmissions which in turn requires a signal and receiver capable of successful low-received-SNR communications. This thesis examines the existing work in this area and investigates the design, development and implementation of a suitable signal and receiver structure capable of successful underwater acoustic communications with low-received-SNR signals in a variety of real-world channels.

1.1 Contributions

1. Design and performance analysis of an M-ary Orthogonal Code Keying modulation scheme.
2. Investigation of a synchronisation technique that combines the energy of multiple unique bandlimited PN symbols to provide improved Doppler tolerance than a single symbol of equivalent bandwidth and duration.
3. Design and investigation of a receiver structure capable of synchronisation and data demodulation at low-received-SNR with optional Doppler compensation structures.
4. Investigation of non-binary LDPC codes compared with Reed-Solomon codes when used with M-ary Orthogonal Code Keying in an underwater acoustic channel.
5. Implementation on an Android mobile device of a receiver structure capable of synchronisation and data demodulation of M-OCK signals in real-time in underwater acoustic channels.

1.2 Publications

The following publications have been produced as a result of the research in this thesis.

1. B. Sherlock, C. C. Tsimenidis, and J. A. Neasham, "Signal and receiver design for low-power acoustic communications using m-ary orthogonal code keying," in *OCEANS 2015-Genova*. IEEE, 2015, pp. 1–10.
   DOI: 10.1109/OCEANS-Genova.2015.7271500
2. B. Sherlock, J. A. Neasham, and C. C. Tsimenidis, "Implementation of a spread-spectrum acoustic modem on an android mobile device," in *OCEANS 2017-Aberdeen*. IEEE, 2017, pp. 1–9.
   DOI: 10.1109/OCEANSE.2017.8084730
3. B. Sherlock, J. A. Neasham, and C. C. Tsimenidis, "Spread-spectrum techniques for bio-friendly underwater acoustic communications," *IEEE Access*, vol. 6, pp. 4506–4520, 2018.
   DOI: 10.1109/ACCESS.2018.2790478

1.3 Thesis Outline

Chapter 2 covers the background physics of underwater acoustics and the challenges faced by underwater acoustic communications. The anthropogenic impact of noise on marine animals is covered with a focus on the theoretical zones of noise influence. The research motivation is then set out followed by coverage of the relevant state-of-the-art in low-received-SNR underwater acoustic communications.

Chapter 3 covers the design of an m-ary orthogonal signal scheme using bandlimited PN sequences. The AWGN performance of the M-ary Orthogonal Code Keying scheme is compared to that of M-ary Quadrature Amplitude Modulation as the modulation depth is increased. Further investigation of the performance in AWGN channel is carried out for varying symbol durations, modulation depths, and data rates.

Chapter 4 covers the design of the receiver structure for successful synchronisation and data demodulation of M-OCK signals. Synchronisation signal structures using multiple unique PN symbols are investigated. Performance of the receiver with two symbol durations and modulation depths are investigated in simulations and experimental sea trials. Multipath exploitation is piloted with the effect on performance investigated.

Chapter 5 covers the addition to the receiver design of Doppler compensation techniques. Synchronisation and data demodulation receiver structure designs are both investigated through experimental marina trials and with channel recordings combined with AWGN. The performance of synchronisation signal structures using multiple unique PN symbols are also investigated in a channel with significant Doppler effects.

Chapter 7 covers the use of non-binary forward error correction codes with m-ary orthogonal code keying scheme. The performance of Reed-Solomon codes are compared with non-binary LDPC codes in simulation and experimental results. A symbol/packet quality measure is proposed for M-OCK modulation scheme signals to determine the confidence in the symbol decisions of the maximum likelihood detector.

Chapter 6 covers the implementation of the receiver structures covered previously on an Android mobile device. A number of spread-spectrum signals are investigated including Chirp-BOK and M-OCK with varying data rates, modulation depths and symbol durations. Simulations show the relative performance of the signaling schemes. Experimental validation in marina trials shows the performance of the Android mobile device and receiver structure in live real-time synchronisation and data demodulation. Channel recordings with AWGN then provide further investigation into the relative performance of the modulation schemes and receiver structure running in real-time on the Android mobile device.

Chapter 8 covers the conclusions and discussions resulting from the work undertaken in this thesis. Comparisons in performance are made with the state-of-the art techniques for low-received-SNR applications. Consideration is also given to the research aims linked to reducing impact on marine life and how the measured performance of the communication system compares. Future work is also identified to take this research further.

Chapter 2

Background, Motivation, and State-of-the-Art

2.1 Introduction

This chapter looks at the background physics of underwater acoustics and the challenges faced by underwater acoustic communication signals. The anthropogenic impact on marine life of underwater noise is covered. The Theoretical Zones of Noise Influence are explored with research on marine mammals and the effects of human generated noise sources: construction, sonar, and acoustic communications.

The desire for low-cost, low-power acoustic transmitters in underwater wireless sensor networks is also introduced as a driving factor in the research. The overall aim is to reduce transmit power, and hence the audible range, in order to minimise the impact on marine life and interference with other acoustic communication systems whilst maintaining a useful receivable range.

State-of-the-art is covered for technologies operating in low-received-SNR covert applications as well as technologies aimed at environmentally-friendly acoustic communications.

Finally, the research aims and objectives for this thesis are set out for the design and development of a signal and receiver structure capable of meeting the requirements for low-received-SNR whilst minimising the impact on marine life.

Underwater acoustics play an important role in many industrial, research and security applications. These range from the oil and gas industry – sea-bed situated equipment; renewable energy applications – off-shore wind turbine and sub-sea tidal-power equipment condition-monitoring, fishery – searching-for and observation of fish-stocks; shipping – depth gauging and remote detection of sea-bed composition; geographical exploration and ecological studies; to maritime security – underwater navigation, detection and ranging (SONAR) [4].

Radio waves are not an option because high-frequency electromagnetic (EM) waves are rapidly attenuated due to the high permittivity of water as well as the high conductivity of sea water. This can also be explained by the "skin effect" whereby AC signals are attenuated exponentially as they travel into such a medium. The attenuation (or skin depth) is frequency-dependent, with attenuation increasing with frequency.

Optical based communications are also limited by range from attenuation as well as being dependent on the clarity of the water.

These physical challenges have led to the development of advanced underwater acoustic signals. Sound waves travel much further and faster underwater than they do in air, especially at lower frequencies which makes it an ideal transmission method [4].

For a broader introduction to the world of underwater acoustics, covering communication as well as sensing, measuring etc., the reader may find [4] a suitable starting point. Acoustic communications, originally used for an analogue underwater telephone, are now used for digital data transmission from remote sensors, divers, automated underwater vehicles, etc. Baggeroer provides an overview of technological progress in the early days pre-1983 [5]. Foote covers many areas of interest in the field of underwater acoustics as part of a review paper [6].

2.2 Physical Properties of Underwater Acoustic Channels

This section sets out to cover the physical properties of underwater acoustic channels and the challenges these will pose to our communication scheme in later chapters. In summary these include, the speed of sound in seawater, multipath and refraction, transmission losses, ambient ocean noise, and the Doppler effect.

2.2.1 Speed of Sound

Sound speed, c, in seawater is a function of temperature, water pressure/depth, and salinity. An example sound speed profile is shown in Fig. 2.1. The equation from [7] is given in (2.1) where:

- c is the speed of sound in m/s;
- T is the temperature in °C;
- S is the salinity in parts per thousand (ppt); and
- Z is the depth in m.

The equation is valid for:

- $0 \leq T \leq 35$°C;
- $0 \leq S \leq 40$ ppt; and

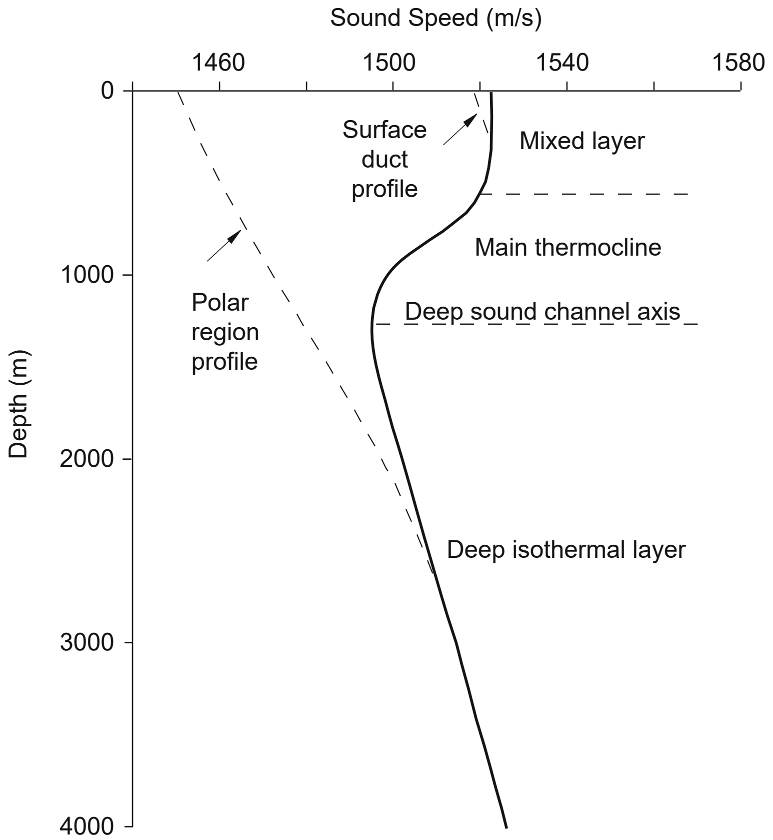

Fig. 2.1 Sound Speed Profile. Original figure from "Computational Ocean Acoustics" [8].

- $0 \leq Z \leq 1000$m.

$$c = 1449.2 + 4.6T - 0.055T^2 + 0.00029T^3 + (1.34 - 0.010T)(S - 35) + 0.016Z \quad (2.1)$$

This general equation has limitations on the input parameters, but also importantly does not necessarily accurately model all environments such as shallow water channels, very deep water channels, or polar regions under icecaps. For more accurate sound speed measurements other models may be more appropriate [8].

2.2.2 Multipath, Reflection, and Refraction

The underwater world is bounded by the sea surface and the sea bottom. The acoustic signals therefore undergo reflections at these boundaries; more so in shallow water channels than in deep water channels. The acoustic signal paths also undergo bending through refraction due to pressure, temperature, and salinity differences altering the speed of sound. Examples are shown in Fig. 2.2. Path reflections are dependent on the angle of incidence and the relative acoustic impedance of the two mediums at the interface. This determines how much energy is reflected back into the original medium, and how much energy is transmitted through the interface and

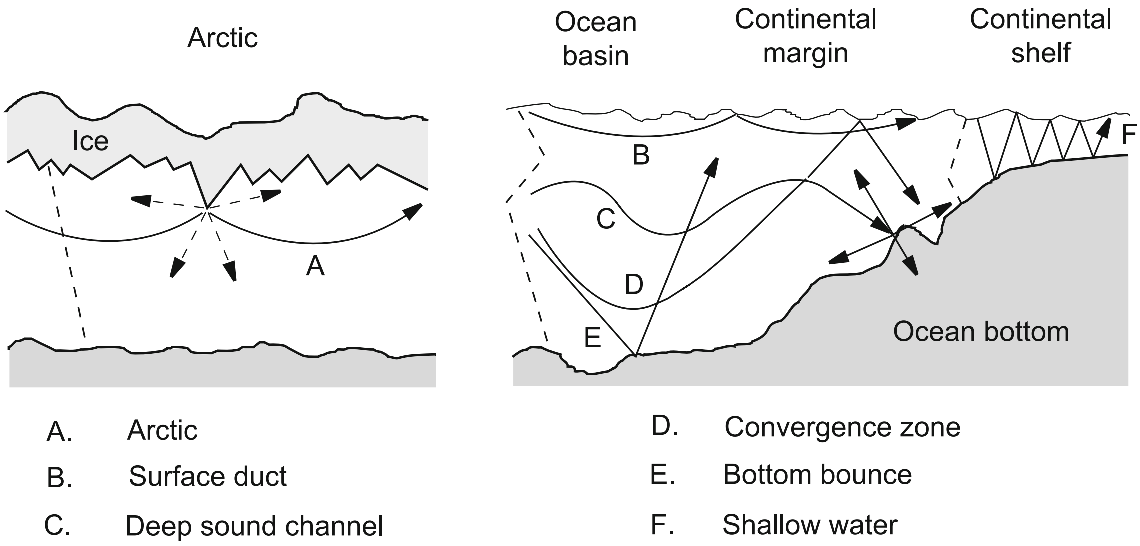

Fig. 2.2 Propagation Paths. Original figure from “Computational Ocean Acoustics” [8]. Includes indications of the sound speed profile for various propagation paths in a variety of underwater environments.

potentially lost to the air, or into the seabed. Snell-Descartes law covers both the refraction throughout a gradually changing medium, as well as the angles of reflection and transmission at an interface between two discretely different mediums [8, 9, 4].

Jensen, Kuperman, Porter, and Schmidt provide an equation (2.2) that best shows how the bending from refraction is directly linked to the speed of sound within the fluid [8]. Where the ray angle, θ, is relative to the horizontal, and c is the local speed of sound:

$$\frac{\cos\theta}{c} = \text{const}, \tag{2.2}$$

The sound therefore bends towards the low-speed region, as seen in the example sound speed profile in Fig. 2.1 the "Deep sound channel axis" is the point of lowest sound speed. In Fig. 2.2 this would correspond to path C.

At interfaces with the sea bottom or clearly defined layer interfaces in the underwater environment, how much energy is either reflected or transmitted is dependent on the relative acoustic impedance at the interface and the angle of incidence of the sound to the interface [7, 8]. Acoustic impedance, Z, is a function of the fluid density, ρ, sound speed, c, and the angle of incidence, θ, as given by (2.3):

$$Z = \frac{\rho c}{\sin\theta} \tag{2.3}$$

Fig. 2.3 shows an example fluid-fluid boundary with the incident, reflected and transmitted rays. The angle of transmission, or refraction, corresponds to Snell’s Law whereby the ratio of the cos of the angle to the horizontal, θ, of the sound path at the interface is related to the ratio

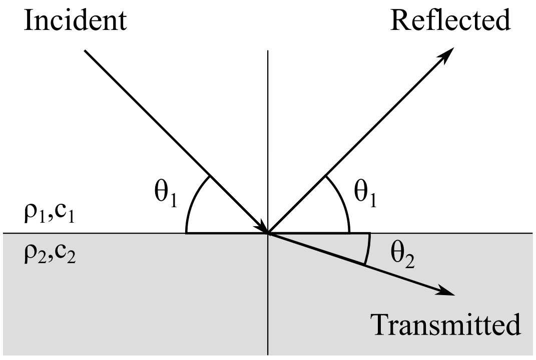

Fig. 2.3 Snell's Law: reflection and transmission at a fluid-fluid boundary.

of the sound velocities, c, in the two media at the interface as shown by (2.4).

$$c_1 \cos\theta_1 = c_2 \cos\theta_2 \tag{2.4}$$

The proportion of the sound transmitted and reflected is related to the acoustic impedances of the two fluids. From [8] the reflection and transmission coefficients are given by (2.5) and (2.6):

$$R = \frac{Z_2 - Z_1}{Z_2 + Z_1} \tag{2.5}$$

$$T = \frac{2Z_2}{Z_2 + Z_1} \tag{2.6}$$

These fluid-fluid boundaries apply to soft sediments on the sea bottom where energy from the propagation path is lost to bottom reflections. If the reflective surface is rough with respect to the wavelength of the acoustic wave, then Rayleigh scattering is another factor affecting the energy and onward paths of the acoustic signal. Lambert's law models the degree of scattering exhibited by a surface. These models are important factors when considering back-scattering for use in sonar applications [4].

A simplified example showing multiple reflected paths in a constant-velocity medium is shown in Fig. 2.4. As many transmitters emit the acoustic signals omni-directionally, viewing the paths as rays emanating from the point source will potentially produce many different paths arriving at the same receiver point with different frequency-dependent energy levels, phases, and time delays. Multiple arrivals can cause constructive and destructive interference resulting in frequency selective fading [4].

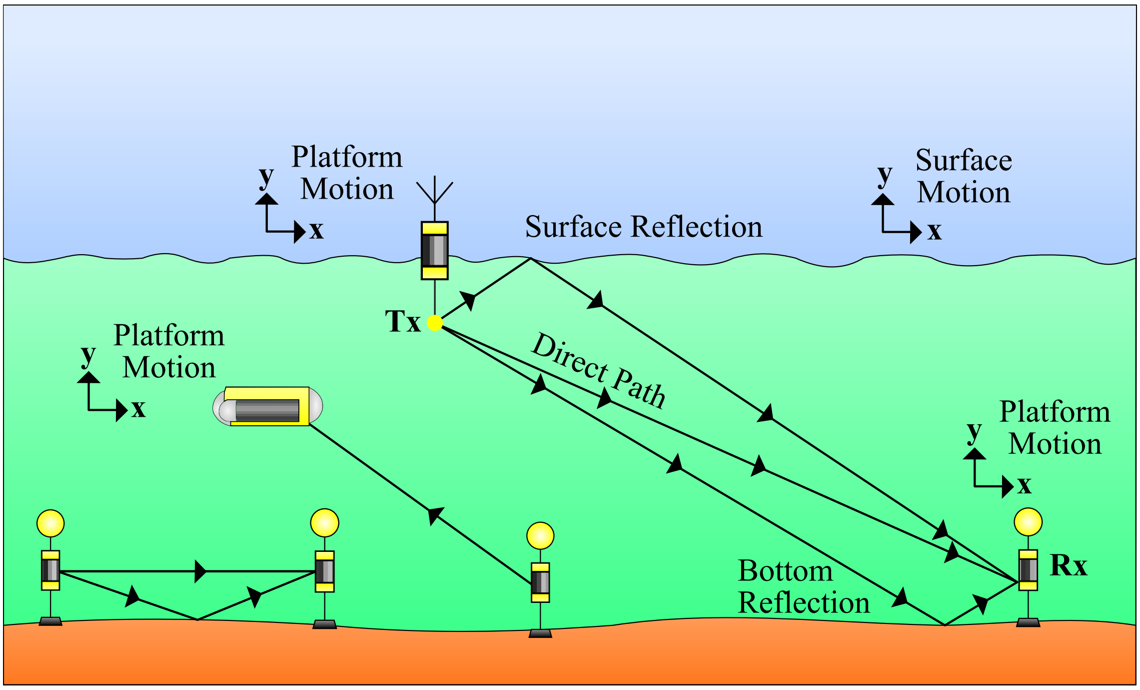

Fig. 2.4 Underwater Acoustic Channel. Examples of applications including surface gateway, automated underwater vehicle, and distributed sensor network on the sea bottom. A simplified environment assuming constant velocity channel to highlight multiple transmission paths and the effect of relative motion of platforms and surface on each individual path.

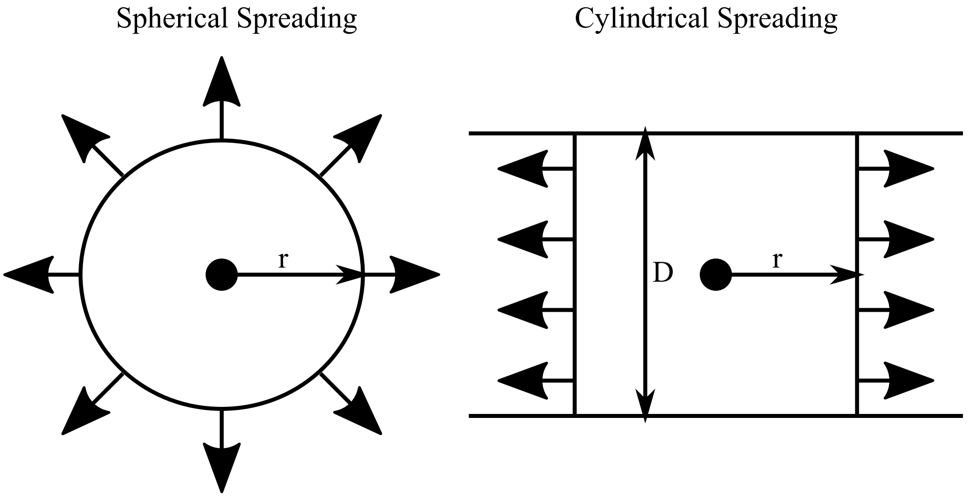

Fig. 2.5 Geometric Spreading Losses. Spherical and Cylindrical.

2.2.3 Transmission Losses

Transmission losses can be viewed independently and then their calculated effects combined to provide expectations of the degree of loss over a given range in a particular environment.

2.2.3.1 Geometric Spreading Losses

Spherical spreading losses from [7] is shown in (2.7) where r is the horizontal range in metres. In shallow water channels where the horizontal range is far greater than the depth of the channel, $r \gg D$, the spreading losses for the near field, ($r \leq D$), are spherical, then thereafter are cylindrical and given by (2.8). Both spherical and cylindrical spreading are displayed in Fig. 2.5.

$$\mathrm{TL} = 20 \log_{10} r \qquad [\mathrm{dB\ re\ 1\ m}] \tag{2.7}$$

$$\mathrm{TL} = 10 \log_{10} r \qquad [\mathrm{dB\ re\ 1\ m}] \tag{2.8}$$

2.2.3.2 Absorption Losses

As sound propagates through the sea some of the energy is lost through the viscosity of the water, and chemical reactions with relaxation of magnesium sulphate and boric acid. The degree to which each factor affects the acoustic wave energy are frequency dependent. The Francois-Garrison model [4, 10, 11] provides an equation (2.9) for attenuation, α, in dB/km based on the

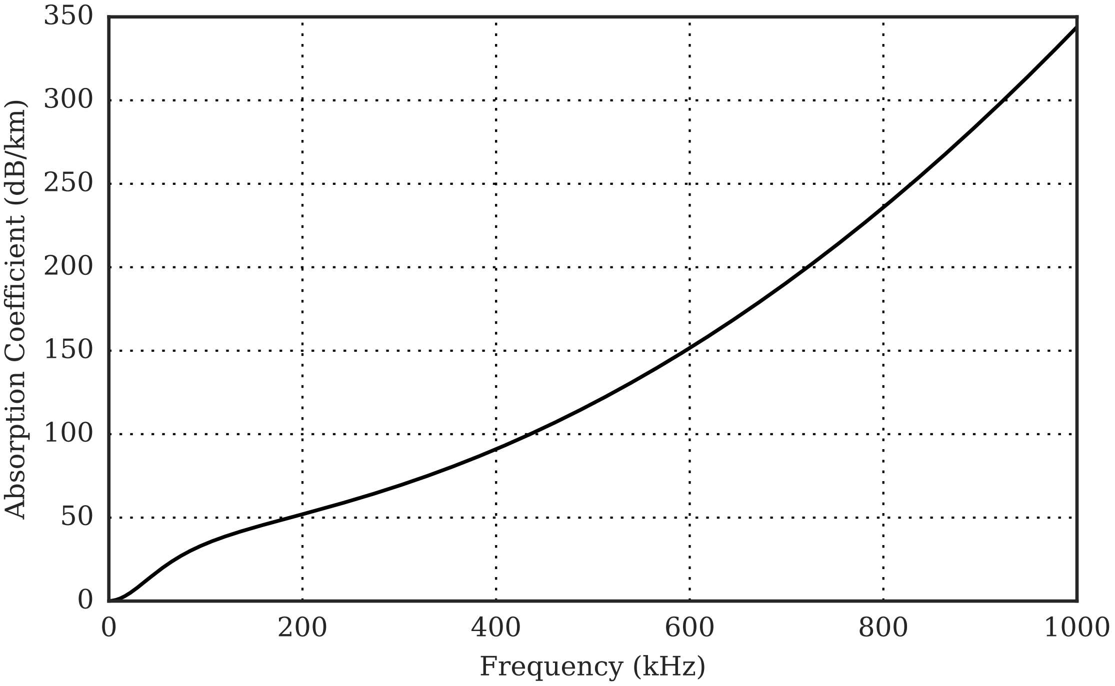

Fig. 2.6 Attenuation due to absorption based on the simplified expression for $\alpha(f)$ in (2.10).

contributions of boric acid, magnesium sulphate and pure water.

$$\alpha = A_1 P_1 \frac{f_1 f^2}{f_1^2 + f^2} + A_2 P_2 \frac{f_2 f^2}{f_2^2 + f^2} + A_3 P_3 f^2 \tag{2.9}$$

A simplified model was devised by Ainslie and McColm in 1998 such that, for a given range of parameters, the result is within 10% of the value produced by the Francois-Garrison model [12].

A further simplified expression for the frequency dependent attenuation, $\alpha(f)$, is (2.10) where f is in kHz, and $\alpha(f)$ is in dB/km [8, 7]:

$$\alpha(f) \approx 3.3 \cdot 10^{-3} + \frac{0.11 f^2}{1 + f^2} + \frac{44 f^2}{4100 + f^2} + 3.0 \cdot 10^{-4} f^2 \tag{2.10}$$

This expression is based on measurements taken for sea conditions of a temperature of 4 °C, salinity of 35 ppt, pH of 8.0, at a depth of 1000 m. This relationship between frequency and attenuation due to absorption using this expression can be shown in Fig. 2.6. Stojanovic also considers these losses with respect to the loss of effective bandwidth as range increases [13].

2.2.3.3 Combined Losses

Taking both geometric spreading loss and absorption losses these can be combined as given by (2.11) from [9]. Where: f is signal frequency; l is the transmission range taken in reference to l_r; k models the spreading loss between 1 and 2, where 1 is for cylindrical and 2 is for spherical spreading; $a(f)$ is the absorption coefficient taken from the equations above.

$$A(l,f) = (l/l_r)^k a(f)^{l-l_r} \tag{2.11}$$

2.2.4 Doppler Effect

Relative motion of the transmit and receive platforms, and any reflective surfaces along the path, can lead to a Doppler shift applied to the acoustic signal. The degree of shift applied is related to the component of the relative motion applied along the propagation path.

The Doppler shift in frequency seen at the receiver, δf, is related to the relative velocity of the platforms along the propagation path, v_r, and the speed of sound, c, given in (2.12) from [4].

$$\delta f = f_0 \frac{v_r}{c} \tag{2.12}$$

This is suitable when considering narrowband signals, however, in underwater acoustic communications especially spread-spectrum signals, the signals are considered wideband. Sabath et al. consider a definition of narrowband and wideband signals based on the fractional bandwidth, B_F, which is the relationship between the Bandwidth, B, and the centre frequency of the signal, f_C, and shown in (2.13) [14]:

$$B_F = \frac{B}{f_C}. \tag{2.13}$$

The boundaries being:

$$\begin{array}{ll} \text{Narrowband,} & \text{if } 0.00 < B_F < 0.01; \\ \text{Wideband,} & \text{if } 0.01 < B_F \leq 0.25; \\ \text{Ultra-wideband,} & \text{if } 0.25 < B_F < 2.00. \end{array}$$

The effect of Doppler shift on a narrowband signal's time and frequency resolution performances can be measured through the ambiguity function, $A(\delta f, \delta t)$, given by (2.14) [4] [7]. Where $s(f_0, \tau)$ is the nominal time-domain signal with carrier frequency f_0, $s(f_0 + \delta f, \tau - \delta t)$ is the signal shifted in time by δt and in frequency by the Doppler shift δf.

$$A(\delta f, \delta t) = \left| \int_{-\infty}^{\infty} s(f_0, \tau) * s(f_0 + \delta f, \tau - \delta t)\, d\tau \right|^2 \tag{2.14}$$

For a wideband signal, the Doppler effect results in non-uniform frequency shift [9, 15, 16]. This is exhibited as a time scaling of the transmitted signal resulting in either compression or dilation in time. The magnitude of the Doppler effect, Δ, is the ratio of the relative platform velocity, v_r, and the speed of sound, c. The ambiguity function, χ_s, for a wideband signal as used by Sharif et al. [16] and Rihaczek [17] is given by (2.15) where $s((1+\Delta)t)$ is the time compressed/dilated time-domain signal, and $s(t-\tau)$ is the signal shifted in time by τ:

$$\chi_s(\tau,\Delta) = (1+\Delta)\int_{-\infty}^{\infty} s((1+\Delta)t)\, s(t-\tau)\, dt \tag{2.15}$$

Sharif et al. also investigate Doppler compensation techniques for wideband signals by focusing on the time compression/dilation through the use of resampling to recover the original signal [16].

2.2.5 Noise

Noise in the oceans has been the subject of a wide range of research, in terms of understanding the sources, power levels and frequency bands, as well as the impact on the marine environment such as marine mammals. It is possible to group noise into three categories for the purpose of this section: ambient noise, self-noise, and acoustic interference [4, 18–20]. The power levels and frequency distributions of such noise sources can be seen in Fig. 2.7.

2.2.5.1 Ambient Noise: Natural Sources

Natural sources of ambient noise include wind, waves, and precipitation on the surface. The wind and waves being related and measured by the current sea state turbulence level. These effects tend to occupy the 100 Hz region with the highest sea state producing the spectrum levels of up to 80 dB re 1 µPa. Volcanic and seismic activity occupy the lower frequency ranges 0.1 Hz to 100 Hz with greater spectrum levels of up to 160 dB re 1 µPa. The mix of ambient noise received is dependent on depth of the reading, for example surface turbulence from waves and precipitation will be more pronounced at shallow depths. The noise also varies greatly between different environments such as deep ocean basins and shallow coastal channels with breaking waves. Arctic seas vary again whereby the surface can be protected from wind effects by ice but noise now originates from the cracking of ice floes or the creaking of glacial movement.

Animal noise can include marine mammal communication and echolocation signals which can extend over a range of 10 Hz to 100 kHz. Fish and shrimp also contribute to the ambient noise. The nature of the animal noise can be considered more intermittent and impulsive than that of the wind and waves.

2.2.5.2 Ambient Noise: Man-made Sources

Man-made sources of ambient noise in the oceans include shipping, drilling for oil and gas, mineral mining, construction of offshore facilities. Worldwide, shipping is one of the main contributors of noise through engines, propeller movement and cavitation. The precise mix of background noise will vary greatly between areas without to areas that possess high levels of shipping and industrial activity, such as ports, commercial shipping lanes, and oil fields. Fig. 2.7 shows that heavy shipping noise peaks around 50 Hz at 90 dB re 1 µPa. These curves originate from the work by Wenz [21]. However, it is important to note that the number and size of vessels in the world fleet has been steadily increasing over time [20] from approximately 40,000 in 1962 (when the original Wenz Curves were created) to 85,000 vessels in 1998.

2.2.5.3 Self-Noise

Self-noise refers to noise originating from within the complete system of the acoustic receiver including the platform and electrical subsystems. Powered vessels will produce noise from hydrodynamic flow and propulsion if the device is underway. Electrical noise on the power supply and thermal noise within the electronic circuitry will also have an effect on the recorded signals [4].

2.2.5.4 Acoustic Interference

Acoustic communication and sonar systems in the vicinity will also potentially contribute to interference with the signals received by the receiver. Particularly powerful transmissions such as sonar may still cause interference even over significant ranges.

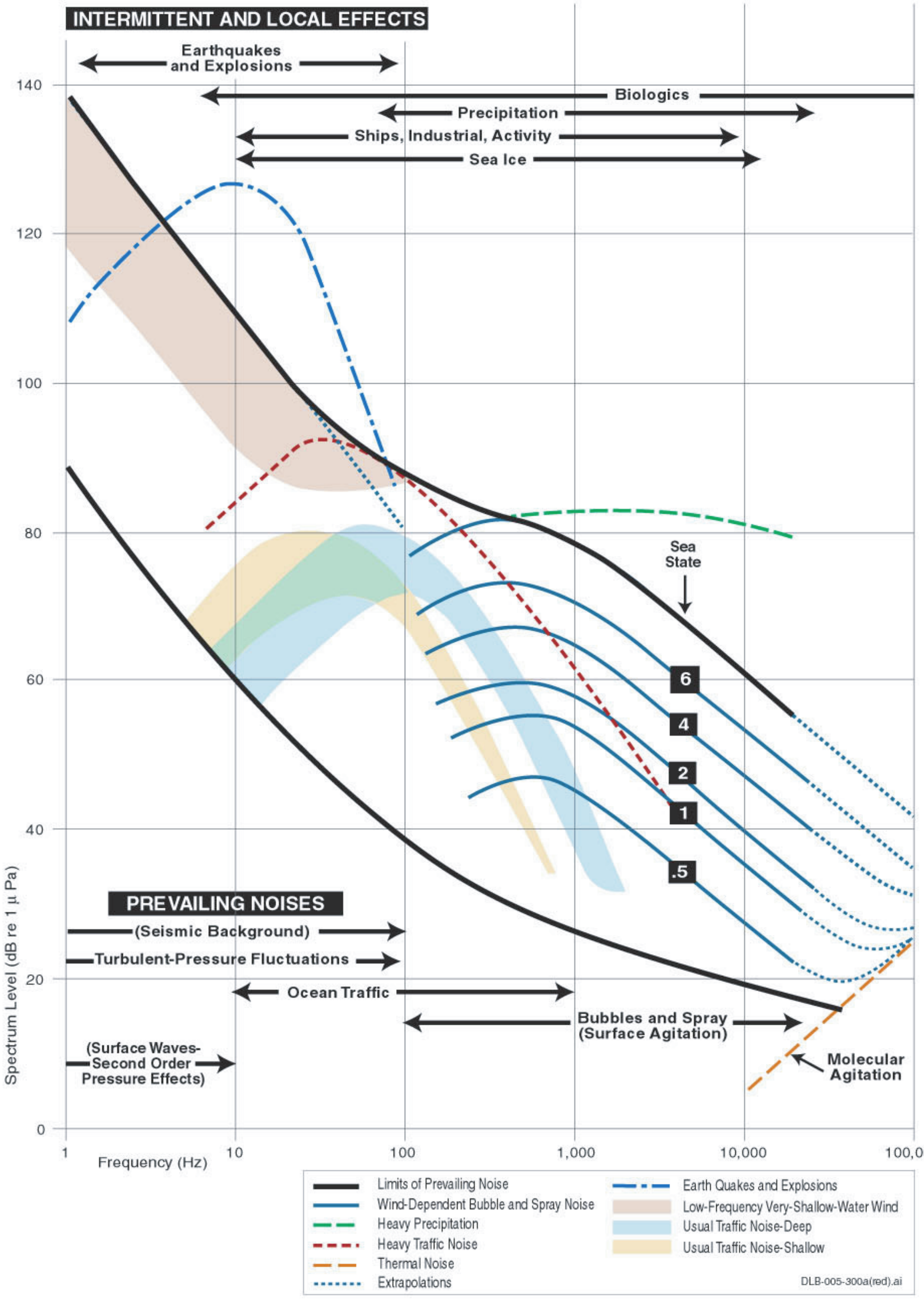

Fig. 2.7 Wenz curves describing pressure spectral density levels of marine ambient noise from weather, wind, geologic activity, and commercial shipping. (Adapted from Wenz [21].). Original figure from “Ocean Noise and Marine Mammals” [20].

2.3 Anthropogenic Impact on Marine Life

Earth's oceans cover more than two thirds of the surface of the planet and are home to a wide variety of marine life, yet over 95% of the world under the seas remains undiscovered.

A great deal of exploration has been taking place for military, scientific, and commercial purposes. Each using a wide array of technologies and acoustic power-levels [4] [22] [23].

Regulation for underwater acoustic transmission power and frequency bands has not yet advanced to the same degree as that for terrestrial radio communications. Although, with respect to high-power sonar exercises, in recent years a number of nations have brought in regulations to protect known populations of marine mammals [24] [20].

A handbook produced by Erbe provides an overview of the physics of underwater acoustics, populations of marine mammals and where they reside around the world, and the impact of anthropogenic noise on said animals [25].

2.3.1 Theoretical Zones of Noise Influence

A conceptual model for categorising the effect of noise on marine mammals was devised by Richardson et al. in 1995 [26] and also included in the OSPAR report [24]. The Theoretical Zones of Noise Influence, as shown in Fig. 2.8, consist of four ranges with the greatest sound energy and hence the greatest severity of impact shown at the centre. The degrees of influence are:

1. Hearing loss, discomfort, injury
2. Response
3. Masking
4. Detection / Audible

2.3.2 Injury and Hearing Loss / Threshold Shift

Non-auditory injury is possible from extremely high intensity sound pressure waves. Damage to the body tissue could include internal hemorrhaging or rupture of lung tissue. Indirect damage from embolism can also occur due to sudden decompression as high intensity sounds force the animal to flee and surface suddenly in an attempt to escape the sound pressure waves [27].

Injury of the auditory system due to exposure to excessive sound can result in Permanent Threshold Shift (PTS) or Temporary Threshold Shift (TTS). Studies have shown that it is not just the peak sound pressure level (SPL) that is important, but also the time of exposure, i.e. the total energy received by the auditory system. The sound exposure level (SEL) measure takes this into account.

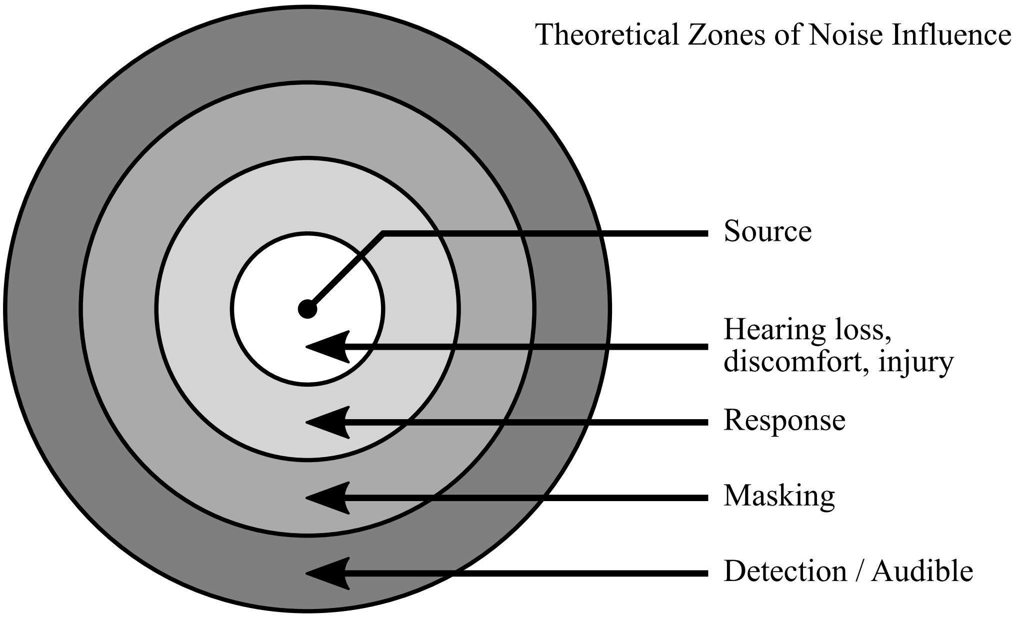

Fig. 2.8 Theoretical Zones of Noise Influence. Originally by Richardson et al. [26]

Lurton summarises the limits of threshold shift based on the work of Southall et al [28]. These state limits of Peak Exposure Level of 230 dB re 1 µPa for cetaceans and 218 dB re 1 µPa for pinnipeds underwater.

Frequency-weighted sound exposure levels are limited to 198 dB re 1 μPa^2-s for cetaceans exposed to pulsed sounds, and 215 dB re 1 μPa^2-s for non-pulsed sounds. For pinnipeds they are 186 dB re 1 μPa^2-s underwater pulsed, and 203 dB re 1 μPa^2-s underwater non-pulsed. Where pulsed is defined as where the sound pressure level measured in a 35 ms window is at least 3 dB greater than that measured in a 125 ms window.

Lurton however indicated that recent studies by Lucke et al suggested that harbour porpoises may have the lowest TTS thresholds of any cetacean studied by 2009. At 4 kHz they showed TTS at a sound pressure level of 199.7 dB_{pk-pk} re 1 µPa and a sound exposure level of 164.3 dB re 1 μPa^2-s. However, the animal also showed behavioural reactions at sound pressure levels of 174 dB_{pk-pk} re 1 µPa and sound exposure level of 145 dB re 1 μPa^2-s [29].

In order to understand the more serious cases of sound-related injury to marine mammals, often when stranding and death also occurs, a necropsy is carried out. In the case of a number of stranding events in the Bahamas, Puerto Rico and Madeira between 1999-2002, the specimens were examined by Ketten [30]. Likewise, specimens from a stranding event in the Canary Islands in 2002 were examined in necropsy as covered by Fernandez et al [31]. Necropsies provide information such as the age and sex of the specimen, as well as evidence of the general state of health of the animal - both recent and historical. A number of specimens examined in the previous necropsies show signs of hemorrhaging in the auditory system that indicates potential pressure wave related injury [30].

The impact is not limited to marine mammals. Hastings and Popper have also studied the impact of activities such as pile-driving on fish [32].

2.3.3 Mass Stranding Events

Table 2.1 Unusual Stranding Events thought to be linked to mid-frequency military sonar use. A summary from [4, Table 10.1]. Also covered by Jasny et al [27, Table 1.3]

Location	Date	Species (number)	Reference
Canary Islands	February 1985	Cuvier's beaked whales (12) Gervais' beaked whale (1)	[33]
Canary Islands	June 1986	Cuvier's beaked whales (4) Gervais' beaked whale (1)	[33]
Canary Islands	November 1986	Cuvier's beaked whales (3) Northern bottlenose whale (1) Pygmy sperm whales (2)	[33]
Canary Islands	October 1989	Cuvier's beaked whales (19) Gervais' beaked whales (3) Blainville's beaked whales (2)	[33]
Greece	May 1996	Cuvier's beaked whales (12)	[34] [35]
Bahamas	March 2000	Cuvier's beaked whales (9) Blainville's beaked whales (3) Unidentified beaked whales (2) Minke whales (2) Spotted dolphin (1)	[36] [37] [35]
Madeira	May 2000	Cuvier's beaked whales (3) Unidentified beaked whale (1)	[30] [37]
Canary Islands	September 2002	Cuvier's beaked whales (10) Blainville's beaked whales (1) Gervais' beaked whales (1) Unidentified beaked whale (1)	[31] [37]
Taiwan	2004-2005	Ginkgo-toothed whale (1) Short-finned pilot whales Pygmy killer whales	[38] [39]
North Carolina, US	January 2005	Short-finned pilot whales (33) Pygmy sperm whales (2) Minke whale (1)	[40]

A number of stranding events of marine mammals, between 1985 and 2005, have been linked with mid-frequency military sonar use [4, Table 10.1] these are summarised in Table 2.1. Further stranding events since 2005 are summarised in Table 2.2. D'Amico, Gisiner, Ketten, Hammock, Johnson, Tyack, and Mead examine a number of historical mass stranding events (including those in the Table 2.1 and Table 2.2) involving beaked whales with a link to naval exercises.

Table 2.2 Unusual Stranding Events Since 2005 thought to be linked to mid-frequency military sonar use.

Location	Date	Species (number)	Reference
Madagascar	May 2008	Melon-headed whales (>50)	[42] [43]
Cornwall, UK	June 2008	Short beaked common dolphin (26 dead, plus a further 26 herded back to sea)	[42] [44]
Corfu, Greece	December 2011	Cuvier's beaked whales (13)	[42]
Crete, Greece	April 2014	Cuvier's beaked whales (5-10)	[42]

2.3.4 Behavioural Response Studies

Referring back to the conceptual model by Richardson of the theoretical zones of noise influence, thus far the more serous effects have been covered surrounding hearing loss, discomfort, and direct or indirect injury. Research into the behavioural responses and effects of anthropogenic sound on marine mammals are the subject of numerous studies. Experiments can take place involving captive animals, or by monitoring wild animals' responses to researcher simulated sounds or sounds occurring as part of independent human activity.

Ellison, Southall, Clark, and Frankel detail an approach to assessing these behavioural responses to anthropogenic sounds for both free-ranging and captive animals [45].

2.3.4.1 Monitoring free-ranging animals

Johnson and Tyack designed, implemented and tested a tag that can be attached to wild animals to record motion, depth, and sound data for retrieval at a later date [46]. Experiments were carried out with the tags attached to free-ranging whales whilst various sound recordings were played into the ocean from a so-called "Playback Vessel". The data gathered by the tags allowed the time-synchronisation of motion data (heading, depth etc.) along with the recording of the audio received by the tag as emitted from the "Playback Vessel". The experiments showed behavioural responses including Sperm Whales interrupting their descent on hearing SONAR playback; and Right whales changing heading on hearing the playback of whale sounds.

Johnson, de Soto, and Madsen conducted a review of tag technologies. This included a detailed look at the design aspects of a recording tag: mechanical design; buoyancy and retrieval methods; multiple hydrophones; analogue front-end and ADC; inertial measurement unit for orientation and dead-reckoning underwater; surface localisation using GPS/ARGOS; and method of attachment to the animal [47]. The review found that, to that date, acoustic recording tags had made significant contributions to understanding "marine mammal ecology, physiology, behaviour, and sound production" [47].

These tagging technologies were used in a number of development projects and behavioural response studies (BRS) summarised as follows. A 5-year project in southern California ("SOCAL-BRS") by Southall, Moretti, Abraham, Calambokidis, DeRuiter, and Tyack [48] where acoustic tags attached to marine mammals were used to confirm the accuracy of the sound source technology developed in the project. The new sound source equipment being considerably smaller in size allowed for the use of smaller research vessels in field trials in monitoring the behavioural effects of marine mammals. Goldbogen, Southall, DeRuiter, Calambokidis, Friedlaender, Hazen, Falcone, Schorr, Douglas, Moretti, et al. made use of the tags to monitor the response of blue whales when they were exposed to simulated mid-frequency sonar (3.5 kHz to 4.0 kHz). The responses were found to vary depending on the whale's current behavioural state, with no change for surface feeding whales. Deep feeding and non-feeding whales however showed responses to the sound either terminating deep dives or with prolonged mid-water dives [49]. Simulated mid-frequency sonar was also used to determine the behavioural effects on Cuvier's beaked whales by DeRuiter, Southall, Calambokidis, Zimmer, Sadykova, Falcone, Friedlaender, Joseph, Moretti, Schorr, et al.. Sonar at short range was shown to have consistent and long-lasting responses, however incidental sonar from distant naval exercises did not produce a similar response despite the received levels being comparable [50].

Claridge conducted population level studies of Blainville's beaked whales using photo-identification of individuals. Two localities were studied, one exposed to naval sonar, the other not. The population demographics are shown to differ where those exposed to naval sonar have smaller populations and a lower female-to-calf ratio [51].

2.3.4.2 Studies on Captive Animals

Kastelein et al. have produced numerous studies into behavioural responses of captive Harbour Porpoises and Harbour Seals on various acoustic signal types and powers.

Kastelein, Verboom, Muijsers, Jennings, and Van der Heul investigate the effect of acoustic data transmissions around 12 kHz on Harbour Porpoises (Phocoena phocoena) [52]. Experiments are carried out with two captive harbour porpoises. Four acoustic wave types are tested: Chirps, DSSS, Frequency Sweep (1 s linear sweep between 10 kHz to 14 kHz) (for reference with previous experiments), and modulated FSK. Based on spectrograms for the four signals, the bandwidth for modulated FSK is 10 kHz to 13 kHz whereas the DSSS is 10 kHz to 18 kHz. The avoidance behaviour of the harbour porpoises was used to determine the discomfort threshold levels for each animal. These being Sound Pressure Levels (SPL) of 97 dB re 1 μPa for chirps and frequency sweep, but SPL of 103 dB re 1 μPa for DSSS, and 111 dB re 1 μPa for modulated FSK. The results were used to calculate estimated radius of the discomfort zone of each sound type based on a given source level (SL). For a source level of 170 dB re 1 μPa @ 1 m, the estimated radius of discomfort zones were 6.3 km for Chirp, 3.1 km for DSSS, 5.6 km for frequency sweep, and 1.26 km for modulated FSK. The sound type of modulated FSK has zero gap between packets so appears as a continuous sound, whereas the DSSS sound occurs in 1.0 s blocks with 0.7 s intervals. Kastelein previously determined that on-off switching sounds affect harbour porpoises [53]. Chirp sounds also have been shown to affect harbour porpoises [54]. From this it can be determined that continuous broadband noise-like signals have less effect than swept chirps and on-off switching sounds.

Kastelein, van der Heul, Verboom, Triesscheijn, and Jennings use the same sound types from [52] to determine the influence on the behaviour of nine captive harbour seals (Phoca vitulina) [55]. For all four of the sound types the estimated discomfort zone radius for a source level (SL) of 170 dB re 1 μPa at 1 m is 2.0 km. The estimated discomfort threshold sound pressure level (SPL) for all four sound types was found to be 107 dB re 1 μPa.

Kastelein, Hoek, Gransier, Rambags, and Claeys study the effects of naval sonar up-sweeps and down-sweeps on the behaviour of a single captive harbour porpoise [56].

Kastelein, Gransier, and Hoek study the effects of continuous and intermittent sound exposure on a harbour porpoise [57]. Specifically, the temporary hearing threshold shifts (TTS) that are induced. The sound type used was a 1 kHz to 2 kHz down-sweep of 1 s. Comparing the effects of sounds with the same cumulative sound exposure level (SEL_{cum}), intermittent sounds result in lower TTS than continuous sounds. Although as already seen, frequency sweep sound types are known to cause behavioural effects on harbour porpoises. It is not known from this study whether noise-like continuous signals would induce the same levels of TTS.

Tougaard, Wright, and Madsen produced a further review paper of published work related to noise influence on harbour porpoises. Much of the work by Kastelein et al. is also covered there [58].

2.3.5 Masking

The third of Richardson's theoretical zones of noise influence covers the concept of masking. Clark, Ellison, Southall, Hatch, Van Parijs, Frankel, and Ponirakis define the term masking as "failure of a person to recognize the occurrence of one type of stimulus as a result of the interfering presence of another stimulus." [59]. In the case of marine mammals this auditory masking can interfere with the reception of echolocation signals; communications between individuals; or detection of prey/predators.

2.3.6 Legislation

Legislation and agreements, both nationally and internationally, have been introduced as a means of mitigating against negative effects on known populations of marine mammals. A number of these agreements are tabulated by Jasny "International Conventions, Agreements, and Treaties with Relevance to Ocean Noise" [27, Table 4.1]. In European regional policy: ACCOBAMS, ASCOBANS and OSPAR [60] [61]. In the US, through litigation and mitigation as covered by Zirbel, Balint, and Parsons [62]. Marine noise pollution management continues to evolve, not just covering naval sonar exercises, but also construction, shipping, seismic survey etc. [63]. High-profile stranding events and the litigation that followed have also been described in a novel by Horwitz [64].

As stated by Scholik-Schlomer, "It is critical to try to avoid or mitigate potential impacts of man-made sounds on protected marine species." [65]. The full impact of anthropogenic noise is difficult to ascertain due to the complexity of the marine environment which becomes more apparent as research progresses. Taking a pragmatic approach to balance the level of protection with the costs/benefits is key.

2.4 Motivation: Low-cost and low-power Underwater Wireless Sensor Networks

Underwater Wireless Sensor Networks (UWSNs) using both mobile and static platforms are suitable for a variety of applications including environmental monitoring of conditions and marine life, equipment condition monitoring around offshore platforms, security monitoring of high value installations, amongst others.

Existing commercial underwater acoustic communication equipment can be both expensive and power-hungry, making it unsuitable for use in large installations of battery-powered sensors.

When considering these permanent battery-powered installations, in light of the impact on marine mammals seen earlier, there is further reason to reduce the transmit power in order to conserve energy.

Porto and Stojanovic show that reducing the transmission power and using more hops over the distance reduces the overall power used by the network. Reducing transmission power to limit receivable range to the nearest receiver node also has the effect of reducing interference elsewhere within the network. Meaning fewer collisions and delays due to retransmission/back-off [66].

Stojanovic also provides further argument for limiting the range of each individual transmission. As attenuation is frequency-dependent, for a given bandwidth there lies an optimum maximum transmission distance to ensure maximum channel capacity. For a nominal centre frequency of 12 kHz the curves presented would indicate an optimal range below 5 km [13]. This relationship between range and usable bandwidth becomes important when considering spread-spectrum signals.

Heidemann, Ye, Wills, Syed, and Li cover many of the applications and challenges faced with the design, implementation and testing of underwater wireless networks. Including stressing the challenges of short-lived battery-operated and expensive equipment [67] [68]. Much work is ongoing into the development of low-power, low-cost acoustic modems for use in research activities [69] [70] [71]. There is a plethora of activity in the area of network protocol design and analysis, all with the focus of increasing robustness whilst decreasing energy usage [72] [73], [74] [75] [76]. It is with such applications and challenges in mind that the research ahead takes place.

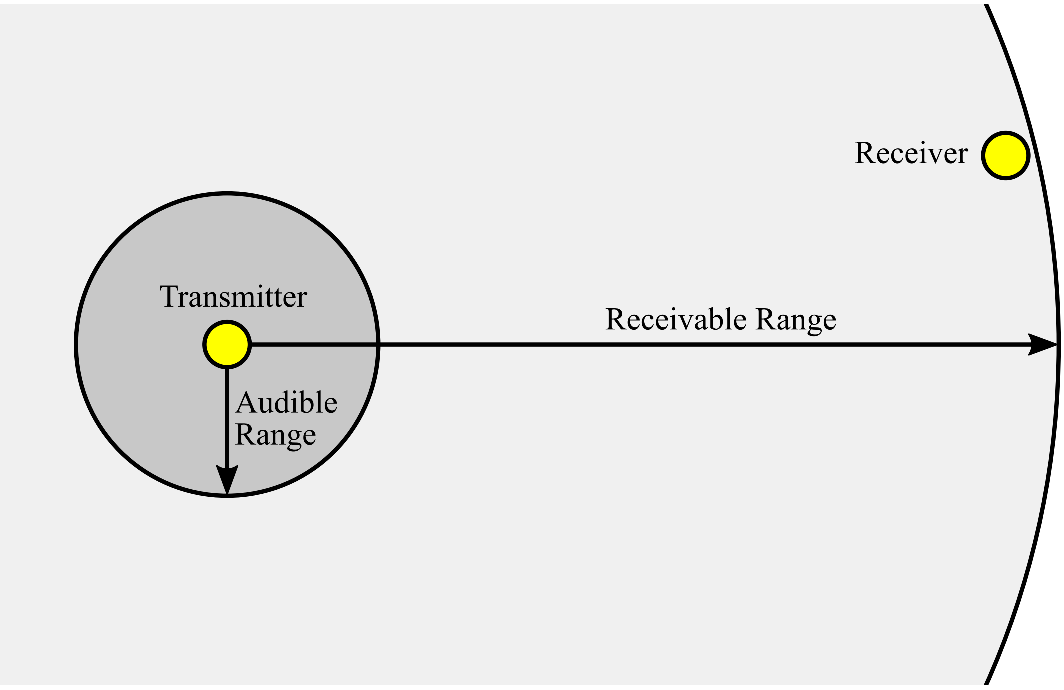

Fig. 2.9 Audible-Receivable Ranges

2.5 Aim: Reducing the Transmit Power and Audible Range

Taking into account the previous sections, there is a clear need for future underwater acoustic communications to both reduce the impact on the environment, and also reduce the energy usage in the drive for low-cost low-power underwater wireless sensor networks. The key objectives can be itemised as follows:

1. First and foremost, reduce the transmitter acoustic power such that there is no zone that results in injury. This also benefits battery-powered applications through reduced energy usage. From the research by Lucke et al [29] this means that the aim should be for a SPL less than 174 dB re 1 µPa near the transmitter.
2. Secondly, through signal and receiver design, increase the ratio of receivable range to audible range as shown in Fig. 2.9. Thus further reducing potential impact on marine mammals through behavioural responses or by masking marine mammal communication/echolocation signals. This allows the transmit power to be further reduced to limit the receivable range to just cover the nodes involved.
3. Thirdly, through signal design, create a signal that is broadly less likely to be detected by marine mammals or cause behavioural interference such as by not directly mimicking their communication styles through the use of chirps.

If the acoustic transmit power is nominally limited to ensure the sound pressure level (SPL) is 170.8 dB re 1 µPa at a distance of 1 m from an omni-directional transmitter then this translates to a Source Level (SL) of 170.8 dB re 1 µPa @ 1 m or 1 W of acoustic power.

2.6 State of the Art: Low-received-SNR and Covert Acoustic Communications

The research aims described previously include the reduction in transmit power and subsequent need for a low-received-SNR capable receiver; as well as a need for noise-like signals that show less discomfort in harbour porpoises than switching noise or chirps.

Many systems targeting low-received-SNR are typically for the purposes of covert acoustic communications. Signals are often described in terms of low probability of detection (LPD), and low probability of interception (LPI).

Diamant, Lampe, and Gamroth have recently provided a benchmark on which the degree of LPD can be determined for a given communication scheme. This is based on the ratio of successful detectable distance to successful receivable distance [78] [77].

Detection techniques used when searching for covert signals are covered by Ginolhac and Jourdain [80] [79], Kuehls and Geraniotis [81], and Burel, Bouder, and Berder [82].

A three year European project "UUV - Covert Acoustic Communications (UCAC)" (Project RTP 110.060) explored covert communication schemes and channel conditions in littoral environments. Acoustic channel conditions were recorded and measured using probe signals, with a simulator subsequently produced [83] [84]. A number of modulation schemes, with constraints on bandwidth and data rate, were designed and tested using this simulator and in sea trials as shown in Table 2.3 [85] [86] [87] [88] [89] [90] [91] [92].

The DSSS with turbo equalization achieved performances of 4 bit/s at -14 dB at a range of 52 km. For data rate of 75 bit/s the performance was -6.5 dB. All with a bandwidth of 3.5 kHz [90]. The channel capacity at -14 dB is 197.12 bit/s indicating a channel utilisation of 2.03% for the lower data rate. The channel capacity at -6.5 dB is 1020.08 bit/s indicating a channel utilisation of 7.35% for the higher data rate.

The multiband OFDM achieved performances of 4.2 bit/s at -17 dB at a range of 52 km. For data rate of 78 bit/s the performance was -8 dB. The performance of the lower data rate packets were ultimately limited by the ability to successfully synchronise. The modulation scheme with coding in simulation showed a potential performance of BER 10^{-4} at SNR of -20 dB. The bandwidth is 3.6 kHz. [89] [88]. The channel capacity at -17 dB is 102.61 bit/s indicating a channel utilisation of 4.09% for the lower data rate. The channel capacity at -8 dB is 764.08 bit/s indicating a channel utilisation of 10.21% for the higher data rate.

Table 2.3 UUV Covert Acoustic Communications Project: Signals

Modulation Scheme	Bandwidth	FEC	Low Data Rate	High Data Rate	Referenced
DSSS	3.5 kHz	⅓-rate turbo code	4.2 bit/s	75 bit/s	[90]
Multiband OFDM	16 bands with total of 3.6 kHz	⅓-rate turbo code	4.2 bit/s	78 bit/s	[88] [89]
Chirp-DSSS	3.5 kHz	None	13 bit/s	226 bit/s	[85]
MCSS	8 BPSK bands of 460 Hz each. Total of 3.68 kHz	⅓-rate turbo code	None	75 bit/s	[86] [87]

The Chirp-DSSS achieved an error-free performance of 13 bit/s at -4.9 dB at a range of 7.5 km. The bandwidth is 3.5 kHz [85]. The channel capacity at -4.9 dB is 1415.61 bit/s indicating a channel utilisation of 0.92%.

The MCSS achieved performances of 75 bit/s at -12 dB at a ranges up to and including 52 km. The bandwidth is 3.68 kHz [86] [87]. The channel capacity at -12 dB is 324.84 bit/s indicating a channel utilisation of 23.09% .

Yang and Yang explore low-received-SNR underwater acoustic communications using BPSK and DSSS [93]. Ling, He, Li, Roberts, and Stoica explore covert underwater acoustic communications using QPSK with DSSS [94] [95]. Lei, Xu, Xu, and Wu focus on LPI through the use of a chaotic sequence for DSSS with BPSK [96]. Ahn, Jung, Sung, Lee, and Park look at turbo equalisation for targeting low-SNR and LPI applications [97].

Liu, Ma, Qiao, Ma, and Yin aims for covertness by mimicking nature. Though in the context of the research aims, this is antithesis to reducing the potential impact on marine mammals [98].

Demirors and Melodia aims for LPD and LPI through the use of Chirp-BOK combined with code-time-frequency spreading. Again, the use of chirps as shown previously is undesirable when reducing potential impact on marine mammals [99].

Hanspach and Goetz explore covert aerial acoustic communications through the use of ultrasonic FHSS signals making them inaudible to humans [100].

2.7 State of the Art: Toward Environmentally-Friendly Acoustic Communications

There are other approaches to creating more environmentally-friendly acoustic communication systems. These approaches, instead of producing coding and modulation schemes to target low-received-SNRs, monitor the spectrum and locality for marine mammal activity and either change spectrum usage through Cognitive Acoustics (CA) [101] [102] [103], or else limit the instantaneous transmit power such that the energy received at the animal's estimated location falls below the level that would induce a hearing threshold shift [104] [105] [106].

These approaches rely heavily on the correct detection, identification, and localisation of all marine life in order for the environmentally-friendly aspects to function well. Any animal that does not emit any call within the vicinity of the network nodes (and hence is not detected) will potentially be subjected to uncomfortable or dangerous levels of acoustic energy.

Dimitrov, Neasham, Sharif, Tsimenidis, and Goodfellow consider the use of m-ary orthogonal signaling using carrierless PN sequences to achieve low-received-SNR underwater acoustic communications [107].

2.8 Research Aims and Objectives

The research aims mentioned previously have indicated a need to reduce the transmit power whilst maintaining receivable range, requiring signals and receiver structures that can operate at low-received-SNRs. The state-of-the-art covered since has explored various approaches to achieving successful communications at such low-received-SNRs. In combination with the research into behavioural responses of marine mammals from different signal types, it is clear that such a system needs to utilise a longer duration, noise-like signal. The state-of-the-art systems targeting covert applications make use of complex receiver structures using turbo coding and equalizers that run converse to the target hardware applications for this research, such as low-power battery-operated wireless sensor networks. There is therefore a need for a simpler receiver structure and signal scheme that can operate with similar performance to the covert communication systems covered in this review. The approach introduced by Dimitrov et al. is worth exploring further due to the relatively simple receiver structure and signaling technique in use whilst still able to target the low-received-SNRs that are required to meet the overall research aims.

The research presented hereafter seeks to explore the design, development and implementation of a holistic communications system with a relatively simple receiver structure able to operate at low-received-SNRs in a range of underwater acoustic channels.

Chapter 3

Signal Design

3.1 Introduction

As identified in Chapter 2, the aim is to design a communication scheme, signal and receiver, suitable for low-power, low-received-SNR signals that have been transmitted through the underwater channel.

This chapter takes a look at the scheme initially introduced by Dimitrov et al. for a carrierless pseudonoise (PN) modulation scheme with a view to expanding on this.

The process of signal spreading is explained with a focus on spreading through the use of PN sequences. Properties of PN sequences, especially maximal length sequences, are detailed with respect to how they apply to such a modulation scheme.

Design of m-ary orthogonal code keying (M-OCK) signals are covered including symbol generation and data packet construction. Spectral properties are compared with LFM Chirps and BPSK modulated m-sequences. Simulations highlight the upper bound performance of ideal m-ary orthgonal signaling in contrast to the theoretical performance of another popular m-ary signaling scheme, m-ary quadrature amplitude modulation (M-QAM).

Simulated performance of the m-ary orthogonal code keying (M-OCK) modulation scheme in AWGN channel allows comparison with the theoretical performances. Effects of independently varying the modulation depth and symbol duration are highlighted with potential received SNR of such a scheme presented.

Doppler effects and the ambiguity function of different duration bandlimited PN sequences in comparison with various LFM and HFM chirp symbols are presented.

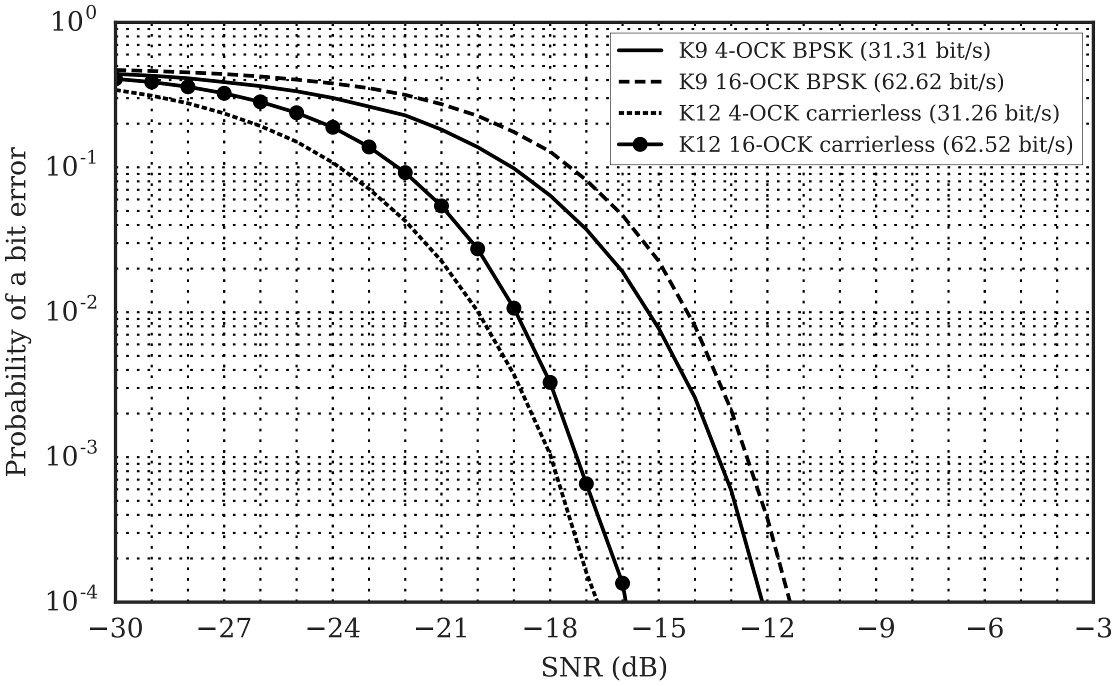

Fig. 3.1 Performance of Carrierless PN and BPSK modulated PN sequence signals with sample frequency of 64 kHz. BPSK has a carrier frequency of 12 kHz. All signals have a frequency band of 8 kHz to 16 kHz and a spreading process gain of 27.1 dB. Based on the simulations by Dimitrov et al. [107].

3.2 Motivation

Work by Dimitrov, Neasham, Sharif, Tsimenidis, and Goodfellow proposed a concept for a low-received-SNR, environmentally-friendly modulation scheme [107]. Based on the premise of carrierless PN sequences to produce an m-ary orthogonal signaling scheme. This work intends to explore this concept in more depth and take it forward to design and test a viable communication system. It also sets out to determine the performance boundaries of the signal design for synchronisation and data demodulation in low-received-SNR channels.

Dimitrov et al. compared carrierless PN sequences and a BPSK modulated PN sequence signal with equivalent bandwidth (8 kHz), modulation depth, and data rates. In AWGN simulations with a modulation depth of 4, a data rate of 31 bit/s and a BER of 10^{-4} the BPSK modulated signal achieved an SNR of -12 dB, however the carrierless signal achieved an SNR of -17 dB. These results can be seen in Fig. 3.1. A low-received SNR is key to reducing the audible range whilst maintaining a useful receivable range. This improvement in performance of carrierless PN signal over BPSK modulated PN sequence signal makes it an attractive modulation scheme.

The carrierless PN signal is trivial to generate with a linear feedback shift register (LFSR) and potentially leads to very low complexity transmitting devices [108].

For other applications where probability of detection by sonar processing must be minimised (e.g. covert submarine communications), the carrierless signal is a better option due to its truly white spectrum. Furthermore the cyclostationarity of BPSK modulated signals means they are vulnerable to simple detection techniques e.g. square law carrier recovery [81, 78, 77]. There is also evidence of non-linearities in the hearing of marine mammals that may also expose this carrier, by acting as an envelope extractor, leading to undesired behavioural responses [109].

3.3 Background

The signal concept proposed takes the narrowband signal and spreads it over a wideband through the use of unique pseudorandom binary sequences. A background of signal spreading, and pseudorandom sequences follows.

3.3.1 Signal Spreading / Spread-Spectrum Signals

Spread-spectrum techniques involve taking a narrowband information signal and spreading the energy over a wider frequency band. There are a number of existing ways of achieving this including frequency-hopping spread spectrum (FHSS), direct-sequence spread spectrum (DSSS), and chirp spread spectrum (CSS).

The Shannon-Hartley theorem [110] in (3.1) provides a way to calculate the channel capacity, C, for a given bandwidth, B, and signal-to-noise ratio (SNR). As the bandwidth is increased through signal spreading, whilst the symbol duration is kept constant, the received signal to noise ratio required for error-free communication is decreased. Example channel capacities for a number of bandwidths are shown in Fig. 3.2.

$$C = B\log_2\left(1+\frac{P_{signal}}{P_{noise}}\right)\ \text{bit/s} \tag{3.1}$$

As shown by Torrieri [111, (2-5), p 58] the effective processing gain of a symbol, PG_s, through signal spreading can be calculated from the spread-spectrum bandwidth, B, and symbol period, T_s, in (3.2). Therefore, doubling the bandwidth effectively increases the performance for a given channel capacity by 3 dB as seen in Fig. 3.2.

$$PG_s = 10\log_{10}(BT_s)\ \text{dB} \tag{3.2}$$

The effect of the signal spreading can be visualised in Fig. 3.3. Here the spread-spectrum signal peak power can be lower than the background noise level, i.e. low received-SNR, but the processing gain through despreading produces a greater information SNR for successful demodulation.

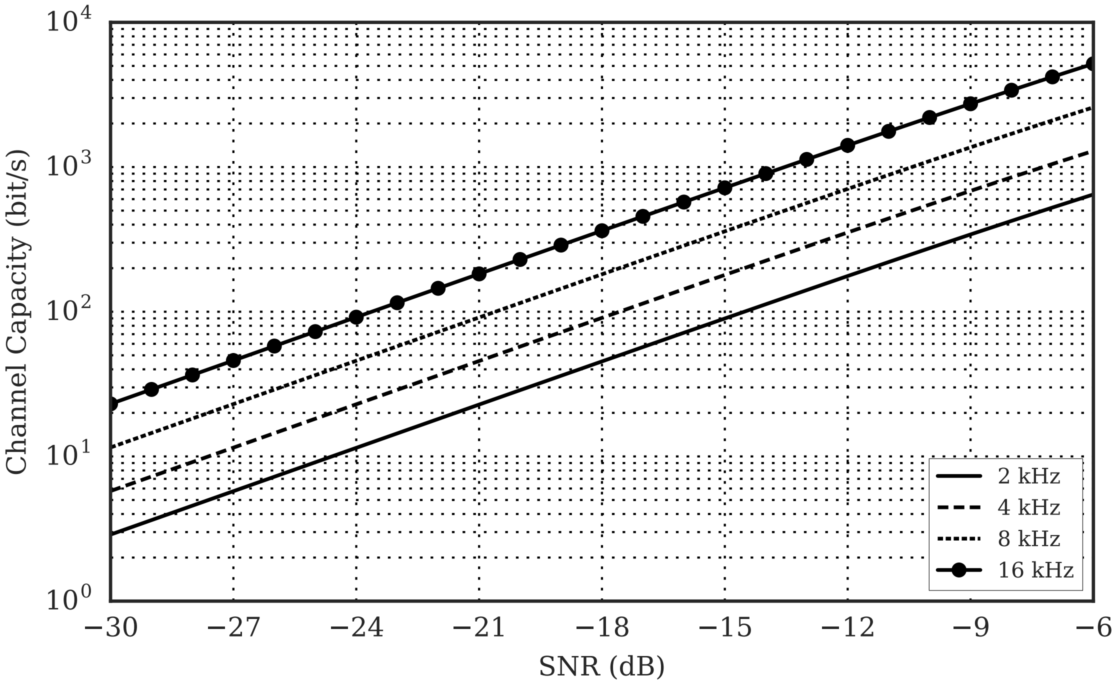

Fig. 3.2 Shannon-Hartley Channel Capacities

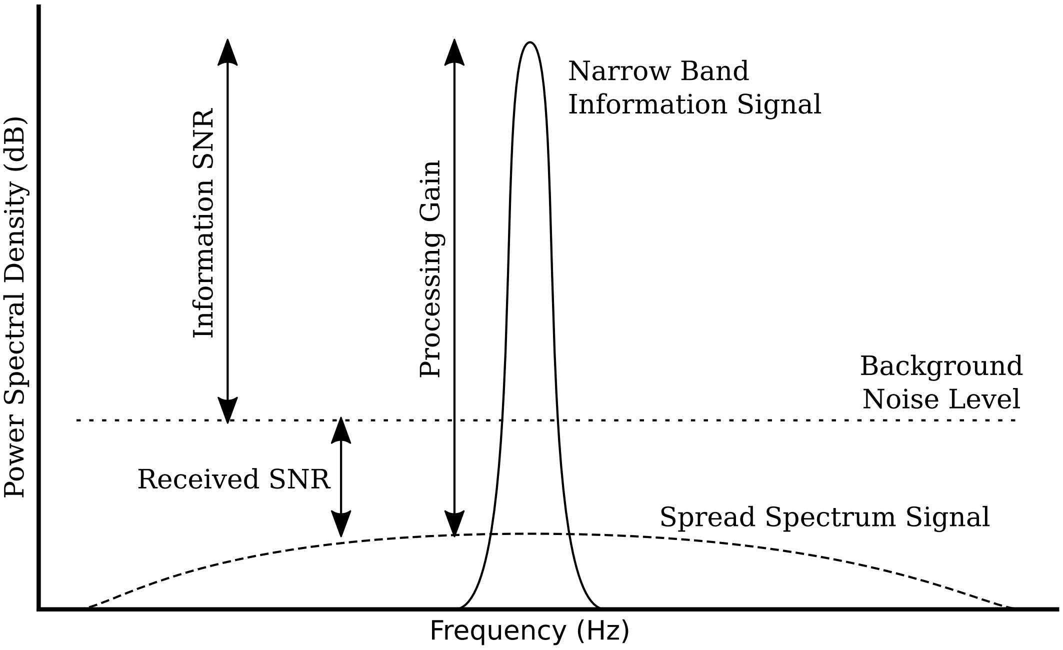

Fig. 3.3 Signal Spreading Diagram

3.3.2 Pseudo Random Binary Sequences

The properties of random binary sequences are defined by Golomb [108, pg43] [112, pg118]. Where the sequence, a has a length of N the autocorrelation function $C_a(\tau)$ is defined by (3.3) and is effectively the unnormalised dot product of two vectors.

$$C_a(\tau) = \sum_{i=0}^{N-1} (-1)^{a_{i+\tau}+a_i} \tag{3.3}$$

Golomb then defines the three randomness postulates as follows:

R1 In a given period the number of zeros and ones differs by only one.

R2 In a given period, there are runs of ones or zeros. Half of these runs have length of one, a fourth have a length of two, an eight have a length of three, a sixteenth have a length of four, and so on.

R3 The autocorrelation function $C(\tau)$ has values of N when $\tau = 0$ and K when $\tau \neq 0$. Where K is a constant.

3.3.3 Maximal Length Sequences

Maximal Length Sequences, also known as M-Sequences, are a form of pseudorandom-noise sequence generated by cycling through a linear feedback shift register with a particular configuration of feedback taps (Galois). For a given order, or shift register length, of K, this would generate a unique sequence of length $N = 2^K - 1$. The feedback tap locations to produce the m-sequence can be derived from the primitive polynomials for the order, K. Each coefficient is either zero or one and determines the existence of a tap at that position. The shift register can be seeded with any sequence with the exception of all zeros.

M-sequences have a number of key properties that make them suitable for use in signal spreading:

1. They possess a zero D.C. component due to the near balance of zeros and ones. The remaining frequency spectrum is flat with the auto-correlation being delta-like.
2. The auto-correlation value of an m-sequence is equal to its length.
3. A number of m-sequences of a given order possess a high degree of orthogonality when cross-correlated with each other compared to their auto-correlation values.

The correlation properties of m-sequences have been studied with tables produced [113, Table 12.2-1] showing the cross correlation values for orders up to $K = 12$. Where $R(0)$ is the auto correlation value, which is equal to the code length, and R_{max} is the peak cross correlation

Table 3.1 M-Sequence Code Properties

Order, K	Code Set Size	Maximum Data bit/symbol, m	Code Length $2^K - 1$	$\frac{R_{max}}{R(0)}$
7^a	18	4	127	0.35
8	16	4	255	0.37
9	48	5	511	0.23
10	60	5	1023	0.37
11	176	7	2047	0.15
12	144	7	4095	0.34
13^a	630	9	8191	0.09
14	756	9	16383	0.34
15	1800	10	32767	0.15
16	2048	11	65535	0.34

[a] Mersenne Prime

value or maximum sidelobe value across all combinations. The ratio $R(0)/R_{max}$ indicates the impact on the degree of orthogonality with lower values having higher degree of orthogonality. This table has been extended to include orders up to $K = 16$ in Table 3.1. We also consider the number of unique codes available for each order and use this as a modulation depth to determine the maximum number of data bits that can be carried per symbol, m.

The auto- and cross-correlation properties of a set of bandlimited m-sequences are shown in Fig. 3.4 for an 11th order m-sequence with a codeset of 64 unique codes all bandpass filtered between 8 kHz to 16 kHz. Every permutation of codes is cross-correlated and the peak value recorded. The 2D image plot shows the peak value for every permutation of codes in the set. There is a clear peak for the autocorrelation value, which is distinct from the cross-correlation values with other codes. Looking at the bar plot of a single code ID cross-correlated against the entire code set shows a strong peak for the auto-correlation and a much lower value across the remaining codes in the set. There is no concept of a nearest neighbour in such an orthogonal modulation scheme, with all other codes equally as likely. This is further demonstrated in Fig. 3.5 which shows the auto- and cross-correlation results for a 13th order m-sequence with a codeset of 256 unique codes, again bandpass filtered as before.

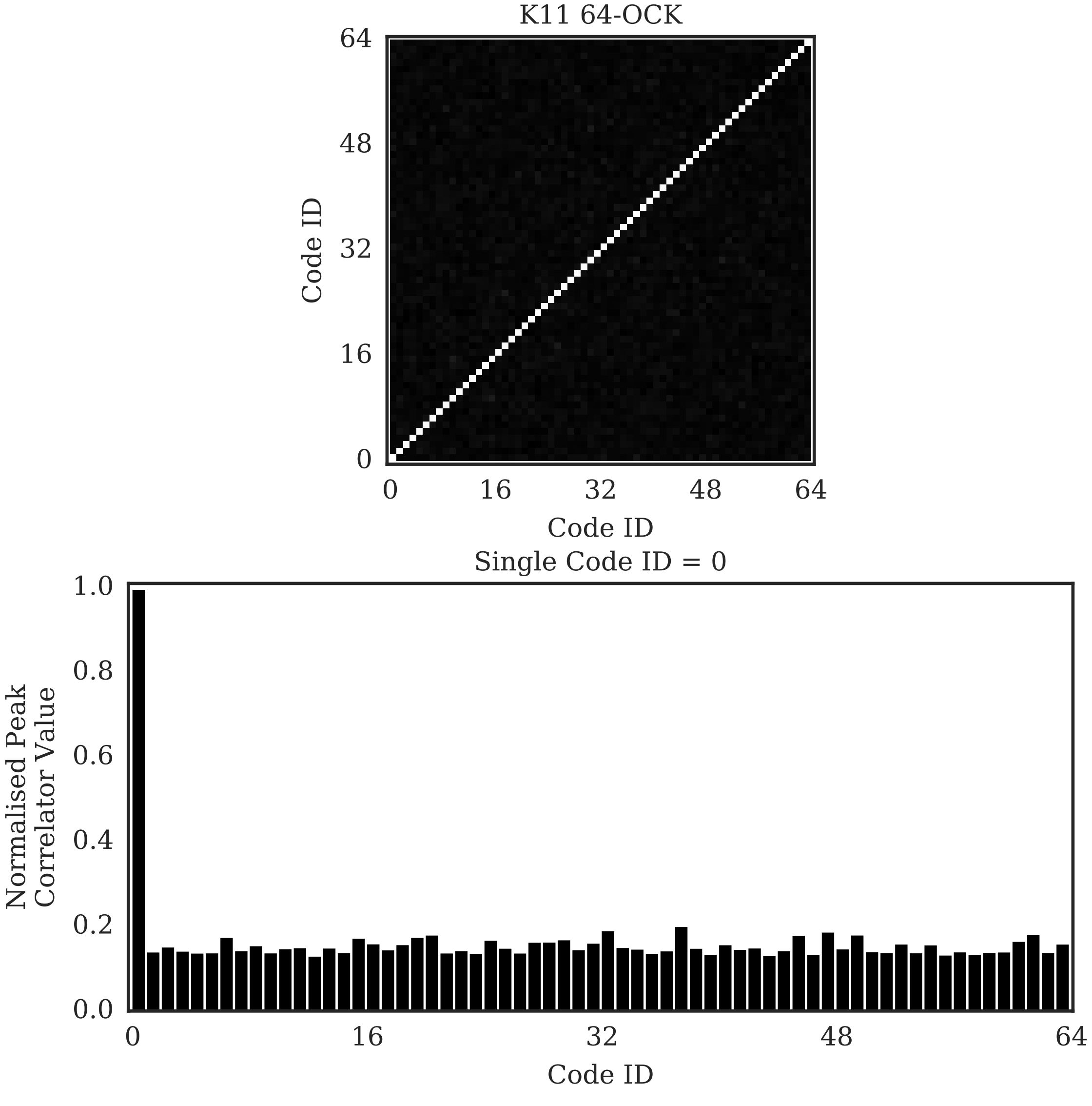

Fig. 3.4 Cross Correlation Properties of Bandlimited M-Sequence Code Set. $K = 11$, Code Set size = 64

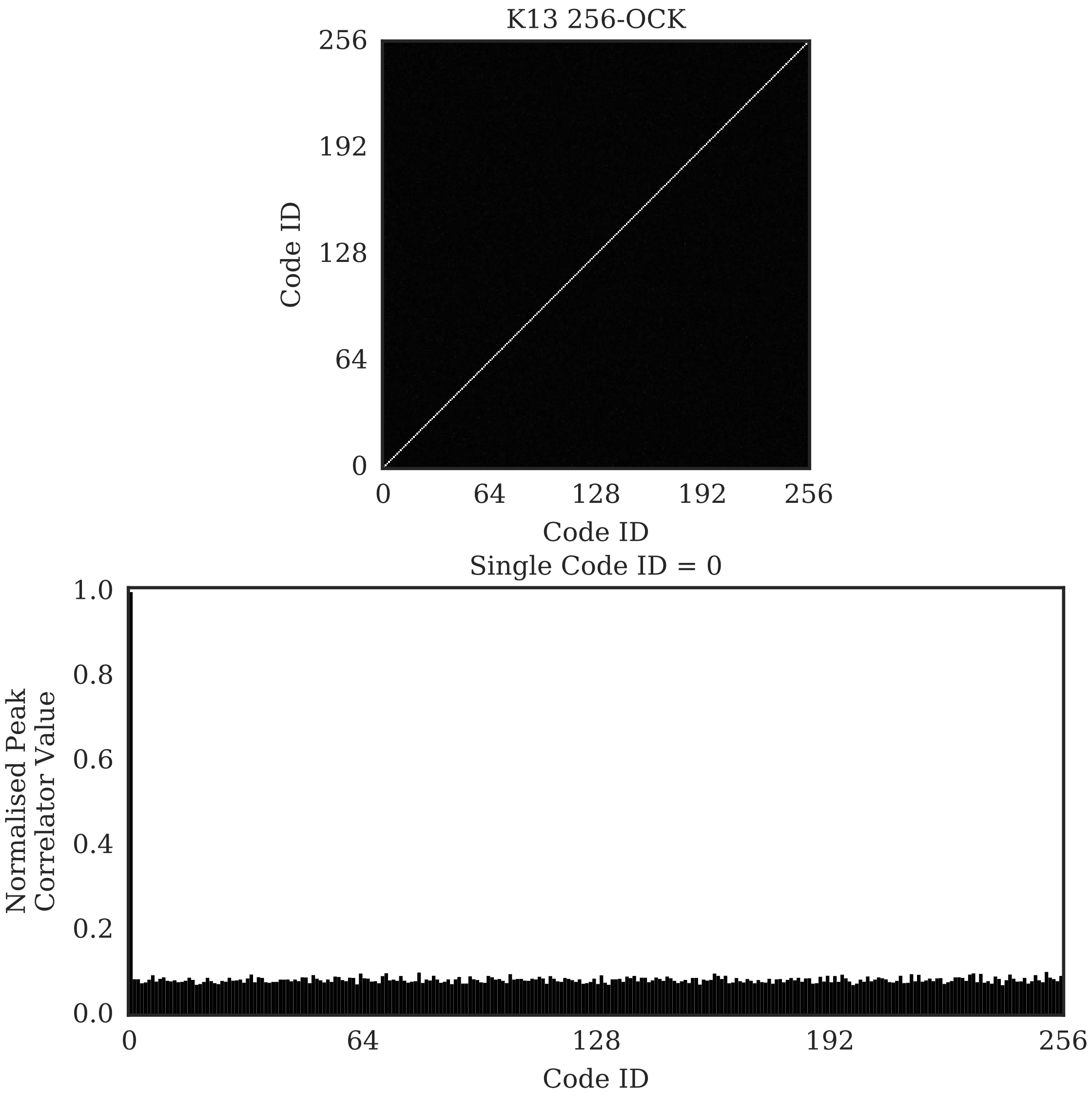

Fig. 3.5 Cross Correlation Properties of Bandlimited M-Sequence Code Set. $K = 13$, Code Set size = 256

3.4 Design of M-ary Orthogonal Code Keying Signal

Having considered the background of signal spreading and pseudorandom binary sequences, the following section covers the generation of symbols and data packets in a m-ary orthogonal signaling modulation scheme.

3.4.1 Symbol Generation

Taking an m-sequence of a given order, K, and applying a nominal sampling frequency, F_s, and spreading bandwidth, B, it is possible to calculate the effective processing gain due to spreading PG_s in (3.2). This equation can be rearranged to directly relate the code length, $N = 2^K - 1$, and the sampling frequency, F_s, where $T_s = N/F_s$ as in (3.4):

$$\begin{aligned} PG_s &= 10\log_{10}(BT_s) \text{ dB}, \\ &= 10\log_{10}\left(B \cdot \frac{N}{F_s}\right), \\ &= 10\log_{10}(N) - 10\log_{10}\left(\frac{F_s}{B}\right). \end{aligned} \tag{3.4}$$

Code generation using m-sequences consists of producing a given sequence from a seeded linear feedback shift register and appropriate feedback taps. The sequence is then converted to bipolar non-return-to-zero level (NRZ Level) form at the given sample frequency. This equates to a positive voltage for a binary one and a negative voltage for a binary zero value.

These codes are then bandpass filtered resulting in a carrierless bandlimited pseudo-noise symbol for use in the M-ary Orthogonal Code Keying (M-OCK) modulation scheme. Example processing gains from spreading, and the maximum data rate based on the code set sizes for m-sequences are shown in Table 3.2.

Terminology used in this thesis to describe a particular M-OCK symbol set is based on the m-sequence order, K, and the modulation depth employed, M. For example, K11 64-OCK refers to 11-order m-sequences with a modulation depth of 64.

3.4.2 Data Packet Construction and Demodulation

As shown in Table 3.1 there are a finite number of primitive polynomials for a given order, K, of m-sequence and hence a finite number of near orthogonal m-sequences available. In constructing a data packet, data bits are mapped to a modulation index and the appropriate m-sequence from the code set is selected and the bipolar non-return-to-zero level (NRZ Level) sequence of ± 1 bits is appended to the packet. The resultant packet is then bandpass filtered ready for eventual transmission through the channel.

Table 3.2 M-OCK Code Properties based on $F_s = 48\,\text{kHz}$ and $B = 8\,\text{kHz}$, where spreading gain is calculated using (3.2), and $T_s = N/F_s$.

Order, K	Code length, N	Symbol Duration, T_s	Symbol Processing Gain, dB	Maximum Data Rate bit/s with spreading
7^a	127	2.65 ms	13.26	1511.81
8	255	5.31 ms	16.28	752.94
9	511	10.65 ms	19.30	469.67
10	1023	21.31 ms	22.32	234.60
11	2047	42.65 ms	25.33	164.14
12	4095	85.31 ms	28.34	82.05
13^a	8191	170.65 ms	31.35	52.74
14	16383	341.31 ms	34.36	26.37
15	32767	682.65 ms	37.37	14.65
16	65535	1365.31 ms	40.38	8.06

[a] Mersenne Prime

Demodulation of the data packet uses maximum-likelihood (ML) detection of the received code by correlating the signal with all codes in the set and taking the code that produces the greatest correlation value within a narrow window.

Orthogonality of the modulation scheme implies that all messages are equiprobable a priori. Proakis provides the equation for maximum likelihood detection of such messages [113, (4.1-11)] in (3.5). Where the prior probabilities, $P_m = \frac{1}{M}$ for all $1 \leq m \leq M$, $\mathbf{r}$ is the received vector, $\mathbf{s}_m$ is the signal vector, $p(\mathbf{r}|\mathbf{s}_m)$ is the likelihood of message m.

$$\hat{m} = \underset{1\leq m\leq M}{\arg\max}\, p(\mathbf{r}|\mathbf{s}_m) \tag{3.5}$$

3.5 Signal Properties

Having considered the generation of symbols and packets in the m-ary orthogonal code keying modulation scheme, the properties and performance are now examined.

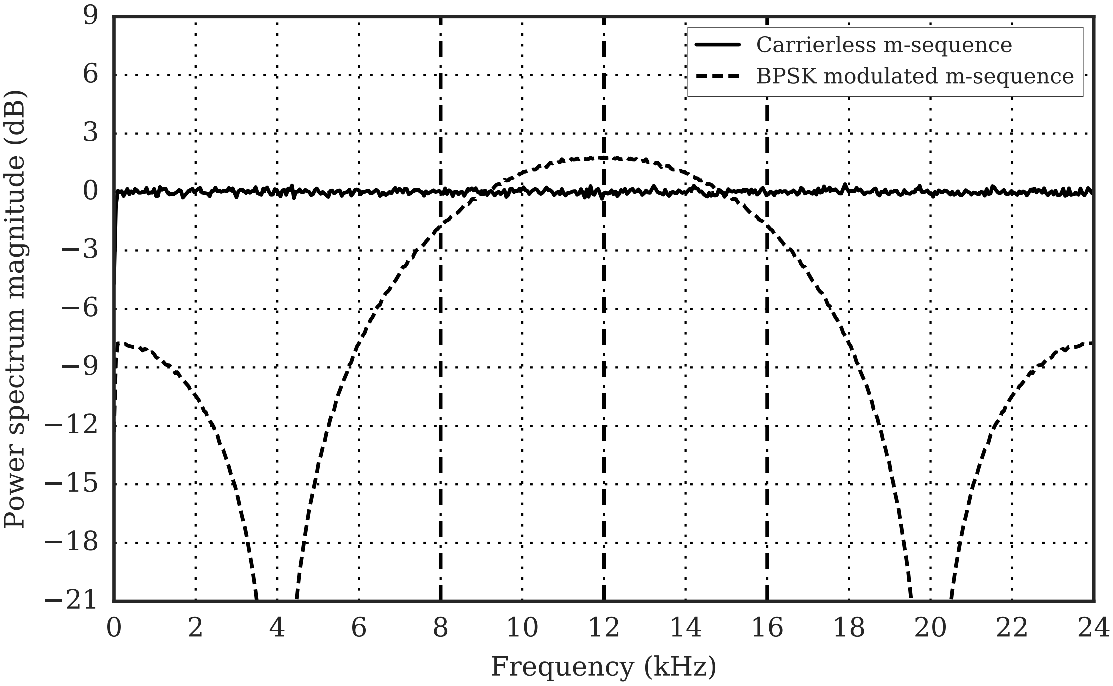

Fig. 3.6 Power spectrum magnitudes of BPSK modulated m-sequence and carrierless m-sequence signals with sample frequency of 48 kHz. BPSK has a carrier frequency of 12 kHz. The vertical lines at 8 kHz and 16 kHz indicate the limits of the subsequently transmitted bandlimited signal. The original figure was produced by the author [1, Fig. 3]

.

The work by Dimitrov et al. compared the performance of a carrierless M-Sequence signal and a BPSK modulated M-Sequence signal with equivalent process gains [107]. The frequency spectrum of both signals is shown in Fig. 3.6. In AWGN simulations with a bandwidth of 8 kHz, a data rate of 31 bit/s and a BER of 10^{-4} the BPSK modulated signal achieved an SNR of -12 dB, however the carrierless signal achieved an SNR of -17 dB as seen in Fig. 3.1.

The noise-like bandlimited PN sequence can be compared with a LFM chirp, as used in Binary Orthogonal Keying (BOK), of equivalent bandwidth and duration combined with varying AWGN as shown in Fig. 3.7. As AWGN increases it is possible to see that the PN becomes lost in the noise whilst it is still possible to identify the linear chirp in Fig. 3.7. Both techniques effectively spread the signal over wide bandwidth, however when considering the instantaneous power distribution, the bandlimited PN is more evenly distributed whereas the LFM chirp is instantaneously narrowband thus concentrating the power and still being visible in the waterfall plot at low SNR.

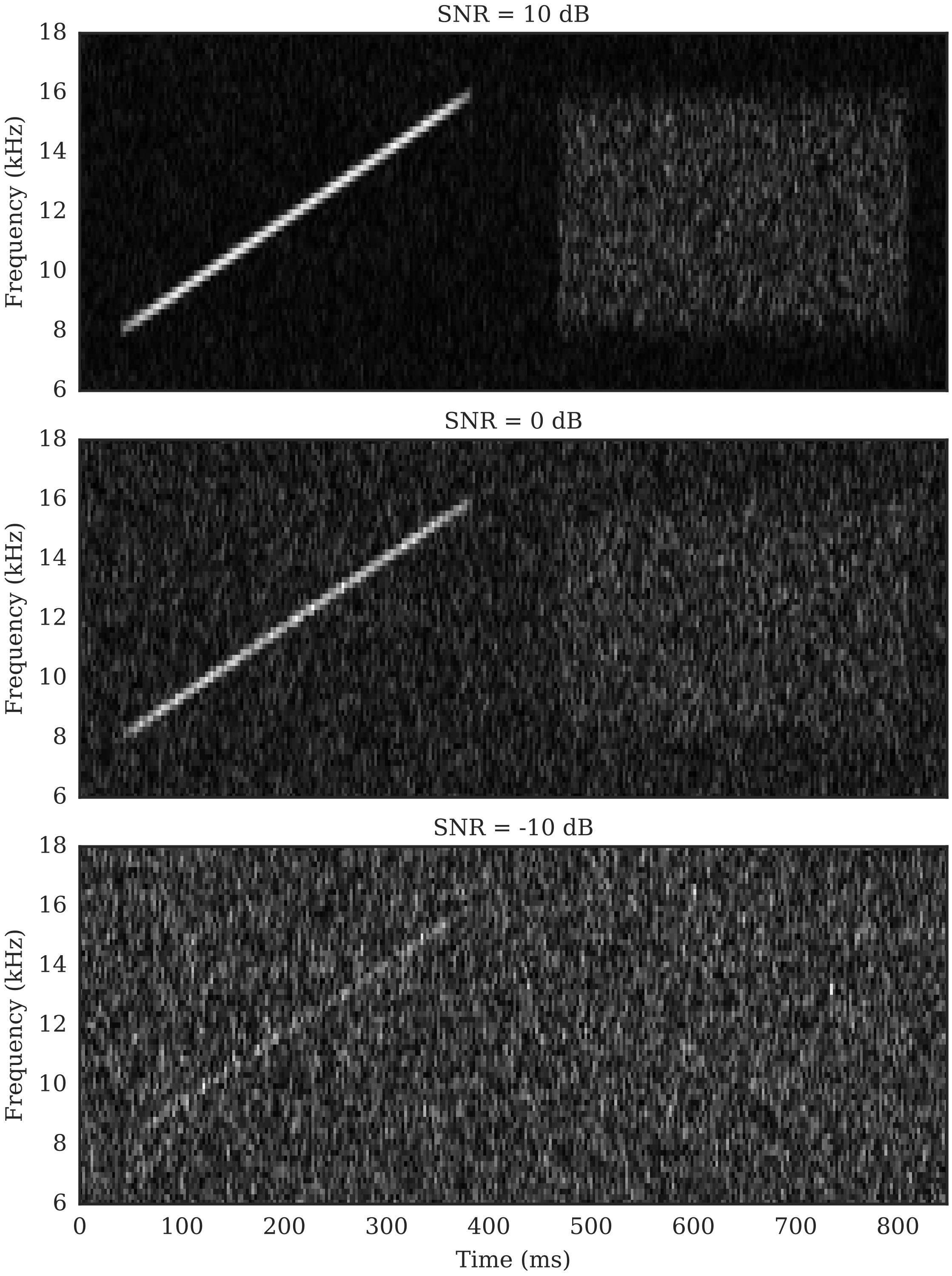

Fig. 3.7 Waterfall plot (Frequency vs Time) of bandlimited PN vs linear chirp with varying AWGN noise

3.6 Error Probability for M-ary Orthogonal Signaling

In considering the development of an m-ary orthogonal modulation scheme, the theoretical performance of m-ary orthogonal signaling is of interest.

Probability of symbol error and bit error for an m-ary orthogonal signaling scheme has been analysed by Proakis [113, Section 4.4-1] who provides the equations below. Where the probability of symbol error, P_e, can be solved for a given symbol energy, ε, noise, N_0, and number of possible orthogonal symbols, M, in (3.6). This can then be used to calculate the bit error, P_b, for a given number of data bits per symbol, k, where $M = 2^k$, in (3.8).

$$P_e = \frac{1}{\sqrt{2\pi}} \int_{-\infty}^{\infty} \left[1-(1-Q(x))^{M-1}\right] e^{-\frac{\left(x-\sqrt{\frac{2\varepsilon}{N_0}}\right)^2}{2}} \mathrm{d}x \tag{3.6}$$

Equation (3.6) has no known closed form, however an upper or union bound equation is provided by Proakis [113] as shown in (3.7) Where $k = \log_2 M$ and $\frac{\varepsilon_b}{N_0} > \ln 2 = 0.693 \approx -1.6\text{dB}$.

$$P_e \leqslant \begin{cases} e^{-\frac{k}{2}\left(\frac{\varepsilon_b}{N_0}-2\ln 2\right)}, & \frac{\varepsilon_b}{N_0} > 4\ln 2 \\ 2e^{-k\left(\sqrt{\frac{\varepsilon_b}{N_0}}-\sqrt{\ln 2}\right)^2}, & \ln 2 \leqslant \frac{\varepsilon_b}{N_0} \leqslant 4\ln 2 \end{cases} \tag{3.7}$$

Taking the upper bound probability of symbol error the respective bit error is calculated using (3.8).

$$P_b = 2^{k-1}\frac{P_e}{2^k-1} \tag{3.8}$$

As the modulation depth is increased, the energy-per-bit required to maintain a given bit error probability is decreased, as shown in Fig. 3.8.

3.6.1 Comparisons with Other M-ary Signaling Techniques

It is possible to compare the theoretical bounds of orthogonal signaling against another m-ary system such as M-ary Quadrature Amplitude Modulation (M-QAM). Fig. 3.9 shows the negative effect on performance as the modulation depth is increased; a stark contrast to the trend shown by orthogonal signaling in Fig. 3.8. The M-QAM performance curves were generated based on recursive approximation 2 by Yang and Hanzo [114].

The decreasing performance of M-QAM with increasing modulation depth can be seen as a result of a decrease in euclidean distance between neigbouring constellation points as seen in the rectangular QAM constellations in Fig. 3.10.

Evidently, m-ary orthogonal signaling schemes outperform m-ary quadrature amplitude modulation for larger values of M.

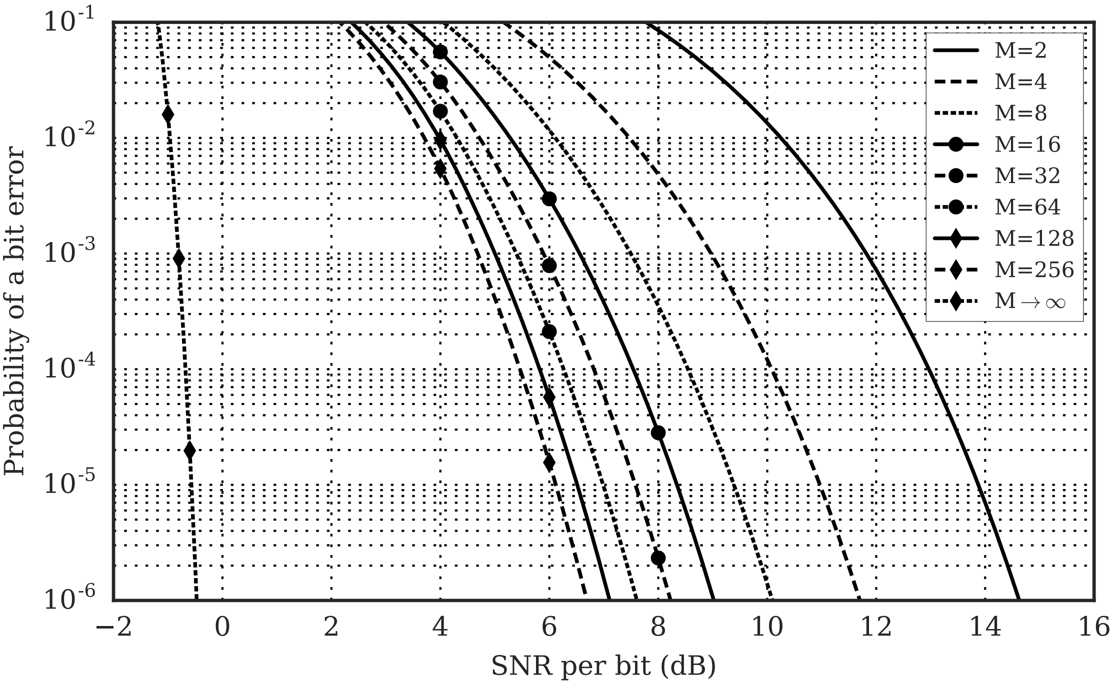

Fig. 3.8 Upper Bound BER vs ε_b/N_0 for various values of M for M-ary Orthogonal Signaling with values of M ranging from 2 to 256. For M→ ∞ the value used is M= 2^{1000}.

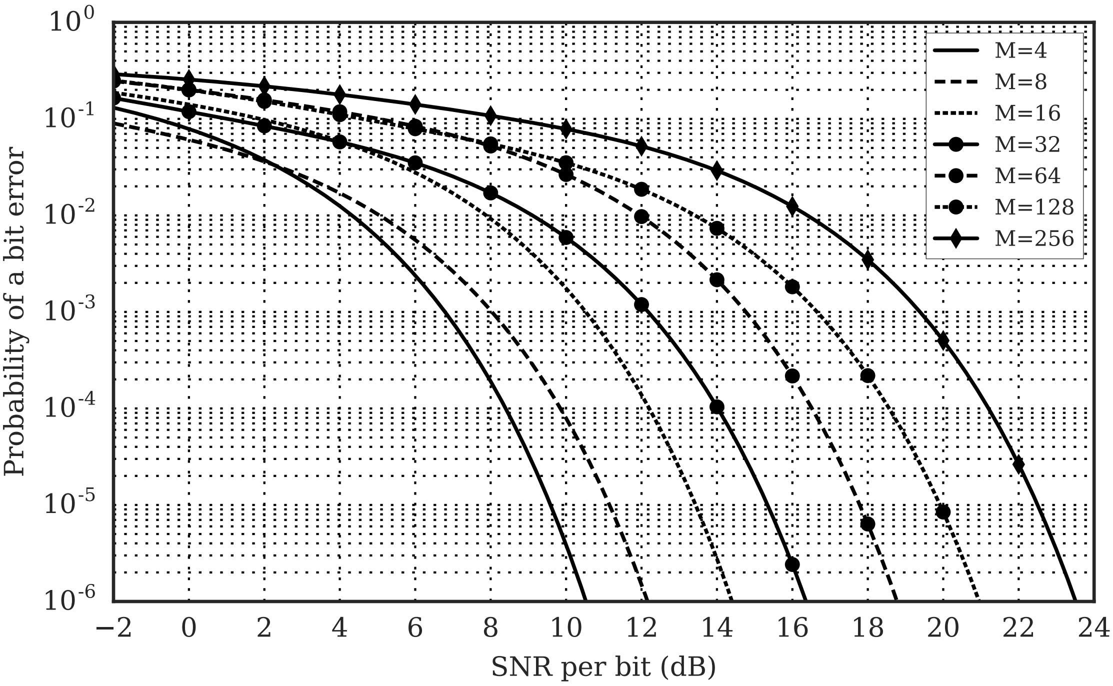

Fig. 3.9 BER vs ε_b/N_0 for various values of M for M-ary Quadrature Amplitude Modulation with values of M ranging from 4 to 256. Generated using approximation 2 by Yang and Hanzo [114].

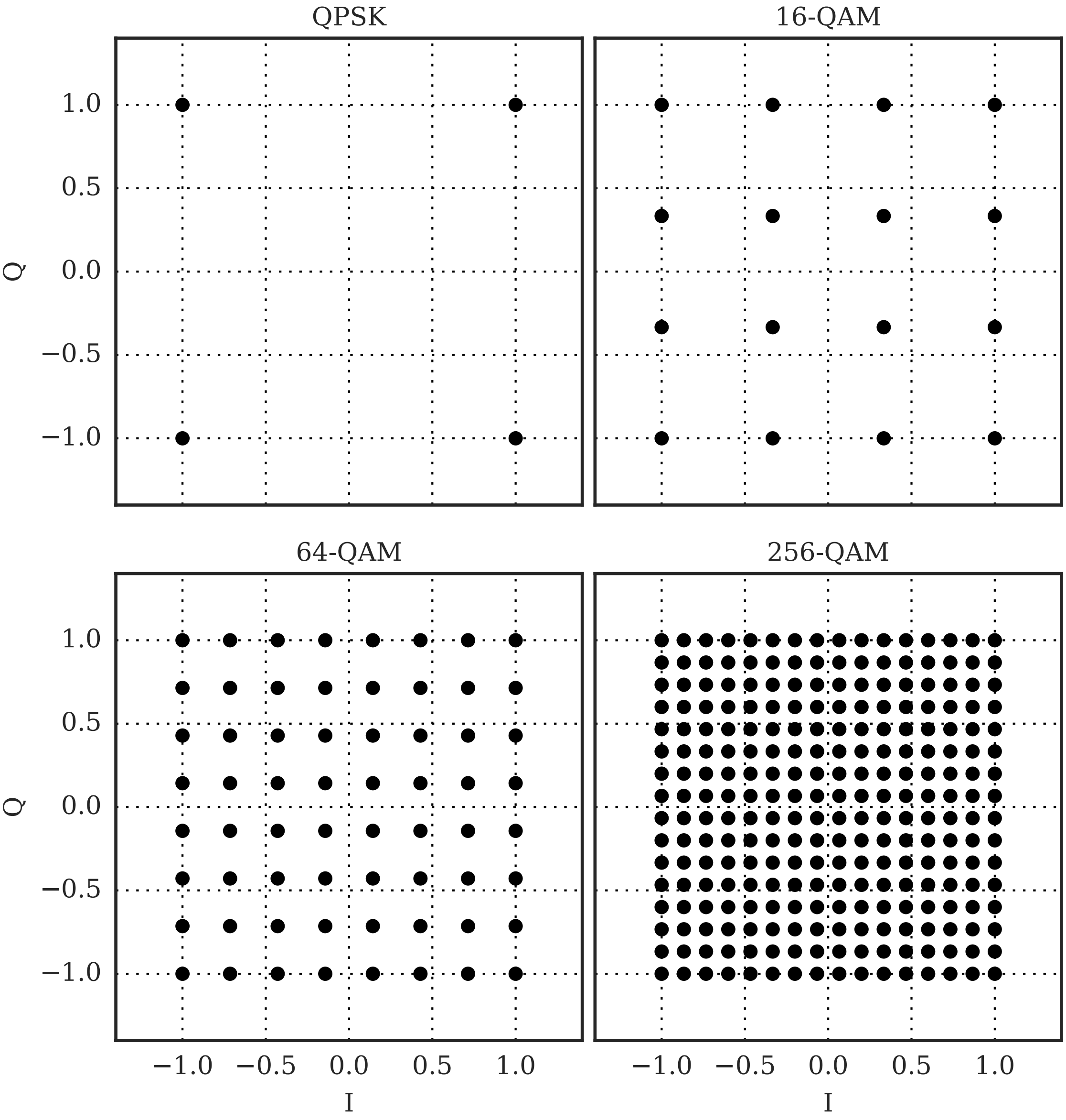

Fig. 3.10 Rectangular M-QAM Constellations for varying values of modulation depth from 4 to 256. It can be seen that as the modulation depth increases, the euclidean distance between constellation points decreases, thus increasing the probability of symbol error.

3.7 Simulated Ideal BER Performance of M-OCK

For a given bandwidth, the duration of the symbol and the modulation depth (bits per symbol) employed are varied to produce a number of different message symbols. These symbols are repeatedly combined with additive white Gaussian noise (AWGN) and demodulated using a maximum-likelihood detector. These simulations assume perfect synchronisation. This allows direct comparison with the theoretical performance displayed previously in Fig. 3.8 and Fig. 3.9.

The simulated performance of M-OCK in an AWGN channel for m-sequence orders, K of 11,12, and 13, and modulation depths, M of 2, 4, 16, 64, and 256, are shown in Fig. 3.11 and Fig. 3.12.

Fig. 3.11 shows BER performance against the SNR per bit (dB) allowing comparison with the theoretical performances seen previously. Fig. 3.12, however, shows BER performance against received SNR (dB) providing an indication of performance bounds in a real AWGN channel.

Fig. 3.11 shows that for each order, K, as the modulation depth, M, increases, the SNR per bit required to achieve the same performance decreases. For a BER value of 10^{-4}, doubling the bits per symbol decreases the SNR per bit required by 2.5 dB. For the equivalent BER value in Fig. 3.8, doubling the bits per symbol decreases the SNR per bit by 3 dB. Overall values of the simulated performance are inline with the theoretical upperbounds of a m-ary orthogonal signaling scheme.

When the symbol processing gain, PG_s, is taken into account in Fig. 3.12 the collective improvement in performance between orders is apparent. For a modulation depth of $M = 2$, as the symbol duration doubles from K11 to K12 and then to K13, the SNR required to achieve the same BER performance of 10^{-4} decreases by 3 dB. Comparing an equivalent data rate (46.9 bit/s), K11 4-OCK, K12 16-OCK, and K13 256-OCK, the SNR required to achieve the same BER performance of 10^{-4} decreases by 2 dB. This would be expected to follow the performance gains shown in Fig. 3.11 where the spreading gains are removed from each of the signals for direct comparison in SNR per bit.

The conversion between SNR and SNR per bit (ε_b/N_0) takes into account the spectral efficiency based on the bit rate, R_b, and the bandwidth, B, as shown in (3.9) [115].

$$\frac{\varepsilon_b}{N_0} = \mathrm{SNR} - 10\log_{10}\left(\frac{R_b}{B}\right)\ \mathrm{dB} \tag{3.9}$$

As an example conversion, taking K11 2-OCK with a bit rate, R_b, of 23.45 bit/s, and bandwidth, B, of 8 kHz, formula in (3.9) becomes:

$$\begin{aligned}\frac{\varepsilon_b}{N_0} &= \mathrm{SNR} - 10\log_{10}\left(\frac{23.45}{8000}\right)\ \mathrm{dB},\\ \frac{\varepsilon_b}{N_0} &= \mathrm{SNR} + 25.33\,\mathrm{dB}.\end{aligned} \tag{3.10}$$

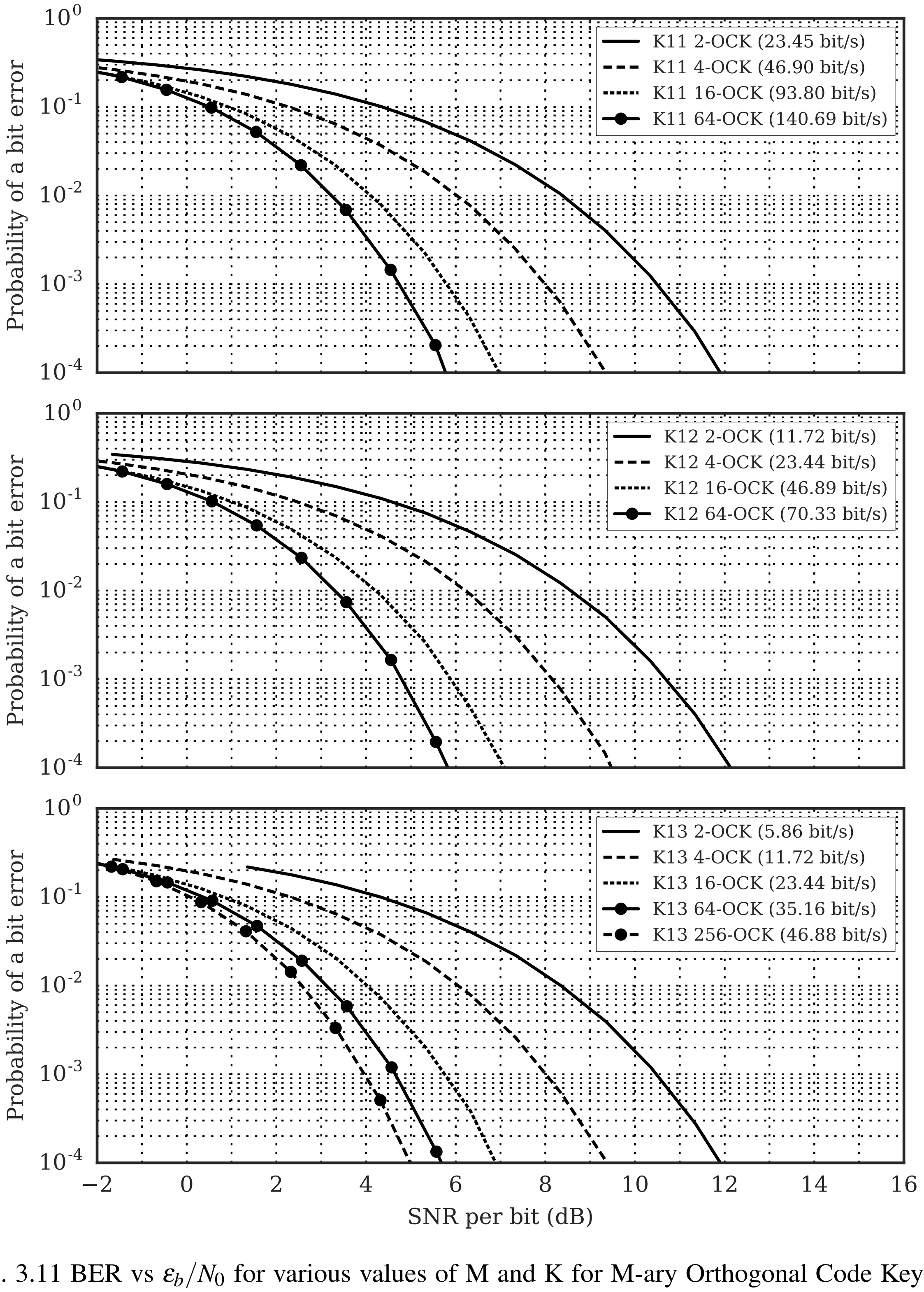

Fig. 3.11 BER vs ε_b/N_0 for various values of M and K for M-ary Orthogonal Code Keying. Spreading bandwidth, B, of 8 kHz and F_s of 48 kHz. Direct comparisons can be made with the theoretical upper bounds of orthogonal signaling.

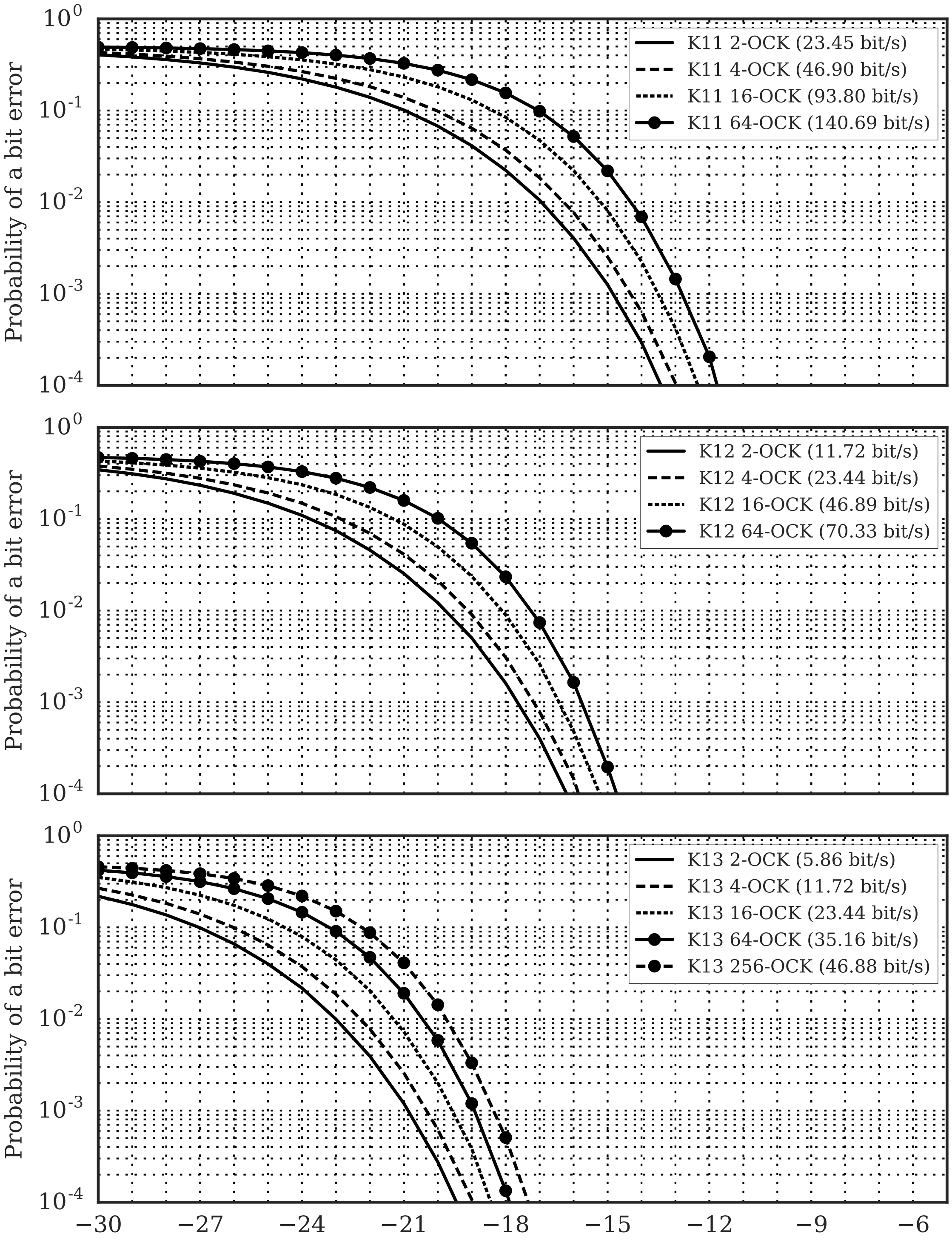

Fig. 3.12 BER vs SNR for various values of M and K for M-ary Orthogonal Code Keying. Spreading bandwidth, *B*, of 8 kHz and F_s of 48 kHz. Process gains due to symbol duration and bandwidth are also evident here.

3.8 Doppler Tolerance

As discussed previously in Section 2.2.4, the underwater channel poses challenges such as Doppler shift and Doppler spread. When considering the effect of Doppler shift on a bandlimited PN symbol in comparison with linear frequency modulation (LFM) and hyperbolic frequency modulation (HFM) chirps with the equivalent processing gain (BT_s product), Fig. 3.13 shows the wideband ambiguity functions from (2.15) over a range of velocities and for two processing gains. $K11$ representing 25.33 dB and $K13$ representing 31.35 dB. Chirps can be considered Doppler tolerant, but it is clear from Fig. 3.13 that bandlimited PN symbols with high BT_s products have a very narrow range of velocities over which they can be successfully correlated. This will need to be accounted for in future receiver structure design.

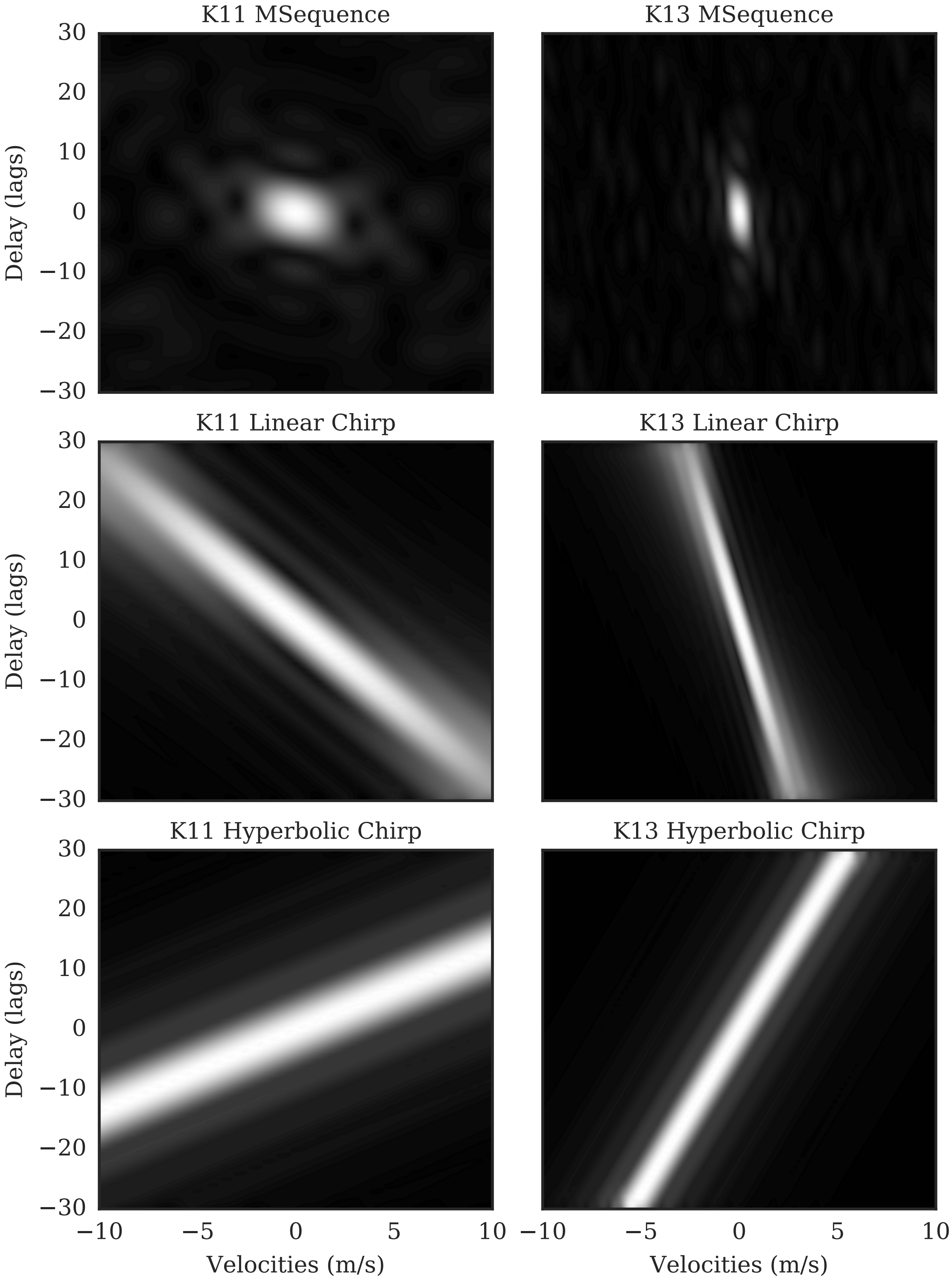

Fig. 3.13 Ambiguity Functions of linear frequency modulation (LFM), hyperbolic frequency modulation (HFM) chirps, and bandlimited PN symbol with equivalent processing gain (BT_s product), 25.33 dB (K11) and 31.35 dB (K13), over a range of velocities $-10.0\,\mathrm{m/s}$ to $10.0\,\mathrm{m/s}$.

3.9 Summary

This chapter has shown a new signaling scheme targeting low received-SNR and wide bandwidth applications. As modulation depth is increased, the orthogonal signaling scheme follows the theoretical performance curves as shown by Proakis. For comparison with a commonly used m-ary signaling scheme, M-OCK has also been shown to outperform M-QAM as modulation depth is increased. Bandlimited m-sequences for example orders and modulation depths, K11 64-OCK and K13 256-OCK, are shown to be orthogonal; all other codes in the set show comparatively low magnitudes when cross-correlated when compared to the auto-correlation magnitude for a given code.

The comparisons with LFM chirps show the relative ease with which bandlimited PN symbols can be hidden in the background noise. Bandlimited PN sequences have been shown to be visibly hidden at low SNRs where LFM Chirps of equivalent bandwidth and duration are still visible in spectrogram plots. This is an important factor when considering the impact of signal types on marine life.

Ambiguity plots show that bandlimited PN symbols with long durations are relatively intolerant of Doppler shift when compared to LFM and HFM Chirp symbols of equal duration and bandwidth. This highlights the need for appropriate Doppler compensation techniques to be included in any receiver structure design for applications with moving platforms.

Two m-sequence orders and modulation depths have been identified for further study in this research to provide a variety of data rates and potential target operating SNRs. Simulated performance in AWGN channels puts the expected operation of uncoded modulation in the low-received-SNR range identified in previous chapters.

Thus far, only the symbol and data packet construction and performance have been considered. Perfect synchronisation has been assumed when simulating the performance of the M-OCK modulation scheme. Successful synchronisation will be an essential part of a complete communication system and will be considered in detail in Chapter 4.

Chapter 4

Receiver Design

4.1 Introduction

Chapter 3 shows the fundamentals of the signal design using m-sequences. This chapter explores in more detail the receiver design and the signal design in relation to these receiver structures. The receiver structure, and associated signal, comprises of two parts: synchronisation and data demodulation. The design and simulation results of each are considered. Experimental validation based on sea trials demonstrates the real-world performance of the receiver structures.

This chapter investigates the concept of synchronisation using multiple unique PN symbols through combining the energy from the correlators compared to a single symbol and correlator. Simulations and experimental validation are used to explore the performance characteristics of this technique.

Normalisation of the correlator outputs based on received signal energy is demonstrated for allowing a fixed threshold detector in the synchronisation process.

Data demodulation is explored continuing with the two symbols and modulation depths covered in Chapter 3, K11 64-OCK and K13 256-OCK, both signals with and without RS coding. AWGN simulations show the ideal operating performance of the signals and receiver structures, whilst experimental validation shows the performance in Sea Trials over ranges from 100 m to 10 km with acoustic transmit power limited to 170.8 dB re 1 μPa @ 1 m or 1 W of acoustic power.

The concept of multipath exploitation is piloted using channel recordings combined with AWGN to determine the performance gain.

4.2 Design and Simulation

4.2.1 Motivation

The signal design for a modulation scheme has been considered in Chapter 3. Two modulation depths and symbol lengths have been selected to develop further, K11 64-OCK and K13 256-OCK. Data transfer also relies on successful synchronisation of the start of the data packet. Therefore, this section will look at the design and simulation of a signal packet and receiver structure necessary for synchronisation and data demodulation in low-received-SNR scenarios.

4.2.2 Synchronisation: Design

Synchronisation is essential before a data packet can be demodulated. As shown in Section 3 the spreading gain of a PN sequence is dependent on both bandwidth and duration; a longer duration symbol, for a given bandwidth, therefore has a greater spreading gain. One approach would therefore to be use a longer PN sequence as the synchronisation header. However, due to the Doppler intolerance of longer PN sequences, as shown in Section 3, and short channel coherence time there would quickly be a mismatch in the autocorrelation. An alternative approach would be to use a number of shorter PN sequences and combine their energy in such a way that minor changes in the channel can be tolerated. The energy can be combined by summing the correlator magnitudes of each symbol in the sequence. Example PN sequences, their combinations, and relative durations are shown in Fig. 4.1 where K represents the order of m-sequence used.

The receiver structure to detect a single PN sequence is shown in Fig. 4.2. The received signal is bandpass filtered and correlated with the stored PN sequence. The envelope of the resultant correlated signal is created by squaring, lowpass filtering, and square-rooting. However, in order to threshold detect the PN sequence using a fixed threshold value, the normalisation block is required. The normalisation process will be considered shortly.

Extending the receiver structure in Fig. 4.2 to accommodate synchronisation signal structures of multiple PN sequences results in the structure shown in Fig. 4.3. Here the input signal is bandpass filtered then fed into respective delay lines before being correlated, in parallel with the individual PN sequences, normalised and enveloped. The outputs of all envelope stages are then analysed over a short window with the maximum value of each window taken and summed in order to combine the energy of each received symbol. This combined energy is then threshold detected for successful synchronisation. The window with a length of 12 samples (250 µs) allows for changes in the channel coherency during the period of the entire synchronisation structure. By taking the peak value of each window this allows the maximum energy of each symbol arrival to be summed prior to the threshold detection. Optimum window length will be application dependent, taking into consideration the expected change in channel coherency over the duration

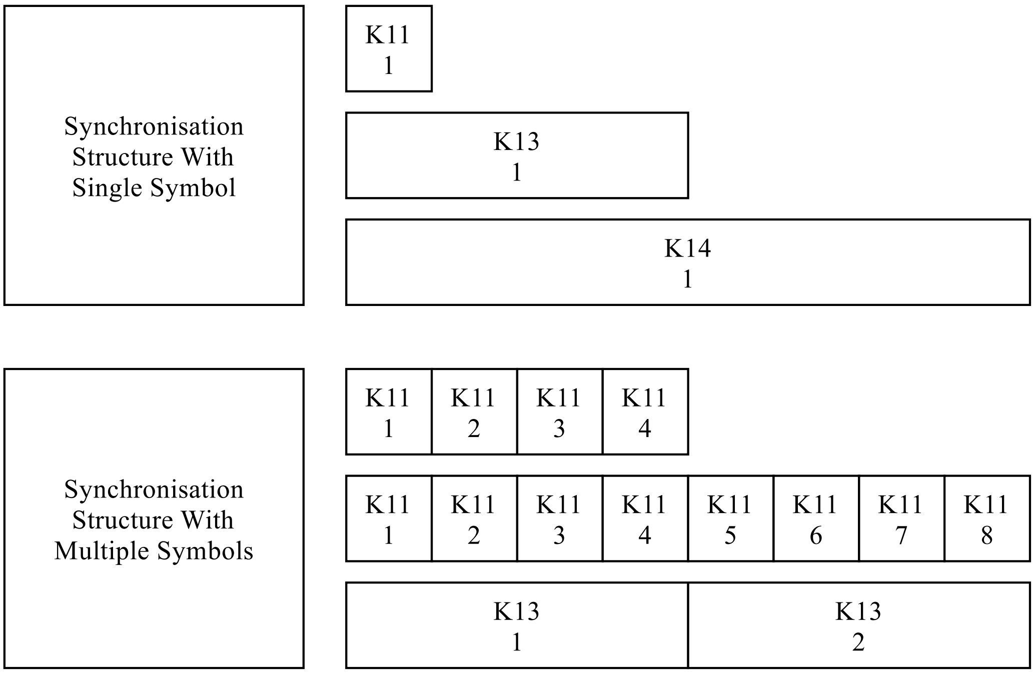

Fig. 4.1 Synchronisation Signal Structures with a single PN Sequence or with multiple PN sequences. Showing the relative duration of each order of PN sequence. 1of K11, 1of K13 and 1of K14 for single symbol structures. 4of K11, 8of K11 and 2of K13 multiple symbol structures.

of the entire synchronisation signal structure. In this case, the window length is set for stationary platforms with some mobility expected on cable-suspended hydrophone and transducer.

4.2.2.1 Normalisation

The normalisation block compensates for variations in the received amplitude which would otherwise affect the magnitude of the correlator values. This technique has been used by Goodfellow [116, p120] also as part of the synchronisation structure albeit for LFM Chirps. The normalisation process can be expressed in (4.1), where h is the code, y is the input signal, L is the length of the code, and μ is the mean of the input signal, y

$$c(t) = \frac{\sum_{n=0}^{L-1} h[n]\, y[n+t]}{\sqrt{\frac{1}{L}\sum_{n=0}^{L-1} \left(y[n]-\mu\right)^2}}. \tag{4.1}$$

This is not the full normalisation as shown in (4.2) which provides a result between ±1.0. However, it does allow the fixed threshold value with reduced computation than the full normalisation.

$$c(t) = \frac{\sum_{n=0}^{L-1} h[n]\, y[n+t]}{\sqrt{\sum_{n=0}^{L-1} \left(h[n]\right)^2 \sum_{n=0}^{L-1} \left(y[n]-\mu\right)^2}} \tag{4.2}$$

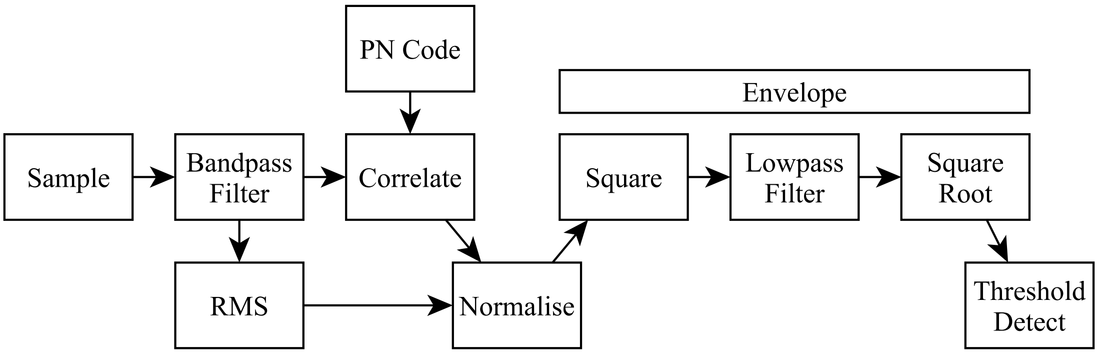

Fig. 4.2 Receiver Structure Block Design: Synchronisation.
a) Single code, correlation, normalisation, threshold detection.

The effect of the normalisation block on the receiver structure can be visualised by independently varying the SNR and RMS of the input signal. Fig. 4.4 shows an input signal with varying SNR yet constant RMS. Although the correlator peaks may decrease with decreasing SNR, the noise floor remains steady with and without normalisation. Fig. 4.5 demonstrates a fixed SNR yet increasing RMS, this is where the normalisation block provides the desired compensation. Without normalisation the increasing RMS results in an increasing magnitude of correlator values, both of the peaks and the noise floor. However, with normalisation this produces the steady noise floor allowing a fixed threshold value to be used. Fig. 4.6 combines a decreasing SNR with an increasing RMS of the input signal. Without normalisation not only does the noise floor increase, but the correlator peaks are also decreasing in magnitude. With normalisation the noise floor becomes a steady level.

It is this normalisation block that allows the use of a fixed threshold value in the Threshold Detect block.

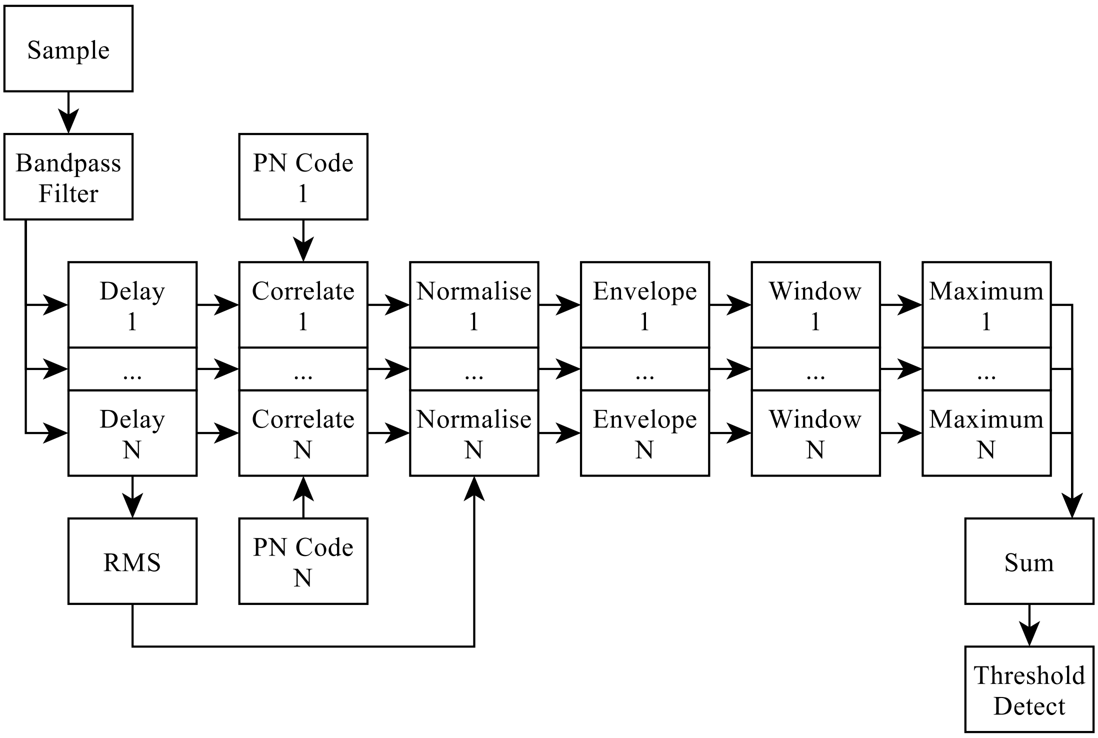

Fig. 4.3 Receiver Structure Block Design: Synchronisation.
b) Multiple codes, correlation, normalisation, envelope, windowing (12 samples), window maxima are then summed prior to threshold detection.

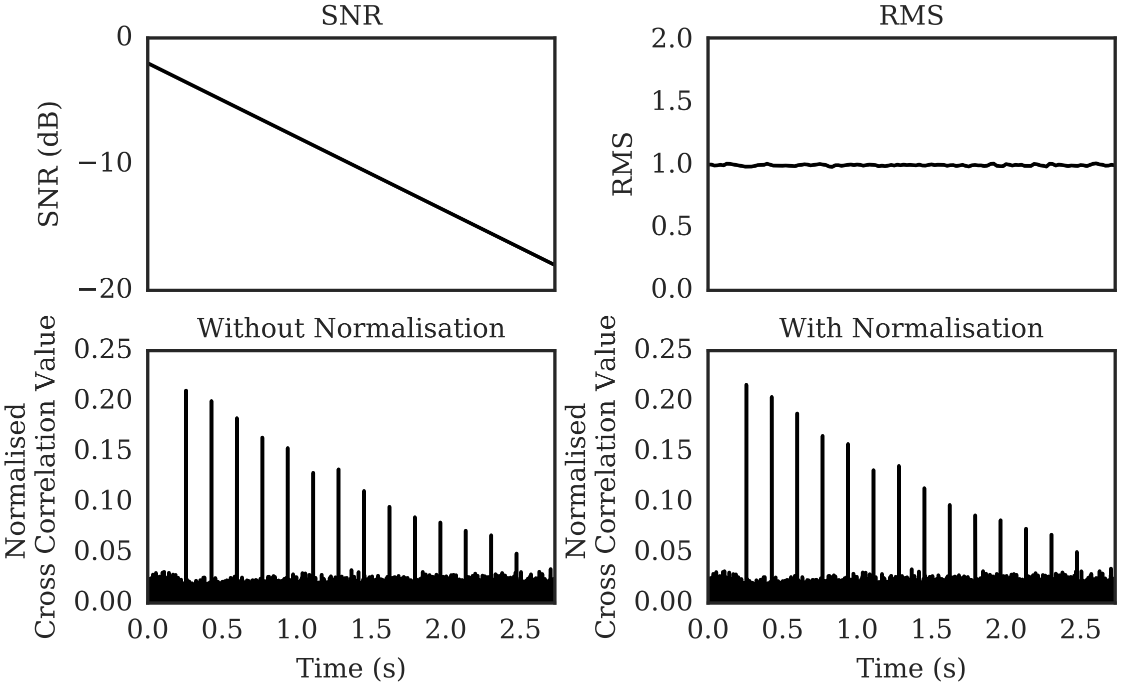

Fig. 4.4 Normalised Cross-Correlation Example. Varying SNR but static RMS showing cross-correlation values with and without normalisation.

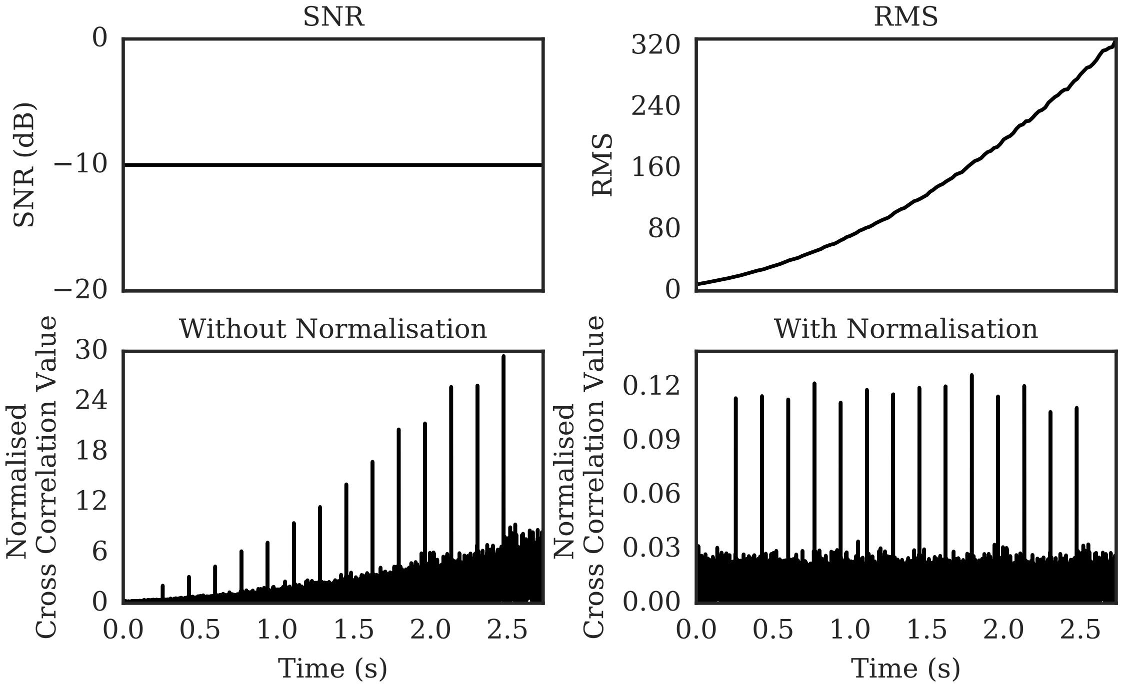

Fig. 4.5 Normalised Cross-Correlation Example. Varying RMS but static SNR showing cross-correlation values with and without normalisation.

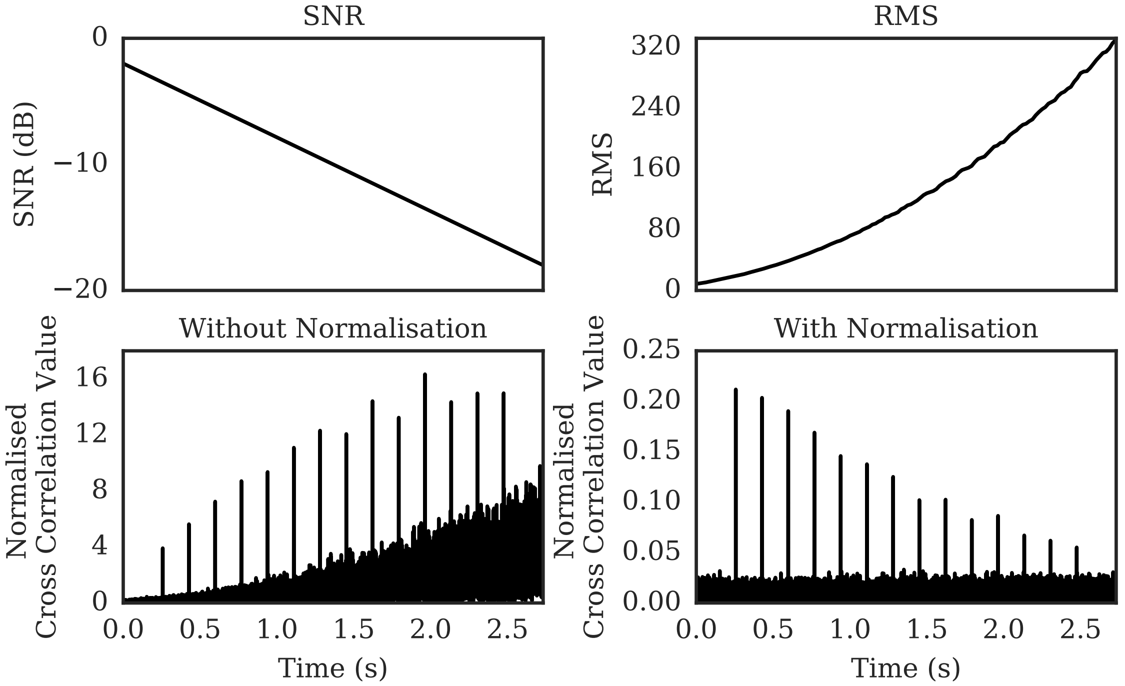

Fig. 4.6 Normalised Cross-Correlation Example. Varying RMS and SNR showing cross-correlation values with and without normalisation.

4.2.3 Synchronisation: Simulations

The synchronisation signal structures shown previously in Fig. 4.1 were constructed using a chip frequency of 48 kHz and bandlimited between 8 kHz to 16 kHz. Varying the AWGN and normalised threshold value in the receiver structure produces the simulation results shown in Fig. 4.7. The envelope shows the bounding normalised threshold level and SNR values within which the receiver structure will successfully synchronise. Decreasing the normalised threshold value below this bound will result in false-positive detection as well as successful synchronisation. Combining the energy of the correlators for multiple symbols produces a visually similar performance to using a single symbol of equivalent total processing gain (bandwidth and duration). For example, 1of K14 with 2of K13 and 8of K11 have similar envelopes; as do 1of K13 and 4of K11. In simulation this approach appears feasible, but the results from experiments with real underwater channels will provide better testing of the technique.

The optimal threshold value to set is a trade-off between targeting low received-SNR and reducing the rate of false-positive detection. With such long packet durations, false-positive detections are a disadvantage as they effectively lock out the receiver for the duration of an expected packet. During which time, there may have been a genuine arrival that the receiver is now unable to process.

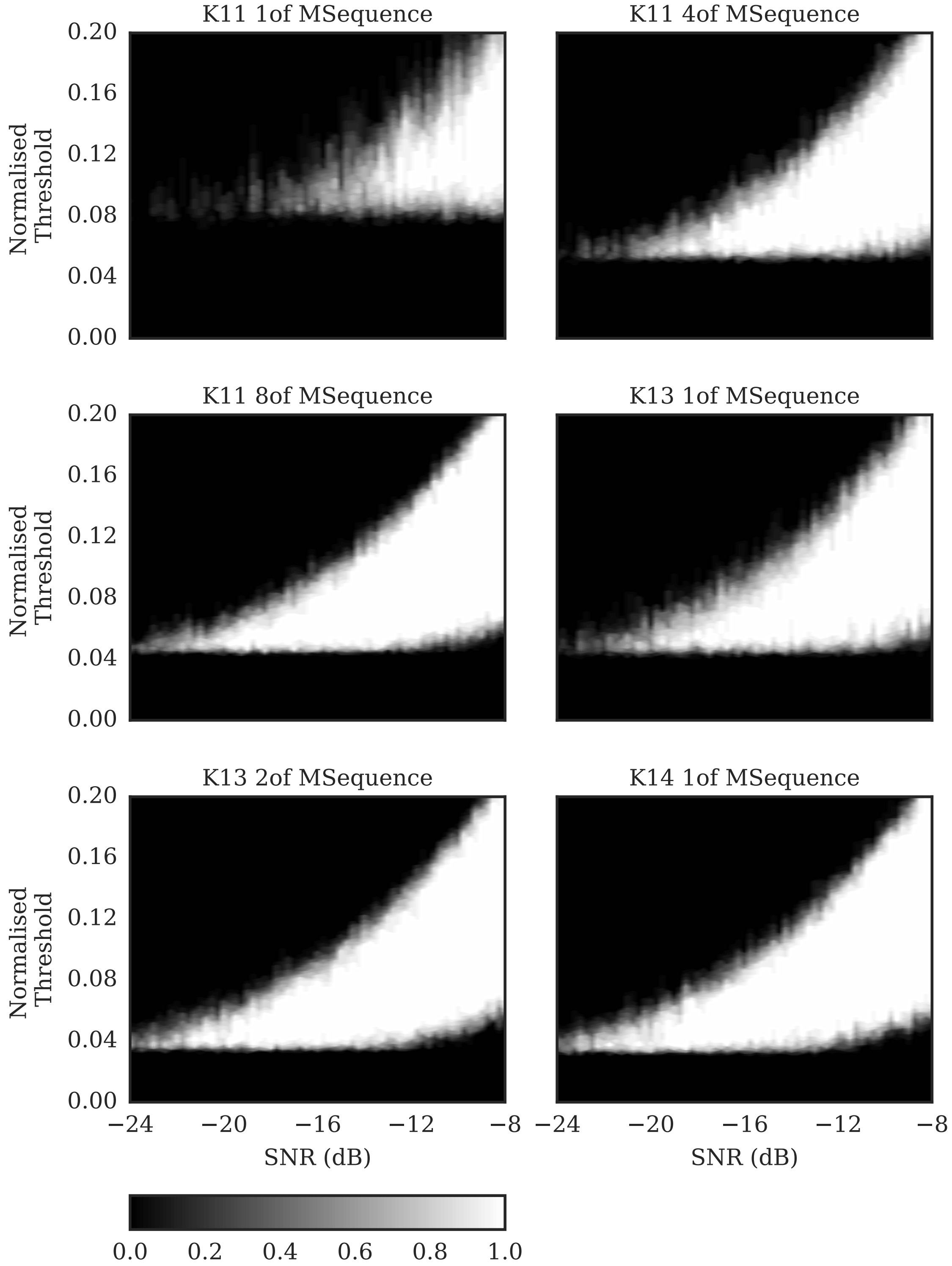

Fig. 4.7 Synchronisation Performance Envelopes in AWGN Channel. For single sequence synchronisation structures, and multiple sequence structures. 1 of K11, 4 of K11, 8 of K11, 1 of K13, 2 of K13, and 1 of K14. These plots provide an indication of where to set the threshold value for successful synchronisation at low SNRs. The threshold values from 0 to 0.04 on 1of K14, for example, also include false-positive synchronisation results. Although these plots were produced using only AWGN channels they do provide a visualisation of the envelope shapes for comparing the relative performance of the different signal structures.

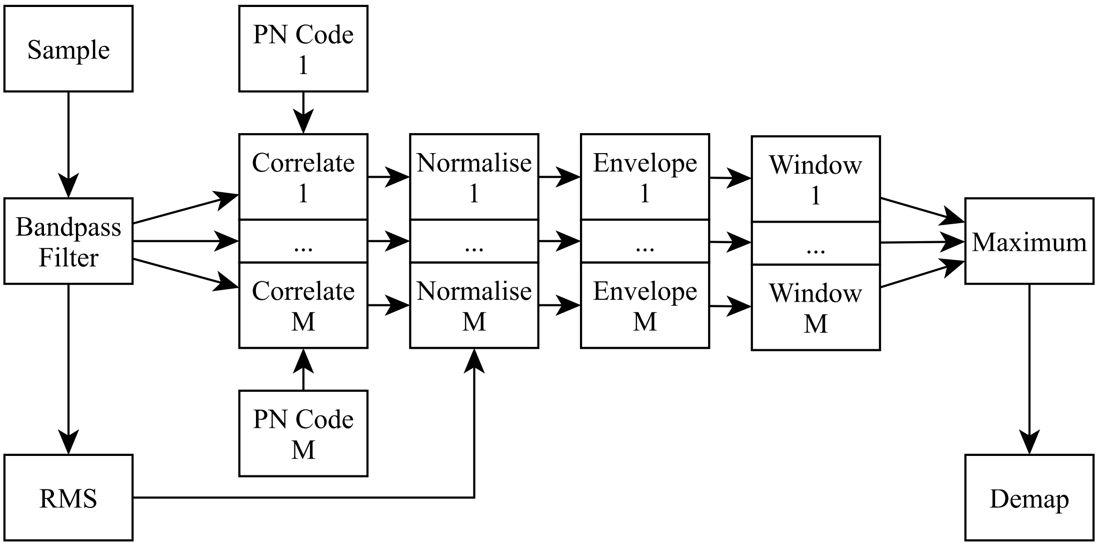

Fig. 4.8 Receiver Structure Block Design: Data Demodulation.
a) Correlation, Normalisation, Envelope, Windowing (12 samples), maximum value selection, demapping.

4.2.4 Data Demodulation: Design

Once the received signal has synchronised, the data payload can be processed. The data is demodulated using a bank of correlators and maximum likelihood decoder for each symbol. Time-windowing is used when comparing the correlator values to reduce inter-symbol interference. The receiver structure for data demodulation can be seen in Fig. 4.8.

4.2.5 Data Demodulation: Simulations

The packet structures used in simulation are shown in Table 4.1. Performance of both K11 64-OCK and K13 256-OCK data symbols will be compared with and without Reed-Solomon error correction codes.

For the Reed-Solomon encoded messages the coderate of 0.76 was chosen such that both packet types would have similar lengths. The properties of the Reed-Solomon codes used are shown in Table 4.2.

The receiver structure shown in Fig. 4.8 was implemented using C++ on a desktop PC. The packets were constructed as described in Table 4.1 and repeatedly combined with varying levels of AWGN and demodulated. The results are shown in Fig. 4.9.

The relative simulated AWGN performance of the receiver structure for uncoded signals is comparable to the results in Chapter 3 of signal performance with AWGN. Although, there is an overall reduction in performance of around 2 dB at BER of 10^{-4}.

Table 4.1 Packet Structure: Data

Structure	Details	FEC	Data rate (bit/s)	Total data bits
100 of K11 64-OCK Symbols	K11M0 to K11M63	Uncoded	140.69	600
100 of K11 64-OCK Symbols	K11M0 to K11M63	RS 0.76 coderate	106.92	456
25 of K13 256-OCK Symbols	K13M0 to K13M255	Uncoded	46.88	200
25 of K13 256-OCK Symbols	K13M0 to K13M255	RS 0.76 coderate	35.63	152

Reed-Solomon coding with 0.76 coderate provides an improvement in performance of 2.5 dB at BER of 10^{-4} but with a reduction in data rate. This also provides a check on the integrity of the packet as well as finite error correction.

Table 4.2 Reed-Solomon Properties

Reed-Solomon Property	K11 64-OCK RS	K13 256-OCK RS
Bits per symbol $m = \log_2 M$	6	8
Alphabet Size $q = p^m$	64	256
Block Length $n = q - 1$	63	255
Parity Length $n - k$	12	6
Distance $n - k + 1$	13	7
Message Length k	51	249
Truncated Message Length	38	19
RS Descriptor $[n, k, n-k+1]_q$–code	2 blocks of $[63, 51, 13]_{64}$–code	1 block of $[255, 249, 7]_{256}$–code
Truncated RS Descriptor $[n, k, n-k+1]_q$–code	2 blocks of $[50, 38, 13]_{64}$–code	1 block of $[25, 19, 7]_{256}$–code

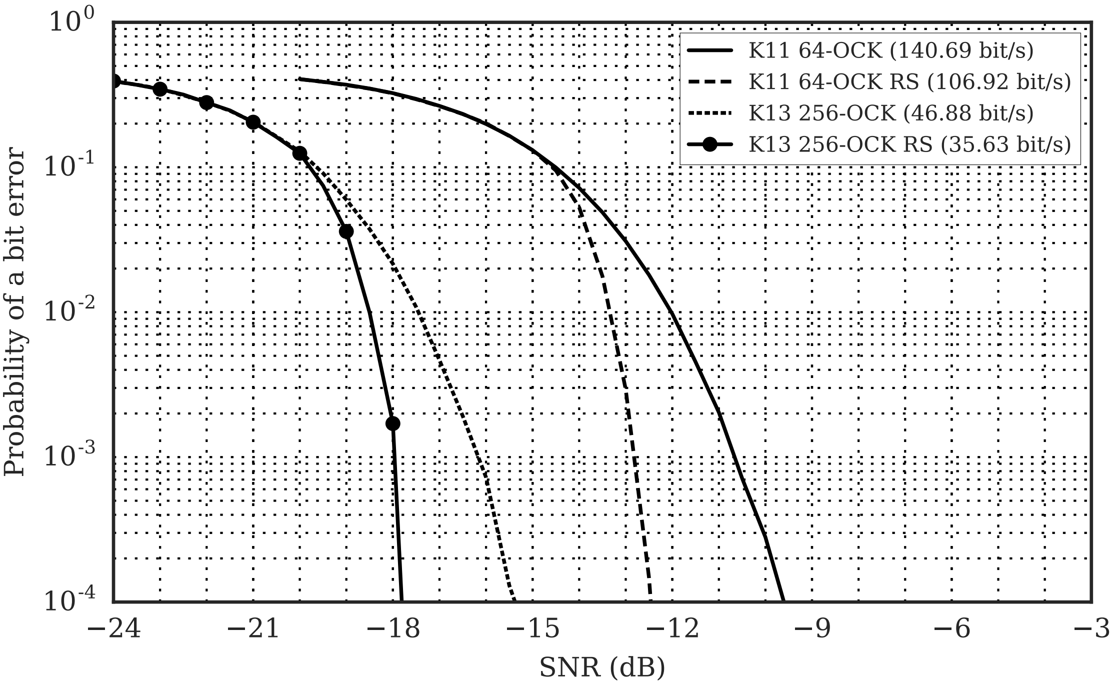

Fig. 4.9 Receiver Structure: Data Demodulation Simulations. BER vs SNR for M-ary Orthogonal Code Keying packets with the receiver structure. Spreading bandwidth, B, of 8 kHz and F_s of 48 kHz. Showing performance of K11 64-OCK (140.69 bit/s) and K13 256-OCK (46.88 bit/s). The performance using Reed-Solomon error correction codes is also shown for direct comparison. K11 64-OCK RS (106.92 bit/s) and K13 256-OCK RS (35.63 bit/s).

Table 4.3 Packet Structure: Synchronisation

ID	Structure	Details
SK11	16 of K11 Symbols	K11M128, K11M129, K11M130, K11M131, K11M132, K11M133, K11M134, K11M135, K11M136, K11M137, K11M138, K11M139, K11M140, K11M141, K11M142, K11M143
SK13	4 of K13 Symbols	K13M520, K13M521, K13M522, K13M523

4.3 Experimental Validation: Sea Trials 2015-03-18

4.3.1 Motivation

Simulations previously have shown the ideal performance of the receiver structures in an AWGN channel. Performance in a real-world channel incorporating time-varying effects of reverberation, Doppler effects, and noise will provide robust validation of the designs.

4.3.2 Transmission

4.3.2.1 Synchronisation Structures

To investigate the performance of synchronisation structures in experimental conditions Table 4.3 shows the sequences to be used. These structures will allow a number of combinations of multiple symbols to be compared in the experiments. In this case 1of, 2of, 4of and 8of K11; and 1of, 2of and 4of K13 symbols.

4.3.2.2 Data Packet Structures

The packet structures used in experimental validation are shown in Table 4.4. There are four distinct data packets to compare performance of both K11 64-OCK and K13 256-OCK data symbols. Chapter 7 will also investigate the performance of Non-binary Low Density Parity Check error correction codes. At this stage, comparisons will only be made between the uncoded packet performance and the Reed-Solomon coded packet performance.

Synchronisation structures for the start of each data packet are two unique K13 symbols to allow comparison in performance between single and double combined symbols.

Table 4.4 Packet Structure: Data

	Packet Synch		Packet Data		
ID	Structure	Details	Structure	Details	Optional FEC
A	2 of K13 Symbols	K13M512 K13M513	100 of K11 64-OCK Symbols	K11M0 to K11M63	Uncoded or RS
B	2 of K13 Symbols	K13M514 K13M515	100 of K11 64-OCK Symbols	K11M0 to K11M63	Uncoded or LDPC
C	2 of K13 Symbols	K13M516 K13M517	25 of K13 256-OCK Symbols	K13M0 to K13M255	Uncoded or RS
D	2 of K13 Symbols	K13M518 K13M519	25 of K13 256-OCK Symbols	K13M0 to K13M255	Uncoded or LDPC

4.3.2.3 Transmit Waveform

Each of the data packets described previously were incorporated into a single transmit audio file along with unique synchronisation headers for each payload as shown in Fig. 4.10. LFM chirps were also incorporated with 10 dB more power than the M-OCK signals. In combination with the silent periods, these chirps allow the received-SNR to be estimated at regular points during the recordings. They also allow clear visualisation of the received signals on the recorder spectrogram where the PN signals would otherwise be hidden in background noise during the field experiments.

4.3.3 Received SNR Measurement

Received-SNR of the recordings is measured using the up and down chirp signals and preceding silent period as shown in Fig. 4.11 and (4.3). This takes account of all signal energy arriving during the duration of the chirp symbol including from multiple paths. The received-SNR of the PN sequences is then 10 dB less than the chirp SNR.

$$\mathrm{SNR} = \frac{\mathrm{Var}\left[signal + noise\right] - \mathrm{Var}\left[noise\right]}{\mathrm{Var}\left[noise\right]} \tag{4.3}$$

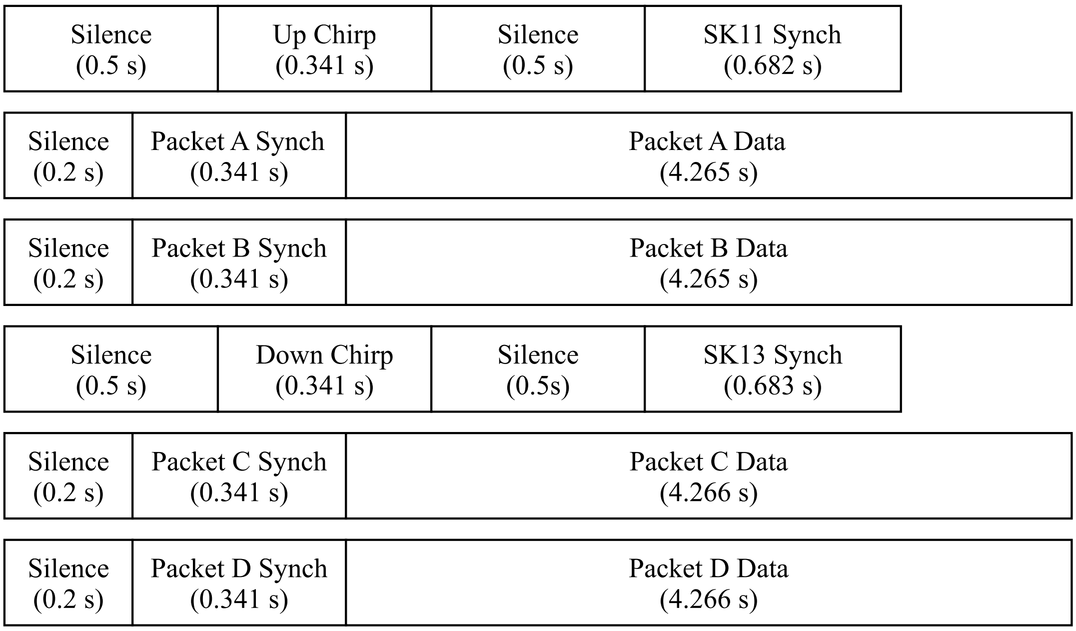

Fig. 4.10 Packet Structure Recording. Total duration of 23.273 seconds.

4.3.4 Experiment Setup

Location North Sea off Blyth

Transmitter Laptop playing audio. Power amplifier such that PN signal is limited to a source level of 170.8 dB re 1 µPa @ 1 m or 1 W of acoustic power. Transducer on cable suspended in water at a depth of 30m.

Receiver Laptop recording audio. Bandpass filter and amplifier. Hydrophone on cable suspended in water at a depth of 10m. Multiple 4 minute recordings taken at each range.

Weather and Sea State Clear skies. Calm sea.

Geology Rock shelf, areas covered with sediment, others exposed. Depth around 40-50m.

Ranges 100 m, 500 m, 1 km, 2 km, 5 km and 10 km.

Table 4.5 lists the recordings taken during the sea trials, along with the filename and range of transmission for each four minute recording. The filenames are referred to in a number of the case study results later in this chapter.

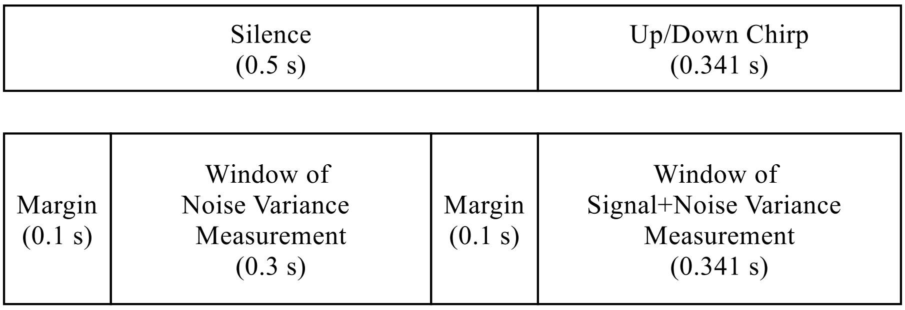

Fig. 4.11 Received SNR Measurement

Table 4.5 Sea Trials Recordings

Recording Index	Recording Name	Range	Recording Number
0	bs-rx-20150318-100m-01	100 m	Recording 01
1	bs-rx-20150318-100m-02	100 m	Recording 02
2	bs-rx-20150318-100m-03	100 m	Recording 03
3	bs-rx-20150318-500m-01	500 m	Recording 01
4	bs-rx-20150318-500m-02	500 m	Recording 02
5	bs-rx-20150318-500m-03	500 m	Recording 03
6	bs-rx-20150318-1km-01	1 km	Recording 01
7	bs-rx-20150318-1km-02	1 km	Recording 02
8	bs-rx-20150318-2km-01	2 km	Recording 01
9	bs-rx-20150318-2km-02	2 km	Recording 02
10	bs-rx-20150318-5km-01	5 km	Recording 01
11	bs-rx-20150318-5km-02	5 km	Recording 02
12	bs-rx-20150318-5km-03	5 km	Recording 03
13	bs-rx-20150318-10km-01	10 km	Recording 01
14	bs-rx-20150318-10km-02	10 km	Recording 02

4.3.5 Results and Discussions

4.3.5.1 Channel Conditions

Received-SNR estimates of the PN signals throughout the recordings were based on the 10 dB offset from the LFM chirps (up and down) between packets along with the silence periods that preceeded them. These can be seen in Fig. 4.12. At each range the received-SNR is seen to be relatively stable and steady throughout the four minute recording. The third recording at 5 km shows a gradual decrease in received-SNR over the last two minutes. The 10 km recordings show steady readings with occasional dips in received-SNR.

Channel impulse responses based on packets provide an indication of the multipath and rapidly changing channel conditions at each range as shown in Fig. 4.13 and Fig. 4.14. The channel impulse responses were based on the correlation outputs for all of the symbols within the packet. The channel impulse responses show the multipath reverberation and changing channel over the duration of a data packet (4.3 s) for each of the ranges under test. There are visibly strong multipath arrivals in the first 5 ms for all apart from 10 km recordings. Paths are also seen to fade in and out during a packet duration, seen clearly in the recording at 2 km.

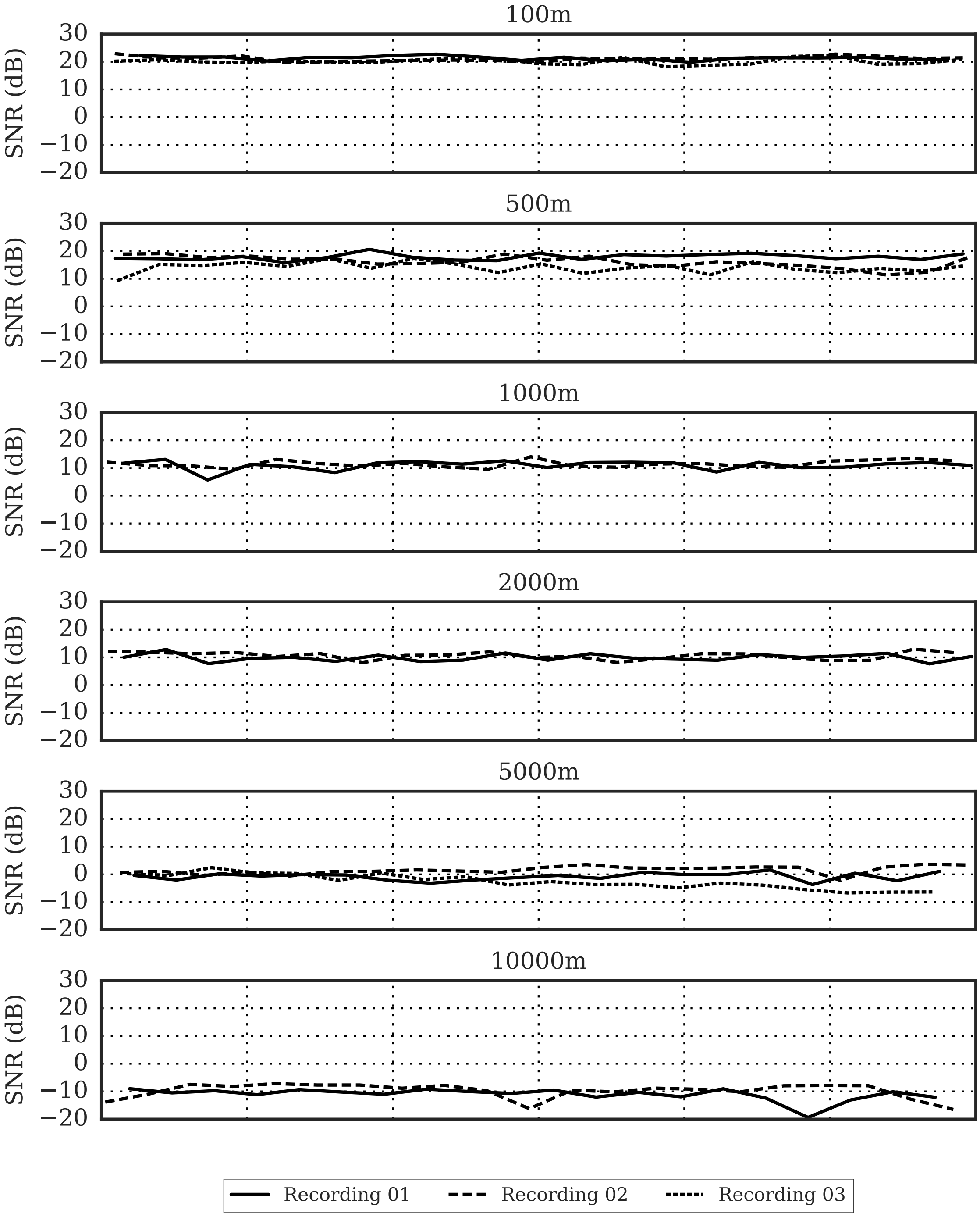

Fig. 4.12 Sea Trials SNR Estimates with multiple recordings at each range.

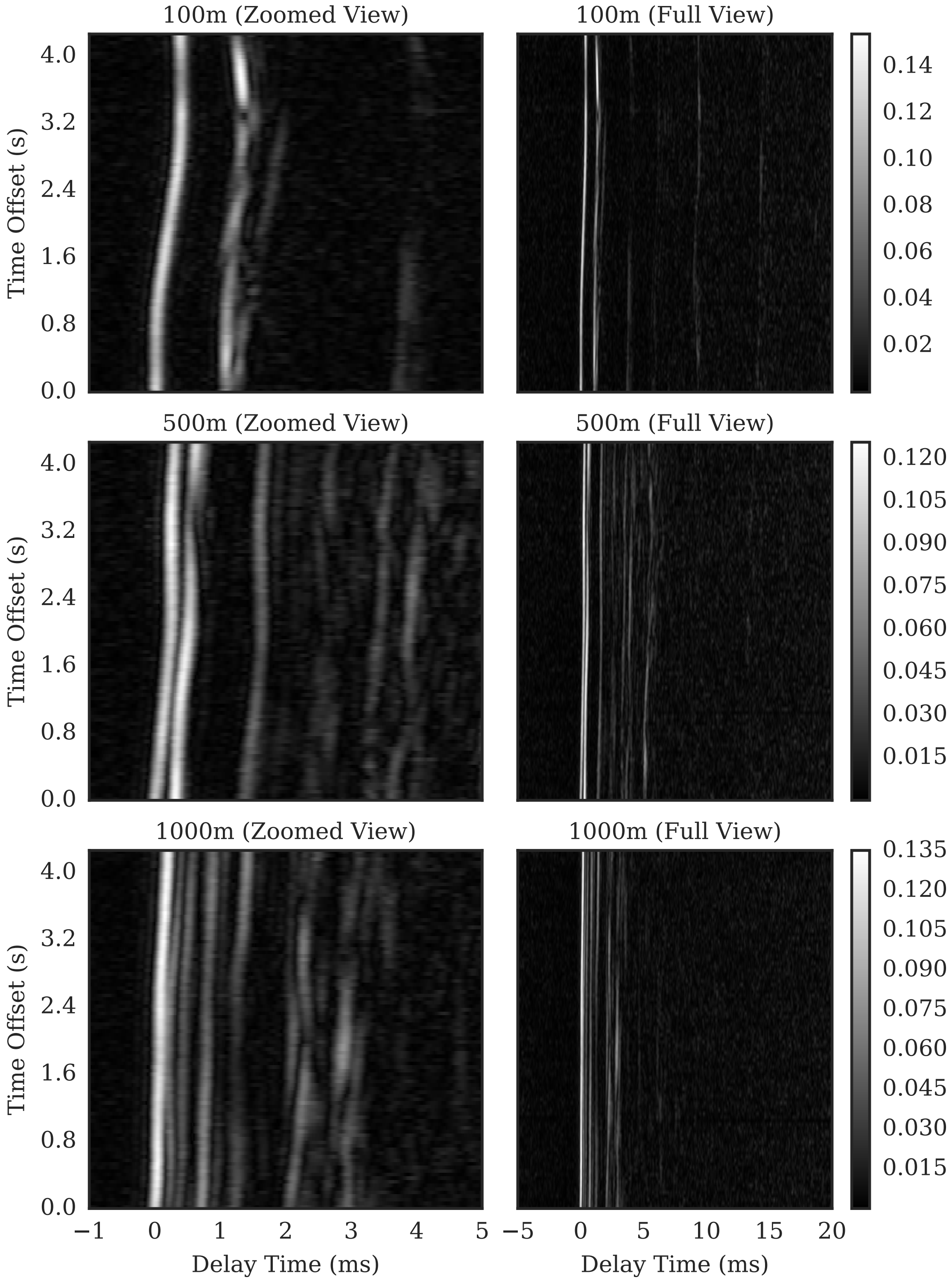

Fig. 4.13 Sea Trials Channel Impulse Responses: 100m, 500m and 1km. Showing zoomed and longer duration views of the packet arrival.

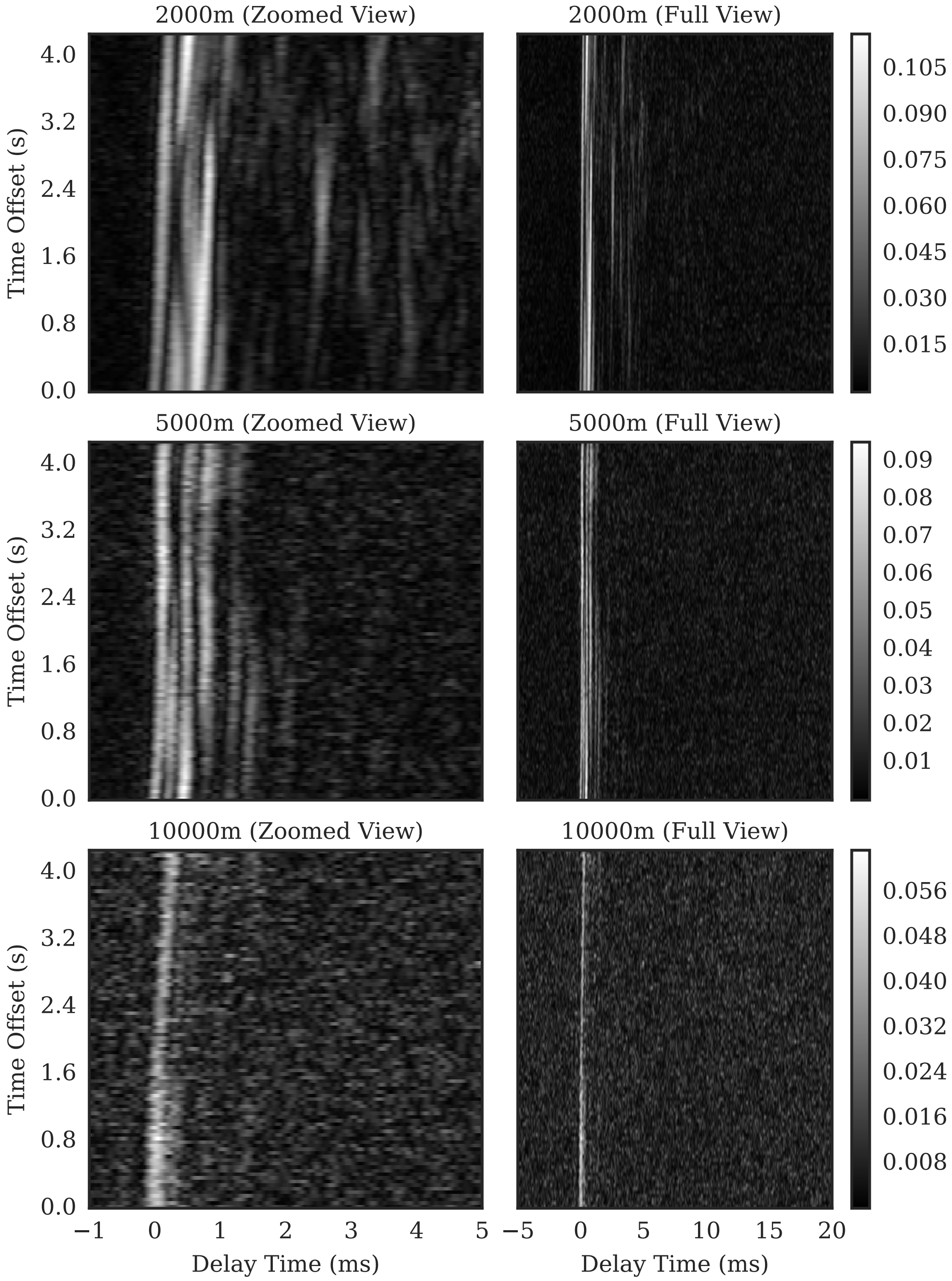

Fig. 4.14 Sea Trials Channel Impulse Responses: 2km, 5km and 10km. Showing zoomed and longer duration views of the packet arrival.

Table 4.6 Sea Trials Results: Synchronisation Counts

	Synchronisation Counts						
	K11 Symbols				K13 Symbols		
Range (m)	1 of	2 of	4 of	8 of	1 of	2 of	4 of
100	34	32	33	32	30	30	31
500	33	31	33	31	32	32	32
1000	22	21	22	21	21	21	21
2000	23	20	20	20	22	22	21
5000	32	31	31	31	30	30	30
10000	10	15	19	20	20	20	21

4.3.5.2 Synchronisation Counts

The results of synchronisation counts for varying synchronisation signal structures are presented in Table 4.6. The duration of the entire transmit waveform is 23.273 s. Therefore a single four minute recording contains 10.3 repetitions of the relevant packets and synchronisation signal structures, which equates to 10 or 11 result points per recording. For ranges with three recordings, a synchronisation count of between 30 and 33 is expected; for two recordings, 20 to 22 synchronisation counts are expected.

In Table 4.6 the expected values are seen for all synchronisation signal structures for all ranges except 10 km. Although, for 1of K11 there do appear to be the possibility of false positive detections. At 10 km where the received-SNR reaches levels around -10 dB there is a clear gradient in performance as the number of K11 symbols used increases. This shows that combining the energy of shorter symbols can produce equivalent results to using single symbols of the same duration/processing gain (1of K13) in a real underwater channel with multipath and changing conditions.

The received-SNR levels seen here are not sufficiently low to begin to test the K13 symbol combinations, which is to be expected when considering the AWGN simulations seen previously in Fig. 4.7.

Table 4.7 Sea Trials Results: K11 64-OCK

	Uncoded (140.69 bit/s)		RS (106.92 bit/s)	
Range (m)	BER	PSR	BER	PSR
100	3.056×10^{-4}	0.933	0.000	1.000
500	4.098×10^{-4}	0.918	0.000	1.000
1000	1.200×10^{-2}	0.975	0.000	1.000
2000	3.252×10^{-4}	0.951	0.000	1.000
5000	9.111×10^{-3}	0.850	5.263×10^{-3}	0.933
10000	5.841×10^{-2}	0.024	3.366×10^{-2}	0.550

4.3.5.3 Data Demodulation

The data demodulation results for each recording are collated by range to produce performance points of bit error rate (BER) and packet success rate (PSR). These are tabulated in Table 4.7 for K11 64-OCK and Table 4.8 for K13 256-OCK.

The uncoded packets for K11 64-OCK and K13 256-OCK show bit errors at all ranges, however there are still significant packet success rates for K13 256-OCK across all ranges; and for K11 64-OCK up to 5 km. Reed-Solomon (RS) error correction coding is able to take the packet success rate up to 100% for K13 256-OCK RS across all ranges; and K11 64-OCK RS up to 2 km. However, RS also improves K11 64-OCK from 0.024 to 0.550 packet success rate at 10 km.

These results show that both modulation schemes were able to be successfully received across a range of 10 km transmitted with less than 1 W of acoustic power. Both with and without error correction coding, albeit a much lower packet success rate for K11 64-OCK, but still greater than zero.

For each recording it is possible to track the received-SNR, the bit error count for each detected packet and whether or not the packet was successful. Performance can be compared of the different symbols, K11 64-OCK and K13 256-OCK, with and without RS coding. A number of select recordings are shown here for comparison and discussion. Fig. 4.15 shows 500 m, Fig. 4.16 shows 5 km, Fig. 4.17 and Fig. 4.18 show 10 km.

Fig. 4.15 for 500 m shows that even with a high received-SNR there are still occasional bit errors on an uncoded K11 64-OCK packet.

Fig. 4.16 for 5 km is of interest as a steady received-SNR of 0 dB for the first half of the recording produces no bit errors for any of the modulation schemes. Then, as the received-SNR

Table 4.8 Sea Trials Results: K13 256-OCK

	Uncoded (46.88 bit/s)		RS (35.63 bit/s)	
Range (m)	BER	PSR	BER	PSR
100	4.098×10^{-4}	0.984	0.000	1.000
500	0.000	1.000	0.000	1.000
1000	0.000	1.000	0.000	1.000
2000	0.000	1.000	0.000	1.000
5000	1.967×10^{-3}	0.967	0.000	1.000
10000	9.756×10^{-4}	0.951	0.000	1.000

decreases down to below -4 dB the errors begin to appear for K11 64-OCK uncoded and RS. As the received-SNR drops below -6 dB there are errors now seen on K13 256-OCK uncoded.

Fig. 4.17 for 10 km shows that with received-SNR below -9 dB there is an error-free K11 64-OCK uncoded packet received, along with several K11 64-OCK RS coded packets. Also, for the entire recording the K13 256-OCK uncoded and RS coded packets are received without errors.

Fig. 4.18 again for 10 km shows that only once the received-SNR drops to below -15 dB does the K13 256-OCK uncoded packet show errors, whilst again the K13 256-OCK RS coded packets were all successfully received.

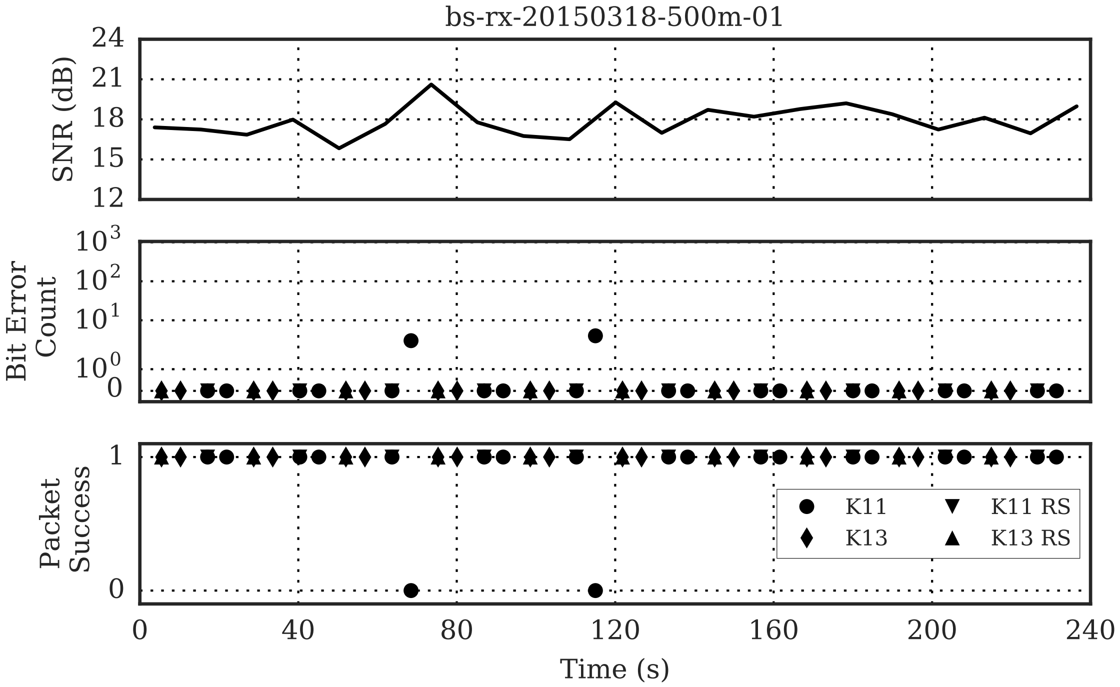

Fig. 4.15 Sea Trials Recording Results: 500m 01. Showing performance of K11 64-OCK (140.69 bit/s), K13 256-OCK (46.88 bit/s), K11 64-OCK RS (106.92 bit/s) and K13 256-OCK RS (35.63 bit/s).

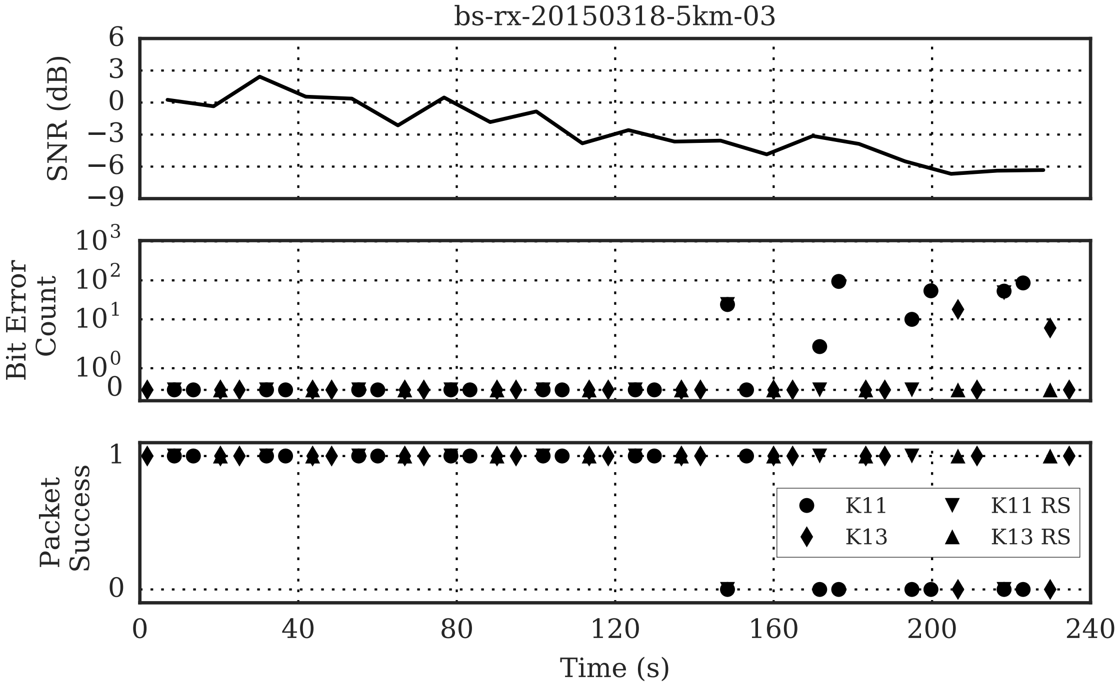

Fig. 4.16 Sea Trials Recording Results: 5km 03. Showing performance of K11 64-OCK (140.69 bit/s), K13 256-OCK (46.88 bit/s), K11 64-OCK RS (106.92 bit/s) and K13 256-OCK RS (35.63 bit/s).

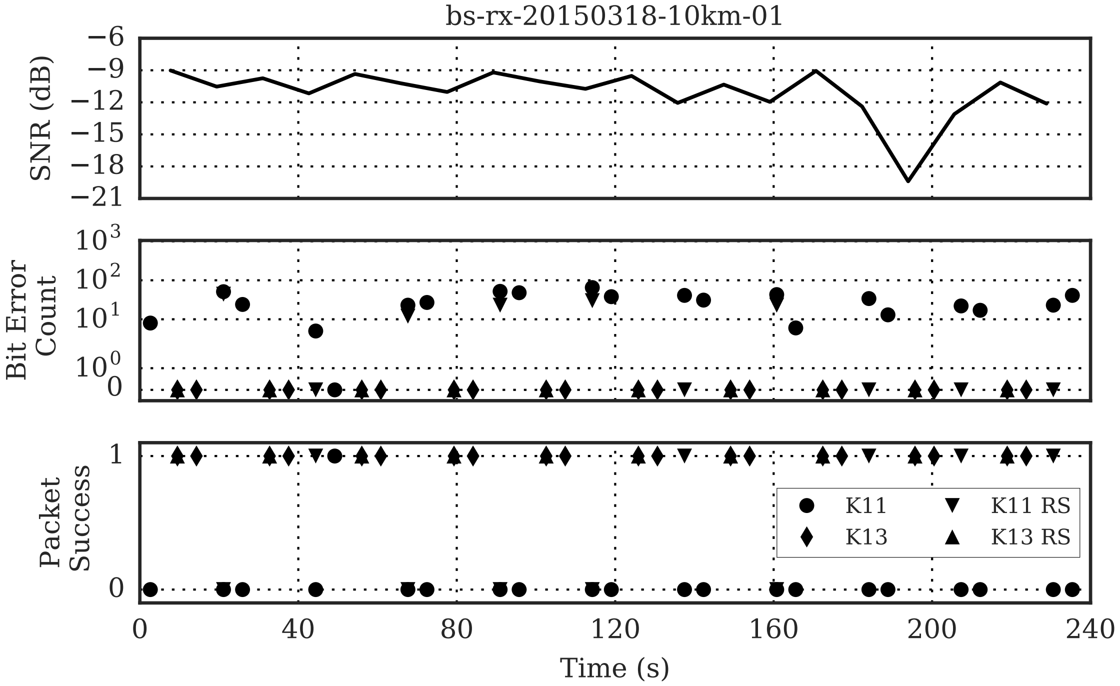

Fig. 4.17 Sea Trials Recording Results: 10km 01. Showing performance of K11 64-OCK (140.69 bit/s), K13 256-OCK (46.88 bit/s), K11 64-OCK RS (106.92 bit/s) and K13 256-OCK RS (35.63 bit/s).

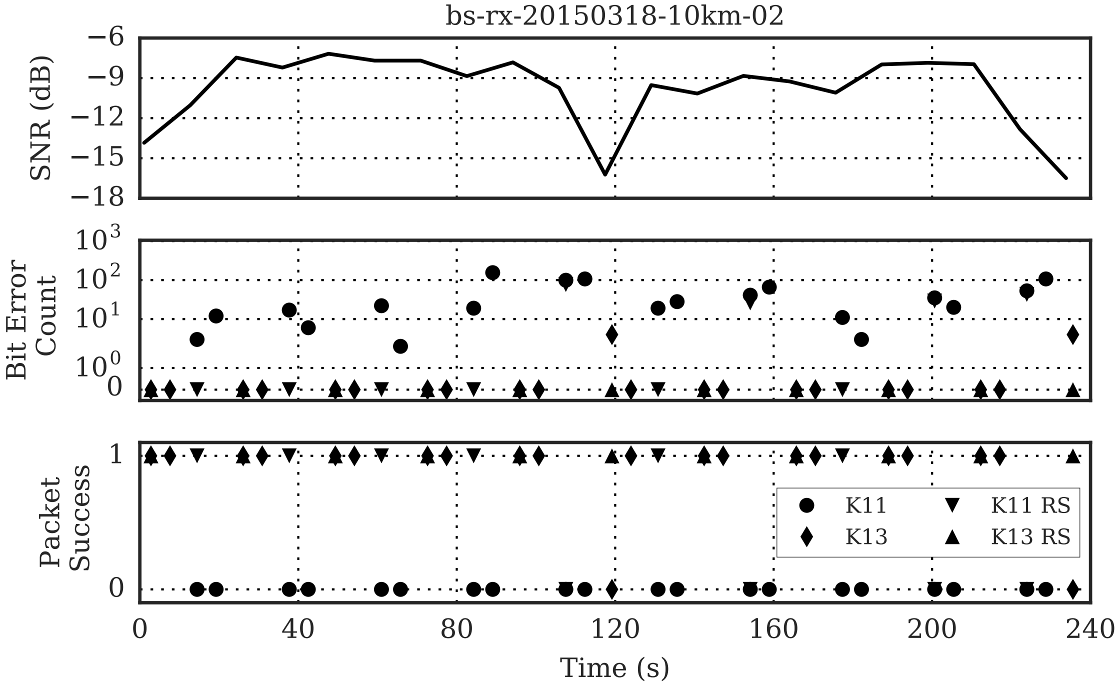

Fig. 4.18 Sea Trials Recording Results: 10km 02. Showing performance of K11 64-OCK (140.69 bit/s), K13 256-OCK (46.88 bit/s), K11 64-OCK RS (106.92 bit/s) and K13 256-OCK RS (35.63 bit/s).

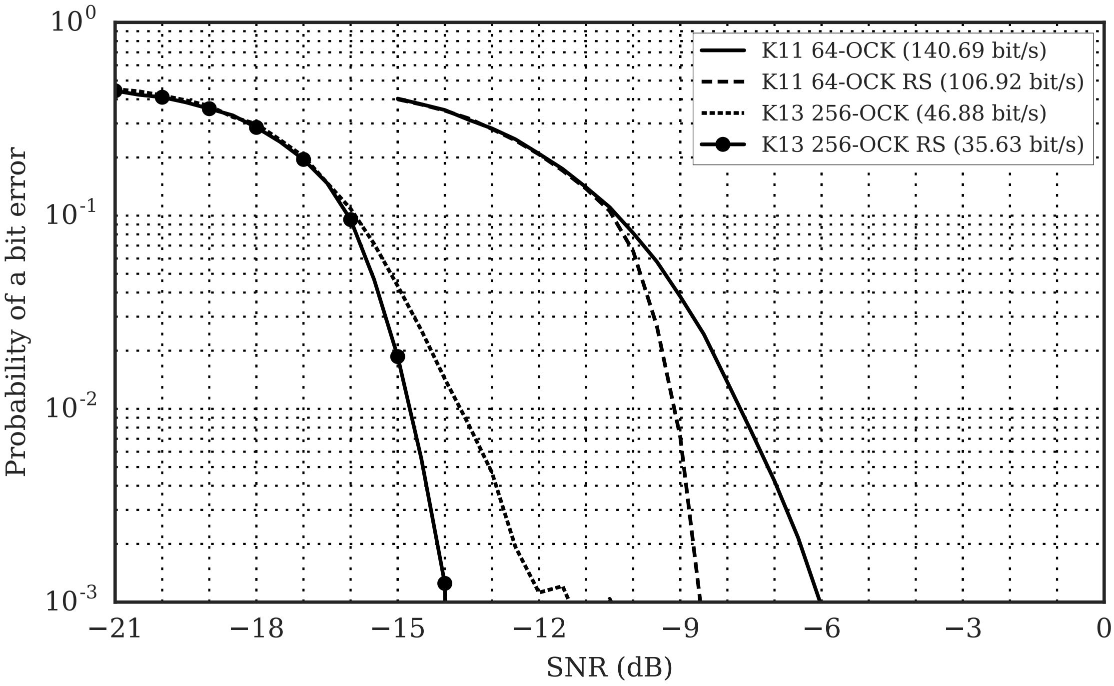

Fig. 4.19 Receiver Structure: Data Demodulation Channel Recording with AWGN. BER vs SNR for M-ary Orthogonal Code Keying packets with the receiver structure. Channel recording for 100 m is combined with AWGN at various levels of SNR and processed with the receiver structure. Spreading bandwidth, B, of 8 kHz and F_s of 48 kHz. Showing performance of K11 64-OCK (140.69 bit/s) and K13 256-OCK (46.88 bit/s). The performance using Reed-Solomon error correction codes is also shown for direct comparison. K11 64-OCK RS (106.92 bit/s) and K13 256-OCK RS (35.63 bit/s).

4.3.5.4 Data Demodulation Recordings with AWGN

The channel recordings, although important to show the potential of the modulation schemes, did not have sufficiently low SNR to fully demonstrate the boundaries of performance.

In order to investigate the performance boundaries of the modulation schemes and receiver structures when the signals are subjected to real channel effects, a subsection of the recording for 100 m is repeatedly combined with AWGN and processed with the receiver structure to produce performance curves as shown in Fig. 4.19.

The AWGN combined with the channel recording at 100 m shows that performance limits for BER of 10^{-3} are -6 dB for K11 64-OCK; -8.5 dB for K11 64-OCK RS; -12 dB for K13 256-OCK; and -14 dB for K13 256-OCK RS.

It is worth noting that the received-SNR estimates are based on the total received signal energy during the duration of a LFM chirp symbol. Given the long duration of the chirp (0.341 s) and the many multipath arrivals within the first 5 ms this means the SNR estimate is based on the total received energy of multiple paths, yet only one of these paths is currently utilised. The next section will consider this in more detail.

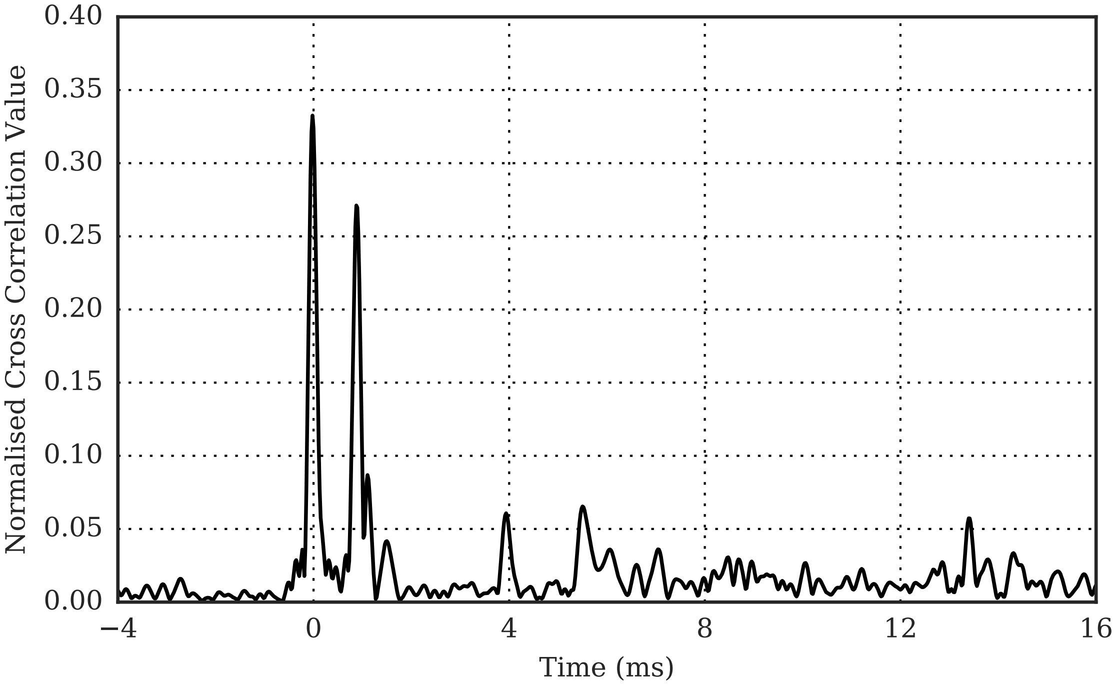

Fig. 4.20 Channel Impulse Response of Packet K11 64-OCK with AWGN. Peaks are observed with values: 0.333 @ 0 ms, 0.271 @ 0.875ms, 0.087 @ 1.104ms, 0.042 @ 1.5ms, 0.061 @ 3.937ms, 0.065 @ 5.5ms, 0.057 @ 13.4ms.

4.4 Multipath Exploitation

The channel impulse response in Fig. 4.20 shows a number of delayed arrivals with significant energy within the duration of a single data symbol (42.6 ms). The receiver structure under investigation only utilises the first arrival path for data demodulation. As SNR estimations are based on the total combined energy arriving within the LFM Chirp duration (341.3 ms) it may be possible to estimate the effective SNR of the arrival path utilised in data demodulation.

The single-path-SNR can be estimated as a ratio of path correlation peaks applied to the received-SNR of all paths as shown in (4.4) where P_0 is the correlator peak value for the first arrival path and P_n is the correlator peak value for the nth arrival path.

$$\mathrm{SNR}_{\mathrm{singlepath}} = \frac{P_0}{\sum_{n=0}^{N-1} P_n} \cdot \mathrm{SNR}_{\mathrm{received}} \tag{4.4}$$

In the case of K11 64-OCK and K11 64-OCK RS performance curves in Fig. 4.19 the packet has two significant arrivals of normalised correlator peak values of 0.333 and 0.271, plus a number of smaller peaks as shown in Fig. 4.20 and listed in Table 4.9.

Calculating the estimated single-path-SNR from (4.4) for this $\mathrm{SNR}_{\mathrm{singlepath}}$ as shown in (4.5) results in a single path SNR of 4.39 dB less than the measured received SNR.

Table 4.9 Multipath Arrival Peak Values and Delays

Path Index	Normalised Peak Value	Delay (ms)
0	0.333	0.000
1	0.271	0.875
2	0.087	1.104
3	0.042	1.500
4	0.061	3.937
5	0.065	5.500
6	0.057	13.400

$$\begin{aligned}
\mathrm{SNR}_{\mathrm{singlepath}} &= \frac{0.333}{(0.333+0.271+0.087+0.042+0.061+0.065+0.057)} \cdot \mathrm{SNR}_{\mathrm{received}} \\
&= \frac{0.333}{0.916} \cdot \mathrm{SNR}_{\mathrm{received}} \\
&= 0.364 \cdot \mathrm{SNR}_{\mathrm{received}}
\end{aligned}$$

In decibels this corresponds to:

$$\mathrm{SNR}_{\mathrm{singlepath}}\mathrm{dB} = -4.39\,\mathrm{dB} + \mathrm{SNR}_{\mathrm{received}}\mathrm{dB} \tag{4.5}$$

Applying this offset to the Channel Recording with AWGN simulation in Fig. 4.19 produces a comparable performance to that shown with the same receiver structure but only AWGN in Fig. 4.9.

Taking into account the peaks of the first two arrivals, the dual-path-SNR, $\mathrm{SNR}_{\mathrm{dualpath}}$, is shown in (4.6) resulting in a dual path SNR of 1.81 dB less than the measured received SNR.

$$
\begin{aligned}
\mathrm{SNR}_{\mathrm{dualpath}} &= \frac{0.333+0.271}{(0.333+0.271+0.087+0.042+0.061+0.065+0.057)} \cdot \mathrm{SNR}_{\mathrm{received}} \\
&= \frac{0.604}{0.916} \cdot \mathrm{SNR}_{\mathrm{received}} \\
&= 0.659 \cdot \mathrm{SNR}_{\mathrm{received}}
\end{aligned}
$$

In decibels this corresponds to:

$$\mathrm{SNR}_{\mathrm{dualpath}}\mathrm{dB} = -1.81\,\mathrm{dB} + \mathrm{SNR}_{\mathrm{received}}\mathrm{dB} \tag{4.6}$$

This produces an estimated potential improvement in performance of 2.58dB moving from utilising only first arrival compared to utilising the first two arrivals in this example.

To better demonstrate the potential for multipath exploitation, the channel recording with AWGN simulation was repeated with the energy from the first two paths combined. The correlator magnitudes in a narrow window for each path arrival are summed in order to combine the energy. This receiver structure does not employ independent path tracking, rather using a fixed delay offset between the two path arrivals based on the delay spread shown in the channel impulse response of the synchronisation header. The resulting AWGN performance can be seen in Fig. 4.21 for the K11 64-OCK and K11 64-OCK RS packets. This shows an improvement in performance, when using the first two arrival paths, of around 2 dB for BER of 10^{-3}.

Received-SNR is a measure of all signal energy arriving at the receiver during a symbol duration. Based on the long symbol durations this accounts for a number of significant arrival paths in these channels. When considering the effective SNR of a single path, the performance of the signal and receiver structure is in-line with the original receiver structure AWGN simulations.

The potential for exploiting the additional paths is demonstrated in the single example whereby the first two paths are utilised. Although, in a changing channel with long packet durations the receiver structure will require adaptive tracking of all paths that are utilised. Especially when considering amplitude variations due to changing geometry (e.g. surface reflections), as well as Doppler effects being unique to each path. This is worthy of further in-depth investigation but will require the foundation of the findings of subsequent chapters of this thesis to successfully develop such an adaptive receiver structure.

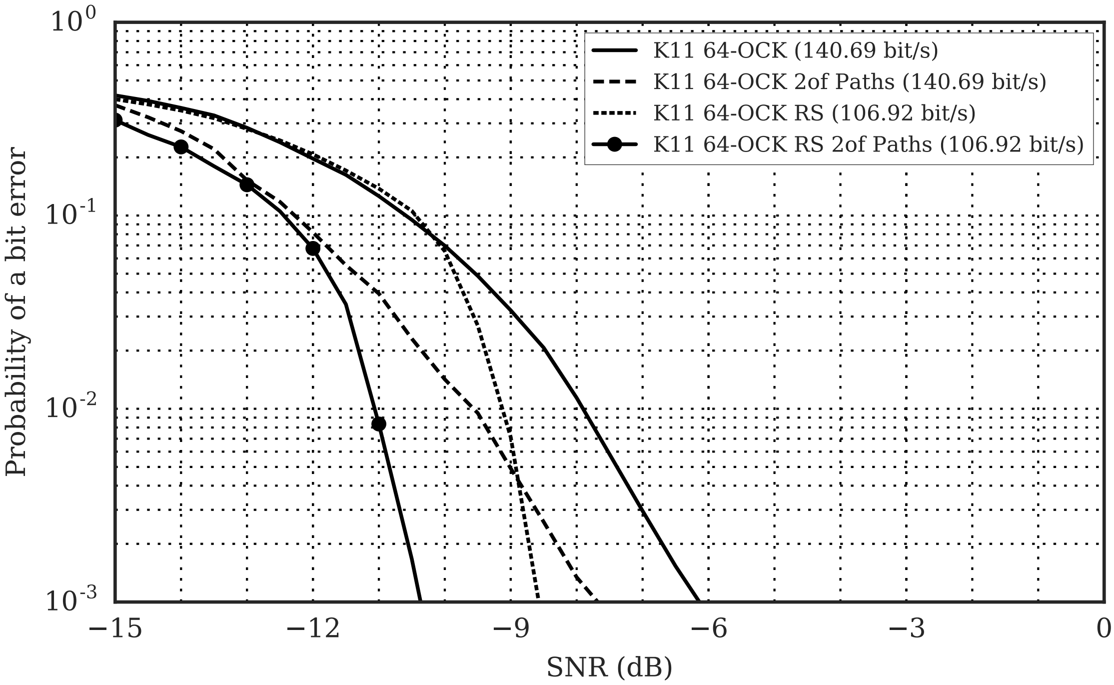

Fig. 4.21 Receiver Structure: Data Demodulation Channel Recording with AWGN for Multipath Exploitation. BER vs SNR for M-ary Orthogonal Code Keying packets with the receiver structure for single path and two arrival paths. Channel recording for 100 m is combined with AWGN at various levels of SNR and processed with the receiver structure. Spreading bandwidth, B, of 8 kHz and F_s of 48 kHz. Showing performance of K11 64-OCK (140.69 bit/s). The performance using Reed-Solomon error correction codes is also shown for direct comparison. K11 64-OCK RS (106.92 bit/s).

4.5 Summary

This chapter has investigated receiver structure design and performance when used with the signals designed in Chapter 3. Both synchronisation and data demodulation have been considered in depth, with simulations and sea trials carried out to validate the performance of the communication system.

The result of using a normalisation process as part of the receiver structure is shown when countering the effects of varying signal amplitude on the correlator outputs. This allows the use of fixed threshold detection during synchronisation. Simulations show that synchronisation signal structures made up of multiple unique PN symbols produce the same performance in AWGN channel as a synchronisation signal structure consisting of a single PN symbol of equivalent processing gain (bandwidth and total duration). Experimental validation of recordings in real world channels shows that the receiver structure utilising multiple symbols is feasible. At the longer ranges, and lower SNR signals, the results show equivalent synchronisation counts for equivalent processing gain symbol combinations.

Simulations show the combined performance of the data demodulating receiver structure with K11 64-OCK and K13 256-OCK modulation schemes, with and without RS coding, is able to operate in the target low-received-SNR region between $-9\,\text{dB}$ and $-18\,\text{dB}$.

Experimental validation in sea trials shows successful synchronisation and numerous error-free packets received at 10 km with a signal transmit power limited to 170.8 dB re 1 µPa @ 1 m or 1 W of acoustic power. Successful packets were received at this range for K11 64-OCK, K11 64-OCK RS, K13 256-OCK, and K13 256-OCK RS.

Recordings combined with AWGN show successful data demodulation with BER of 10^{-3} down to $-14\,\text{dB}$ of the K13 256-OCK RS at a data rate of $35.63\,\text{bit/s}$. Given packet sizes of 200 bits this BER would equate to successful error-free packets. Channel capacity according to Shannon-Hartley for this SNR and bandwidth is $450.57\,\text{bit/s}$ resulting in a channel capacity utilisation of 7.91%.

The K11 64-OCK RS signal with a data rate of $106.92\,\text{bit/s}$ shows BER of 10^{-3} at $-8.5\,\text{dB}$, with packet sizes of 600 bits again this would result in successful packets. Channel capacity at this SNR and bandwidth is $1524.96\,\text{bit/s}$ resulting in a channel capacity utilisation of 7.01%.

Multipath exploitation has been piloted with K11 64-OCK RS signals showing a 2 dB gain in performance from using one extra path in recordings combined with AWGN. Channel capacity at SNR of $-10.5\,\text{dB}$ is $985.36\,\text{bit/s}$ resulting in a channel capacity utilisation of 10.85%.

Single-path-SNR has been shown to be 4.39 dB less than the measured received-SNR in the channel impulse response from 100 m sea trials recordings. Applying this offset to the previous example to focus on the single path performance, the channel capacity of $-14\,\text{dB} - 4.39\,\text{dB} = -18.39\,\text{dB}$ is $166.01\,\text{bit/s}$ so a data rate of $35.63\,\text{bit/s}$ results in a channel capacity utilisation of 21.46%.

Chapter 5

Doppler Compensation

5.1 Introduction

As shown in Chapter 3 the PN sequences with long durations suffer greatest from Doppler shift. This chapter looks at receiver structure designs to compensate for this weakness in the signal properties. Through experimental validation the performance of different synchronisation and data demodulation structures is investigated.

The ambiguity plots show the peak correlator values with respect to relative platform velocity indicating poor Doppler tolerance in bandlimited PN symbols of long duration.

Receiver structure designs for Doppler compensation are shown for synchronisation with single or multiple symbol signal structures; and for data demodulation with static or tracking resamplers.

Experimental validation is carried out in a marina utilising a powerboat to produce a range of motion types, and relative velocities and accelerations. These test the performance of receiver structures and signals in channels with significant Doppler effect.

Channel recordings are combined with AWGN to test the performance of receiver structures and signals in channels with significant Doppler effect and realistic target SNR levels.

5.2 Motivation

Non-stationary platforms, even those anchored by a short chain to the seabed, will to varying degrees experience the Doppler effect on the received acoustic signals. These effects are introduced by Lurton [4, Section 2.5.1] and covered in detail by Stojanovic [9].

The ambiguity function plots of the two PN sequences used throughout this research, K11 and K13 symbols, are shown in Fig. 5.1. The longer duration symbols, K13, suffer greatest with Doppler shift, with the autocorrelation peak value falling away to 70% with a relative velocity of only $\pm 0.33\,\mathrm{m/s}$. Even with the shorter symbol duration of K11 the drop to 70% occurs after

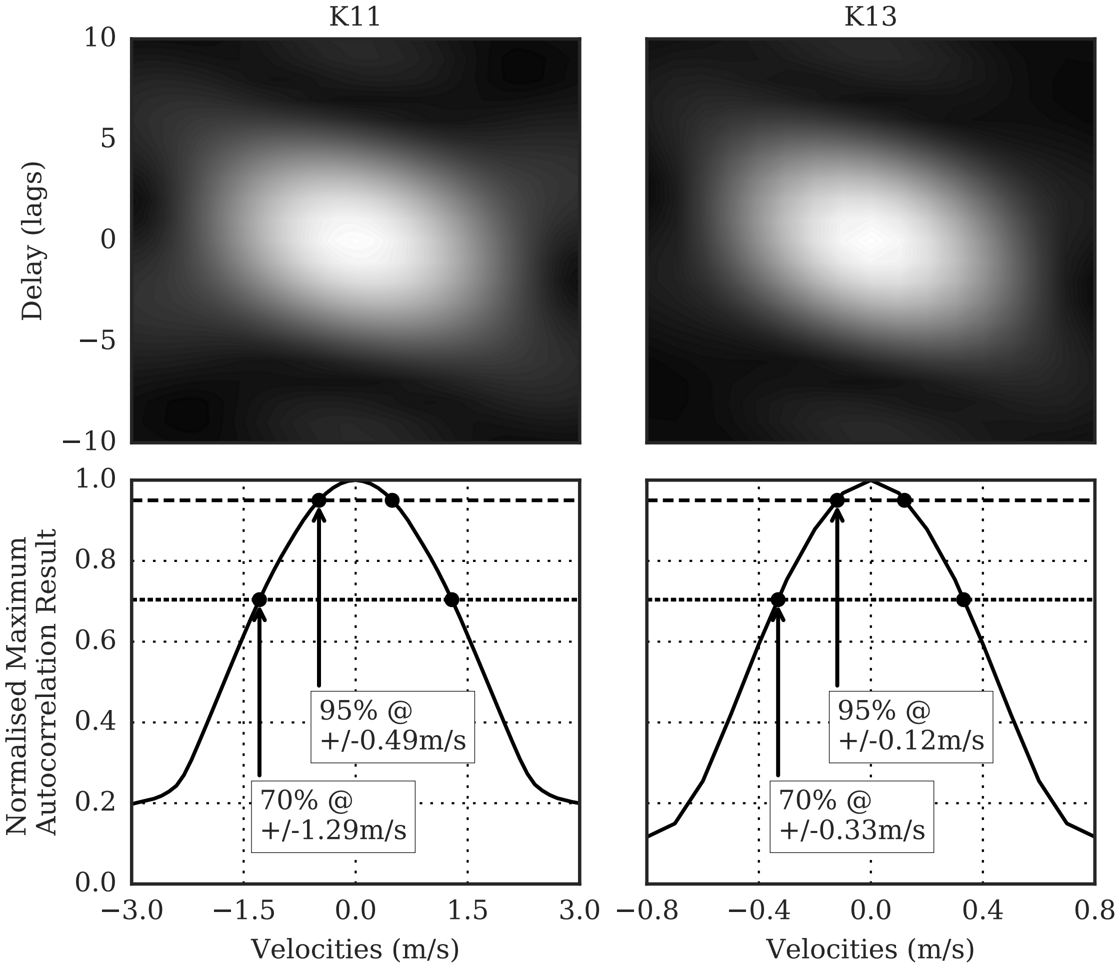

Fig. 5.1 Ambiguity Functions of K11 and K13 Symbols. Cross section figures show peak autocorrelation values at a range of velocities. For $c = 1500\,\mathrm{m/s}$, $F_s = 48\,\mathrm{kHz}$ and $B = 8\,\mathrm{kHz}$ with K11 (42.65 ms) and K13 (170.65 ms). K11 autocorrelation reaches 95% at $\pm 0.49\,\mathrm{m/s}$, and 70% at $\pm 1.29\,\mathrm{m/s}$. K13 autocorrelation reaches 95% at $\pm 0.12\,\mathrm{m/s}$, and 70% at $\pm 0.33\,\mathrm{m/s}$.

$\pm 1.29\,\mathrm{m/s}$. To put this into perspective, the velocity of an AUV can be in the range of $0\,\mathrm{m/s}$ to $2.6\,\mathrm{m/s}$. Evidently, the receiver design will require compensation for Doppler effect in these applications.

5.3 Doppler Compensation Techniques

Techniques for Doppler compensation with PN sequences have been covered before by Johnson, Freitag, and Stojanovic [117], and also referred to by Sharif, Neasham, Hinton, and Adams [16]. Here, a bank of correlators is loaded with Doppler shifted versions of the sequence across a range of Doppler shifts. The input signal is correlated across the entire bank and the maximum correlator value is then used to test for synchronisation and to estimate the starting Doppler shift of the signal.

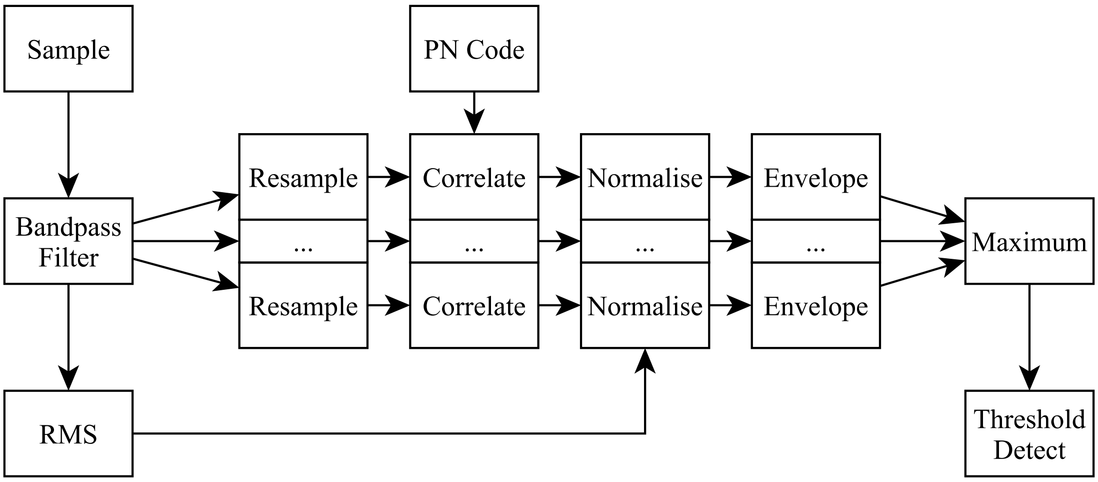

Fig. 5.2 Receiver Structure Block Design: Synchronisation.
c) Single code, resampling, correlation, normalisation, envelope, maximum threshold detection.

5.4 Synchronisation: Design

It is possible to use the Doppler compensation technique by Johnson, Freitag, and Stojanovic [117] mentioned previously, but with the key difference of loading each correlator in the bank with the same PN sequence, and instead resampling the input signal to each correlator to potentially remove the frequency shift due to Doppler effect. Resampling is then performed in the method shown by Sharif, Neasham, Hinton, and Adams [16].

Taking the receiver structures for synchronisation in Chapter 4, and starting with the single PN sequence synchronisation header, the block design incorporating the resamplers and correlator bank is shown in Fig. 5.2. The number and distribution of the resamplers and correlators is dependent on the ambiguity functions shown previously. To cover a suitable range, of say $\pm 2.7\,\mathrm{m/s}$, with minimum ripple in correlator peak value of 95%, this would give 25 resampler streams spaced at $0.225\,\mathrm{m/s}$ steps for a K13 symbol.

With synchronisation structures containing multiple sequences the receiver structure again continues from that in Chapter 4 but to each symbol in the structure there exists again a bank of resamplers and correlators before the maximum correlator values are combined for threshold detection. This is shown in Fig. 5.3.

Both synchronisation receiver structures, as well as searching for the synchronisation header across a range of Doppler shifts, will also provide the starting Doppler estimate for the data packet demodulation.

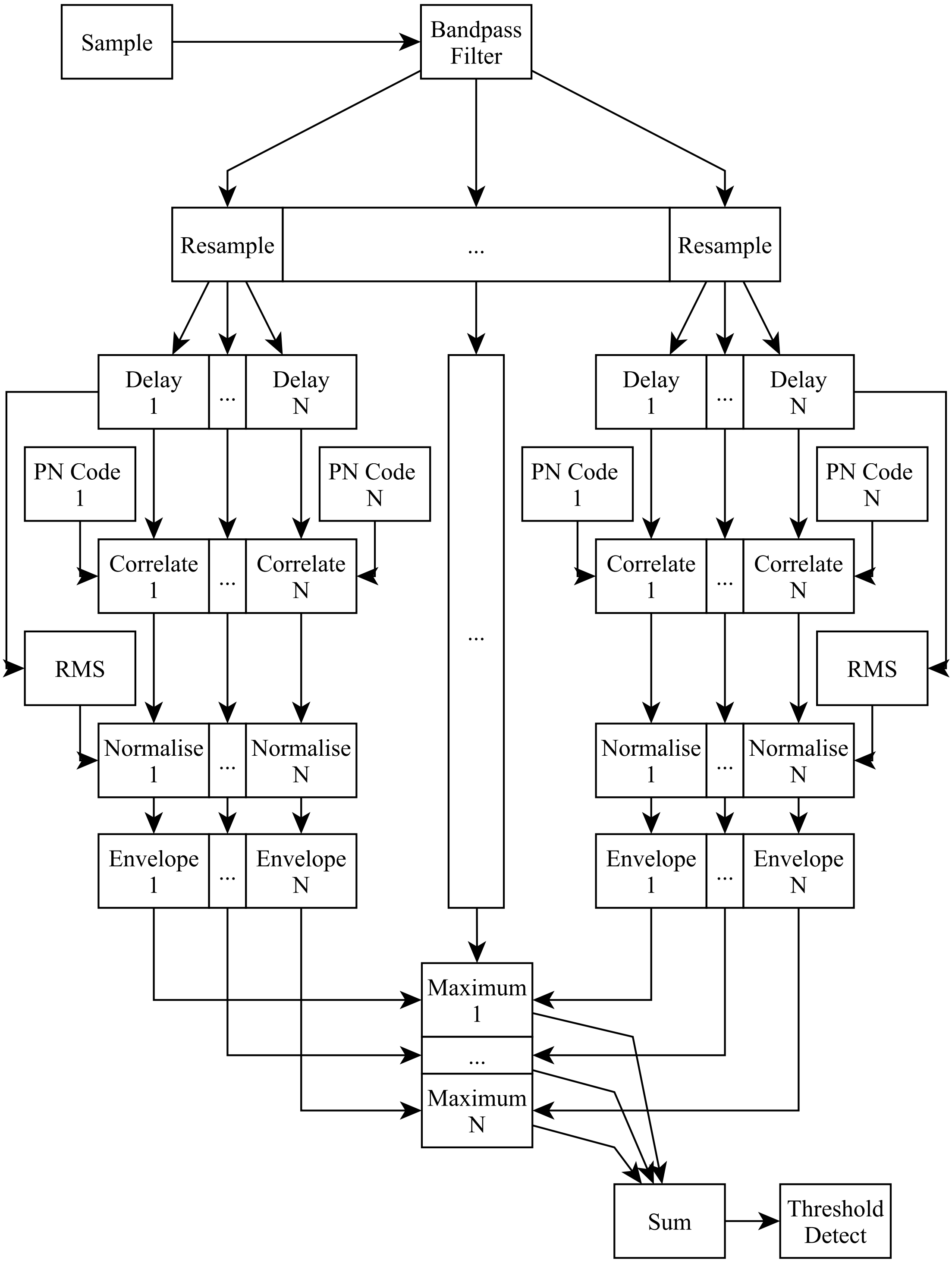

Fig. 5.3 Receiver Structure Block Design: Synchronisation.
d) Multiple codes, resampling, correlation, normalisation, envelope, maximum summed threshold detection.

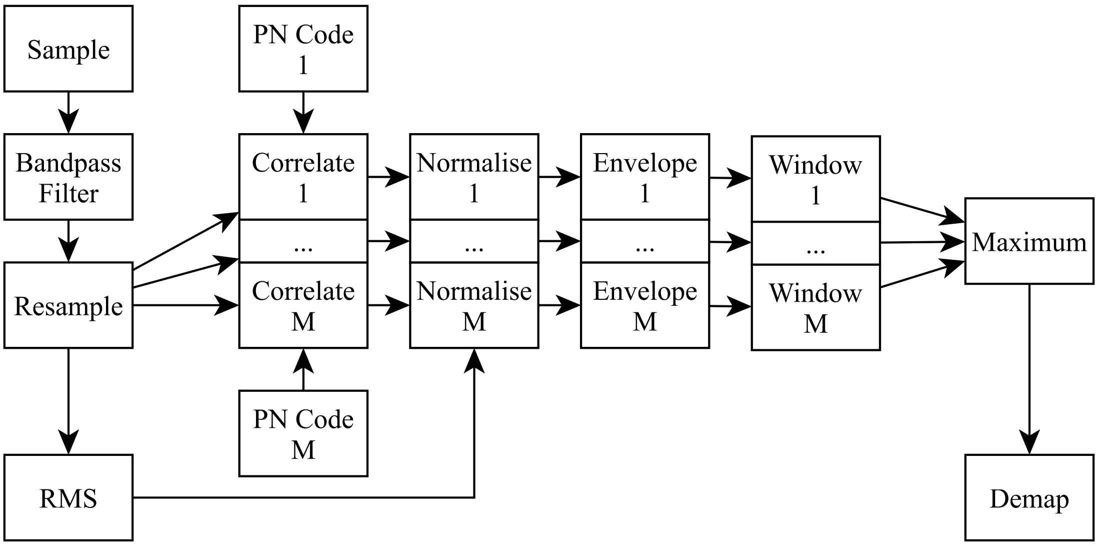

Fig. 5.4 Receiver Structure Block Design: Data Demodulation.
b) Resampling, correlation, normalisation, envelope, maximum value selection, demapping.

5.5 Data Demodulation: Design

The simplest Doppler compensation that can be applied here is to take the receiver structure from Chapter 4 and prepend a single resampler stage which is set to the Doppler estimate determined by the synchronisation structure. This static resampler receiver structure is shown in Fig. 5.4.

Taking the Doppler compensation further, to account for longer duration packets and channel changes, it is possible to employ the approach used in the synchronisation structures to track change in Doppler shift on a symbol-by-symbol basis in the data packet. This tracking resampler structure is shown in Fig. 5.5. The distribution of resampler values is 7 streams targeting a 95% ripple so for K11 symbols this is a range of $\pm 2.7\,\mathrm{m/s}$ in steps of $0.9\,\mathrm{m/s}$. For the K13 symbols this is a range of $\pm 0.675\,\mathrm{m/s}$ in steps of $0.225\,\mathrm{m/s}$.

However, the absolute resampler values of the seven streams are relative to the value used in the centre stream. This centre stream value is initially set to the Doppler estimate produced by the synchronisation receiver structure. As the receiver processes the received signal symbol-by-symbol the centre resampler value is adjusted and results in the absolute resampler values of the other size streams also shifting accordingly. This allows the receiver to cover a much larger overall range of Doppler shifts throughout the duration of the whole packet, but on a symbol-by-symbol basis provides fine resolution refinement. The full range of the resamplers sets the maximum acceleration that can be accommodated by the receiver structure.

For example, for the K11 symbols if the initial Doppler estimate is $1.0\,\mathrm{m/s}$ then the absolute resampler values will cover the range of $-1.7\,\mathrm{m/s}$ to $3.7\,\mathrm{m/s}$.

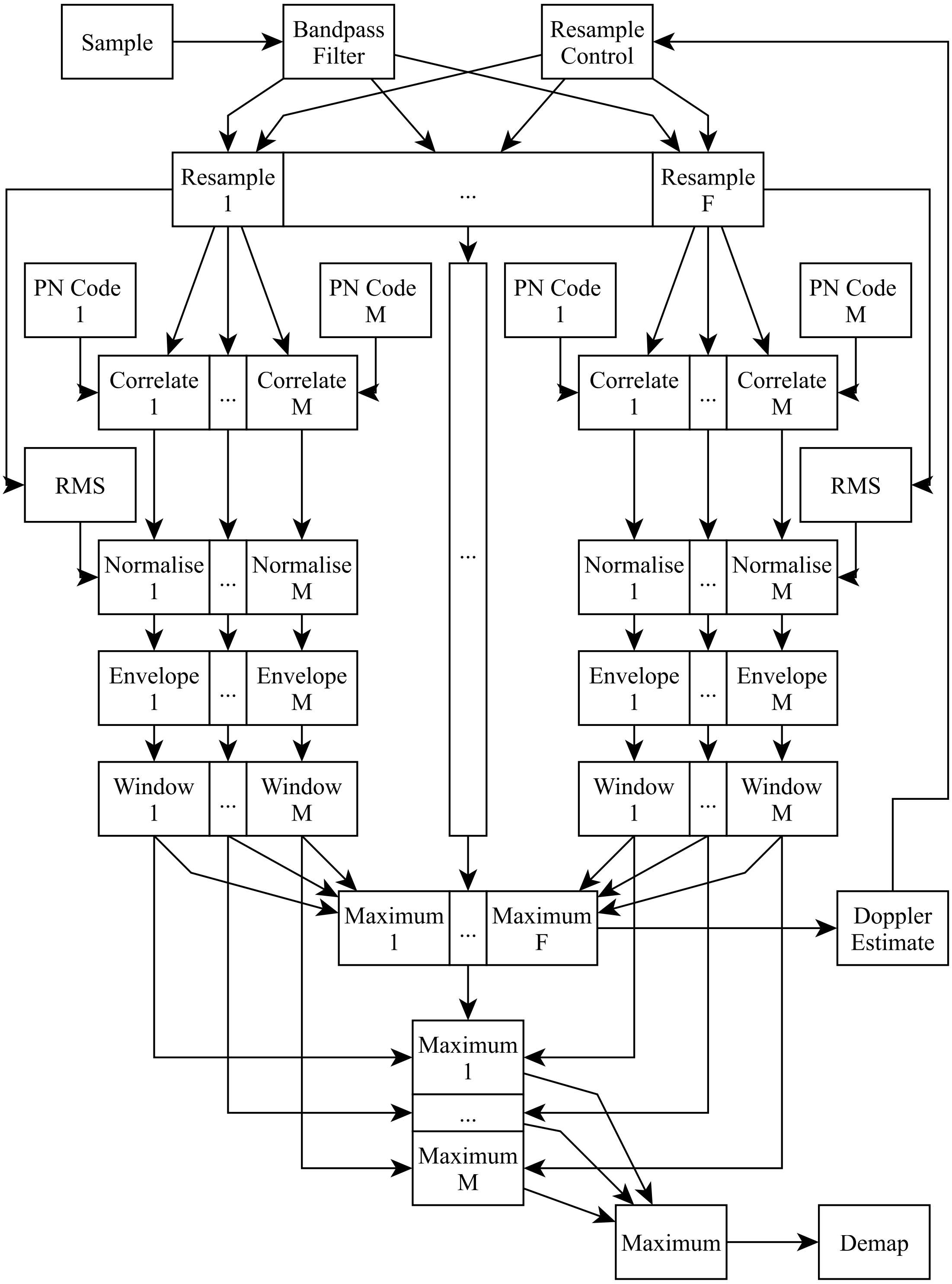

Fig. 5.5 Receiver Structure Block Design: Data Demodulation.
b) Resampling, correlation, normalisation, maximum value selection, tracking, demapping.

5.6 Experimental Validation: Marina Trials 2016-02-10

5.6.1 Experiment Setup

An aerial view of the Royal Quays Marina, North Shields can be seen in Fig. 5.6. This shows the location of the receiver and the paths, A, B and C, that were taken by the powerboat towing the transmitter. The details for each recording are listed in Table 5.1 which includes the recording filename, path taken by the powerboat, and the motion type.

Location Royal Quays Marina, North Shields

Transmitter Power boat platform in motion. Laptop playing audio. Acoustic power amplifier. Transducer on cable suspended in water at a depth of 2m. Additional mass was added to the transducer end of the cable in order to maintain depth as it was towed by the boat.

Receiver Laptop recording audio. Bandpass filter and amplifier. Hydrophone on cable suspended in water at a depth of 5m. Multiple 4 minute recordings taken for each motion type.

Weather and Water State Clear skies. Calm water.

Geology Stone wall marina with floating pontoons. Depth around 10m.

Motion Types Constant 1.11 m/s along Path A, Constant 2.22 m/s along Path A, Varying 0 m/s to 2.22 m/s along Path A, Perpendicular Constant 2.22 m/s along Path B and Path C.

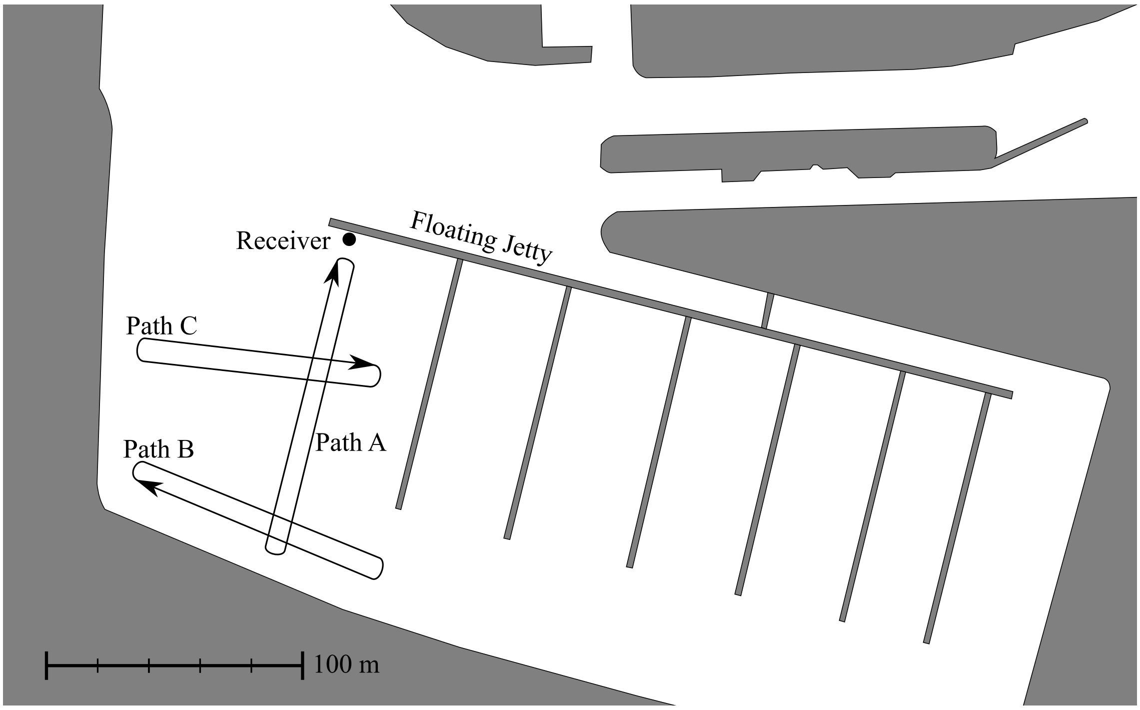

Fig. 5.6 Marina Aerial View

Table 5.1 Marina Trials Recordings. Note: There is no motion14 recording.

Recording Index	Recording Name	Path Of Boat	Motion Type
0	bs-rx-20160210-motion01	Path A	Constant 1.11 m/s
1	bs-rx-20160210-motion02	Path A	Constant 1.11 m/s
2	bs-rx-20160210-motion03	Path A	Constant 1.11 m/s
3	bs-rx-20160210-motion04	Path A	Constant 1.11 m/s
4	bs-rx-20160210-motion05	Path A	Constant 2.22 m/s
5	bs-rx-20160210-motion06	Path A	Constant 2.22 m/s
6	bs-rx-20160210-motion07	Path A	Constant 2.22 m/s
7	bs-rx-20160210-motion08	Path A	Constant 2.22 m/s
8	bs-rx-20160210-motion09	Path A	Varying 0 m/s to 2.22 m/s
9	bs-rx-20160210-motion10	Path A	Varying 0 m/s to 2.22 m/s
10	bs-rx-20160210-motion11	Path A	Varying 0 m/s to 2.22 m/s
11	bs-rx-20160210-motion12	Path B	Perpendicular Constant 2.22 m/s
12	bs-rx-20160210-motion13	Path B	Perpendicular Constant 2.22 m/s
13	bs-rx-20160210-motion15	Path C	Perpendicular Constant 2.22 m/s
14	bs-rx-20160210-motion16	Path C	Perpendicular Constant 2.22 m/s

5.6.2 Channel Conditions

Received SNR estimates of the PN signals throughout the recordings were based on the LFM chirps (up and down) between packets along with the silence periods that preceded them. These can be seen in figures with Fig. 5.7 for Constant 1.11 m/s, Fig. 5.8 for Constant 2.22 m/s, Fig. 5.9 for Varying 0 m/s to 2.22 m/s, and Fig. 5.10 for Perpendicular Constant 2.22 m/s.

The received SNR plots for the recordings show a gradual and cyclical change during the four minute duration. The location of the boat and transmitter relative to the receiver is one factor, with high SNR readings as the boat draws close to the receiver platform. As well as general background noise, there is a noise source attached to the boat in the outboard engine along with the propeller generated noise. This varies as the throttle is adjusted to maintain speed and there is some directionality in the propeller induced noise.

Fig. 5.7 and Fig. 5.8 show the periodicity linked to boat position along path A, where high SNR indicates the transmitter being in close proximity to the receiver. The periodicity in the Constant 2.22 m/s shows more frequent peaks than in the Constant 1.11 m/s recording, which is to be expected.

In Fig. 5.9, although the path of the boat is as before along path A, the varying speed and sudden changes in engine usage greatly affect the noise generation which may be a factor in the fluctuating SNR readings.

Fig. 5.10 shows peaks where the boat draws closer to the receiver, but the remainder of the recording is generally a steady SNR level.

Fig. 5.11 shows the channel impulse responses for each motion type. For all recordings there are strong multipath arrivals, sometimes up to 20 ms after the first arrival. The stone walls of the marina provide strong acoustic reflectors. The channel changes over the duration of a data packet (4.3 s) are more pronounced than in the sea trials in the previous chapter. Again, the multipath arrivals show fading in and out through the packet duration. In the Varying 0 m/s to 2.22 m/s impulse response it is possible to see that the later arrivals, after 15 ms show a mirror image shift to the first arrivals. This is an important factor in any future receiver structure that combines energy from multiple paths - each path has an independent Doppler shift to take account of and to track throughout the packet duration.

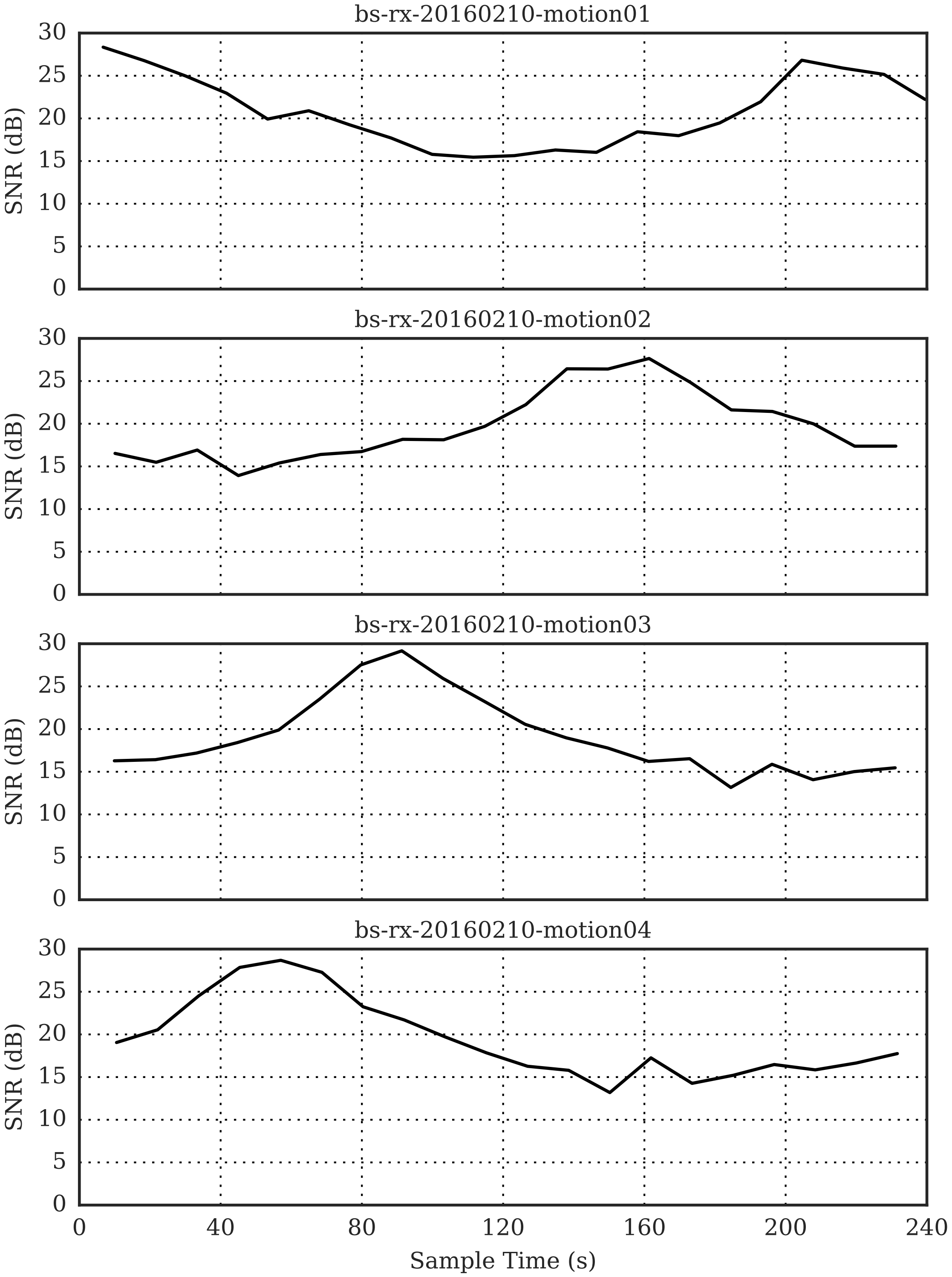

Fig. 5.7 Marina Trials SNR Estimates with multiple recordings for motion type Constant 1.11m/s.

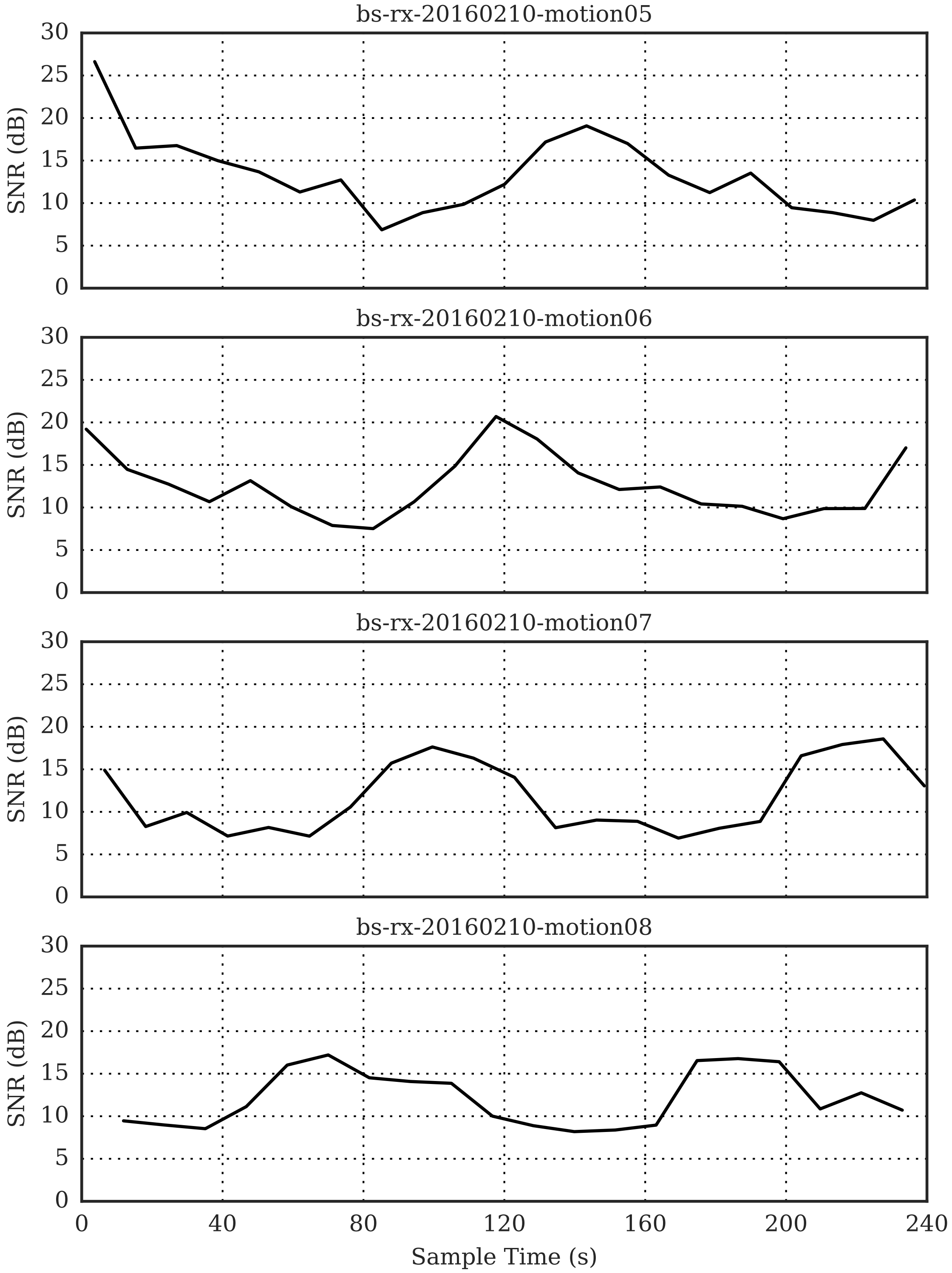

Fig. 5.8 Marina Trials SNR Estimates with multiple recordings for motion type Constant 2.22m/s.

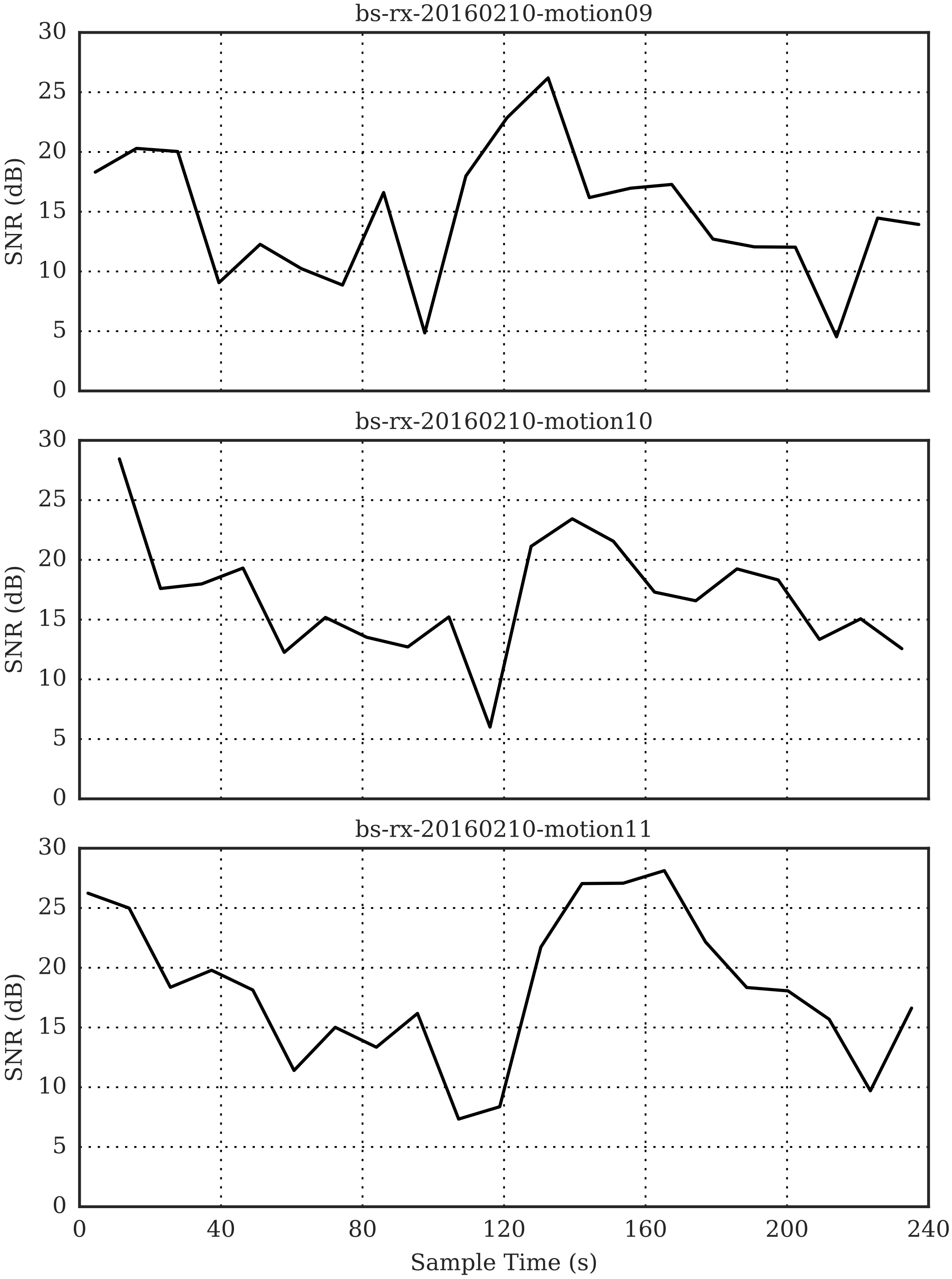

Fig. 5.9 Marina Trials SNR Estimates with multiple recordings for motion type Varying 0m/s to 2.22m/s.

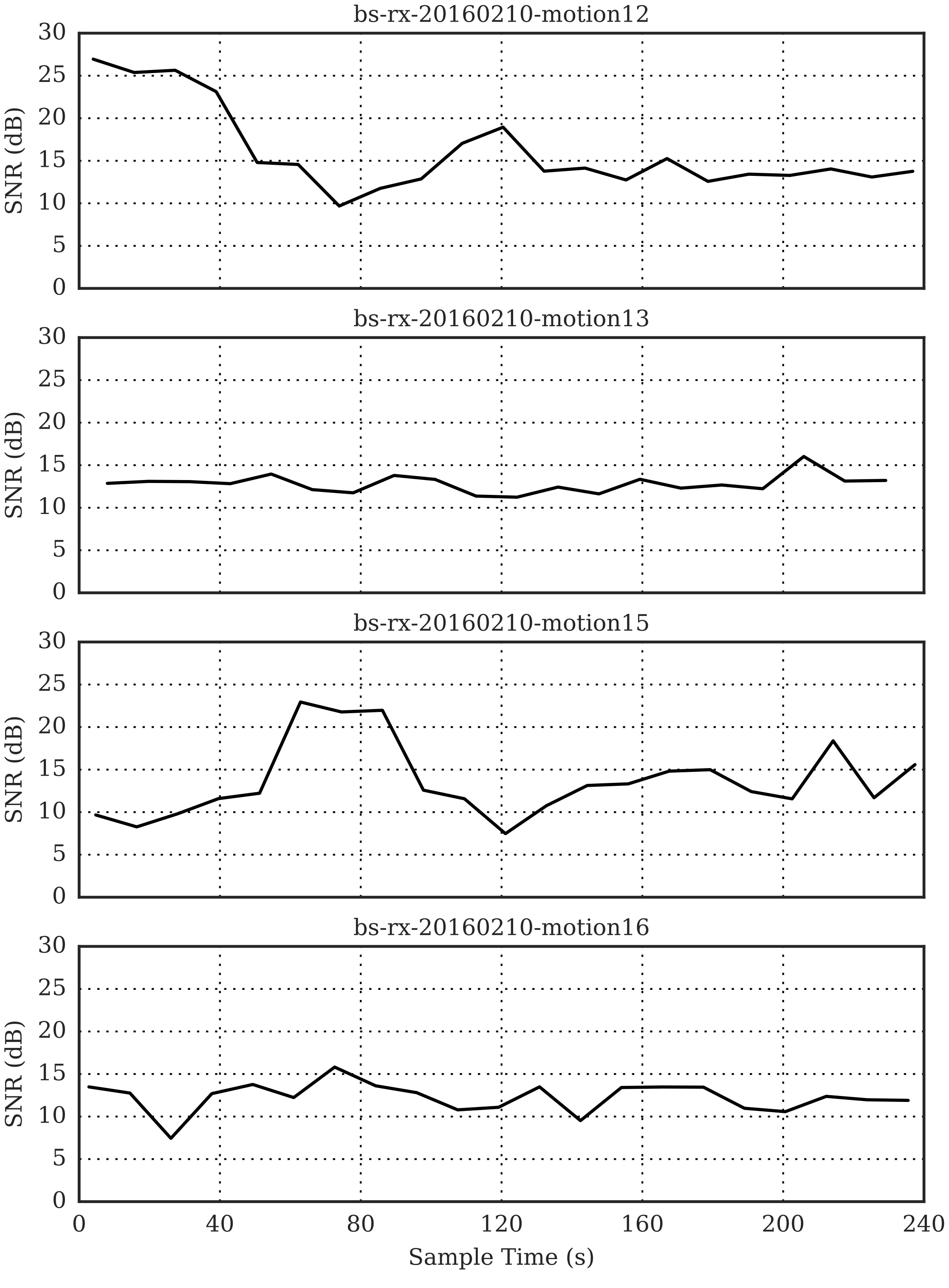

Fig. 5.10 Marina Trials SNR Estimates with multiple recordings for motion type Perpendicular Constant 1.11m/s.

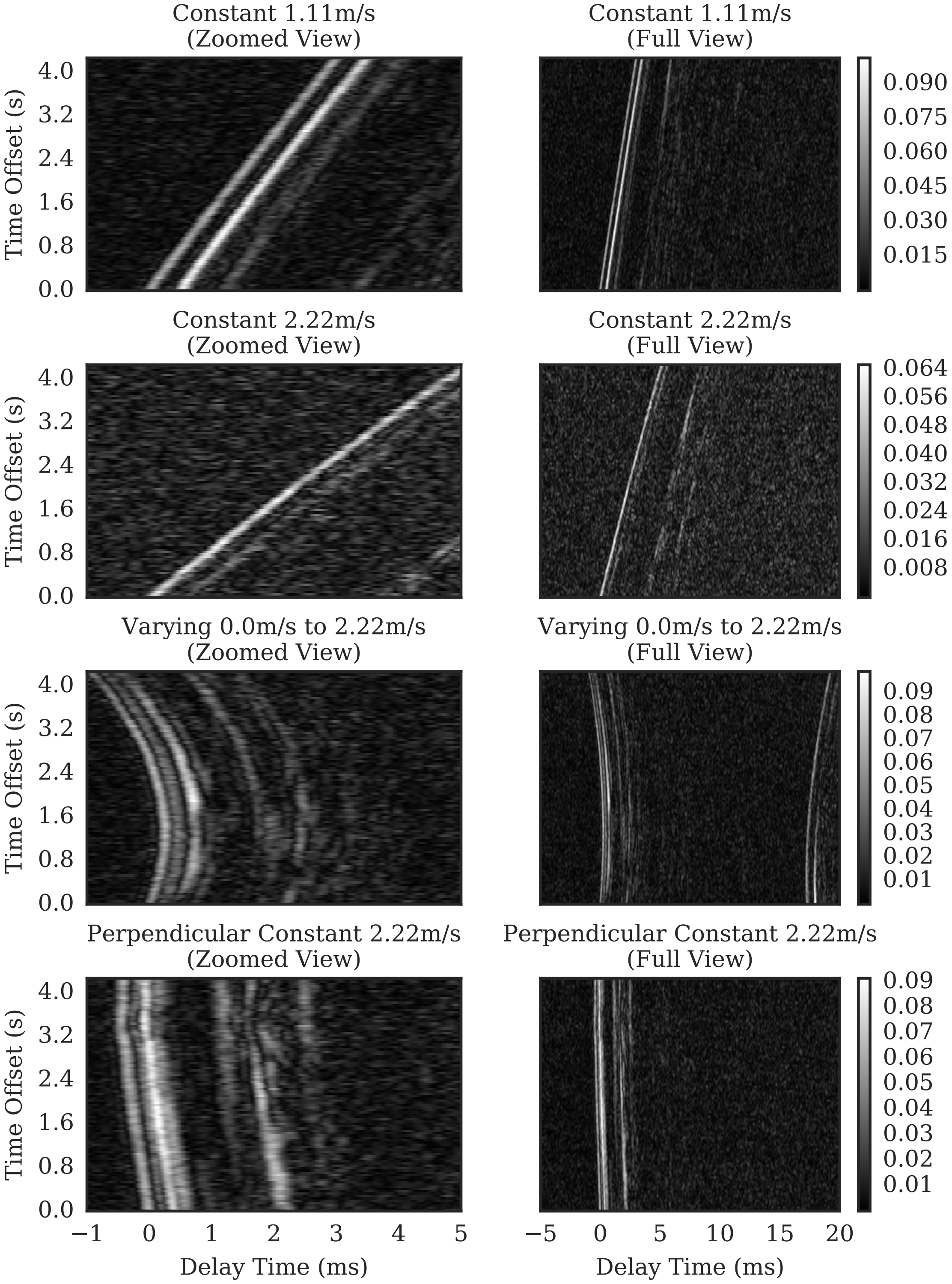

Fig. 5.11 Marina Channel Impulse Responses. Showing zoomed and longer duration views of the packet arrival.

Table 5.2 Marina Trials Results: Synchronisation Counts: No Doppler compensation

	Synchronisation Counts						
	K11 Symbols				K13 Symbols		
Motion Type	1 of	2 of	4 of	8 of	1 of	2 of	4 of
Constant 1.11m/s	42	41	40	40	8	9	11
Constant 2.22m/s	16	21	27	31	0	0	1
Varying 0.0m/s to 2.22m/s	29	28	30	29	1	1	2
Perpendicular Constant 2.22m/s	43	40	41	41	24	26	31

5.7 Synchronisation: Results

5.7.1 Synchronisation Signal Structures

The performance of the synchronisation signal structures described in Table 4.3 was investigated in a channel with significant Doppler shift using the receiver structures in Chapter 4, namely Fig. 4.2 and Fig. 4.3. These are the receiver structures without any Doppler compensation included. The aim here is to determine the performance of the signal structures in a channel with significant Doppler effects.

The results of synchronisation counts for varying synchronisation signal structures are presented in Table 5.2. The results for each recording have been collated by motion type. The sea trials results in the previous chapter showed the effect of SNR, here with high SNR readings the effect of Doppler is the dominant factor on performance. As before, the duration of the entire transmit waveform is 23.273 s. Therefore a single four minute recording contains 10.3 repetitions of the relevant packets and synchronisation signal structures, which equates to 10 or 11 result points per recording. For motion types with four recordings, a synchronisation count of between 40 and 44 is expected; for three recordings, 30 to 33 synchronisation counts are expected. For the lower speed of Constant 1.11 m/s the K11 symbol structures synchronise successfully, whereas for the K13 symbol structures the synchronisation counts are greatly reduced. As the speed is increased to 2.22 m/s the K13 symbol structures drop to almost total failure to synchronise. The K11 symbols show a gradient increasing as more symbols are combined which indicates a general loss of peak correlator value; the ambiguity plots in Fig. 5.1 show that as the velocity reaches 2.22 m/s the peak has dropped to 50% by this speed.

The varying and perpendicular motion types contain periods of low speed, and hence Doppler effect, so both K11 and K13 symbol structures have successful synchronisation counts for part of this period.

In general, both symbol types K11 and K13, even when used in multiple symbol structures, suffer from Doppler beyond certain speeds. However, for K11 symbols this velocity is much higher than K13 before it fails to synchronise. In conjunction with the sea trials results in the previous chapter this may be a suitable technique to create a signal structure with inbuilt Doppler tolerance whilst retaining total processing gain due to signal spreading over long durations.

5.7.2 Synchronisation Receiver Structures

The performance of the Doppler compensation receiver structures in Fig. 5.2 and Fig. 5.3 was investigated in the same channel with significant Doppler shift using two sets of parameters. For coarse resampling this covers a range of $\pm 2.7\,\mathrm{m/s}$ in steps of $0.675\,\mathrm{m/s}$ resulting in a total of 9 streams. For fine resampling this covers a range of $\pm 2.7\,\mathrm{m/s}$ in steps of $0.225\,\mathrm{m/s}$ resulting in a total of 25 streams.

Doppler compensation receiver structures discussed previously were investigated using the packet synchronisation headers PK13. The successful synchronisation counts are shown in Table 5.3. A single four minute recording contains 10.3 repetitions of the four relevant packets and synchronisation signal structures, which equates to 41 or 42 result points per recording. For ranges with four recordings, a synchronisation count of between 164 and 168 is expected; for three recordings, 123 to 126 synchronisation counts are expected.

The results in Table 5.3 show a clear improvement between no Doppler compensation and both coarse and fine search Doppler compensation across the four motion types. There is no clear differentiation in the performance of coarse compared to fine search. This is most likely due to the high received-SNR. Even with a 70% drop in correlator peak value the coarse search receiver structure will still produce peaks that are well clear of the noise floor for successful threshold detection. However, these results do show that the receiver structure and signal resamplers are a viable solution to compensating for Doppler effects on the transmitted signal.

Table 5.3 Marina Trials Results: Synchronisation Counts with Doppler Compensation

	Synchronisation Counts					
Doppler Compensation	None		Coarse Search		Fine Search	
	K13 Symbols		K13 Symbols		K13 Symbols	
Motion Type	1 of	2 of	1 of	2 of	1 of	2 of
Constant 1.11m/s	26	29	167	166	168	167
Constant 2.22m/s	12	11	165	165	165	166
Varying 0.0m/s to 2.22m/s	15	16	126	123	126	124
Perpendicular Constant 2.22m/s	81	94	164	164	165	164

5.8 Data Demodulation Results

5.8.1 Data Demodulation Receiver Structure Configurations

The performance of the receiver structures in Fig. 5.4 and Fig. 5.5 was investigated in channels with significant Doppler effect. The receiver structures and details of relevant Doppler compensation parameters are described in Table 5.4.

Table 5.4 Marina Trials Receiver Configuration

Doppler Compensation	K11 64-OCK	K13 256-OCK
None	As per Chapter 4 Fig. 4.8.	
Static Resampler	As per Fig. 5.4 with the resampler value set to the estimate provided by the synchronisation stage.	
Tracking	As per Fig. 5.5 with the resampler values set to a total of 7 streams covering $\pm 2.7\,\mathrm{m/s}$ in steps of $0.9\,\mathrm{m/s}$.	As per Fig. 5.5 with the resampler values set to a total of 7 streams covering $\pm 0.675\,\mathrm{m/s}$ in steps of $0.225\,\mathrm{m/s}$.

5.8.2 Results For All Marina Trials Recordings

Collated results for all of the Marina Trials recordings have been tabulated in Table 5.5 for K11 64-OCK and K11 64-OCK RS; and in Table 5.6 for K13 256-OCK and K13 256-OCK RS.

These results show that any Doppler compensation in the receiver structure has a positive effect when compared to the uncompensated signals for both K11 64-OCK and K13 256-OCK modulation schemes. Although there is little difference in performance for K11 64-OCK between static and tracking resampler compensation. For K13 256-OCK there is a differentiation in performance with tracking resampler showing improvement over the static resampler.

Table 5.5 Marina Trials Recording Results: K11 64-OCK - All Recordings

	K11 64-OCK Uncoded		K11 64-OCK RS	
Doppler Compensation	BER	PSR	BER	PSR
None	3.205×10^{-1}	0.197	3.118×10^{-1}	0.211
Static Resampler	3.213×10^{-2}	0.704	2.458×10^{-2}	0.836
Tracking Resampler	3.548×10^{-2}	0.714	2.751×10^{-2}	0.822

Table 5.6 Marina Trials Recording Results: K13 256-OCK - All Recordings

	K13 256-OCK Uncoded		K13 256-OCK RS	
Doppler Compensation	BER	PSR	BER	PSR
None	4.256×10^{-1}	0.095	4.286×10^{-1}	0.110
Static Resampler	4.757×10^{-2}	0.744	3.426×10^{-2}	0.844
Tracking Resampler	2.425×10^{-2}	0.875	2.589×10^{-2}	0.890

5.8.3 Data Demodulation Results By Motion Type

The performance results from each recording at a given motion type are collated and tabulated. Constant 1.11 m/s results are shown in Table 5.7 and Table 5.8. Constant 2.22 m/s results are shown in Table 5.9 and Table 5.10. Varying 0 m/s to 1.11 m/s results are shown in Table 5.11 and Table 5.12. Perpendicular Constant 2.22 m/s results are shown in Table 5.13 and Table 5.14.

Across all motion types and modulation schemes, K11 64-OCK and K13 256-OCK, there is a clear improvement in performance when using either Doppler compensation technique in the receiver structure versus none at all, as shown in Table 5.7 to Table 5.14. Between static and tracking resampler Doppler compensation there appears to be a general improvement in performance for K13 256-OCK and K11 64-OCK. But also instances where there is actually a decrease in performance, as seen in Table 5.8 and Table 5.11. In order to better understand these scenarios it is useful to view the actual relative velocities and Doppler effect experienced by the signal for each received packet during a given recording. The next section looks at these case studies.

Table 5.7 Marina Trials Recording Results: K11 64-OCK - Constant 1.11m/s

	K11 64-OCK Uncoded		K11 64-OCK RS	
Doppler Compensation	BER	PSR	BER	PSR
None	2.873×10^{-1}	0.181	2.815×10^{-1}	0.190
Static Resampler	9.779×10^{-3}	0.819	2.872×10^{-3}	0.952
Tracking Resampler	1.504×10^{-2}	0.880	3.081×10^{-3}	0.952

Table 5.8 Marina Trials Recording Results: K13 256-OCK - Constant 1.11m/s

	K13 256-OCK Uncoded		K13 256-OCK RS	
Doppler Compensation	BER	PSR	BER	PSR
None	4.555×10^{-1}	0.037	4.321×10^{-1}	0.073
Static Resampler	9.321×10^{-3}	0.963	1.444×10^{-2}	0.951
Tracking Resampler	6.667×10^{-3}	0.951	1.123×10^{-2}	0.976

Table 5.9 Marina Trials Recording Results: K11 64-OCK - Constant 2.22m/s

	K11 64-OCK Uncoded		K11 64-OCK RS	
Doppler Compensation	BER	PSR	BER	PSR
None	4.388×10^{-1}	0.025	4.477×10^{-1}	0.025
Static Resampler	3.514×10^{-2}	0.593	3.300×10^{-2}	0.850
Tracking Resampler	4.938×10^{-2}	0.642	5.493×10^{-2}	0.775

Table 5.10 Marina Trials Recording Results: K13 256-OCK - Constant 2.22m/s

	K13 256-OCK Uncoded		K13 256-OCK RS	
Doppler Compensation	BER	PSR	BER	PSR
None	4.840×10^{-1}	0.000	4.961×10^{-1}	0.000
Static Resampler	6.024×10^{-2}	0.683	4.041×10^{-2}	0.833
Tracking Resampler	2.104×10^{-2}	0.902	2.961×10^{-2}	0.881

Table 5.11 Marina Trials Recording Results: K11 64-OCK - Varying 0m/s to 2.22m/s

	K11 64-OCK Uncoded		K11 64-OCK RS	
Doppler Compensation	BER	PSR	BER	PSR
None	3.607×10^{-1}	0.133	3.228×10^{-1}	0.233
Static Resampler	6.417×10^{-2}	0.567	5.965×10^{-2}	0.600
Tracking Resampler	6.172×10^{-2}	0.450	4.934×10^{-2}	0.633

Table 5.12 Marina Trials Recording Results: K13 256-OCK - Varying 0m/s to 2.22m/s

	K13 256-OCK Uncoded		K13 256-OCK RS	
Doppler Compensation	BER	PSR	BER	PSR
None	4.770×10^{-1}	0.016	4.904×10^{-1}	0.032
Static Resampler	8.656×10^{-2}	0.508	5.985×10^{-2}	0.710
Tracking Resampler	6.238×10^{-2}	0.689	6.367×10^{-2}	0.710

Table 5.13 Marina Trials Recording Results: K11 64-OCK - Perpendicular Constant 2.22m/s

	K11 64-OCK Uncoded		K11 64-OCK RS	
Doppler Compensation	BER	PSR	BER	PSR
None	2.049×10^{-1}	0.438	1.995×10^{-1}	0.400
Static Resampler	2.825×10^{-2}	0.800	1.266×10^{-2}	0.875
Tracking Resampler	2.294×10^{-2}	0.812	9.375×10^{-3}	0.875

Table 5.14 Marina Trials Recording Results: K13 256-OCK - Perpendicular Constant 2.22m/s

	K13 256-OCK Uncoded		K13 256-OCK RS	
Doppler Compensation	BER	PSR	BER	PSR
None	2.978×10^{-1}	0.309	3.061×10^{-1}	0.325
Static Resampler	4.364×10^{-2}	0.765	2.829×10^{-2}	0.850
Tracking Resampler	1.636×10^{-2}	0.914	7.730×10^{-3}	0.950

Table 5.15 Marina Trials Recording Results: K11 64-OCK - motion08

	K11 64-OCK Uncoded		K11 64-OCK RS	
Doppler Compensation	BER	PSR	BER	PSR
None	4.572×10^{-1}	0.050	4.886×10^{-1}	0.000
Static Resampler	3.883×10^{-2}	0.700	7.237×10^{-2}	0.800
Tracking Resampler	5.433×10^{-2}	0.700	8.750×10^{-2}	0.700

5.8.4 Data Demodulation Result Case Studies

Here individual recordings are examined in more detail to better understand the signal conditions at the instance each packet is received.

5.8.4.1 Constant 2.22m/s: Recording Motion08

The performance for recording motion08 - Constant 2.22m/s is shown in Fig. 5.12 for No Doppler Compensation; in Fig. 5.13 for Static Resampler Doppler Compensation; and in Fig. 5.14 for Tracking Resampler Doppler Compensation. The results are tabulated in Table 5.15 for K11 64-OCK and K11 64-OCK RS; and in Table 5.16 for K13 256-OCK and K13 256-OCK RS.

Fig. 5.12, Fig. 5.13 and Fig. 5.14 show the correlation between the received-SNR and the velocities, where the peak SNR values occur as the boat draws near the receiver platform, and the velocity crosses zero as the boat makes the turn along Path A. The relative velocities experienced based on the Doppler estimates show the steady 2.22 m/s at the peaks and troughs with rapid acceleration/deceleration as the boat makes the turn. In this recording, with no Doppler compensation all packets fail apart from a single K11 64-OCK packet which occurs as the velocity crosses 0 m/s.

With the use of the static resampler Doppler compensation Fig. 5.13 shows a distinct improvement in packet successes for the durations where the velocity is constant. The period of rapid relative acceleration/deceleration shows failed packets.

Fig. 5.14 shows that with tracking resampler Doppler compensation the number of failed packets is again reduced. However, there are now additional K11 64-OCK packet failures that were otherwise successful with the static resampler Doppler compensation. Table 5.15 shows the packet success rate total for K11 64-OCK remains the same for static to tracking resampler Doppler compensation. However, as seen between Fig. 5.13 and Fig. 5.14 there is a change in specifically which packets are successful or not.

Table 5.16 shows that there is an improvement in K13 256-OCK performance from static to tracking resampler Doppler compensation with only a single failed packet remaining.

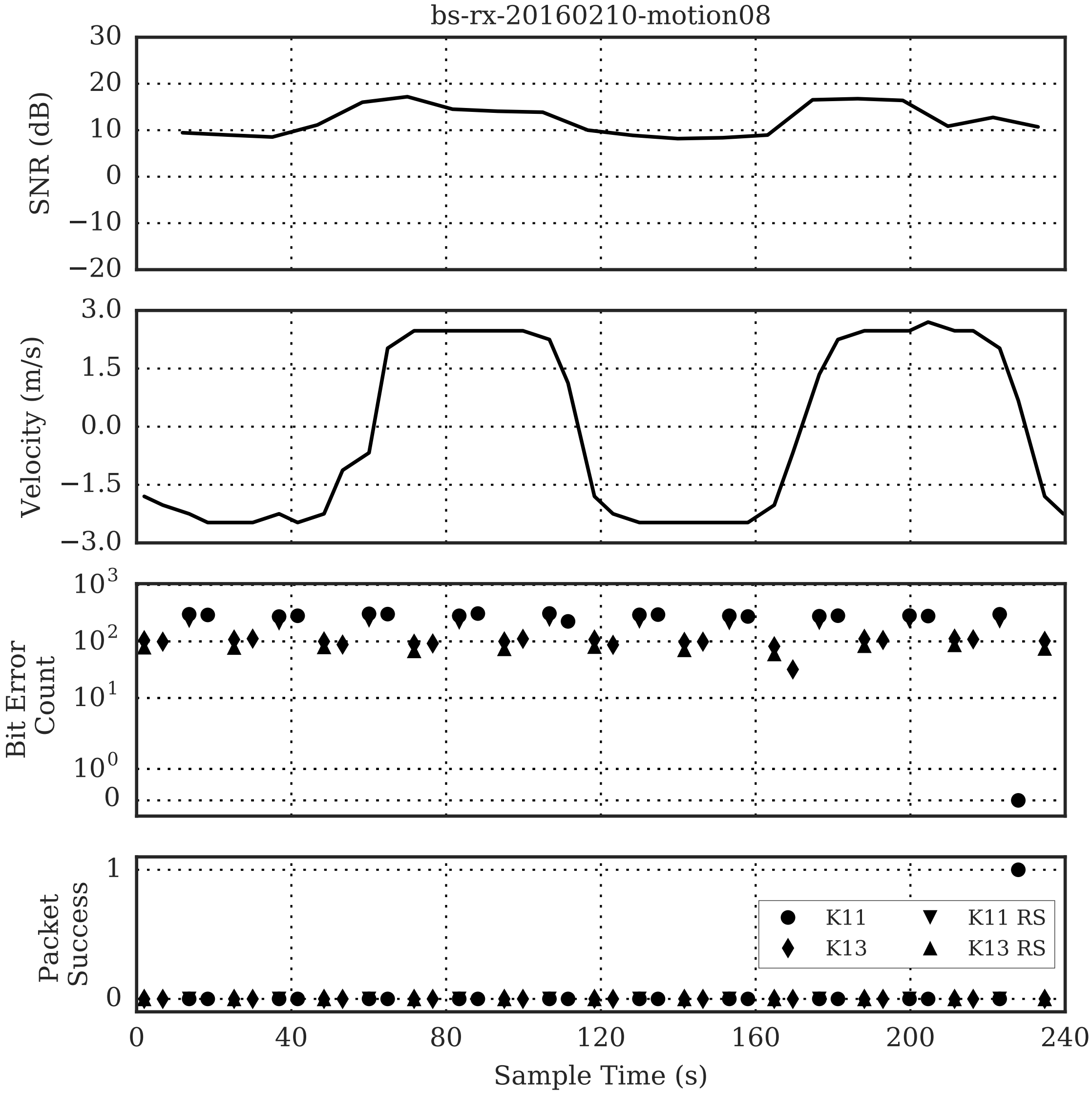

Fig. 5.12 Marina Trials Recording Results: motion08. Showing performance of K11 64-OCK (140.69 bit/s), K13 256-OCK (46.88 bit/s), K11 64-OCK RS (106.92 bit/s) and K13 256-OCK RS (35.63 bit/s).

Table 5.16 Marina Trials Recording Results: K13 256-OCK - motion08

	K13 256-OCK Uncoded		K13 256-OCK RS	
Doppler Compensation	BER	PSR	BER	PSR
None	4.886×10^{-1}	0.000	5.006×10^{-1}	0.000
Static Resampler	3.429×10^{-2}	0.714	2.990×10^{-3}	0.909
Tracking Resampler	1.190×10^{-3}	0.952	0.000	1.000

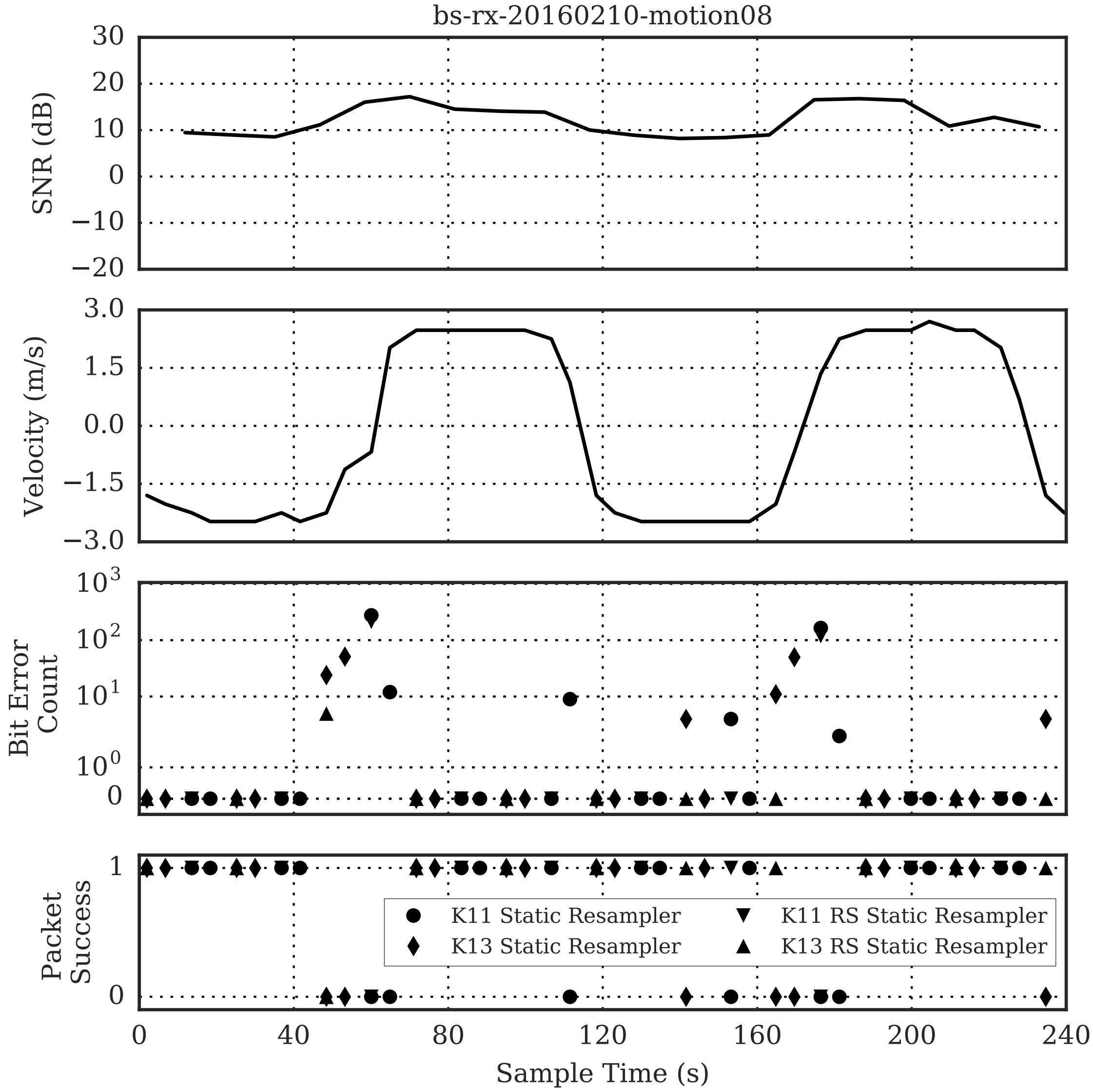

Fig. 5.13 Marina Trials Recording Results: Static Resampler - motion08. Showing performance of K11 64-OCK (140.69 bit/s), K13 256-OCK (46.88 bit/s), K11 64-OCK RS (106.92 bit/s) and K13 256-OCK RS (35.63 bit/s). With static resampler.

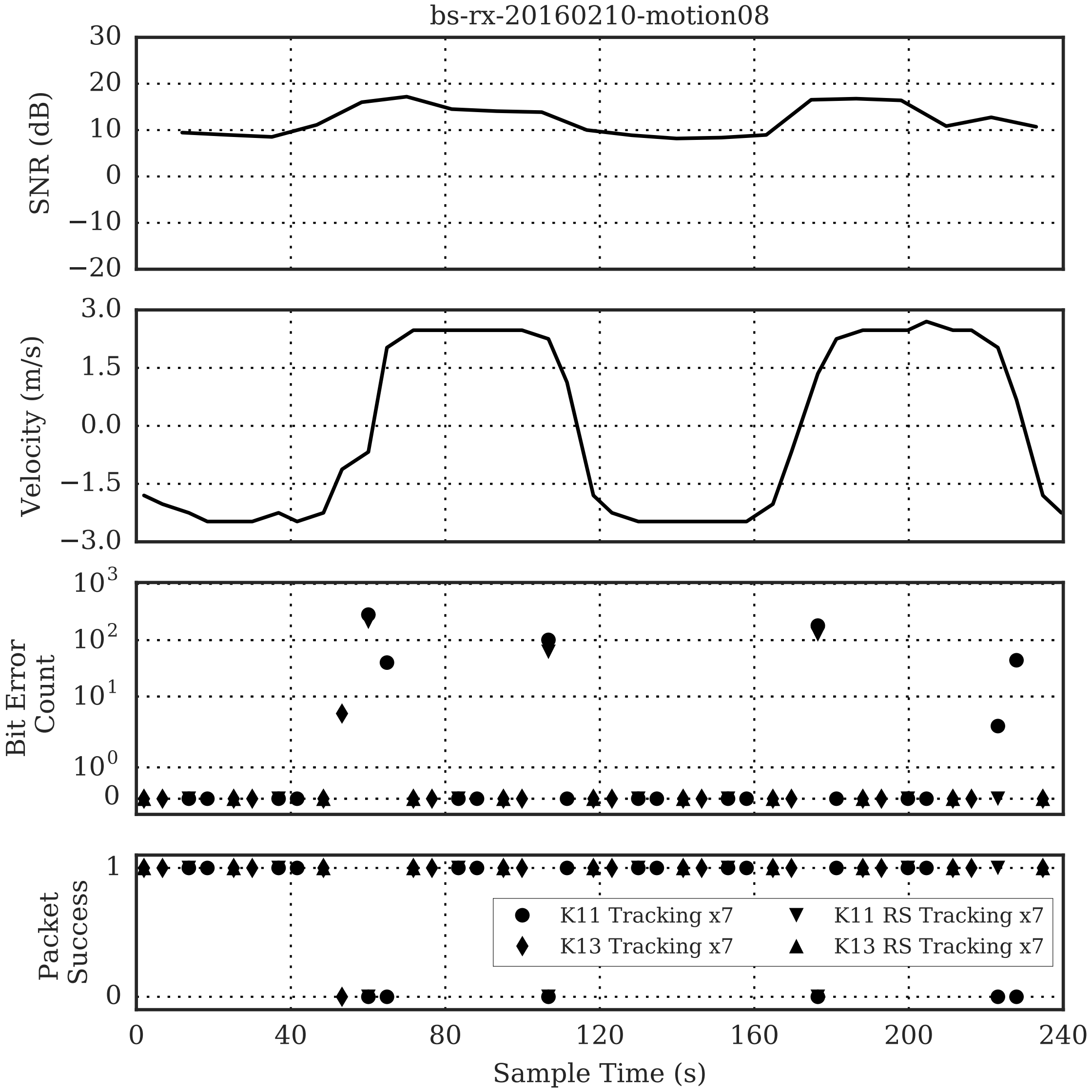

Fig. 5.14 Marina Trials Recording Results: Tracking Resampler - motion08. Showing performance of K11 64-OCK (140.69 bit/s), K13 256-OCK (46.88 bit/s), K11 64-OCK RS (106.92 bit/s) and K13 256-OCK RS (35.63 bit/s). With tracking resampler.

Table 5.17 Marina Trials Recording Results: K11 64-OCK - motion13

	K11 64-OCK Uncoded		K11 64-OCK RS	
Doppler Compensation	BER	PSR	BER	PSR
None	5.658×10^{-2}	0.800	2.522×10^{-2}	0.800
Static Resampler	0.000	1.000	0.000	1.000
Tracking Resampler	0.000	1.000	0.000	1.000

Table 5.18 Marina Trials Recording Results: K13 256-OCK - motion13

	K13 256-OCK Uncoded		K13 256-OCK RS	
Doppler Compensation	BER	PSR	BER	PSR
None	1.676×10^{-1}	0.524	1.539×10^{-1}	0.600
Static Resampler	3.452×10^{-2}	0.810	2.434×10^{-2}	0.800
Tracking Resampler	1.619×10^{-2}	0.905	0.000	1.000

5.8.4.2 Perpendicular Constant 2.22m/s: Recording Motion13

The performance for recording motion13 - Perpendicular Constant 2.22m/s is shown in Fig. 5.15 for No Doppler Compensation; in Fig. 5.16 for Static Resampler Doppler Compensation; and in Fig. 5.17 for Tracking Resampler Doppler Compensation. The results are tabulated in Table 5.17 for K11 64-OCK and K11 64-OCK RS; and in Table 5.18 for K13 256-OCK and K13 256-OCK RS.

The velocities experienced by the signal, as shown in Fig. 5.15, Fig. 5.16 and Fig. 5.17, are considerably less steady here with numerous rapid changes in velocity. Although with lower magnitudes than previously seen in motion08 recordings:- $\pm 1.5\,\mathrm{m/s}$ rather than $\pm 2.22\,\mathrm{m/s}$. In the uncompensated receiver results, shown in Fig. 5.15, the packet errors occur around the peaks linked to the sudden reversal in direction. The static resampler Doppler compensation, Fig. 5.16, reduces these packet errors with K11 64-OCK now showing 100% success. Tracking resampler Doppler compensation, Fig. 5.17, further reduces the packet errors for K13 256-OCK. These results also follow in Table 5.17 and Table 5.18.

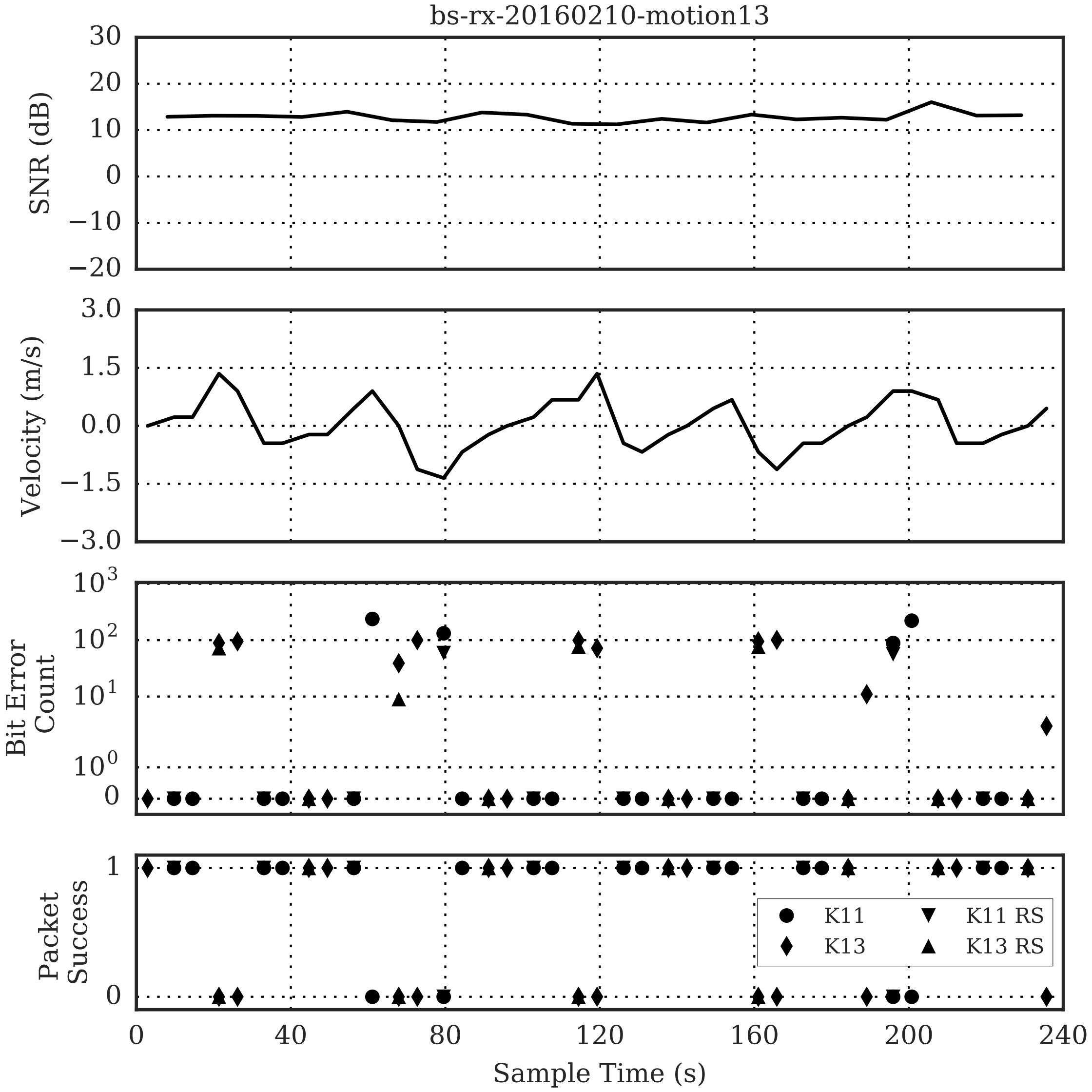

Fig. 5.15 Marina Trials Recording Results: motion13. Showing performance of K11 64-OCK (140.69 bit/s), K13 256-OCK (46.88 bit/s), K11 64-OCK RS (106.92 bit/s) and K13 256-OCK RS (35.63 bit/s).

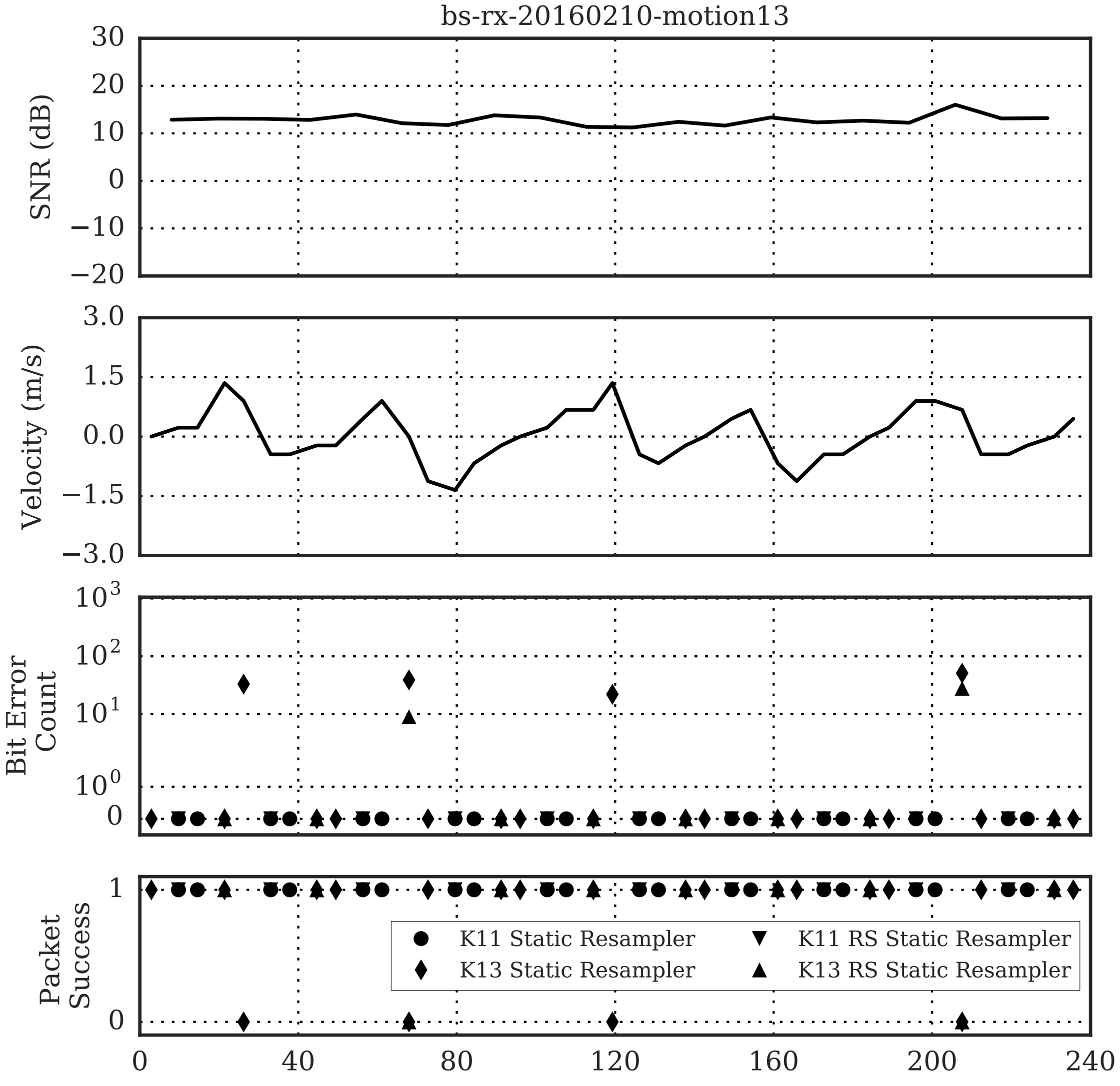

Fig. 5.16 Marina Trials Recording Results: Static Resampler - motion13. Showing performance of K11 64-OCK (140.69 bit/s), K13 256-OCK (46.88 bit/s), K11 64-OCK RS (106.92 bit/s) and K13 256-OCK RS (35.63 bit/s). With static resampler.

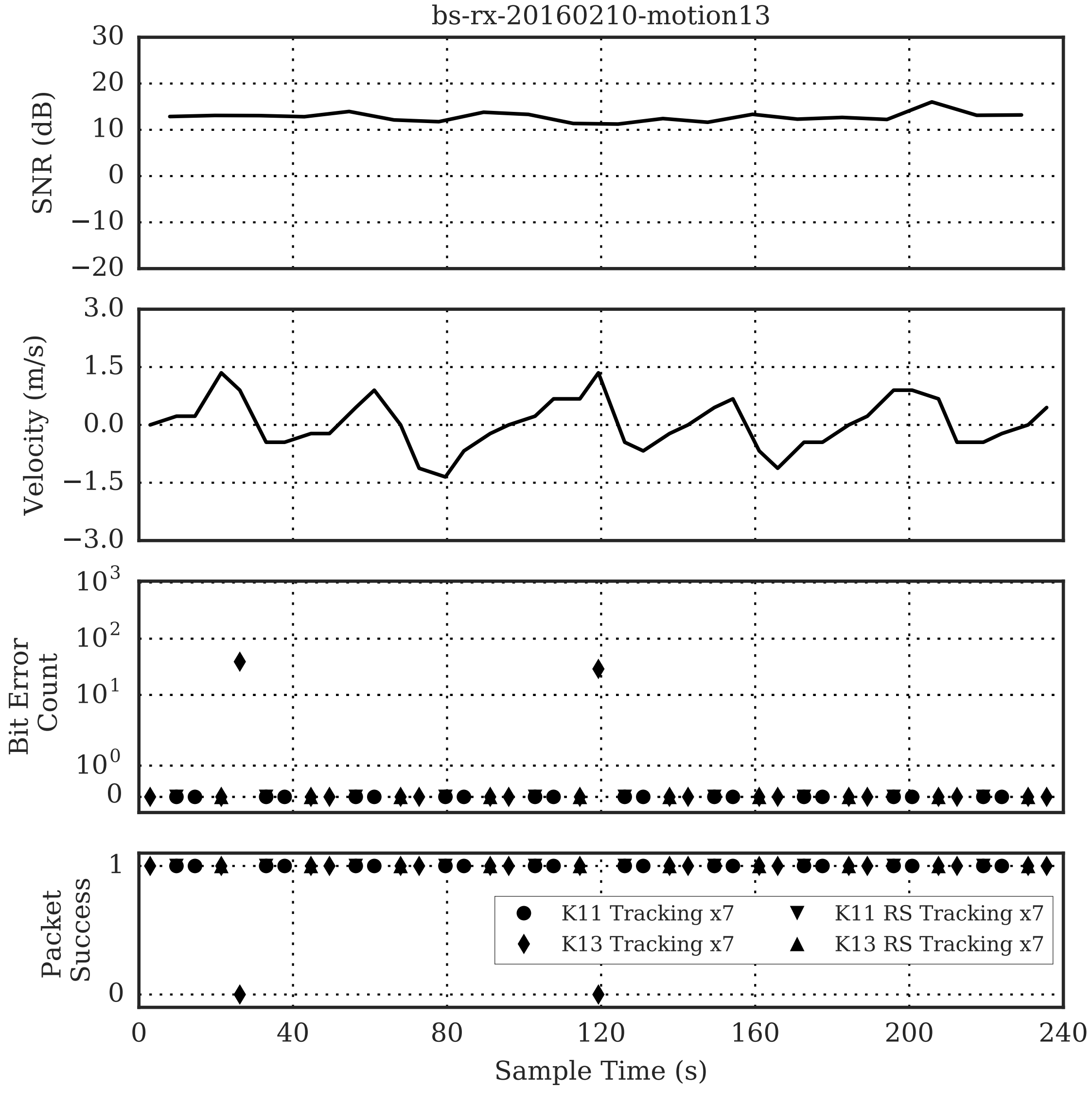

Fig. 5.17 Marina Trials Recording Results: Tracking Resampler - motion13. Showing performance of K11 64-OCK (140.69 bit/s), K13 256-OCK (46.88 bit/s), K11 64-OCK RS (106.92 bit/s) and K13 256-OCK RS (35.63 bit/s). With tracking resampler.

Table 5.19 Marina Trials Recording Results: K11 64-OCK - motion08 recording combined with simulated AWGN to shift the received SNR closer to 0 dB

	K11 64-OCK Uncoded		K11 64-OCK RS	
Doppler Compensation	BER	PSR	BER	PSR
None	4.779×10^{-1}	0.000	4.971×10^{-1}	0.000
Static Resampler	2.834×10^{-1}	0.111	3.387×10^{-1}	0.222
Tracking Resampler	3.067×10^{-1}	0.222	3.665×10^{-1}	0.222

5.8.5 Data Demodulation Result Case Study with AWGN

To demonstrate the performance of the Doppler compensation techniques in realistic SNR environments, the recordings motion08 and motion13 were combined with AWGN to take the SNR closer to 0 dB and processed again using the synchronisation and subsequent data demodulation receiver structures.

5.8.5.1 Constant 2.22m/s: Recording Motion08

The performance for recording motion08 with AWGN - Constant 2.22m/s is shown in Fig. 5.18 for No Doppler Compensation; in Fig. 5.19 for Static Resampler Doppler Compensation; and in Fig. 5.20 for Tracking Resampler Doppler Compensation. The results are tabulated in Table 5.19 for K11 64-OCK and K11 64-OCK RS; and in Table 5.20 for K13 256-OCK and K13 256-OCK RS.

Fig. 5.18, Fig. 5.19 and Fig. 5.20 now show the reduced received-SNR as the recording is combined with AWGN. The peaks are still clear where the boat and transmitter are close to the receiver. The velocity estimates are derived from the synchronisation symbols and the fine search receiver structure discussed previously. There are now noticeable errors in the velocity estimates, especially at periods of low SNR.

Again, with no Doppler compensation, all packets fail to demodulate successfully in Fig. 5.18. With the addition of the static resampler Doppler compensation, Fig. 5.19, a number of packets are now received successfully, especially at periods of constant velocity. The tracking resampler in Fig. 5.20 then shows further improvement in performance with many K13 256-OCK packets now being received successfully.

Table 5.19 shows greatly reduced number of packets received successfully for K11 64-OCK, even with Doppler compensation. This is linked to the greatly reduced SNR which reaches -10 dB at points. Table 5.20 for K13 256-OCK shows a marked improvement in performance when moving from static to tracking resampler Doppler compensation.

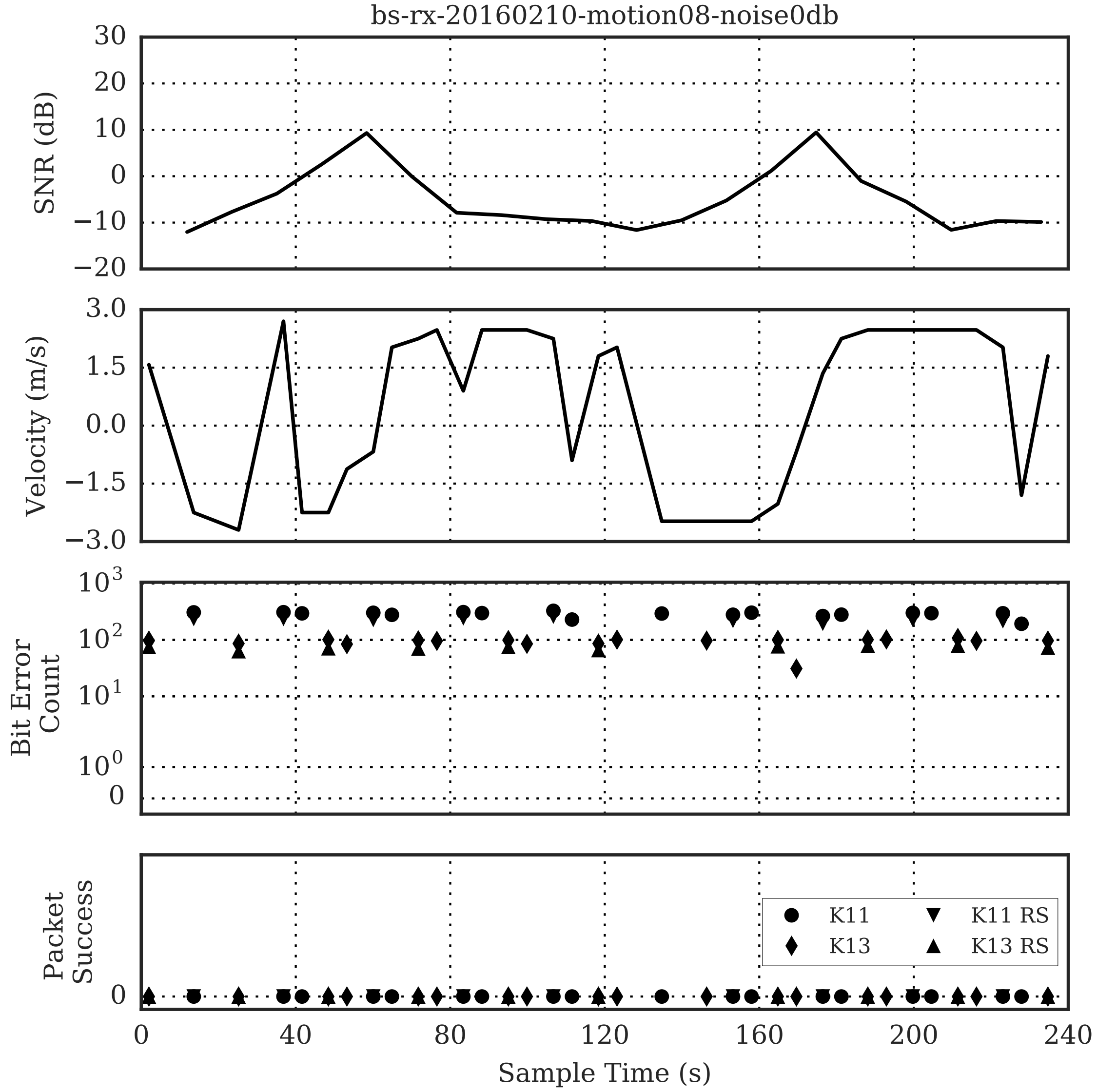

Fig. 5.18 Marina Trials Recording Results: motion08 recording combined with simulated AWGN to shift the received SNR closer to 0 dB. Showing performance of K11 64-OCK (140.69 bit/s), K13 256-OCK (46.88 bit/s), K11 64-OCK RS (106.92 bit/s) and K13 256-OCK RS (35.63 bit/s).

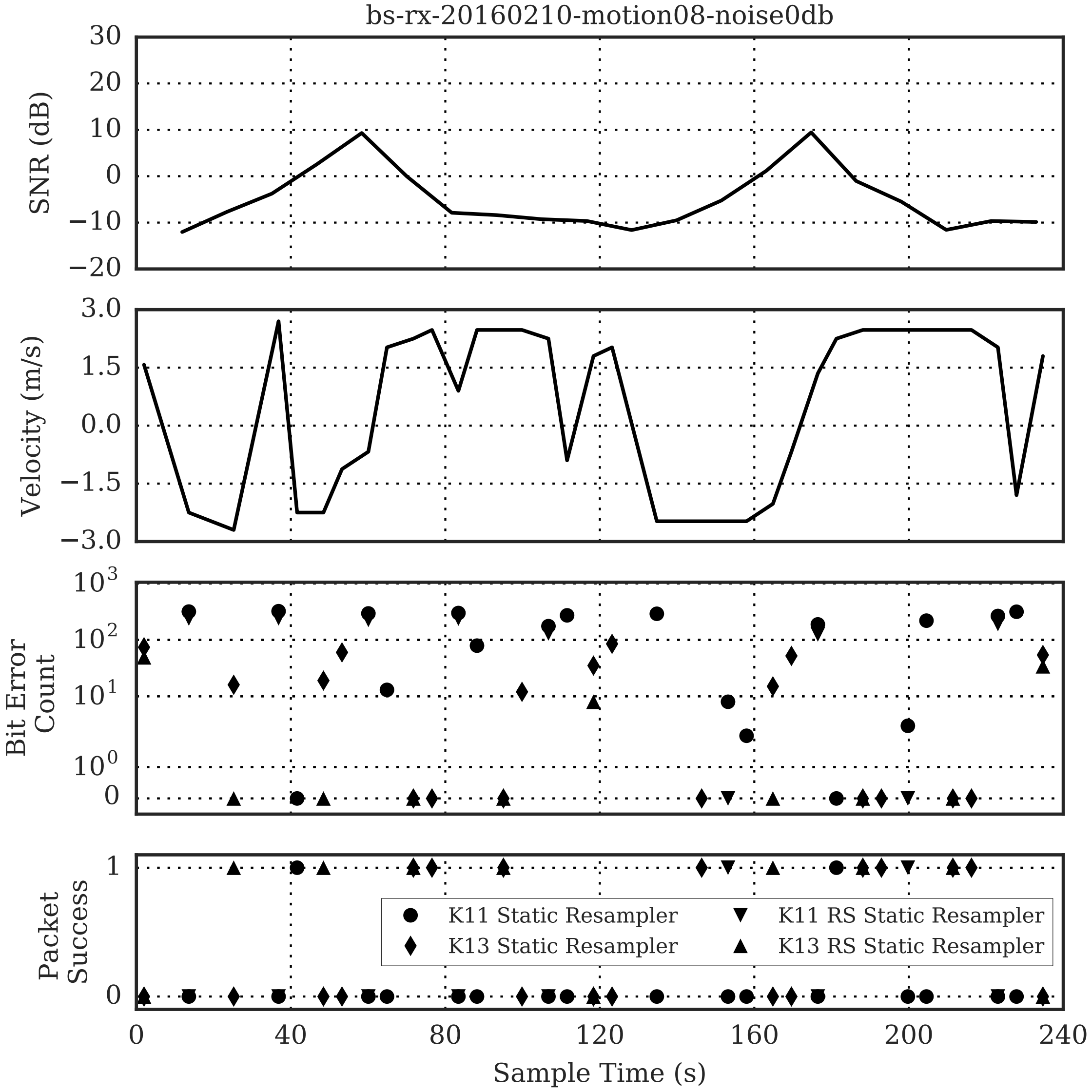

Fig. 5.19 Marina Trials Recording Results: Static Resampler - motion08 recording combined with simulated AWGN to shift the received SNR closer to 0 dB. Showing performance of K11 64-OCK (140.69 bit/s), K13 256-OCK (46.88 bit/s), K11 64-OCK RS (106.92 bit/s) and K13 256-OCK RS (35.63 bit/s). With static resampler.

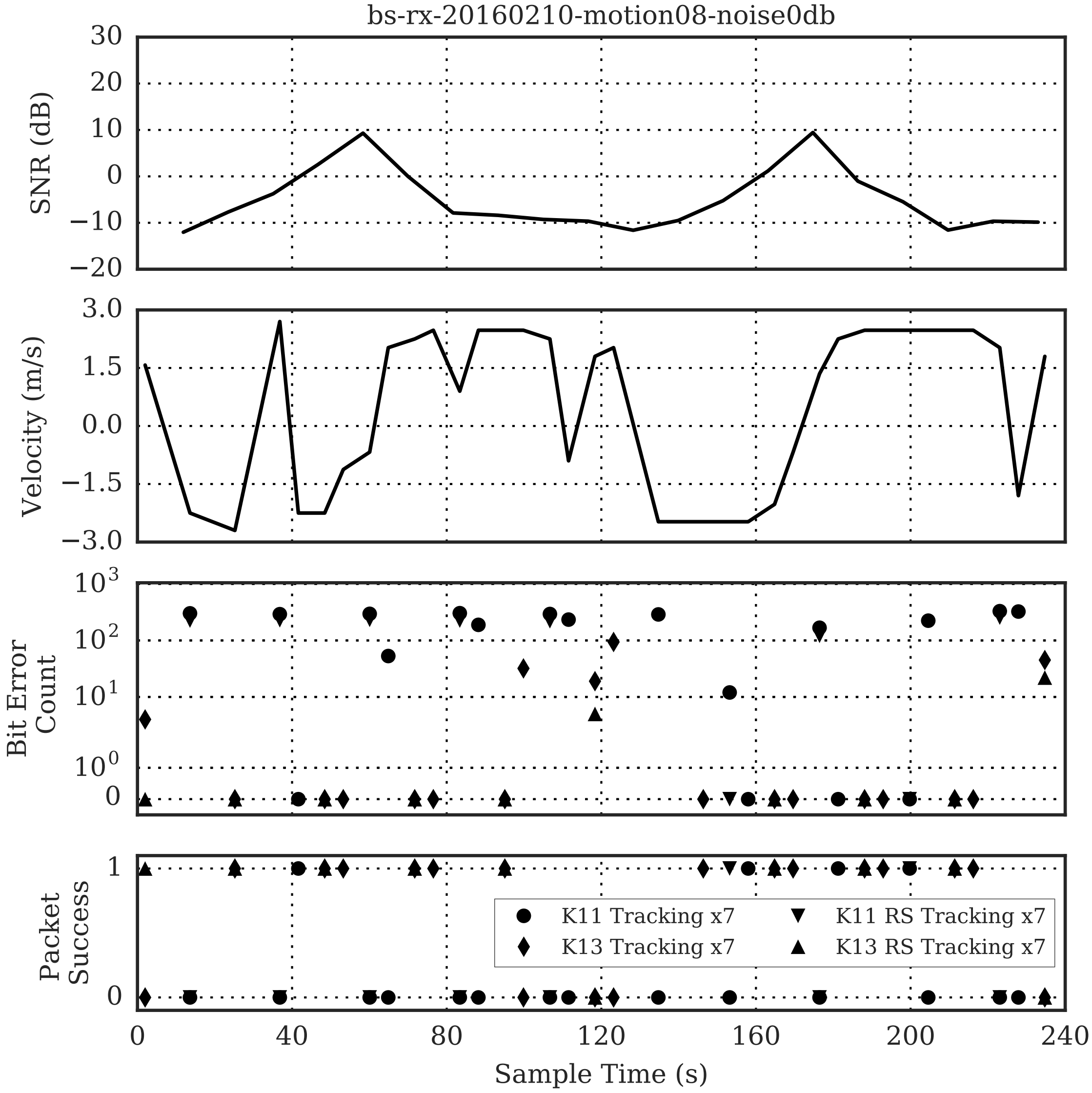

Fig. 5.20 Marina Trials Recording Results: Tracking Resampler - motion08 recording combined with simulated AWGN to shift the received SNR closer to 0 dB. Showing performance of K11 64-OCK (140.69 bit/s), K13 256-OCK (46.88 bit/s), K11 64-OCK RS (106.92 bit/s) and K13 256-OCK RS (35.63 bit/s). With tracking resampler.

Table 5.20 Marina Trials Recording Results: K13 256-OCK - motion08 recording combined with simulated AWGN to shift the received SNR closer to 0 dB

	K13 256-OCK Uncoded		K13 256-OCK RS	
Doppler Compensation	BER	PSR	BER	PSR
None	4.625×10^{-1}	0.000	4.789×10^{-1}	0.000
Static Resampler	1.172×10^{-1}	0.444	5.987×10^{-2}	0.700
Tracking Resampler	5.389×10^{-2}	0.722	1.776×10^{-2}	0.800

Table 5.21 Marina Trials Recording Results: K11 64-OCK - motion13 recording combined with simulated AWGN to shift the received SNR closer to 0 dB

	K11 64-OCK Uncoded		K11 64-OCK RS	
Doppler Compensation	BER	PSR	BER	PSR
None	6.442×10^{-2}	0.550	3.750×10^{-2}	0.800
Static Resampler	1.500×10^{-3}	0.800	0.000	1.000
Tracking Resampler	5.092×10^{-2}	0.600	2.851×10^{-2}	0.900

Table 5.22 Marina Trials Recording Results: K13 256-OCK - motion13 recording combined with simulated AWGN to shift the received SNR closer to 0 dB

	K13 256-OCK Uncoded		K13 256-OCK RS	
Doppler Compensation	BER	PSR	BER	PSR
None	1.769×10^{-1}	0.524	3.750×10^{-2}	0.800
Static Resampler	4.000×10^{-2}	0.762	2.566×10^{-2}	0.800
Tracking Resampler	1.881×10^{-2}	0.905	0.000	1.000

5.8.5.2 Perpendicular Constant 2.22m/s: Recording Motion13

The performance for recording motion13 with AWGN - Perpendicular Constant 2.22m/s is shown in Fig. 5.21 for No Doppler Compensation; in Fig. 5.22 for Static Resampler Doppler Compensation; and in Fig. 5.23 for Tracking Resampler Doppler Compensation. The results are tabulated in Table 5.21 for K11 64-OCK and K11 64-OCK RS; and in Table 5.22 for K13 256-OCK and K13 256-OCK RS.

As before, Fig. 5.21, Fig. 5.22, and Fig. 5.23 show a steady received-SNR throughout the recording, although now at a lower level around 0 dB. The velocity estimates in this case are still much as they were before the combination of AWGN.

Again, moving from no Doppler compensation to static resampler Doppler compensation shows improvement in both K11 64-OCK and K13 256-OCK packets. However, static to tracking resampler Doppler compensation shows improvement for K13 256-OCK but an increase in bit errors for K11 64-OCK.

Table 5.21 and Table 5.22 show as before that static resampler Doppler compensation gives better performance for K11 64-OCK packets, and tracking resampler Doppler compensation produces better performance for K13 256-OCK packets.

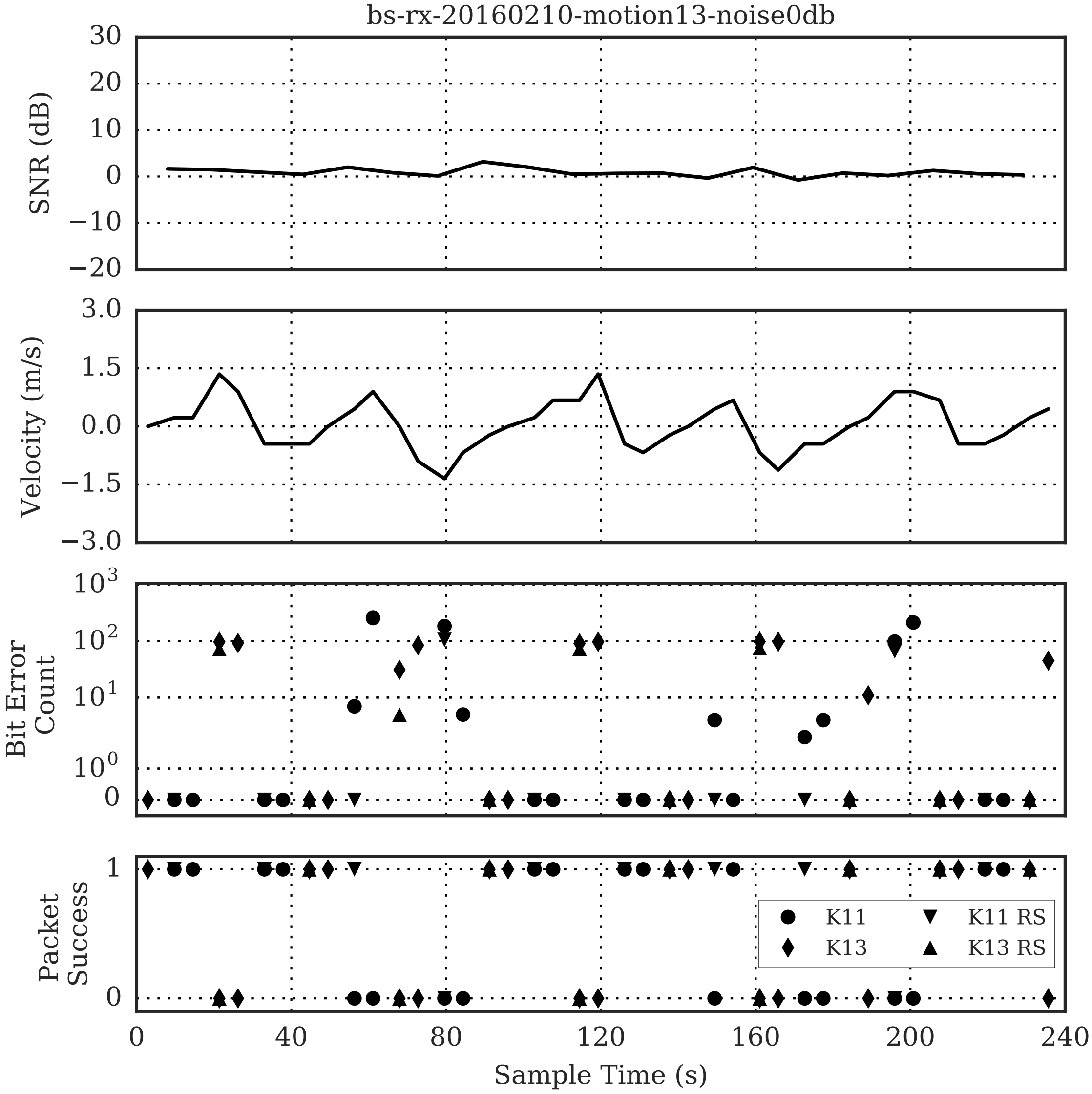

Fig. 5.21 Marina Trials Recording Results: motion13 recording combined with simulated AWGN to shift the received SNR closer to 0 dB. Showing performance of K11 64-OCK (140.69 bit/s), K13 256-OCK (46.88 bit/s), K11 64-OCK RS (106.92 bit/s) and K13 256-OCK RS (35.63 bit/s).

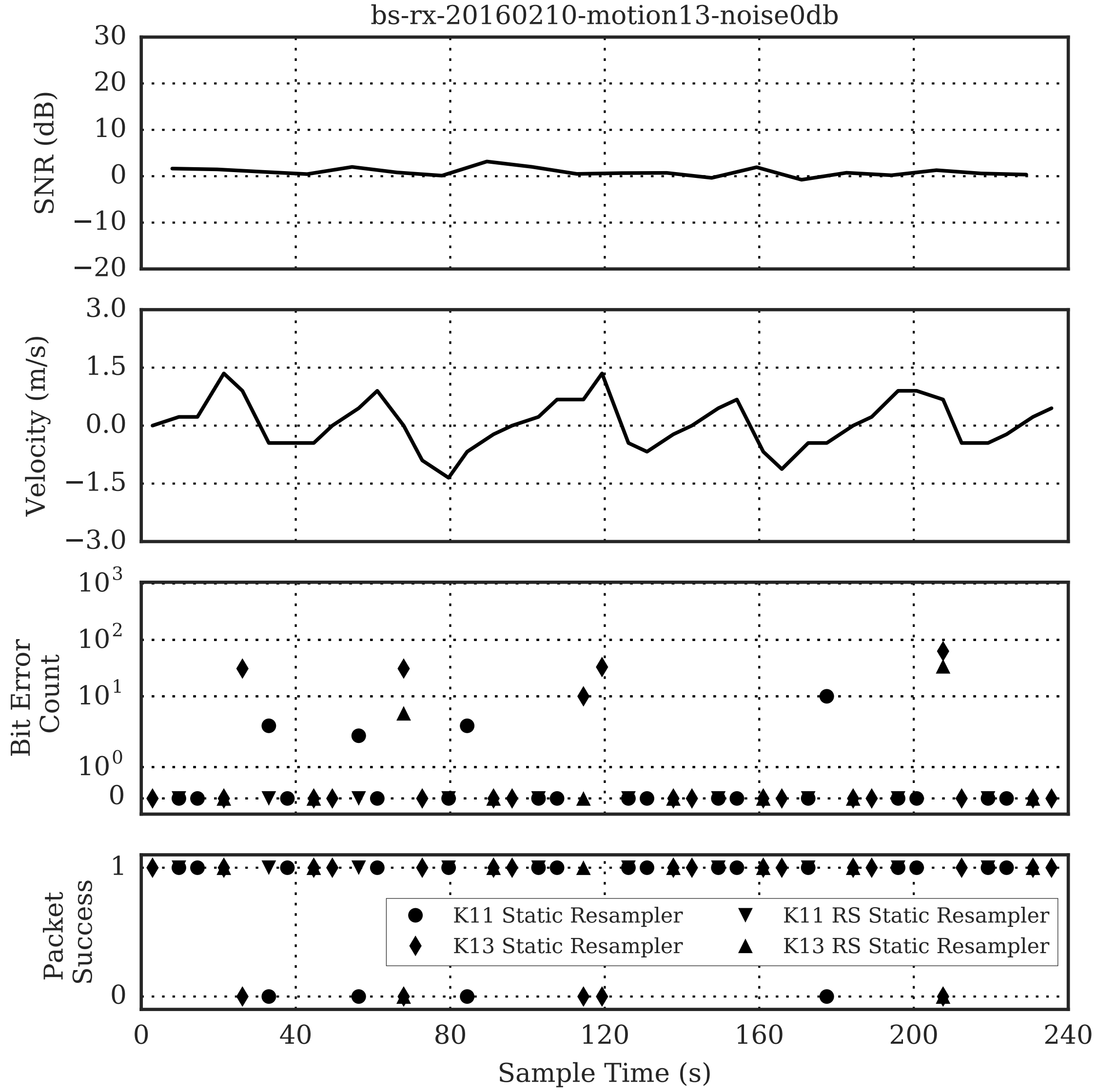

Fig. 5.22 Marina Trials Recording Results: Static Resampler - motion13 recording combined with simulated AWGN to shift the received SNR closer to 0 dB. Showing performance of K11 64-OCK (140.69 bit/s), K13 256-OCK (46.88 bit/s), K11 64-OCK RS (106.92 bit/s) and K13 256-OCK RS (35.63 bit/s). With static resampler.

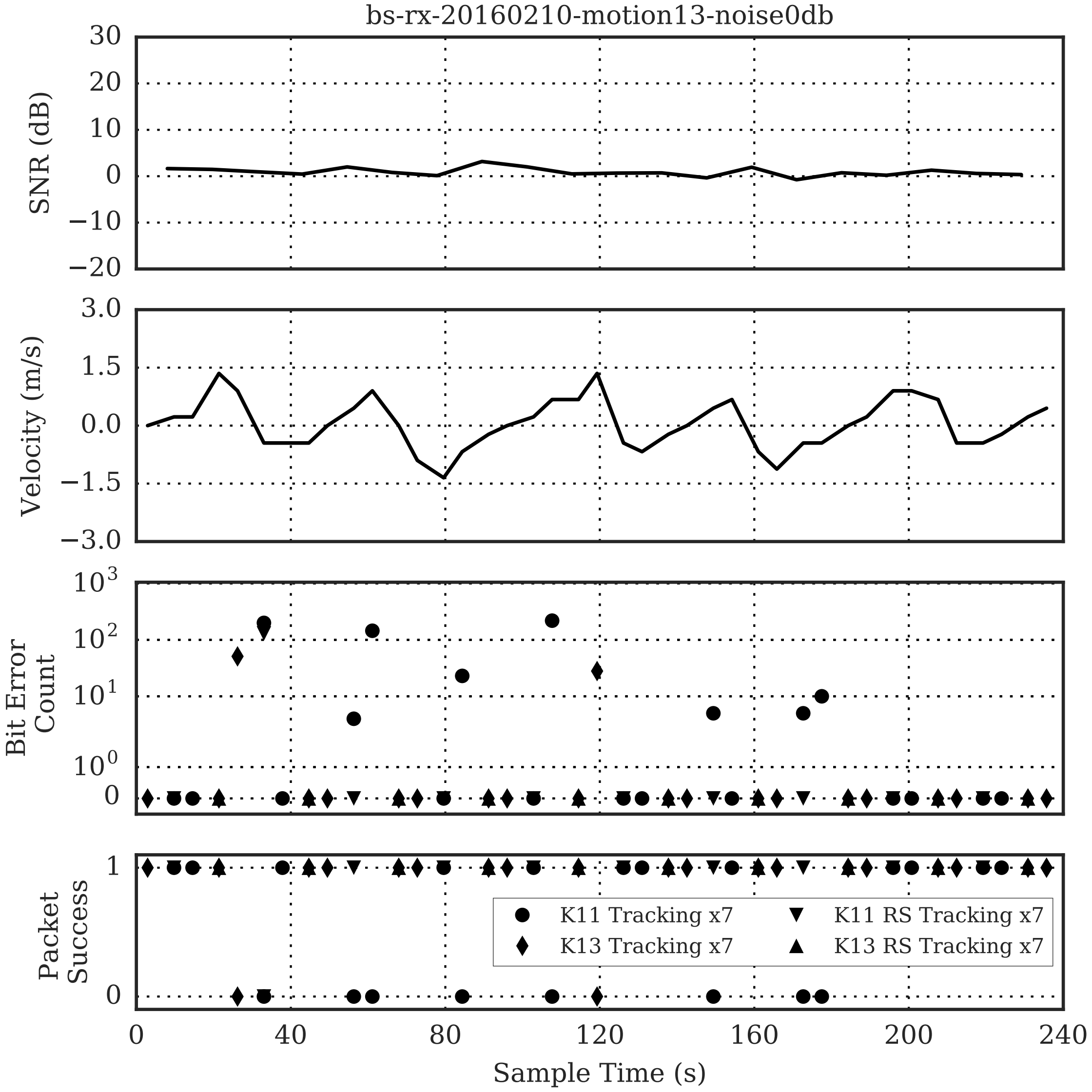

Fig. 5.23 Marina Trials Recording Results: Tracking Resampler - motion13 recording combined with simulated AWGN to shift the received SNR closer to 0 dB. Showing performance of K11 64-OCK (140.69 bit/s), K13 256-OCK (46.88 bit/s), K11 64-OCK RS (106.92 bit/s) and K13 256-OCK RS (35.63 bit/s). With tracking resampler.

5.8.5.3 Tracking Resampler Doppler Compensation Performance

The results have shown that in these experiments the tracking resampler performance, although improving the K13 256-OCK packet success rate, has often had the inverse effect on K11 64-OCK packets. However, when considering the parameters used when configuring the tracking resamplers, for K11 64-OCK the receiver covers a much wider range of velocities, $\pm 2.7\,\mathrm{m/s}$, than that for K13 256-OCK, $\pm 0.675\,\mathrm{m/s}$. The steps are also considerably greater for K11 64-OCK, $0.9\,\mathrm{m/s}$, versus K13 256-OCK, $0.225\,\mathrm{m/s}$. The decisions taken at each symbol using the maximum of the peak resampler stream correlator values can therefore result in a much larger jump in velocity estimate for K11 64-OCK than for K13 256-OCK. Inaccurate velocity estimates can therefore lead to larger jumps in the wrong direction and very quickly all tracking is lost, especially at lower received-SNR levels.

The static resampler Doppler compensation has been shown to be sufficient provided the velocity is constant or within suitable bounds based on the ambiguity function of the symbol and the channel received-SNR.

Selection of the symbol length, e.g. K11 or K13, is driven by the target operating SNR of the application. The longer symbol providing greater processing gain leads to K13 being the preferred choice. With the higher orders of M-Sequence, the number of available PN codes increases leading to greater potential modulation depth, and hence data rates. However, the longer symbol durations also lead to the need for effective Doppler compensation in the receiver structure in channels with considerable relative platform motion.

The type of expected relative platform motion and its effect on the channel will determine the more suitable Doppler compensation. If a steady velocity is expected of the two platforms then the static resampler Doppler compensation technique is preferred for the limited increase in processing required. However, where acceleration is expected throughout a packet that would move the Doppler shift beyond the operating bounds of the static resampler, then the tracking resampler Doppler compensation will be required. The operating limits of the static resampler Doppler compensation become tighter where the longer K13 symbols are used due to the narrower ambiguity function of longer duration symbols.

From the above it can be seen that the application design decisions of codeset selection and Doppler compensation technique will be driven by factors such as desired data rate, operating SNR, expected platform motion, and available processing time/energy.

5.9 Summary

The ambiguity functions of the two symbol lengths, K11 (42.65 ms) and K13 (170.65 ms), show the degree to which each is affected by Doppler shift, along with the range of velocities for which they produce usable correlator peaks. Therefore, in situations with high SNR and low relative velocities it is still possible to successfully synchronise and demodulate the data packets for both. As relative velocity increases the K13 symbol correlation value will be rapidly diminished long before the K11 symbol's correlation value.

Using the ambiguity plots in Fig. 5.1 it is possible to determine a desired ripple or acceptable loss in synchronisation correlator peak and set the steps and range according to the user application. Finer steps and a greater range will improve synchronisation performance at lower SNR values over a range of motion but at the cost of increased computational processing load. In addition, the finer resampling steps provide a more accurate estimation of the relative platform velocity for the subsequent data demodulation stage.

Successful synchronisation using the multiple symbol signal structures has been shown in a real underwater acoustic channel with significant Doppler effects that otherwise results in failed synchronisation for single symbol signal structures of the equivalent processing gain.

Doppler compensation has been shown to enable successful synchronisation with 1of and 2of K13 symbols in real underwater channels with Doppler effects over a range of different motion types, speeds, and accelerations.

Data demodulation in a real underwater acoustic channel with Doppler effects has been shown to become successful when a static resampler receiver structure is used for constant velocity scenarios. But also, the tracking resampler receiver structure has been shown to enable successful demodulation of the longer symbols. Parameters used in this structure for the K11 symbols have been shown to be less effective than the parameters used for the K13 symbols. Recordings combined with AWGN have also shown the performance in real channels with Doppler effects and realistic operating SNR levels.

Chapter 6

Implementation of Modem on Mobile Device

6.1 Introduction

Software-defined underwater acoustic modems are able to provide a flexible approach to receiving from multiple transmitters or multiple modulation schemes and network protocols whilst using the same hardware platform. They also allow for adaptive links, as channel conditions change the modulation schemes can be switched at run time.

In this chapter a receiver is implemented in software on an Android mobile device which is connected to a hydrophone via the microphone/headphone jack. Two modulation schemes are investigated, binary orthogonal keying (BOK) using linear frequency modulation (LFM) chirps, i.e. Chirp-BOK [118], and pseudo random noise m-ary orthogonal code keying (PN M-OCK) covered in previous chapters. Both signals used possess large bandwidth-time products.

The simulated performance of a number of signals is investigated. The receiver design and implementation on the Android mobile device is covered. Experimental validation takes place in Marina Trials to show the ability of the mobile device receiver to operate in real-time with signals through a real underwater channel. Further experimentation takes channel recordings and combines AWGN which are then played into the mobile device and real-time receiver to investigate the performance bounds of the receiver and signal schemes.

6.2 Motivation

There is potential in using low-cost mobile devices to receive underwater acoustic signals. The signals and receiver structures investigated so far in this thesis are well suited to low-power transmission and low-received-SNR applications. Therefore the aim of this chapter is to determine whether a mobile device is able to successfully receive the M-OCK spread-spectrum signals in real-time in a real world channel.

This chapter looks at using low-cost mobile devices to receive underwater acoustic signals with frequencies up to 24 kHz. Specifically, spread-spectrum modulation schemes with large bandwidth-time products such as Chirp-BOK [118] and the M-OCK modulation scheme investigated throughout this thesis.

The receiver structures presented throughout this thesis can be implemented in a number of ways on various low-cost platforms. These include off-the-shelf single-board computers (SBC) with operating systems; as well as bespoke electronic systems using readily available embedded microcontrollers. These approaches will still require development and manufacture of a complete hardware product with housing and user interfaces, which lead to further risk and costs. In contrast, making use of an off-the-shelf mobile device such as a phone or tablet moves the development costs and risks into the software which are typically much lower than those for hardware. These devices typically already contain the single-board computer, battery and power management circuitry, wireless connectivity, suitable housing, and human interface through touchscreen display. Further, making use of ecosystems such as those provided by Google with Android or Apple with iOS means that many different devices can potentially be leveraged. There are also the software development frameworks providing ease of development through tools, and distribution of the bespoke software applications through online markets. Typical applications that would benefit from this model may include field engineers using ruggedized tablets to visit installations such as those found in the water treatment industry, and to download diagnostics data from distributed underwater sensor networks. Bespoke user application software can be combined with the acoustic modem library to communicate with the underwater devices, obtain the data, and using the other features of the mobile device instantly upload the data to the company's cloud-based system.

6.3 Background

Dol, Casari, van der Zwan, and Otnes review software-defined modems based on off-the-shelf acoustic modems with the potential for altering the software/firmware. They also cover the design of a general processor-based acoustic modem with an open-source operating system [119].

Demirors, Shankar, Santagati, and Melodia developed a software defined acoustic modem (SDAM) along with a network stack, SEANet. This is based on specialist hardware using a software defined radio platform on an FPGA [120] [121].

Lee, Kim, Choi, and Choi have investigated the use of mobile devices as aerial acoustic modems. They use ultrasonic frequencies in order to be inaudible to humans with a Chirp-BOK modulation scheme. The developed software transmitted and received a 16-bit token over the audio link before connecting to a server via the internet. Their research also highlights the wide range of performance characteristics of the speakers and microphones across mobile devices [122].

Research in previous chapters has introduced the use of carrierless PN M-OCK in low-power, low-received-SNR underwater acoustic communication. Increasing the modulation depth in orthogonal signaling has a positive impact on the BER performance [113] as shown in Chapter 3. It can be seen that PN M-OCK is more attractive than Chirp-BOK as modulation depth is increased.

6.4 Signal Design and Packet Structure

Packets were constructed to demonstrate and compare the two modulation schemes as described in Table 6.1. Synchronisation symbols consisted of a single symbol with duration 170.6 ms using either a LFM chirp (up or down) or a unique 13th order m-sequence. All signals were bandlimited between 8 kHz and 16 kHz.

Table 6.1 Packet Structure using Chirp-BOK and PN M-OCK with $F_s = 48\,\text{kHz}$ for a transmission of 32 data bits.

ID	Synchronisation Header (0.17 s)	Data (32 bit)	Bits per symbol	Symbol Duration (ms)	Spreading Process Gain (dB)	Bit Rate Uncoded (bit/s)	Total Data Symbols
A	Up chirp	Chirp-BOK	1	42.6	25.3	23.4	32
B	K13M512	K11 2-OCK	1	42.6	25.3	23.4	32
C	K13M513	K11 4-OCK	2	42.6	25.3	46.9	16
D	K13M514	K11 16-OCK	4	42.6	25.3	93.8	8
E	Down chirp	Chirp-BOK	1	10.6	19.3	93.9	32
F	K13M515	K10 16-OCK	4	21.3	22.3	187.7	8
G	K13M516	K9 16-OCK	4	10.6	19.3	375.7	8

The results of the simulations for the modulation schemes are shown in Fig. 6.1. The respective performance of each modulation scheme is shown for an AWGN channel. For a given modulation depth as M-OCK symbol duration is halved, K11 16-OCK (42.6 ms), K10 16-OCK (21.3 ms), and K9 16-OCK (10.6 ms), the performance degrades for BER of 10^{-4} of 3 dB each time. This is to be expected, as the process gain due to spreading is related linearly to the bandwidth-time product.

For a given data rate, but differing modulation schemes (such as A and B), at BER of 10^{-4} Chirp-BOK shows a gain in performance of 0.5 dB over K11 2-OCK. However, as different modulation depths are compared (such as D and E), at BER of 10^{-4} K11 16-OCK produces a gain in performance of 4 dB for the equivalent data rate over Chirp-BOK.

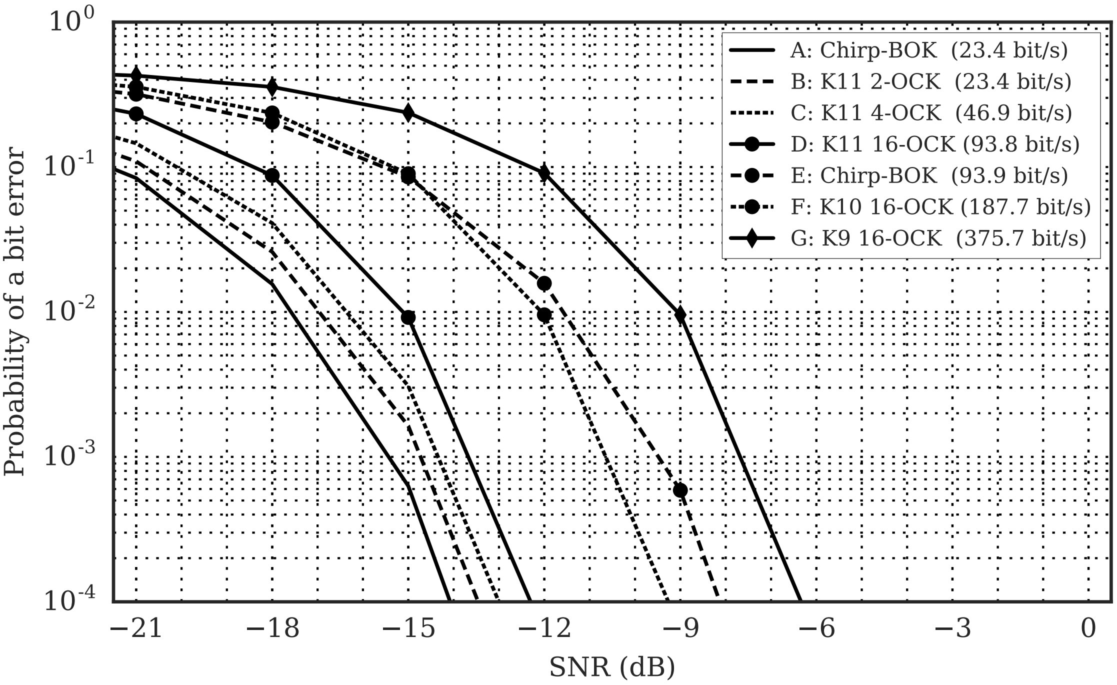

Fig. 6.1 Simulated performance of each modulation scheme in AWGN channel with Sample Frequency of 48 kHz and bandwidth of 8 kHz to 16 kHz. A. Chirp-BOK (23.4 bit/s); B. K11 2-OCK (23.4 bit/s); C. K11 4-OCK (46.9 bit/s); D. K11 16-OCK (93.8 bit/s); E. Chirp-BOK (93.9 bit/s); F. K10 16-BOK (187.7 bit/s); G. K9 16-OCK (375.7 bit/s)

6.5 Receiver Structure Design and Implementation

The receiver structure covers two discrete functions, synchronisation and data demodulation. This section looks at the design and implementation of each part. Implementation is targeted at a standard Android mobile device, in this case the Nexus 5 (2013).

The receiver structures were implemented in C++ using the native development kit (NDK) for Android devices. The user interface and audio sampling processes were implemented in Java with multiple threads used to ensure the audio samples were provided to the receiver as soon as the buffer became full. Results such as packet success counts and bit errors from the demodulator were saved to comma separated variable (CSV) files for analysis.

6.5.1 Synchronisation

The synchronisation receiver structure is shown in Fig. 6.2. Audio signals provided via the microphone jack are sampled at the native sample frequency of the given device, typically this is 48 kHz or 44.1 kHz. In the case of the Nexus 5, used here, it is 48 kHz.

The signal is then bandpass filtered in the time domain with band 8 kHz to 16 kHz. This is then converted to the frequency domain using a FFT library. The frequency domain signal is then point-multiplied with the frequency domain instance of the time-reversed synchronisation symbol. A copy of the correlated signal is taken and the Hilbert transform is applied by point multiplying by $-i$. The correlated signal and its Hilbert transform are then converted back into the time domain by the inverse FFT. The magnitude of the Analytic Signal is then formed by summing the square of each result in the cross-correlation and Hilbert transformation. This envelope of the cross-correlation is then normalised using the root mean square of the bandpass filtered signal. The normalisation step removes fluctuations due to amplitude variance in the received signal and allows the use of a fixed threshold for detecting the synchronisation symbol as discussed in previous chapters.

6.5.2 Data Demodulation

The data demodulation receiver structure, shown in Fig. 6.3, is based in the time domain. Again the incoming signal is bandpass filtered between 8 kHz and 16 kHz. A window at the point the symbol is expected to arrive is cross correlated with the bank of symbols in the codeset. The maximum-likelihood detector selects the code that produces the greatest magnitude cross-correlation result within the expected window. The identified symbol is then demapped to produce the binary data bits. The size of the codebank is equal to the modulation depth, M.

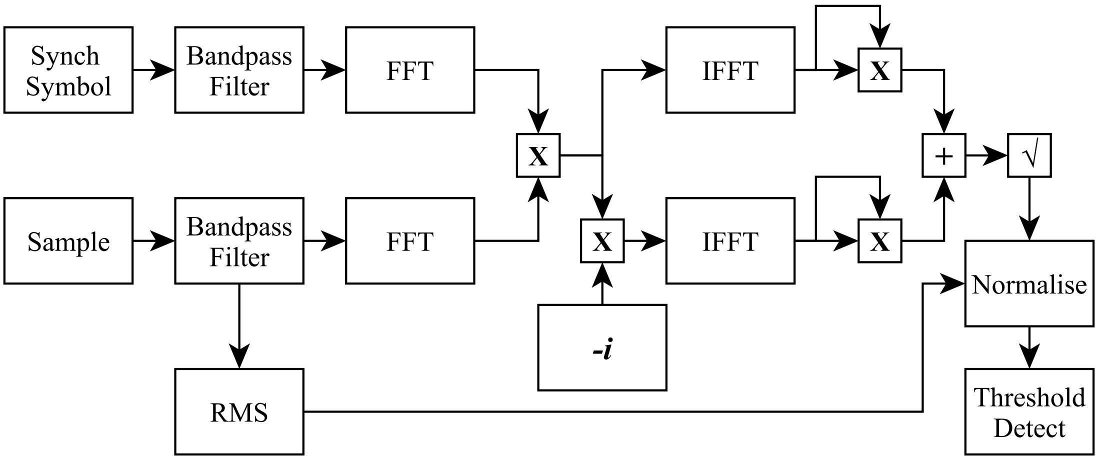

Fig. 6.2 Receiver Structure Block Design: Synchronisation. Implementation.

6.5.3 Implementation

The ecosystem for Android mobile development is well supported with tools, documentation, examples and community support. All of which are factors when considering platforms for use in research of commercial products. The Android NDK provides compilers for C/C++ so that signal processing techniques that are used on traditional modem microcontrollers can also be ported to this environment. The mobile device also contains analogue front-end circuitry used to: provide phantom power to microphones; amplify the audio signals; and low-pass filter the audio signals. A number of recent mobile devices also incorporate automatic gain control (AGC) which is configurable at run-time by the application software. These features make it possible to further reduce the external electronics required to receive signals via a hydrophone/transducer.

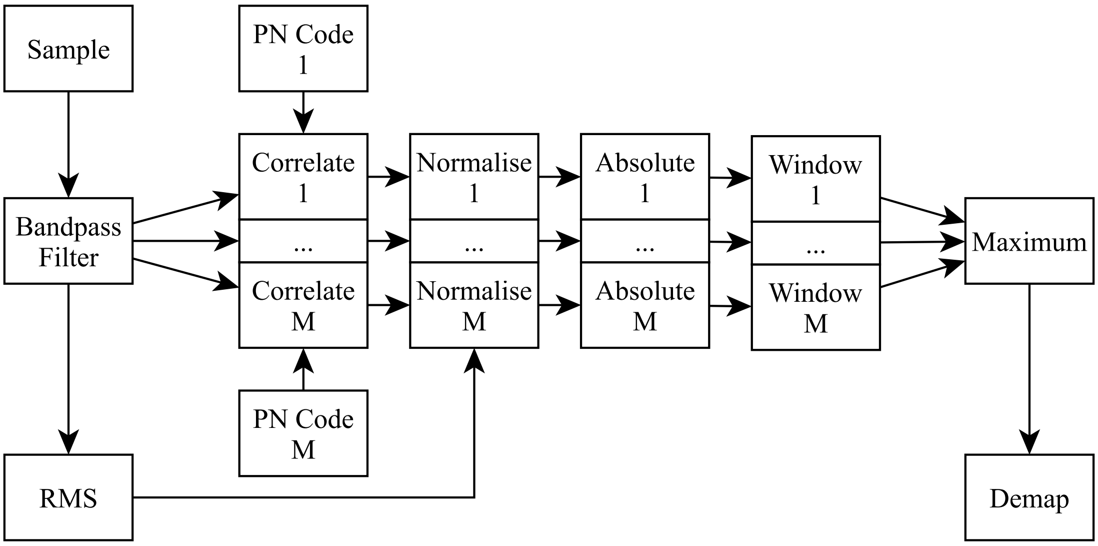

Fig. 6.3 Receiver Structure Block Design: Data Demodulation. Correlation, Normalisation, maximum value selection, demapping.

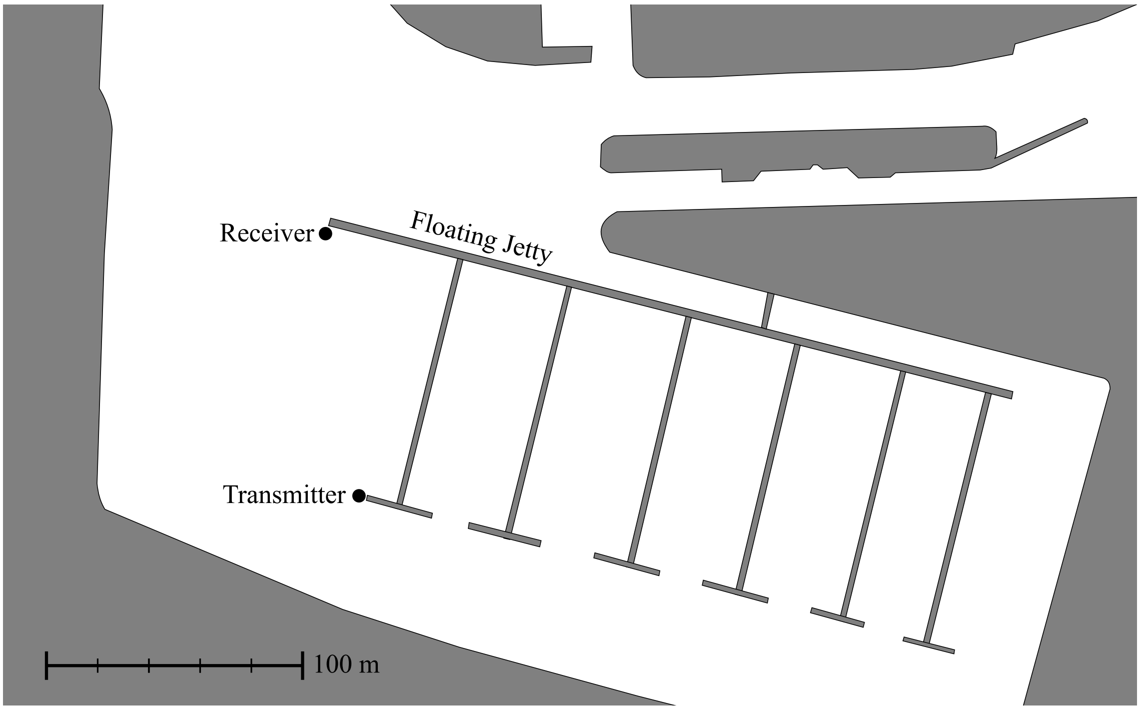

Fig. 6.4 Marina Aerial View

6.6 Experimental Validation: Marina Trials 2017-03-10

6.6.1 Experiment Setup

An aerial view of the Royal Quays Marina, North Shields can be seen in Fig. 6.4. This shows the location of the transmitter and the receiver.

Location Royal Quays Marina, North Shields

Transmitter Laptop playing audio. Acoustic power amplifier. Transducer in water at depth of 5m.

Receiver Laptop recording audio. Android Nexus 5 (2013) running receiver application decoding the live audio stream. Bandpass filter and amplifier. Hydrophone in water at depth of 5m. 2 minute recording taken by laptop for each packet type. 2 minutes of decoding by Android modem.

Weather and Water State Cloudy skies. Calm water.

Geology Stone wall marina with floating pontoons. Depth around 10m.

Channel conditions can be observed in Fig. 6.5 with a strong multipath reverberation during the first 4 ms.

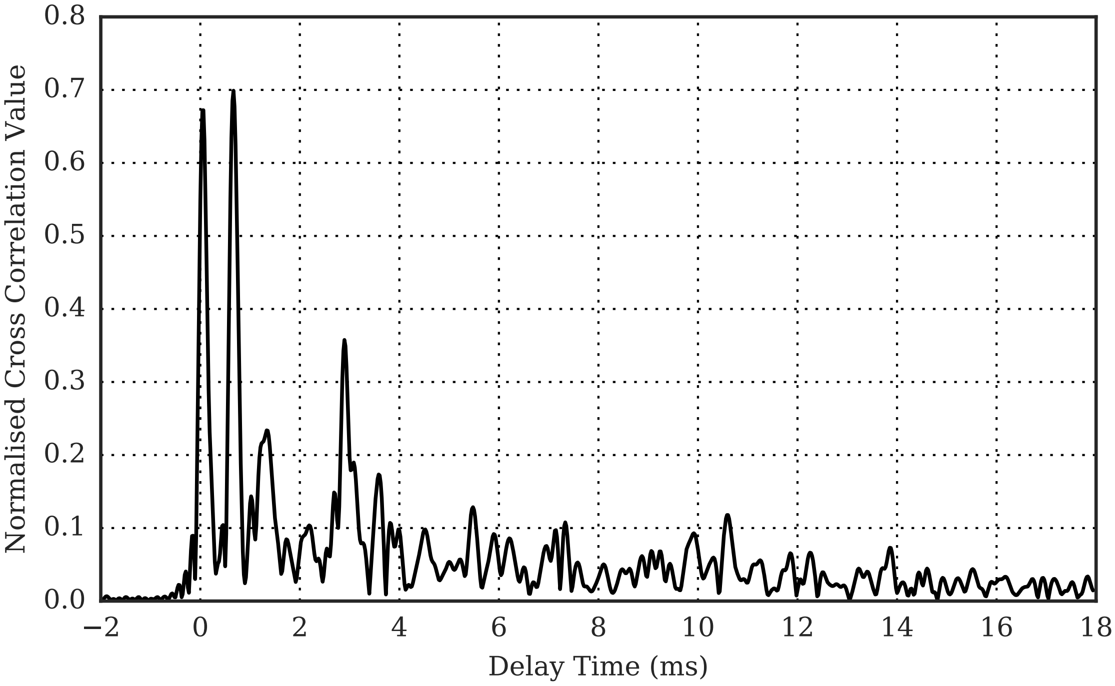

Fig. 6.5 Channel Impulse Response

6.6.2 Results

The results of the live real-time synchronisation and demodulation of the Android mobile device are shown in Table 6.2. These show that it is possible to produce a software-defined underwater acoustic modem that is capable of operating successfully in real-time with signals from an underwater channel. The marina channel in this case is relatively noise-free with a received SNR of 34 dB. This did not therefore show the performance boundaries of the modulation schemes. However, it does show that the device and application are able to synchronise and demodulate the received signal in real-time.

Table 6.2 Results of Packets Received and Demodulated by Mobile Device in Real-time at the Marina Trials. SNR was measured based on the recordings as 34 dB

			Packets		Symbols		Bits	
ID	Data Modulation	Bit Rate Uncoded (bit/s)	Success	Total	Errors	Total	Errors	Total
A	Chirp-BOK	23.4	17	17	0	544	0	544
B	K11 2-OCK	23.4	17	17	0	544	0	544
C	K11 4-OCK	46.9	17	17	0	272	0	544
D	K11 16-OCK	93.8	17	17	0	136	0	544
E	Chirp-BOK	93.9	17	17	0	544	0	544
F	K10 16-OCK	187.7	17	17	0	136	0	544
G	K9 16-OCK	375.7	17	17	0	136	0	544

6.7 Channel Recording combined with AWGN

Recordings from the marina incorporating channel effects such as multipath were combined with generated AWGN to produce further recordings with realistic SNR conditions of 0 dB, −6 dB, −12 dB, and −21 dB. These recordings were played into the mobile device microphone jack and synchronised and demodulated in real-time by the device and application. This is to investigate the performance bounds of the different modulation schemes and receiver structure running on the mobile device. Results of recordings from the marina trials combined with AWGN then played back into the mobile device and demodulated in real-time are tabulated as 0 dB in Table 6.3, −6 dB in Table 6.4, −12 dB in Table 6.5, and −21 dB in Table 6.6. These are combined into graphical form in Fig. 6.6.

These results demonstrate the limits of the combined modulation schemes, application and hardware. There aren't the number of data points to produce performance curves as smooth as those in the AWGN simulations in Fig. 6.1, however the results in Fig. 6.6 do correspond with respect to the relative performance of each packet type. When comparing the modulation schemes of K11 16-OCK and Chirp-BOK with equivalent data rate the results show an improvement in performance at BER 10^{-4} of 12 dB for M-OCK.

Table 6.3 Results of Packets Received And Demodulated In Real-time by Mobile Device Of Marina Trials Recordings With Added AWGN. SNR measured at 0 dB

			Packets		Symbols		Bits	
ID	Data Modulation	Bit Rate Uncoded (bit/s)	Success	Total	Errors	Total	Errors	Total
A	Chirp-BOK	23.4	17	17	0	544	0	544
B	K11 2-OCK	23.4	17	17	0	544	0	544
C	K11 4-OCK	46.9	16	16	0	256	0	512
D	K11 16-OCK	93.8	17	17	0	136	0	544
E	Chirp-BOK	93.9	15	17	2	544	2	544
F	K10 16-OCK	187.7	17	17	0	136	0	544
G	K9 16-OCK	375.7	15	17	2	136	5	544

Table 6.4 Results of Packets Received And Demodulated In Real-time by Mobile Device Of Marina Trials Recordings With Added AWGN. SNR measured at $-6\,\text{dB}$

ID	Data Modulation	Bit Rate Uncoded (bit/s)	Packets		Symbols		Bits	
			Success	Total	Errors	Total	Errors	Total
A	Chirp-BOK	23.4	16	17	1	544	1	544
B	K11 2-OCK	23.4	16	17	1	544	1	544
C	K11 4-OCK	46.9	15	15	0	240	0	480
D	K11 16-OCK	93.8	17	17	0	136	0	544
E	Chirp-BOK	93.9	0	17	80	544	80	544
F	K10 16-OCK	187.7	11	17	7	136	18	544
G	K9 16-OCK	375.7	1	17	48	136	104	544

Table 6.5 Results of Packets Received And Demodulated In Real-time by Mobile Device Of Marina Trials Recordings With Added AWGN. SNR measured at $-12\,\text{dB}$

ID	Data Modulation	Bit Rate Uncoded (bit/s)	Packets		Symbols		Bits	
			Success	Total	Errors	Total	Errors	Total
A	Chirp-BOK	23.4	7	17	15	544	15	544
B	K11 2-OCK	23.4	5	16	13	512	13	512
C	K11 4-OCK	46.9	8	16	13	256	18	512
D	K11 16-OCK	93.8	9	17	15	136	36	544
E	Chirp-BOK	93.9	0	17	167	544	167	544
F	K10 16-OCK	187.7	0	17	49	136	106	544
G	K9 16-OCK	375.7	0	17	89	136	190	544

Table 6.6 Results of Packets Received And Demodulated In Real-time by Mobile Device Of Marina Trials Recordings With Added AWGN. SNR measured at −21 dB

			Packets		Symbols		Bits	
ID	Data Modulation	Bit Rate Uncoded (bit/s)	Success	Total	Errors	Total	Errors	Total
A	Chirp-BOK	23.4	0	15	74	480	74	480
B	K11 2-OCK	23.4	0	16	106	512	106	512
C	K11 4-OCK	46.9	0	15	53	240	68	480
D	K11 16-OCK	93.8	0	17	61	136	136	544
E	Chirp-BOK	93.9	0	18	260	576	260	576
F	K10 16-OCK	187.7	0	17	92	136	177	544
G	K9 16-OCK	375.7	0	17	118	136	228	544

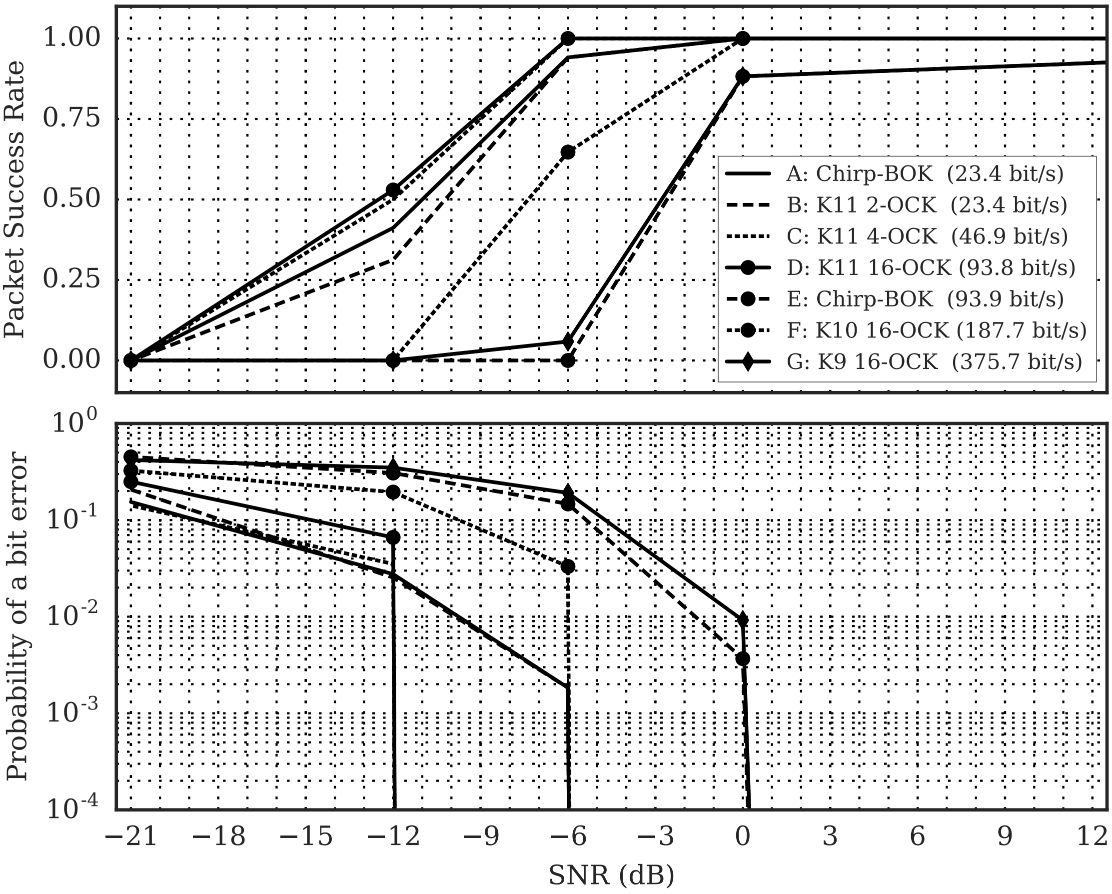

Fig. 6.6 AWGN Performance

6.8 Summary

It has been shown that is possible to implement a software-defined underwater acoustic modem using an Android mobile device, for a variety of spread spectrum signals, including the M-OCK scheme developed throughout this thesis. A single App is shown to be able to execute a number of different transceivers for differing modulation schemes. Experimental validation in a real-world channel with a strong multipath effect shows that the long symbol durations provide resilience to channels with relatively long delay spreads. The implemented receiver structure is able to incorporate a number of the previously covered additions such as normalisation for a fixed synchronisation threshold; and windowed partial cross correlation for data demodulation to reduce computational load.

Simulations and underwater channel recordings with AWGN have been used to show that M-OCK outperforms Chirp-BOK modulation scheme for the same data rate as the modulation depth, M, is increased.

It has been shown that it is possible to implement a receiver on an Android mobile device and to synchronise and demodulate received packets in real-time in live real channels and in recordings with AWGN. The device processor is not only running the receiver structure, but also the operating system and numerous services and applications simultaneously.

The simulations are compared with the channel recordings and AWGN which are demodulated by the Android mobile device and receiver. The respective performance of the modulation schemes follows that of the simulations, for BER 10^{-4} the performance of K11 16-OCK showed the same SNR of $-12\,\text{dB}$. However, K9 16-OCK in simulations showed $-6\,\text{dB}$, but in the channel recordings and AWGN showed $0\,\text{dB}$ for BER of 10^{-4}.

M-OCK has been shown to outperform Chirp-BOK by $12\,\text{dB}$ in channel recordings with AWGN using the Android receiver in real-time for a datarate of $93.8\,\text{bit/s}$.

The low SNR of $-12\,\text{dB}$ also demonstrates the dynamic range of the mobile device's inbuilt front-end analogue circuitry.

Chapter 7

Non-binary LDPC Forward Error Correction Codes

7.1 Introduction

The previous chapters of the thesis have presented research in the context of having the aim of targeting low-power, and low-complexity, receiver platforms. This chapter takes a different angle of approach and considers scenarios where more processing power and energy is available and investigates M-OCK in combination with the more computationally intensive non-binary LDPC error correction codes.

Previous chapters have shown how increasing the modulation depth of an m-ary orthogonal signaling scheme can improve performance by reducing the energy per bit for a given bit error probability. To further improve on this, and move closer to the Shannon-Hartley limit, additional measures such as forward error correction codes can be used. As the m-ary orthogonal code keying system is essentially a non-binary scheme this will be a factor when considering possible forward error correction codes. This chapter looks at the use of Reed-Solomon codes and Non-binary LDPC codes with M-OCK in both simulations and real-world underwater channels.

This thesis has already covered the signal design and the receiver design with Doppler compensation techniques. Results have also included the use of Reed-Solomon forward error correction codes. This chapter will look at non-binary low density parity check (LDPC) forward error correction codes and how they compare with Reed-Solomon codes in this application.

Simulations in AWGN channel show the relative performance of non-binary LDPC codes and RS codes with M-OCK signals.

Experimental validation using the sea trials and marina trials recordings from previous chapters shows the relative performance of non-binary LDPC and RS codes in real underwater channels.

Recordings combined with AWGN provide further analysis of the relative performance of non-binary LDPC and RS codes with M-OCK signals in an underwater acoustic channel.

A packet/symbol quality measure is introduced for determining the confidence of a given symbol decision from the maximum likelihood detector.

7.2 Motivation

M-ary orthogonal code keying (M-OCK), as covered throughout this thesis, is essentially a non-binary modulation scheme. Simulations and experiments have already shown how the use of Reed-Solomon (RS) codes can improve the performance of M-OCK in AWGN and real underwater acoustic channels. Binary and non-binary LDPC codes have been shown to improve performance and move closer to the Shannon-Hartley limit when compared to RS codes. This work seeks to investigate the use of non-binary LDPC codes in conjunction with M-OCK in an underwater channel and to compare performance with the RS codes used so far.

7.3 Non-binary Block Codes

Reed-Solomon (RS) codes are non-binary block codes able to identify and correct multiple symbol errors in a block. First developed in 1960 by Reed and Solomon [123].

RS codes found early use in the 1977 Voyager's deep space communications system and are in widespread use today including in television broadcasting systems such as DVB-T. For a guide to using RS codes the reader is directed to NASA's tutorial [124] and to the BBC Whitepaper by Clarke [125].

The low density parity check (LDPC) code was first presented by Gallager [126] and then rediscovered by Mackay in 1995 [127]

The performance of non-binary LDPC codes was investigated in 1998 by Davey and MacKay, showing that they outperformed the binary variants [128]. Ganepola, Carrasco, Wassell, and Le Goff show that for GF(q) as q increases as does the performance of the non-binary LDPC code [129].

Huang, Zhou, and Willett investigate the use of non-binary LDPC in underwater acoustic communications with multicarrier modulation, OFDM. This was shown to improve the BER performance as well as reducing the peak to average power ratio (PAPR).

Comparisons between RS codes and non-binary LDPC codes have shown the non-binary LDPC codes to perform closer to the Shannon-Hartley limit [131].

In m-ary modulation schemes such as M-ary Quadrature Amplitude Modulation (M-QAM) the euclidean distance between constellation points produces likelihood of a decoded symbol being a nearby defined symbol. In M-ary Orthogonal Code Keying (M-OCK), every symbol is orthogonal with all decoded symbols being equally likely as shown in Chapter 3. Therefore,

Table 7.1 Packet Structure: Data

	Packet Synch		Packet Data		
ID	Structure	Details	Structure	Details	Optional FEC
A	2 of K13 Symbols	K13M512 K13M513	100 of K11 64-OCK Symbols	K11M0 to K11M63	Uncoded or RS
B	2 of K13 Symbols	K13M514 K13M515	100 of K11 64-OCK Symbols	K11M0 to K11M63	Uncoded or LDPC
C	2 of K13 Symbols	K13M516 K13M517	25 of K13 256-OCK Symbols	K13M0 to K13M255	Uncoded or RS
D	2 of K13 Symbols	K13M518 K13M519	25 of K13 256-OCK Symbols	K13M0 to K13M255	Uncoded or LDPC

there is no nearest neighbour symbol. Decoders that rely on symbol likelihoods are therefore unsuitable for an orthogonal modulation scheme.

The decoders for RS codes and non-binary LDPC codes used in this investigation are covered in the next section.

7.4 Experiment Setup

These simulations and experiments set out to directly compare the performance of Reed-Solomon and non-binary LDPC Codes when used with the M-OCK modulation scheme. Simulations in an AWGN channel will provide an initial benchmark. Experimental results using the receiver structures described in previous chapters will show the relative performance across a range of underwater acoustic channels - Sea Trials and Marina Trials.

Data packets were constructed as described in Table 7.1. For the Reed-Solomon encoded messages the coderate of 0.76 was chosen such that both encoded packet types, K11 and K13, would have similar durations. The properties of the Reed-Solomon codes used are shown in Table 7.2. The RS decoder uses the Berlekamp-Massey algorithm to determine the error and erasure locator polynomial. The roots of the polynomial are then found using Chien search.

The non-binary LDPC encoded packets possess the same block sizes, coderate and alphabet size as the RS encoded packets. The non-binary LDPC decoder uses the correlator values of all codes for each symbol in the message to create the input metrics. The average correlator value for the entire block is taken as the centre point and the distance of each correlator value to this centre point is used as the metric. The decoder algorithm used is SD-QSPA: a soft distance sum-product algorithm. As shown by Johnston, Sharif, Tsimenidis, and Chen a SD-QSPA decoder is

Table 7.2 Reed-Solomon Properties

Reed-Solomon Property	K11 64-OCK RS	K13 256-OCK RS
Bits per symbol $m = \log_2 M$	6	8
Alphabet Size $q = p^m$	64	256
Block Length $n = q - 1$	63	255
Parity Length $n - k$	12	6
Distance $n - k + 1$	13	7
Message Length k	51	249
Truncated Message Length	38	19
RS Descriptor $[n,k,n-k+1]_q$–code	2 blocks of $[63,51,13]_{64}$–code	1 block of $[255,249,7]_{256}$–code
Truncated RS Descriptor $[n,k,n-k+1]_q$–code	2 blocks of $[50,38,13]_{64}$–code	1 block of $[25,19,7]_{256}$–code

comparable to the log-QSPA decoder which utilises log likelihood ratios (LLR) instead of soft distances [132]. Byers and Takawira showed how utilising the Fourier transform reduced the decoding complexity for non-binary LDPC codes [133]. The combination of all of these results in the SD-QSPA decoder.

The LDPC messages were encoded to the author's specifications by Zhen Mei, Newcastle University. The C source code for the log-FFT-QSPA decoder was provided by Zhen Mei and Martin Johnston, Newcastle University and the operation is described in [134]. The decoder source code was then modified by the author to operate as a SD-FFT-QSPA decoder using the correlator values as the input metric.

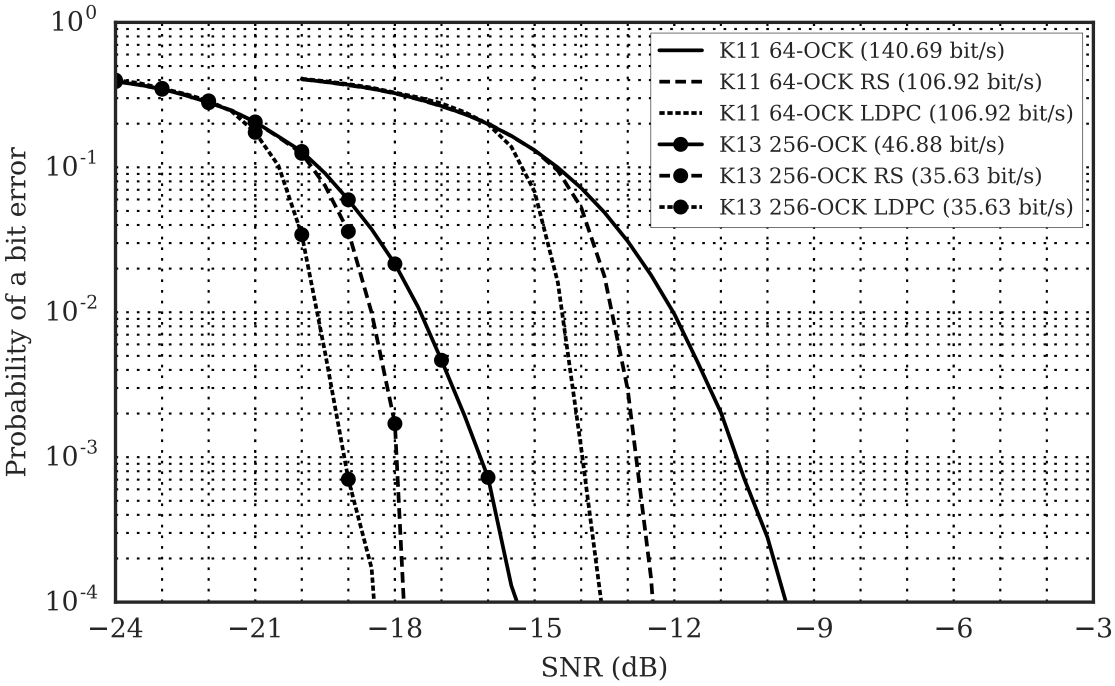

Fig. 7.1 Receiver Structure: Data Demodulation Simulations. BER vs SNR for M-ary Orthogonal Code Keying packets with the receiver structure. Spreading bandwidth, B, of 8 kHz and F_s of 48 kHz. Showing performance of K11 64-OCK (140.69 bit/s) and K13 256-OCK (46.88 bit/s). The performance using Reed-Solomon and Non-binary LDPC error correction codes is also shown for direct comparison. K11 64-OCK RS and K11 64-OCK LDPC (106.92 bit/s), and K13 256-OCK RS and K13 256-OCK LDPC (35.63 bit/s).

7.5 Simulations

The performance of the receiver structure and error correction codes is analysed after transmitting the packet through a simulated AWGN channel. Fig. 7.1 shows the performance of K11 64-OCK (140.69 bit/s), K13 256-OCK (46.88 bit/s), K11 64-OCK RS (106.92 bit/s), K13 256-OCK RS (35.63 bit/s), K11 64-OCK LDPC (106.92 bit/s) and K13 256-OCK LDPC (35.63 bit/s) packets. The LDPC decoder is limited to a maximum of 20 iterations.

Looking at the simulation results in Fig. 7.1 the non-binary LDPC codes produce a 1 dB performance gain at BER 10^{-4} over the equivalent RS coderate. This gain applies to both the K11 64-OCK and K13 256-OCK modulation schemes. This is a 3 dB performance gain over uncoded K13 256-OCK, and a 4 dB gain over uncoded K11 64-OCK.

7.6 Experimental Validation: Sea and Marina Trials

The setup for the experimental trials were discussed in detail in Chapter 4 for the Sea Trials and in Chapter 5 for the Marina Trials. These same recordings also provide the data for comparing the two forms of error correction. The same packets described in the previous simulations were also used here.

The results tables compare uncoded, RS and non-binary LDPC performance for K11 64-OCK and K13 256-OCK. Sea Trials results for each range are shown in Table 7.3 and Table 7.4. Marina Trials results for the motion types and static Doppler compensation are shown in Table 7.5 and Table 7.6. Tracking Doppler compensation results are shown in Table 7.7 and Table 7.8.

Table 7.3 Sea Trials Recording Results: K11 64-OCK FEC

	K11 64-OCK Uncoded		K11 64-OCK RS		K11 64-OCK LDPC	
Range (m)	BER	PSR	BER	PSR	BER	PSR
100	3.056×10^{-4}	0.933	0.000	1.000	0.000	1.000
500	4.098×10^{-4}	0.918	0.000	1.000	0.000	1.000
1000	1.200×10^{-2}	0.975	0.000	1.000	2.412×10^{-2}	0.950
2000	3.252×10^{-4}	0.951	0.000	1.000	0.000	1.000
5000	9.111×10^{-3}	0.850	5.263×10^{-3}	0.933	1.623×10^{-2}	0.933
10000	5.841×10^{-2}	0.024	3.366×10^{-2}	0.550	5.482×10^{-2}	0.619

The Sea Trials results in Table 7.3 and Table 7.4 show that both RS and non-binary LDPC codes improve performance over uncoded. But performance of RS and non-binary LDPC codes is comparable in these results. The high received SNR for the K13 256-OCK symbols doesn't allow for differentiation between RS and non-binary LDPC codes performance.

The Marina Trials results for the various motion types using Static Resampler Doppler Compensation, in Table 7.5 and Table 7.6, show improvement in performance for both RS and non-binary LDPC codes. For the K11 64-OCK modulation, the non-binary LDPC shows a noticeable improvement in performance over RS codes. Though for K13 256-OCK the RS and non-binary LDPC performance is very similar.

When considering the Tracking Resampler Doppler Compensation results, in Table 7.7 and Table 7.8, again there is an improvement in performance for both non-binary LDPC and RS codes. Once again, with K11 64-OCK the non-binary LDPC provides gains over RS codes, and also for K13 256-OCK where there is a significant Doppler shift (Constant 1.11m/s, Constant 2.22m/s and Varying 0m/s to 2.2m/s).

Table 7.4 Sea Trials Recording Results: K13 256-OCK FEC

	K13 256-OCK Uncoded		K13 256-OCK RS		K13 256-OCK LDPC	
Range (m)	BER	PSR	BER	PSR	BER	PSR
100	4.098×10^{-4}	0.984	0.000	1.000	0.000	1.000
500	0.000	1.000	0.000	1.000	0.000	1.000
1000	0.000	1.000	0.000	1.000	0.000	1.000
2000	0.000	1.000	0.000	1.000	0.000	1.000
5000	1.967×10^{-3}	0.967	0.000	1.000	0.000	1.000
10000	9.756×10^{-4}	0.951	0.000	1.000	0.000	1.000

Table 7.5 Marina Trials Recording Results: K11 64-OCK FEC with Static Doppler Compensation

	K11 64-OCK Uncoded		K11 64-OCK RS		K11 64-OCK LDPC	
Motion Type	BER	PSR	BER	PSR	BER	PSR
Constant 1.11m/s	9.779×10^{-3}	0.819	2.872×10^{-3}	0.952	0.000	1.000
Constant 2.22m/s	3.514×10^{-2}	0.593	3.300×10^{-2}	0.850	1.952×10^{-2}	0.927
Varying 0.0m/s to 2.22m/s	6.417×10^{-2}	0.567	5.965×10^{-2}	0.600	3.728×10^{-3}	0.967
Perpendicular Constant 2.22m/s	2.825×10^{-2}	0.800	1.266×10^{-2}	0.875	0.000	1.000

Table 7.6 Marina Trials Recording Results: K13 256-OCK FEC with Static Doppler Compensation

	K13 256-OCK Uncoded		K13 256-OCK RS		K13 256-OCK LDPC	
Motion Type	BER	PSR	BER	PSR	BER	PSR
Constant 1.11m/s	9.321×10^{-3}	0.963	1.444×10^{-2}	0.951	0.000	1.000
Constant 2.22m/s	6.024×10^{-2}	0.683	4.041×10^{-2}	0.833	6.414×10^{-2}	0.800
Varying 0.0m/s to 2.22m/s	8.656×10^{-2}	0.508	5.985×10^{-2}	0.710	1.033×10^{-1}	0.667
Perpendicular Constant 2.22m/s	4.364×10^{-2}	0.765	2.829×10^{-2}	0.850	4.734×10^{-2}	0.829

Table 7.7 Marina Trials Recording Results: K11 64-OCK FEC with Tracking Doppler Compensation

	K11 64-OCK Uncoded		K11 64-OCK RS		K11 64-OCK LDPC	
Motion Type	BER	PSR	BER	PSR	BER	PSR
Constant 1.11m/s	1.504×10^{-2}	0.880	3.081×10^{-3}	0.952	2.567×10^{-3}	0.976
Constant 2.22m/s	4.938×10^{-2}	0.642	5.493×10^{-2}	0.775	2.033×10^{-2}	0.927
Varying 0.0m/s to 2.22m/s	6.172×10^{-2}	0.450	4.934×10^{-2}	0.633	2.434×10^{-2}	0.933
Perpendicular Constant 2.22m/s	2.294×10^{-2}	0.812	9.375×10^{-3}	0.875	0.000	1.000

Table 7.8 Marina Trials Recording Results: K13 256-OCK FEC with Tracking Doppler Compensation

	K13 256-OCK Uncoded		K13 256-OCK RS		K13 256-OCK LDPC	
Motion Type	BER	PSR	BER	PSR	BER	PSR
Constant 1.11m/s	6.667×10^{-3}	0.951	1.123×10^{-2}	0.976	0.000	1.000
Constant 2.22m/s	2.104×10^{-2}	0.902	2.961×10^{-2}	0.881	7.895×10^{-3}	0.975
Varying 0.0m/s to 2.22m/s	6.238×10^{-2}	0.689	6.367×10^{-2}	0.710	2.610×10^{-2}	0.833
Perpendicular Constant 2.22m/s	1.636×10^{-2}	0.914	7.730×10^{-3}	0.950	2.696×10^{-2}	0.902

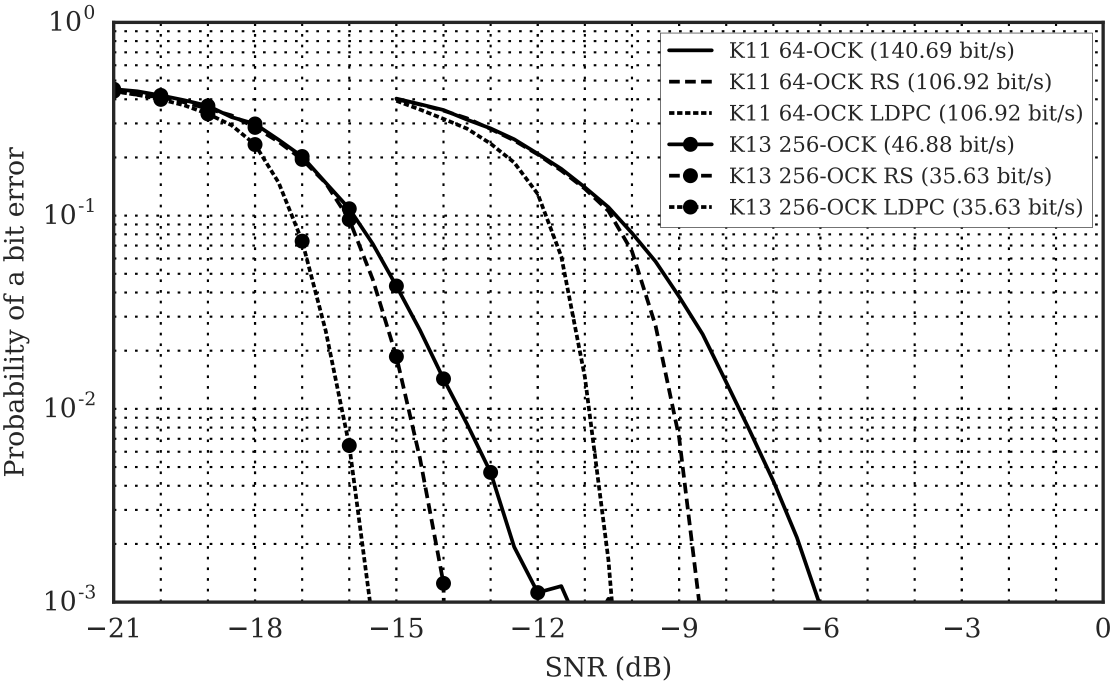

Fig. 7.2 Data Demodulation Channel Recording with AWGN. BER vs SNR for M-ary Orthogonal Code Keying packets with the receiver structure. Channel recording for 100 m is combined with AWGN at various levels of SNR and processed with the receiver structure. Spreading bandwidth, B, of 8 kHz and F_s of 48 kHz. Showing performance of K11 64-OCK (140.69 bit/s) and K13 256-OCK (46.88 bit/s). The performance using Reed-Solomon error correction codes is also shown for direct comparison. K11 64-OCK RS (106.92 bit/s) and K13 256-OCK RS (35.63 bit/s). The performance using Non-binary LDPC error correction codes is also shown. K11 64-OCK LDPC (106.92 bit/s) and K13 256-OCK LDPC (35.63 bit/s).

7.7 Channel Recording Combined With AWGN

A subsection of the recording for Sea Trials 100 m is then repeatedly combined with AWGN and processed with the receiver structure to produce performance curves as shown in Fig. 7.2.

With channel effects combined with AWGN the improvement in performance of non-binary LDPC over RS codes is apparent in Fig. 7.2. For K11 64-OCK there is an improvement of 2 dB at BER 10^{-3} of non-binary LDPC over RS codes. This is a total performance gain of 4.5 dB at BER 10^{-3} of non-binary LDPC over uncoded K11 64-OCK. In the original simulations shown in Fig. 7.1 the performance gain at BER 10^{-3} was 3.5 dB with an absolute performance of BER 10^{-3} at -14 dB. The channel recording combined with AWGN shows an absolute performance of BER 10^{-3} at -10.5 dB in Fig. 7.2.

K13 256-OCK also sees an improvement using non-binary LDPC over RS codes of 1.5 dB at BER 10^{-3}.

7.8 Packet Quality Measure

In phase-shift keying (PSK) modulation it is possible to produce constellation plots to visually determine the effects of noise on the quality of a data packet. It could be considered useful to have an equivalent visual plot of the quality of M-OCK packets.

For a given symbol in the packet it is possible to analyse the output values of the entire correlator bank and how the maximum-likelihood selected value compares with the rest of the correlator outputs. It is then possible to track the quality of a packet, symbol-by-symbol, for the full duration. To determine the confidence of a given symbol, the Distance Metric, Q, in (7.1) is based on the maximum correlator value across the codebank for a given symbol, $MaxValue_0$, along with the second maximum correlator value, $MaxValue_1$. As the $MaxValue_1$ tends to 0, so Q tends to 1.0.

$$Q = \frac{MaxValue_0 - MaxValue_1}{MaxValue_0 + MaxValue_1} \tag{7.1}$$

Example packet quality plots are shown for Sea Trials 100 m in Fig. 7.3 and Sea Trials 10 km in Fig. 7.4. It is possible to see the strength of the signal by the difference between the maximum and second maximum correlator values in Fig. 7.3. This leads to the distance metric remaining above 0.5 and zero symbol errors in the packet. In contrast, the signal at Fig. 7.4 gives much weaker maximum correlator values leaving very little distance to the second maximum correlator value. This in turn produces a low distance metric and numerous symbol errors throughout the packet.

Analysing the Marina recordings at Constant 2.22m/s motion, with static resampler Doppler compensation, it is possible to see the quality of the packet trail off as the velocity changes, the symbol errors then appear as the quality drops as shown in Fig. 7.5. With tracking resampler Doppler compensation the improvement in packet quality is clear in Fig. 7.6. Incidentally, the non-binary LDPC error correction for both static and tracking resampler Doppler compensation results in zero errors for this specific packet.

7.9 Closing Points

The quality measure for symbols during the packet would also prove useful in other soft decoders such as list decoders for RS codes.

Non-binary LDPC and RS have been shown to be effective error correction codes when used in conjunction with M-OCK signals in both AWGN and underwater acoustic channels. The performance gains of non-binary LDPC over RS codes are limited as seen in AWGN simulations and channel recordings combined with AWGN, between 1 dB and 2 dB. Non-binary LDPC codes also require greater computational time/energy using the soft decoder than RS codes using the hard decoder.

To compare the computational load of the RS decoder versus the non-binary LDPC decoder, each were repeatedly run with an all-zeros codeword with a single iteration for the non-binary LDPC decoder. The relative processing time per decode operation on a desktop PC are: K11 64-OCK RS: 1 µs; K11 64-OCK LDPC: 69.6 µs; K13 256-OCK RS: 1 µs; K13 256-OCK LDPC: 567.3 µs. Changing the input codeword to all ones (an uncorrectable block) and limiting to a single iteration for LDPC the timings become: K11 64-OCK RS: 7 µs; K11 64-OCK LDPC: 70.2 µs; K13 256-OCK RS: 11 µs; K13 256-OCK LDPC: 559.6 µs. This is a substantial increase in computational time moving from RS to non-binary LDPC decoding for equivalent block sizes.

In applications targeting low-power, low-complexity receivers the non-binary LDPC decoder becomes unappealing when compared to using RS codes. Especially when considering the limited gains in performance seen with the packets used in this chapter.

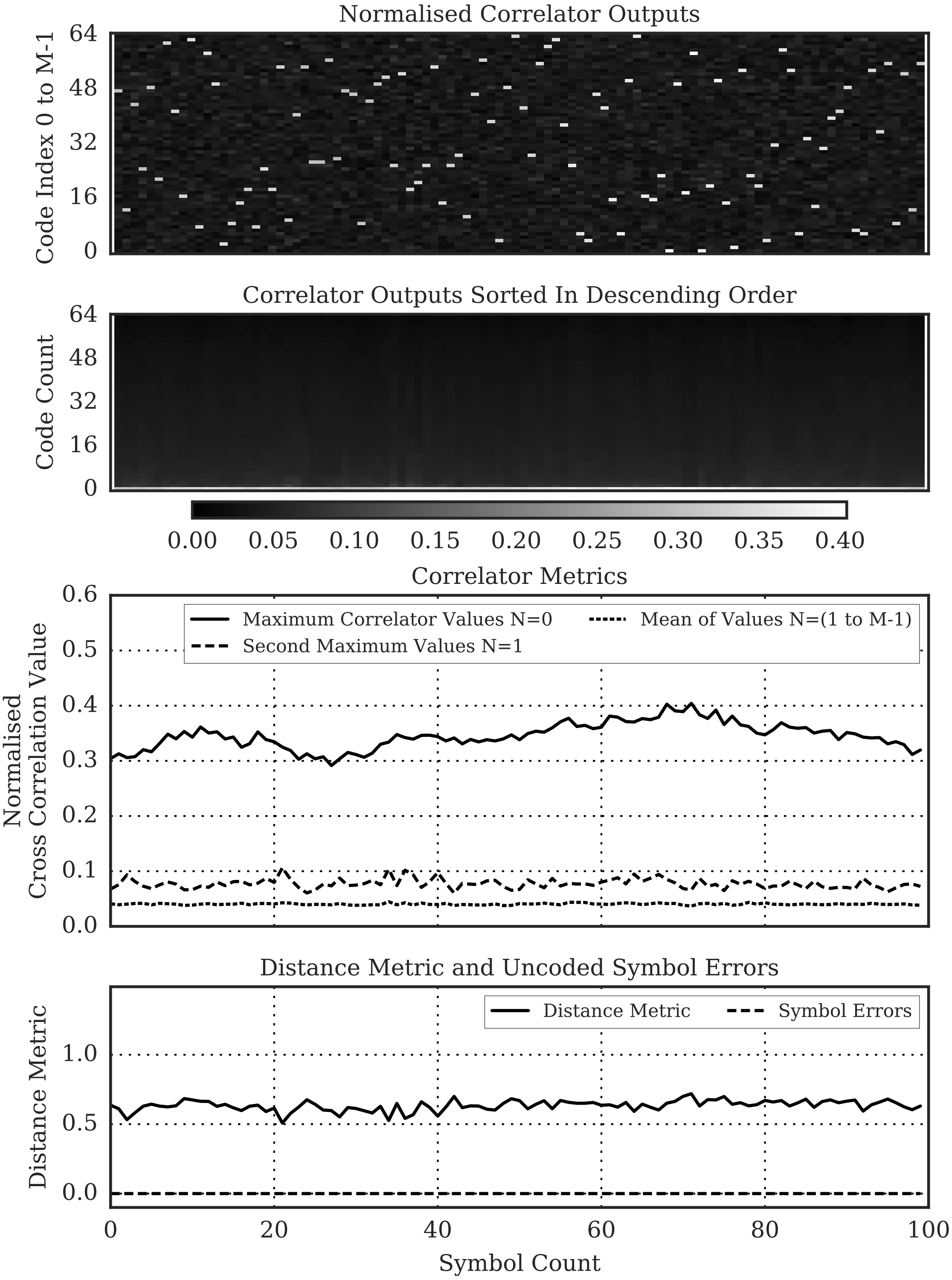

Fig. 7.3 Packet Quality: Sea Trials 100m for K11 64-OCK.

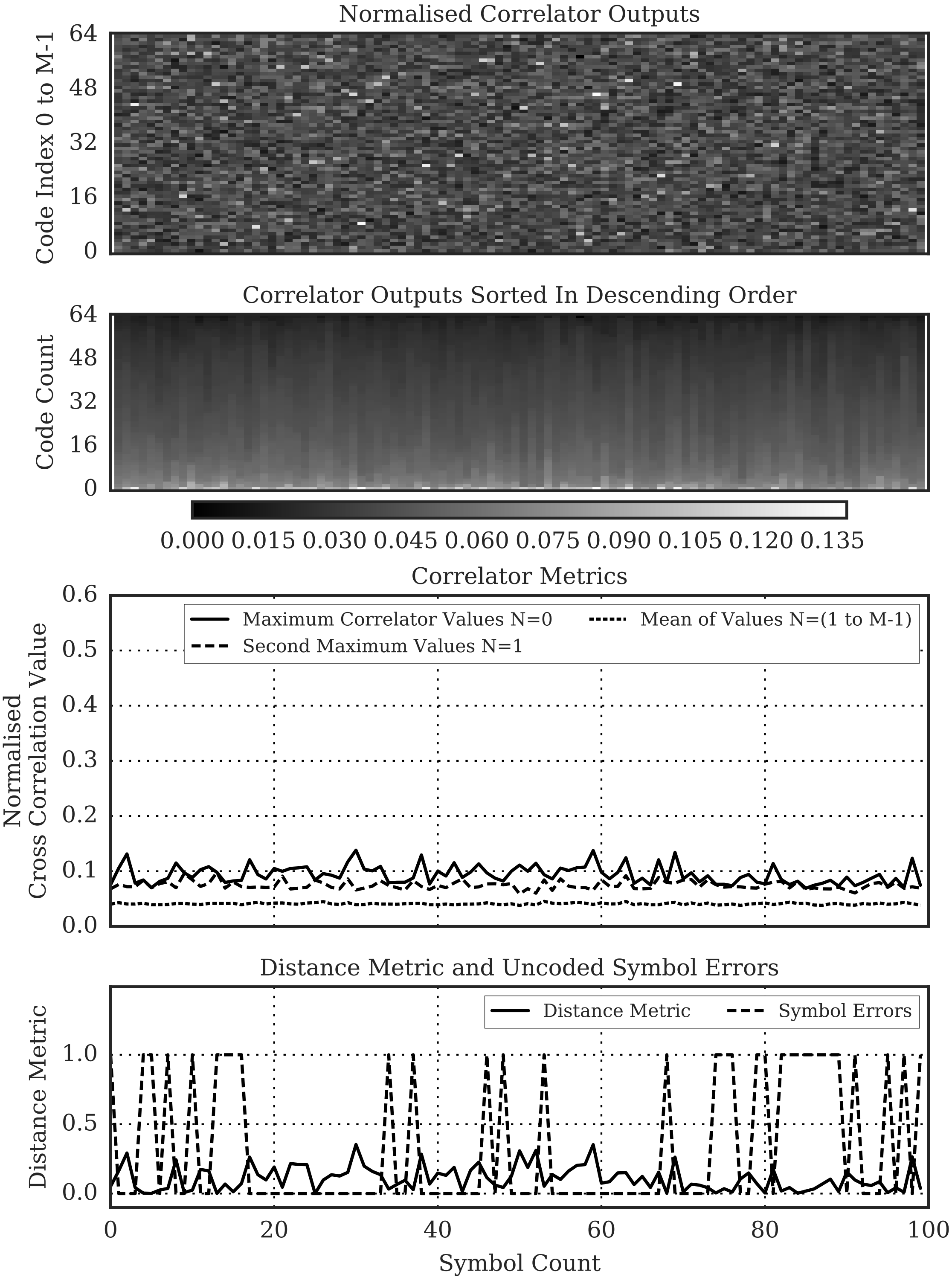

Fig. 7.4 Packet Quality: Sea Trials 10km for K11 64-OCK.

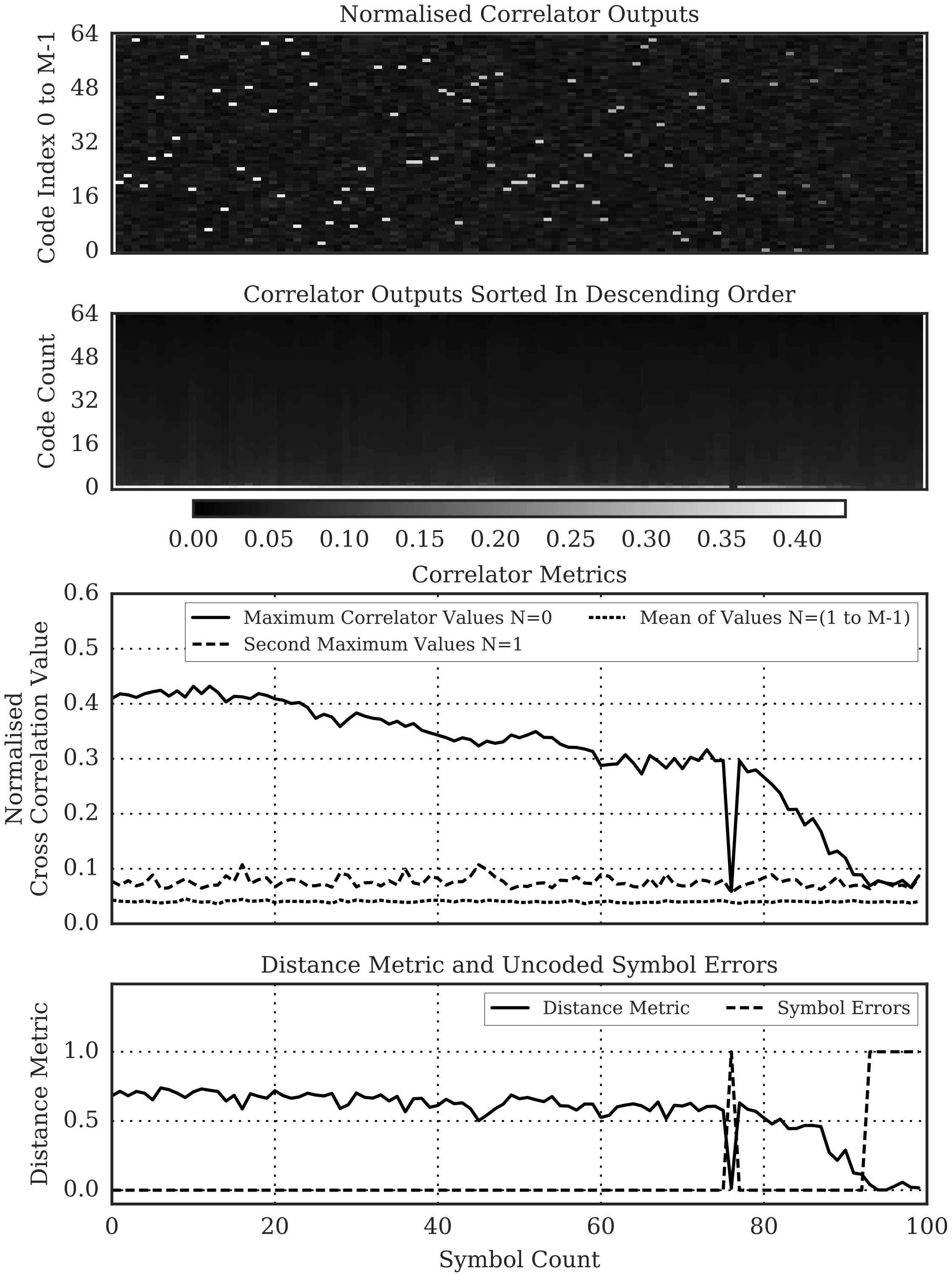

Fig. 7.5 Packet Quality: Marina Trials for K11 64-OCK with Static Resampler Doppler Compensation.

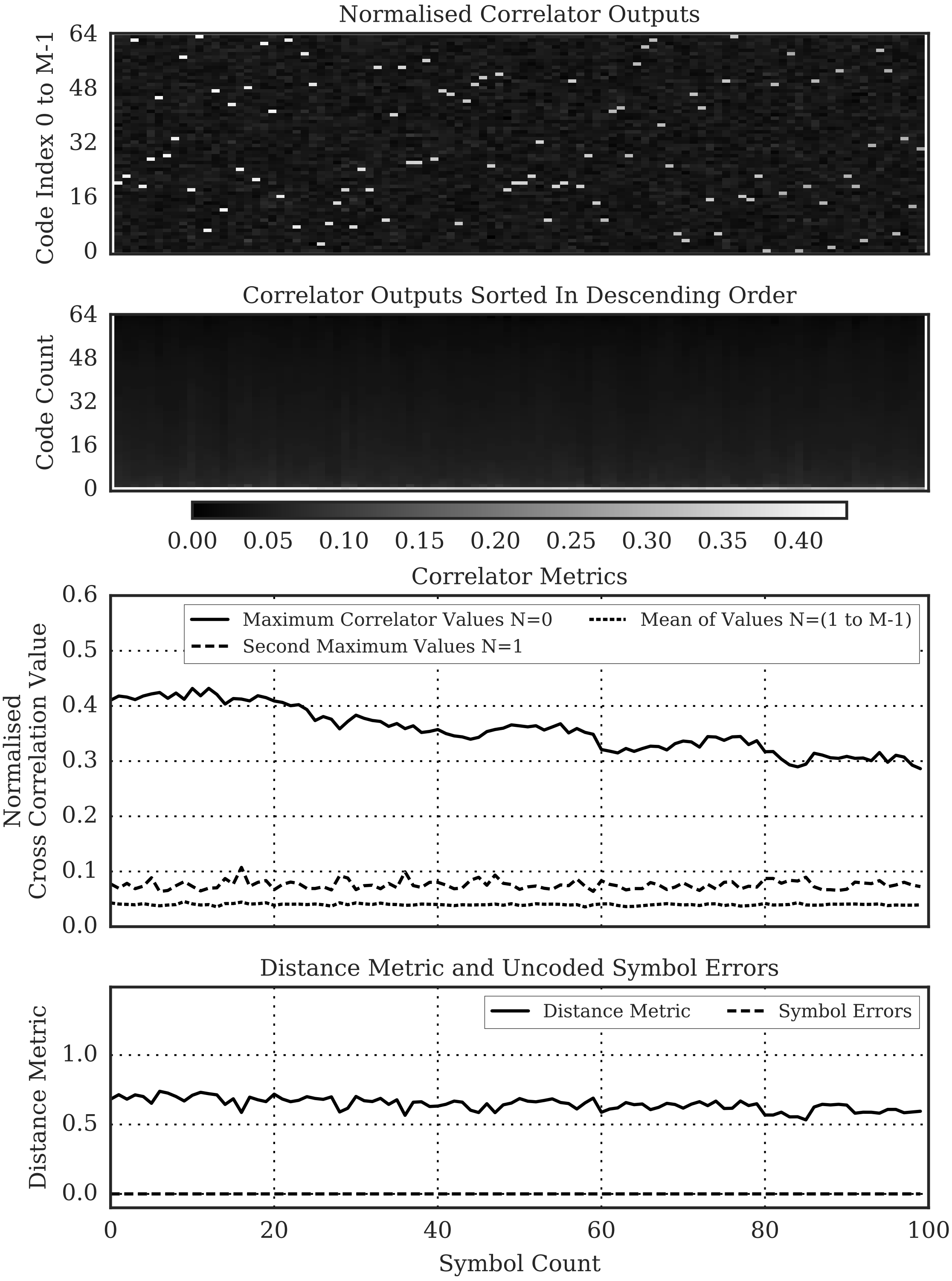

Fig. 7.6 Packet Quality: Marina Trials for K11 64-OCK with Tracking Resampler Doppler Compensation.

7.10 Summary

Non-binary LDPC codes have been shown to improve performance of data demodulation when used with M-OCK in simulations, underwater acoustic channels, and when recordings are combined with AWGN.

Non-binary LDPC codes have been shown to offer performance gains over RS codes of equivalent coderates in these channels. Performance gains of non-binary LDPC over RS are 2 dB for K11 64-OCK and 1.5 dB for K13 256-OCK channel recordings combined with AWGN at a BER of 10^{-3}.

A symbol/packet quality measure has been introduced to determine the confidence in symbol decisions by the maximum likelihood detector, along with a visual method to show this measure throughout the duration of a data packet.

Chapter 8

Conclusion

This chapter brings together the key results and conclusions from the technical chapters, along with additional discussions of the thesis as a whole. Further work stemming from this research is also identified.

The background research in Chapter 2 identified the need to limit transmit power to less than 170.8 dB re 1 µPa @ 1 m or 1 W of acoustic power in order to minimise the impact on marine life, and to potentially remove the theoretical zone of influence for which injury would occur from acoustic noise. This requires a signal and receiver structure that can operate at low-received-SNRs in order to maintain a usable range for the limited transmit power.

In Chapter 3, bandlimited carrierless pseudonoise symbols were used to create an m-ary orthogonal signaling scheme: M-ary Orthgonal Code Keying (M-OCK). Symbols with large bandwidth-time provide processing gain from spreading that enables successful despreading and demodulation in low-received-SNR channels. The M-OCK modulation scheme is shown, through AWGN simulations, to follow the same theoretical performance as an m-ary orthogonal signaling scheme. As modulation depth is increased, M-OCK quickly outperforms M-QAM signals.

Comparisons with LFM chirps in AWGN show the relative ease with which bandlimited PN symbols can be hidden in the background noise. With equivalent bandwidth and duration the LFM chirps remain visible in a spectrogram long after the bandlimited PN has become indistinguishable from the noise.

Simulations show the performance in an AWGN channel of several bandlimited m-sequence code lengths and modulation depths. K11, K12 and K13 with M = 2, 4, 16, 64 and 256. For BER of 10^{-4} SNRs of -17.5 dB are shown for K13 256-OCK; -14.5 dB for K12 64-OCK; and -11.5 dB for K11 64-OCK.

Ambiguity plots show the relative Doppler intolerance of bandlimited PN sequences with long durations when compared to LFM and HFM chirps. Highlighting the need for effective Doppler compensation to be included as part of the receiver structure.

Chapter 4 investigated the receiver structure designs to demodulate the M-OCK signals. Synchronisation signals and the receiver structure were also introduced. The normalisation process was explained in reducing the effects of varying signal energy on the correlator so that a fixed threshold detector could be used for synchronisation. Synchronisation using multiple unique bandlimited PN symbols, and combining the energy of each of the narrow windows from the respective correlators, was shown to produce equal performance to a single symbol of equivalent bandwidth and total duration; this was in both AWGN simulations and sea trials.

Investigations into the data demodulation receiver structure focussed on two example modulation depths and code lengths: K11 64-OCK and K13 256-OCK. Both uncoded and RS coded packets were included in the analysis. Simulations in AWGN channel including the signals and receiver structures showed performances with BER of 10^{-4} and SNR -18 dB for K13 256-OCK RS (35.63 bit/s); -15.5 dB for K13 256-OCK (46.88 bit/s); -12.5 dB for K11 64-OCK RS (106.92 bit/s); and -9.5 dB for K11 64-OCK (140.69 bit/s).

Sea trials showed successful synchronisation and data demodulation of packets for all schemes under test across ranges 100 m, 500 m, 1 km, 2 km, 5 km, and 10 km with a bandwidth of 8 kHz and a transmit power limited to less than 170.8 dB re 1 µPa @ 1 m or 1 W of acoustic power. At 10 km, received-SNR levels between -9 dB and -20 dB were observed.

Channel recordings combined with AWGN were used to further test the signals and receiver structures. These showed performances with BER of 10^{-3} and SNR -14 dB for K13 256-OCK RS (35.63 bit/s); -12 dB for K13 256-OCK (46.88 bit/s); -8.5 dB for K11 64-OCK RS (106.92 bit/s); and -6 dB for K11 64-OCK (140.69 bit/s).

The strong multipath arrivals and the long symbol durations meant that the SNR measurements included all signal energy arriving, not just the first single arrival that was being used for synchronisation and data demodulation. Using the channel impulse response and the measured correlator peak values for each arrival, a single-path-SNR was calculated to be 4.39 dB less than the measure received-SNR. Which when applied to the performance from the channel recordings with AWGN, takes the results closer to the AWGN simulations of signal and receiver structure. A pilot experiment was carried out to exploit the extra signal energy arriving on the second path using a channel recording combined with AWGN as before. For K11 64-OCK this produced an improvement in performance of 1.5 dB, and for K11 64-OCK RS an improvement of 2 dB.

Ambiguity plots in Chapter 5 show the range of velocities and the effect on correlator peak values for the two symbols K11 (42.65 ms) and K13 (170.65 ms). K11 correlator peak value drops to 70% as velocity reaches ±1.29 m/s; K13 when velocity reaches ±0.33 m/s.

A receiver structure design for synchronisation with Doppler compensation is presented that resamples the signal into multiple streams and correlates each against the PN sequence. The largest peak is used for threshold detection as before, with the identified stream then providing a Doppler estimate for subsequent data demodulation. The resampler steps are set to be fine or coarse based on the ambiguity plots, and to cover a total range of ±2.7 m/s.

The data demodulation receiver structure has two designs proposed for Doppler compensation. One that prepends a single resampler to the beginning of the receiver structure in Chapter 4; and another that uses multiple resampler streams, as per the synchronisation structure, in order to track the changes in Doppler shift throughout the packet. Both take their initial starting Doppler estimate from the output of the synchronisation stage.

Experimental validation carried out in marina trials also investigates the performance of the synchronisation signal structures introduced in Chapter 4. The signal structures consisting of multiple shorter unique PN symbols are shown to perform better than a single symbol of equivalent bandwidth and total duration in channels with significant Doppler effect. This is without any Doppler compensation included in the receiver structure.

The Doppler compensation in the receiver structure is shown to enable successful synchronisation using 1of and 2of K13 symbols in the channels with significant Doppler effect, over a range of different motion types, relative velocities and accelerations.

Data demodulation performance also improved greatly when Doppler compensation was added for these experiments. Both static and tracking resamplers improved the performance for K11 64-OCK signals. The tracking resampler also improved the performance of the K13 256-OCK signals.

Recordings were combined with AWGN to show the performance in real channels with realistic SNR levels. Again, the static and tracking resamplers for data demodulation were shown to improve performance.

Chapter 7 investigated the relative performance of RS and non-binary LDPC codes when used with M-OCK signals. AWGN simulations showed that for equivalent coderate, and data rate, non-binary LDPC codes outperformed RS codes by 1 dB for K11 64-OCK and 0.5 dB for K13 256-OCK at a BER of 10^{-4}. Experimental validation using both sea and marina trials recordings confirmed that non-binary LDPC produced improvement over RS codes.

Channel recordings with AWGN showed non-binary LDPC codes outperformed RS codes by 2 dB for K11 64-OCK and 1.5 dB for K13 256-OCK at a BER of 10^{-3}.

A symbol/packet quality measure was introduced that provides a confidence level in symbol decisions by the maximum likelihood detector. This is based on the relative correlator peak values of the largest and second largest peak values in the codebank. Given that Chapter 3 showed that all other codes are equally unlikely due to the orthogonality of the PN sequences, as the distance between largest and second largest decreases, the confidence in symbol selection also decreases accordingly. Results show the negative correlation between the symbol quality measure and the symbol error rate. Such a measure would be a useful input metric for soft-decision error correction code decoders.

A receiver including synchronisation and data demodulation structures was implemented on an Android mobile device in Chapter 6. The software was able to switch modulation schemes at run-time and to synchronise and demodulate live signals played into the microphone jack in real-time. A number of spread-spectrum modulation schemes were employed including Chirp-BOK and M-OCK with various data rates, symbol durations, and modulation depths; each spread over an 8 kHz bandwidth.

AWGN simulations showed the relative performance of each of the signal modulation schemes under investigation, with M-OCK signals outperforming Chirp-BOK signals of the same data rate and bandwidth. 93.8 bit/s K11 16-OCK outperformed Chirp-BOK by 4 dB at BER of 10^{-4}.

Marina trials showed that the Android mobile device and implemented receiver were able to receive all transmitted packets error-free in real-time over a range of 100 m. The received SNR was relatively high at 34 dB, so a recording was combined with varying levels of AWGN and also synchronised and demodulated in real-time by the Android mobile device to produce further performance results. 93.8 bit/s K11 16-OCK now outperformed Chirp-BOK by 12 dB at BER of 10^{-4}, with K11 16-OCK successfully receiving a number of packets at -12 dB.

The low SNR of -12 dB also demonstrates the dynamic range of the mobile device's inbuilt front-end analogue circuitry. The device processor is not only running the receiver structure, but also the operating system and numerous services and applications simultaneously. This highlights the need for effective software implementation of the receiver structures.

The studies by Kastelein et al. [52], covered in Chapter 2, showed that for a source level of 170 dB re 1 µPa @ 1 m the modulated FSK signal, with no on/off switching, produced an estimated discomfort zone radius of 1.26 km. The modulated FSK signal spectrogram more closely resembled that of the M-OCK signal based on bandwidth spreading and message duration in these experiments.

Therefore, given that the same source level was used in the Sea Trials with successful communication at the 10 km range, compared with the modulated FSK signal this would produce a receivable-audible ratio of 10:1.26 = 7.94. Though at this range the K13 256-OCK signals were still producing high packet success rates, so for the lower data rate and with error correction codes this ratio could be further improved upon.

Performance as a proportion of channel capacity according to the Shannon-Hartley can be used to compare M-OCK with the state-of-the-art techniques covered in Chapter 2. M-OCK was shown in Chapter 4 to have a channel capacity utilisation of 7.01% for K11 64-OCK RS signal with a data rate of 106.92 bit/s with SNR of -8.5 dB. K13 256-OCK RS at a data rate of 35.63 bit/s was shown to have a channel capacity utilisation of 7.91% at -14 dB. When the multipath exploitation was piloted, K11 64-OCK RS signal resulted in a channel capacity utilisation of 10.85% at -10.5 dB.

The techniques using multiband OFDM [89][88] had a channel capacity utilisation of 4.09% for the lower data rate of 4.2 bit/s at -17 dB, and a channel capacity utilisation of 10.21% for the higher data rate of 78 bit/s at -8 dB, both with a bandwidth of 3.6 kHz. The techniques using DSSS with turbo equalization [90] showed channel capacity utilisation rates of 2.03%

and 7.35% for the lower and higher data rates at -14 dB and -6.5 dB respectively. The MCSS technique [86][87] produced the highest channel capacity utilisation rate of 23.09% for 75 bit/s at -12 dB.

With these SNR levels in mind, the 7.91% and 7.01% channel capacity utilisation by M-OCK signals and receivers fall well within the region of performance by the state-of-the-art techniques.

8.1 Concluding Remarks

The techniques proposed in this thesis concerning signal and receiver structures have achieved channel capacity utilisation at SNR levels that compare favourably with previously published work. Advantages are demonstrated in terms of impact on marine life and the likely discomfort zone, as well as the implementation complexity when compared to state-of-the-art techniques.

With future work on optimum error correction coding as well as the multipath signal exploitation, the performance and channel capacity utilisation could be increased further.

8.2 Future Work

Based on the work and results in this thesis, a number of further areas of research that build on this are outlined below.

Synchronisation needs to be via an omni-directional receiver as the location of the source is as yet unknown. But once the direction of the channel path is known then, using a receiver with a hydrophone array, directivity can be utilised to improve the performance of data demodulation. This would most likely occur at a topside receiver where more resource is available.

Data modulation schemes used in this thesis make use of m-sequences. It would be interesting to investigate the performance of other PN codes in such a modulation scheme, with a view to larger codeset sizes (and greater modulation depths) for the shorter symbol durations.

Error correction coding in conjunction with M-OCK is worthy of further investigation including soft decoding of Reed-Solomon codes making use of the quality measures covered in Chapter 7. The suitability of different error correction codes and associated decoders is application dependent. The computational resources available vary greatly, and can be asymmetric with the topside receiver having more resource to iteratively decode the data packet. Whereas a battery operated embedded wireless sensor will be limited to less intensive decoders. Error correction codes that can exploit this asymmetry will be worth exploring.

The receiver has been successfully implemented on an Android mobile device, but it is also worth considering implementation on embedded hardware such as an FPGA with a view to efficient synchronisation for low-power battery-operated systems. The correlation of PN codes is essentially a summation of point-multiplications of the signal with the code which consists of

+1 or -1 values. This can be simplified to only additions and subtractions which in a hardware implementation would be worth exploring.

The behavioural effects of the M-OCK signal on marine mammals is worth investigating to determine the source levels that produce both minimal impact on the marine mammals, and suitable receivable range for example applications.

Multipath exploitation as piloted in this thesis requires further work to properly identify and track the secondary paths. As well as the optimal way to combine this signal energy with that of the primary path that is currently utilised. Independent paths, as well as being separated by varying delay, are also subject to different Doppler shift, all of which will need to be handled by the receiver structure.

For use in underwater wireless networks, the network layer and multiple access control techniques will need to be investigated when using M-OCK signals.

References

[1] B. Sherlock, C. C. Tsimenidis, and J. A. Neasham, “Signal and receiver design for low-power acoustic communications using m-ary orthogonal code keying,” in *OCEANS 2015-Genova*. IEEE, 2015, pp. 1–10.

[2] B. Sherlock, J. A. Neasham, and C. C. Tsimenidis, “Implementation of a spread-spectrum acoustic modem on an android mobile device,” in *OCEANS 2017-Aberdeen*. IEEE, 2017, pp. 1–9.

[3] B. Sherlock, J. A. Neasham, and C. C. Tsimenidis, “Spread-spectrum techniques for bio-friendly underwater acoustic communications,” *IEEE Access*, vol. 6, pp. 4506–4520, 2018.

[4] X. Lurton, *An Introduction to Underwater Acoustics: Principles and Applications*, 2nd ed., ser. Springer Praxis Books. Springer Berlin Heidelberg, 2010. [Online]. Available: https://books.google.co.uk/books?id=PFXgLQAACAAJ

[5] A. Baggeroer, “Acoustic telemetry - an overview,” *IEEE Journal of Oceanic Engineering*, vol. 9, no. 4, pp. 229–235, Oct. 1984.

[6] K. G. Foote, “Underwater acoustic technology: review of some recent developments,” in *OCEANS 2008*, vol. 2008. IEEE, 2008, pp. 1–6.

[7] NURC, *Sonar Acoustics Handbook*. NURC. La Spezia, Italy. 2008, 2008.

[8] F. B. Jensen, W. A. Kuperman, M. B. Porter, and H. Schmidt, *Computational ocean acoustics*, 2nd ed. Springer Science & Business Media, 2011.

[9] M. Stojanovic, “Underwater acoustic communications: Design considerations on the physical layer,” in *Wireless on Demand Network Systems and Services, 2008. WONS 2008. Fifth Annual Conference on*. IEEE, 2008, pp. 1–10. [Online]. Available: http://ieeexplore.ieee.org/xpl/articleDetails.jsp?arnumber=4459349

[10] R. Francois and G. Garrison, “Sound absorption based on ocean measurements: Part i: Pure water and magnesium sulfate contributions,” *The Journal of the Acoustical Society of America*, vol. 72, no. 3, pp. 896–907, 1982.

[11] R. Francois and G. Garrison, “Sound absorption based on ocean measurements. part ii: Boric acid contribution and equation for total absorption,” *The Journal of the Acoustical Society of America*, vol. 72, no. 6, pp. 1879–1890, 1982.

[12] M. A. Ainslie and J. G. McColm, “A simplified formula for viscous and chemical absorption in sea water,” *The Journal of the Acoustical Society of America*, vol. 103, no. 3, pp. 1671–1672, 1998.

[13] M. Stojanovic, “On the relationship between capacity and distance in an underwater acoustic communication channel,” *ACM SIGMOBILE Mobile Computing and Communications Review*, vol. 11, no. 4, pp. 34–43, 2007.

[14] F. Sabath, E. Mokole, and S. Samaddar, “Definition and classification of ultra-wideband signals and devices,” *URSI Radio Science Bulletin*, vol. 78, no. 2, pp. 12–26, 2005.

[15] M. Stojanovic and J. Preisig, “Underwater acoustic communication channels: Propagation models and statistical characterization,” *IEEE Communications Magazine*, vol. 47, no. 1, pp. 84–89, 2009.

[16] B. S. Sharif, J. Neasham, O. R. Hinton, and A. E. Adams, “A computationally efficient doppler compensation system for underwater acoustic communications,” *Oceanic Engineering, IEEE Journal of*, vol. 25, no. 1, pp. 52–61, 2000.

[17] A. W. Rihaczek, *Principles of high-resolution radar*. McGraw-Hill New York, 1969.

[18] W. M. Carey and R. B. Evans, *Ocean ambient noise: measurement and theory*. Springer Science & Business Media, 2011.

[19] J.-P. Marage and Y. Mori, *Sonar and Underwater Acoustics*. John Wiley & Sons, 2010.

[20] G. Frisk, D. Bradley, J. Caldwell, G. D’Spain, J. Gordon, M. Hastings, D. Ketten, J. Miller, D. Nelson, A. Popper *et al.*, “Ocean noise and marine mammals,” *National Research Council, Committee on Potential Impacts of Ambient Noise in the Ocean on Marine Mammals*, 2003.

[21] G. M. Wenz, “Acoustic ambient noise in the ocean: Spectra and sources,” *The Journal of the Acoustical Society of America*, vol. 34, no. 12, pp. 1936–1956, 1962.

[22] A. Gibbons, “What’s the sound of one ocean warming?” *Science*, vol. 248, no. 4951, pp. 33–35, 1990.

[23] W. H. Munk, R. C. Spindel, A. Baggeroer, and T. G. Birdsall, “The heard island feasibility test,” *The Journal of the Acoustical Society of America*, vol. 96, no. 4, pp. 2330–2342, 1994.

[24] OSPAR Commission, “Overview of the impacts of anthropogenic underwater sound in the marine environment,” *Report*, vol. 441/2009, p. 134, 2009.

[25] C. Erbe, “Underwater acoustics: Noise and the effects on marine mammals,” *A pocket handbook 3rd edition JASCO Applied Sciences*, 2011.

[26] W. J. Richardson, C. R. Greene Jr, C. I. Malme, and D. H. Thomson, *Marine mammals and noise*. Academic press, 1995.

[27] M. Jasny, *Sounding the depths II: The rising toll of sonar, shipping and industrial ocean noise on marine life*. Natural Resources Defense Council, 2005.

[28] B. L. Southall, A. E. Bowles, W. T. Ellison, J. J. Finneran, R. L. Gentry, C. R. Greene Jr, D. Kastak, D. R. Ketten, J. H. Miller, P. E. Nachtigall *et al.*, “Marine mammal noise exposure criteria: Initial scientific recommendations,” *Aquatic mammals*, vol. 33, no. 4, p. 411, 2007.

[29] K. Lucke, U. Siebert, P. A. Lepper, and M.-A. Blanchet, “Temporary shift in masked hearing thresholds in a harbor porpoise (phocoena phocoena) after exposure to seismic airgun stimuli,” *The Journal of the Acoustical Society of America*, vol. 125, no. 6, pp. 4060–4070, 2009.

[30] D. R. Ketten, “Beaked whale necropsy findings for strandings in the bahamas, puerto rico, and madeira, 1999-2002,” DTIC Document, Tech. Rep., 2005.

[31] A. Fernández, J. Edwards, F. Rodriguez, A. E. De Los Monteros, P. Herraez, P. Castro, J. Jaber, V. Martin, and M. Arbelo, ““gas and fat embolic syndrome” involving a mass stranding of beaked whales (family ziphiidae) exposed to anthropogenic sonar signals,” *Veterinary Pathology*, vol. 42, no. 4, pp. 446–457, 2005.

[32] M. C. Hastings and A. N. Popper, “Effects of sound on fish,” California Department of Transportation, Tech. Rep., 2005.

[33] M. Simmonds and L. Lopez-Jurado, “Whales and the military,” *Nature*, vol. 351, no. 6326, pp. 448–448, 1991.

[34] A. Frantzis, “Does acoustic testing strand whales?” *Nature*, vol. 392, no. 6671, p. 29, 1998.

[35] G. L. D’Spain, A. D’Amico, and D. M. Fromm, “Properties of the underwater sound fields during some well documented beaked whale mass stranding events,” *Journal of Cetacean Research and Management*, vol. 7, no. 3, pp. 223–238, 2006.

[36] K. Balcomb III and D. Claridge, “A mass stranding of cetaceans caused by naval sonar in the bahamas,” *Bahamas Journal of Science*, vol. 8, no. 2, pp. 2–12, 2001.

[37] T. M. Cox, T. Ragen, A. Read, E. Vos, R. Baird, K. Balcomb, J. Barlow, J. Caldwell, T. Cranford, and L. Crum, “Understanding the impacts of anthropogenic sound on beaked whales,” DTIC Document, Tech. Rep., 2006.

[38] J. Wang and S. Yang, “Unusual cetacean stranding events of taiwan in 2004 and 2005,” *Journal of Cetacean Research and Management*, vol. 8, no. 3, p. 283, 2006.

[39] E. Parsons, S. J. Dolman, A. J. Wright, N. A. Rose, and W. Burns, “Navy sonar and cetaceans: Just how much does the gun need to smoke before we act?” *Marine Pollution Bulletin*, vol. 56, no. 7, pp. 1248–1257, 2008.

[40] A. A. Hohn, D. S. Rotstein, C. A. Harms, and B. L. Southall, “Report on marine mammal unusual mortality event umese0501sp: Multispecies mass stranding of pilot whales (globicephala macrorhynchus), minke whale (balaenoptera acutorostrata), and dwarf sperm whales (kogia sima) in north carolina on 15-16 january 2005,” 2006.

[41] A. D’Amico, R. C. Gisiner, D. R. Ketten, J. A. Hammock, C. Johnson, P. L. Tyack, and J. Mead, “Beaked whale strandings and naval exercises,” *Aquatic Mammals*, vol. 35, no. 4, p. 452, 2009.

[42] D. R. Ketten, “Sonars and strandings: Are beaked whales the aquatic acoustic canary,” *Acoustics Today*, vol. 10, no. 3, pp. 46–56, 2014.

[43] B. L. Southall, T. Rowles, F. Gulland, R. Baird, and P. Jepson, "Final report of the independent scientific review panel investigating potential contributing factors to a 2008 mass stranding of melonheaded whales (peponocephala electra) in antsohihy, madagascar," *Independent Scientific Review Panel*, 2013.

[44] P. D. Jepson, R. Deaville, K. Acevedo-Whitehouse, J. Barnett, A. Brownlow, R. L. Brownell Jr, F. C. Clare, N. Davison, R. J. Law, J. Loveridge *et al.*, "What caused the uk's largest common dolphin (delphinus delphis) mass stranding event?" *PLoS ONE*, 2013. [Online]. Available: http://dx.doi.org/10.1371/journal.pone.0060953

[45] W. Ellison, B. Southall, C. Clark, and A. Frankel, "A new context-based approach to assess marine mammal behavioral responses to anthropogenic sounds," *Conservation Biology*, vol. 26, no. 1, pp. 21–28, 2012.

[46] M. P. Johnson and P. L. Tyack, "A digital acoustic recording tag for measuring the response of wild marine mammals to sound," *IEEE journal of oceanic engineering*, vol. 28, no. 1, pp. 3–12, 2003.

[47] M. Johnson, N. A. de Soto, and P. T. Madsen, "Studying the behaviour and sensory ecology of marine mammals using acoustic recording tags: a review," *Marine Ecology Progress Series*, vol. 395, pp. 55–73, 2009.

[48] B. L. Southall, D. Moretti, B. Abraham, J. Calambokidis, S. L. DeRuiter, and P. L. Tyack, "Marine mammal behavioral response studies in southern california: advances in technology and experimental methods," *Marine Technology Society Journal*, vol. 46, no. 4, pp. 48–59, 2012.

[49] J. A. Goldbogen, B. L. Southall, S. L. DeRuiter, J. Calambokidis, A. S. Friedlaender, E. L. Hazen, E. A. Falcone, G. S. Schorr, A. Douglas, D. J. Moretti *et al.*, "Blue whales respond to simulated mid-frequency military sonar," *Proceedings of the Royal Society of London B: Biological Sciences*, vol. 280, no. 1765, p. 20130657, 2013. [Online]. Available: http://dx.doi.org/10.1098/rspb.2013.0657

[50] S. L. DeRuiter, B. L. Southall, J. Calambokidis, W. M. Zimmer, D. Sadykova, E. A. Falcone, A. S. Friedlaender, J. E. Joseph, D. Moretti, G. S. Schorr *et al.*, "First direct measurements of behavioural responses by cuvier's beaked whales to mid-frequency active sonar," *Biology letters*, vol. 9, no. 4, p. 20130223, 2013. [Online]. Available: http://dx.doi.org/10.1098/rsbl.2013.0223

[51] D. E. Claridge, "Population ecology of blainville's beaked whales (mesoplodon densirostris)," Ph.D. dissertation, University of St Andrews, 2013.

[52] R. Kastelein, W. Verboom, M. Muijsers, N. Jennings, and S. Van der Heul, "The influence of acoustic emissions for underwater data transmission on the behaviour of harbour porpoises (phocoena phocoena) in a floating pen," *Marine Environmental Research*, vol. 59, no. 4, pp. 287–307, 2005. [Online]. Available: http://dx.doi.org/10.1016/j.marenvres.2004.05.005

[53] R. Kastelein, D. De Haan, N. Vaughan, C. Staal, and N. Schooneman, "The influence of three acoustic alarms on the behaviour of harbour porpoises (phocoena phocoena) in a floating pen," *Marine Environmental Research*, vol. 52, no. 4, pp. 351–371, 2001.

[54] R. Kastelein, H. Rippe, N. Vaughan, N. Schooneman, W. Verboom, and D. D. Haan, “The effects of acoustic alarms on the behavior of harbor porpoises (phocoena phocoena) in a floating pen,” *Marine Mammal Science*, vol. 16, no. 1, pp. 46–64, 2000.

[55] R. A. Kastelein, S. van der Heul, W. C. Verboom, R. J. Triesscheijn, and N. V. Jennings, “The influence of underwater data transmission sounds on the displacement behaviour of captive harbour seals (phoca vitulina),” *Marine Environmental Research*, vol. 61, no. 1, pp. 19–39, 2006.

[56] R. A. Kastelein, L. Hoek, R. Gransier, M. Rambags, and N. Claeys, “Effect of level, duration, and inter-pulse interval of 1–2 khz sonar signal exposures on harbor porpoise hearing,” *The Journal of the Acoustical Society of America*, vol. 136, no. 1, pp. 412–422, 2014.

[57] R. A. Kastelein, R. Gransier, and L. Hoek, “Cumulative effects of exposure to continuous and intermittent sounds on temporary hearing threshold shifts induced in a harbor porpoise (phocoena phocoena),” in *The Effects of Noise on Aquatic Life II*. Springer, 2016, pp. 523–528.

[58] J. Tougaard, A. J. Wright, and P. T. Madsen, “Noise exposure criteria for harbor porpoises,” *The Effects of Noise on Aquatic Life II*, Jan. 2016. [Online]. Available: http://dx.doi.org/10.1007/978-1-4939-2981-8_146

[59] C. W. Clark, W. T. Ellison, B. L. Southall, L. Hatch, S. M. Van Parijs, A. Frankel, and D. Ponirakis, “Acoustic masking in marine ecosystems: intuitions, analysis, and implication,” *Marine Ecology Progress Series*, vol. 395, pp. 201–222, 2009.

[60] S. J. Dolman, P. G. Evans, G. Notarbartolo-di Sciara, and H. Frisch, “Active sonar, beaked whales and european regional policy,” *Marine pollution bulletin*, vol. 63, no. 1, pp. 27–34, 2011.

[61] A. MAGLIO, G. PAVAN, M. C. S. FREY, M. BOUZIDI, B. CLARO, N. ENTRUP, M. FOUAD, F. LEROY, and J. MUELLER, “Overview of the noise hotspots in the accobams area,” *Final Report to the ACCOBAMS Secretariat*, 2015.

[62] K. Zirbel, P. Balint, and E. Parsons, “Navy sonar, cetaceans and the us supreme court: A review of cetacean mitigation and litigation in the us,” *Marine pollution bulletin*, vol. 63, no. 1, pp. 40–48, 2011.

[63] S. J. Dolman and M. Jasny, “Evolution of marine noise pollution management,” *Aquatic Mammals*, vol. 41, no. 4, p. 357, 2015.

[64] J. Horwitz, *War of the Whales: a true story*. Simon and Schuster, 2015.

[65] A. R. Scholik-Schlomer, “Where the decibels hit the water: perspectives on the application of science to real-world underwater noise and marine protected species issues,” *Acoustics Today*, vol. 11, no. 3, pp. 36–44, 2015.

[66] A. Porto and M. Stojanovic, “Optimizing the transmission range in an underwater acoustic network,” in *OCEANS 2007*. IEEE, 2007, pp. 1–5.

[67] J. Heidemann, W. Ye, J. Wills, A. Syed, and Y. Li, “Research challenges and applications for underwater sensor networking,” in *Wireless Communications and Networking Conference, 2006. WCNC 2006. IEEE*, vol. 1. IEEE, 2006, pp. 228–235.

[68] J. Heidemann, M. Stojanovic, and M. Zorzi, “Underwater sensor networks: applications, advances and challenges,” *Phil. Trans. R. Soc. A*, vol. 370, no. 1958, pp. 158–175, 2012.

[69] B. Benson, Y. Li, B. Faunce, K. Domond, D. Kimball, C. Schurgers, and R. Kastner, “Design of a low-cost underwater acoustic modem,” *IEEE Embedded Systems Letters*, vol. 2, no. 3, pp. 58–61, Sep. 2010.

[70] B. Benson, Y. Li, R. Kastner, B. Faunce, K. Domond, D. Kimball, and C. Schurgers, “Design of a low-cost, underwater acoustic modem for short-range sensor networks,” in *OCEANS 2010 IEEE - Sydney*, May 2010, pp. 1–9.

[71] E. Gallimore, J. Partan, I. Vaughn, S. Singh, J. Shusta, and L. Freitag, “The whoi micromodem-2: A scalable system for acoustic communications and networking,” in *OCEANS 2010*. IEEE, 2010, pp. 1–7.

[72] J. G. Proakis, E. M. Sozer, J. A. Rice, and M. Stojanovic, “Shallow water acoustic networks,” *IEEE communications magazine*, vol. 39, no. 11, pp. 114–119, 2001.

[73] D. E. Lucani, M. Médard, and M. Stojanovic, “Underwater acoustic networks: Channel models and network coding based lower bound to transmission power for multicast,” *IEEE Journal on Selected Areas in Communications*, vol. 26, no. 9, 2008.

[74] P. Casari, M. Stojanovic, and M. Zorzi, “Exploiting the bandwidth-distance relationship in underwater acoustic networks,” in *OCEANS 2007*. IEEE, 2007, pp. 1–6.

[75] A. Wahid, S. Lee, and D. Kim, “A reliable and energy-efficient routing protocol for underwater wireless sensor networks,” *International Journal of Communication Systems*, vol. 27, no. 10, pp. 2048–2062, 2014.

[76] A. F. Harris III, M. Stojanovic, and M. Zorzi, “When underwater acoustic nodes should sleep with one eye open: idle-time power management in underwater sensor networks,” in *Proceedings of the 1st ACM international workshop on Underwater networks*. ACM, 2006, pp. 105–108.

[77] R. Diamant, L. Lampe, and E. Gamroth, “Bounds for low probability of detection for underwater acoustic communication,” *IEEE Journal of Oceanic Engineering*, vol. PP, no. 99, pp. 1–13, 2016.

[78] R. Diamant, L. Lampe, and E. Gamroth, “Low probability of detection for underwater acoustic communication,” in *Oceans-St. John’s, 2014*. IEEE, 2014, pp. 1–6.

[79] G. Ginolhac and G. Jourdain, “"principal component inverse" algorithm for detection in the presence of reverberation,” *IEEE Journal of oceanic engineering*, vol. 27, no. 2, pp. 310–321, 2002.

[80] G. Ginolhac and G. Jourdain, “Detection in presence of reverberation,” in *OCEANS 2000 MTS/IEEE Conference and Exhibition*, vol. 2. IEEE, 2000, pp. 1043–1046.

[81] J. F. Kuehls and E. Geraniotis, “Presence detection of binary-phase-shift-keyed and direct-sequence spread-spectrum signals using a prefilter-delay-and-multiply device,” *IEEE Journal on Selected Areas in Communications*, vol. 8, no. 5, pp. 915–933, 1990.

[82] G. Burel, C. Bouder, and O. Berder, “Detection of direct sequence spread spectrum transmissions without prior knowledge,” in *Global Telecommunications Conference, 2001. GLOBECOM’01. IEEE*, vol. 1. IEEE, 2001, pp. 236–239.

[83] W. Jans, I. Nissen, F. Gerdes, E. Sangfelt, C.-E. Solberg, and P. van Walree, *UUV-Covert Acoustic Communications Prelininary Results of the First Sea Experiment*. neuily-sur-Seine: NATO RTO, 2006.

[84] P. A. Van Walree, T. Jenserud, and M. Smedsrud, “A discrete-time channel simulator driven by measured scattering functions,” *IEEE journal on selected areas in communications*, vol. 26, no. 9, 2008.

[85] M. Palmese, G. Bertolotto, A. Pescetto, and A. Trucco, “Experimental validation of a chirp-based underwater acoustic communication method,” in *Proceedings of Meetings on Acoustics*, vol. 4, no. 1. Acoustical Society of America, 2008, p. 030002.

[86] P. Van Walree, E. Sangfelt, and G. Leus, “Multicarrier spread spectrum for covert acoustic communications,” in *OCEANS 2008*. IEEE, 2008, pp. 1–8.

[87] P. A. van Walree and G. Leus, “Robust underwater telemetry with adaptive turbo multiband equalization,” *IEEE Journal of Oceanic Engineering*, vol. 34, no. 4, pp. 645–655, Oct. 2009.

[88] G. Leus, P. van Walree, J. Boschma, C. Fanciullacci, H. Gerritsen, and P. Tusoni, “Covert underwater communications with multiband ofdm,” in *OCEANS 2008*, Sept 2008, pp. 1–8.

[89] G. Leus and P. van Walree, “Multiband OFDM for covert acoustic communications,” vol. 26, no. 9, pp. 1662–1673, 2008. [Online]. Available: http://ieeexplore.ieee.org/stamp/stamp.jsp?arnumber=4686805

[90] E. Sangfelt, B. Nilsson, and J. Israelsson, “Covert underwater communication experiments using dsss and turbo equalization,” *UDT Europe 2008*, 2008.

[91] P. van Walree, T. Ludwig, C. Solberg, E. Sangfelt, A. Laine, G. Bertolotto, and A. Ishøy, “Uuv covert acoustic communications,” in *Proceedings of the 3rd conference on Underwater Acoustic Measurements: Technologies and Results*, vol. 254, 2009.

[92] H. Dol and P. Van Walree, “Underwater acoustic communication research at tno past and present,” in *OCEANS, 2011 IEEE-Spain*. IEEE, 2011, pp. 1–6.

[93] T. Yang and W.-B. Yang, “Performance analysis of direct-sequence spread-spectrum underwater acoustic communications with low signal-to-noise-ratio input signals,” *The Journal of the Acoustical Society of America*, vol. 123, no. 2, pp. 842–855, 2008. [Online]. Available: http://scitation.aip.org/content/asa/journal/jasa/123/2/10.1121/1.2828053

[94] J. Ling, H. He, J. Li, W. Roberts, and P. Stoica, “Covert underwater acoustic communications,” *The Journal of the Acoustical Society of America*, vol. 128, no. 5, pp. 2898–2909, 2010. [Online]. Available: http://scitation.aip.org/content/asa/journal/jasa/128/5/10.1121/1.3493454

[95] J. Ling, H. He, J. Li, W. Roberts, and P. Stoica, “Covert underwater acoustic communications: Transceiver structures, waveform designs and associated performances,” in *OCEANS 2010*. IEEE, 2010, pp. 1–10.

[96] L. Lei, F. Xu, Y. Xu, and Y. Wu, “A chaotic direct sequence spread spectrum communication system in shallow water,” in *Control, Automation and Systems Engineering (CASE), 2011 International Conference on*. IEEE, 2011, pp. 1–4.

[97] T.-S. Ahn, J.-W. Jung, H.-H. Sung, D.-W. Lee, and T.-D. Park, “Turbo equalization for covert communication in underwater channel,” in *Ubiquitous and Future Networks (ICUFN), 2016 Eighth International Conference on*. IEEE, 2016, pp. 462–464.

[98] S. Liu, T. Ma, G. Qiao, L. Ma, and Y. Yin, “Biologically inspired covert underwater acoustic communication by mimicking dolphin whistles,” *Applied Acoustics*, vol. 120, pp. 120–128, 2017.

[99] E. Demirors and T. Melodia, “Chirp-based lpd/lpi underwater acoustic communications with code-time-frequency multidimensional spreading,” in *Proceedings of the 11th ACM International Conference on Underwater Networks & Systems*. ACM, 2016, p. 9.

[100] M. Hanspach and M. Goetz, “Recent developments in covert acoustical communications.” in *Sicherheit*. Citeseer, 2014, pp. 243–254.

[101] Y. Luo, L. Pu, M. Zuba, Z. Peng, and J.-H. Cui, “Cognitive acoustics: Making underwater communications environment-friendly,” in *Proceedings of the International Conference on Underwater Networks & Systems*. ACM, 2014, p. 48.

[102] Y. Luo, L. Pu, M. Zuba, Z. Peng, and J.-H. Cui, “Challenges and opportunities of underwater cognitive acoustic networks,” *IEEE Transactions on Emerging Topics in Computing*, vol. 2, no. 2, pp. 198–211, 2014.

[103] Y. Luo, L. Pu, Z. Peng, Y. Zhu, and J.-H. Cui, “Rism: An efficient spectrum management system for underwater cognitive acoustic networks,” in *Sensing, Communication, and Networking (SECON), 2014 Eleventh Annual IEEE International Conference on*. IEEE, 2014, pp. 414–422.

[104] Q. Yang, Y. Su, Z. Jin, and G. Yao, “Efpc: An environmentally friendly power control scheme for underwater sensor networks,” *Sensors*, vol. 15, no. 11, pp. 29 107–29 128, 2015.

[105] G. Yao, Z. Jin, and Y. Su, “An environment-friendly spectrum decision strategy for underwater wireless sensor networks,” in *Communications (ICC), 2015 IEEE International Conference on*. IEEE, 2015, pp. 6370–6375.

[106] G. Yao, Z. Jin, and Y. Su, “An environment-friendly spectrum decision strategy for underwater acoustic networks,” *Journal of Network and Computer Applications*, vol. 73, pp. 82–93, 2016.

[107] K. Dimitrov, J. Neasham, B. Sharif, C. Tsimenidis, and G. Goodfellow, “Low-power environmentally friendly underwater acoustic communication using pseudo-noise spreading sequences,” in *OCEANS, 2012 - Yeosu*, 2012, pp. 1–5. [Online]. Available: http://ieeexplore.ieee.org/stamp/stamp.jsp?arnumber=6263622

[108] S. W. Golomb, *Shift Register Sequences*, ser. Holden-Day Series in Information Systems. Holden-Day, 1967. [Online]. Available: https://books.google.co.uk/books?id=3tpQAAAAMAAJ

[109] W. W. Au and R. R. Fay, *Hearing by whales and dolphins*. Springer Science & Business Media, 2000, vol. 12.

[110] C. E. Shannon, “Communication in the presence of noise,” *Proceedings of the IRE*, vol. 37, no. 1, pp. 10–21, 1949.

[111] D. Torrieri, *Principles of Spread-Spectrum Communication Systems*. Springer, 2005. [Online]. Available: https://books.google.co.uk/books?id=f5mMqZHGnusC

[112] S. W. Golomb and G. Gong, *Signal design for good correlation: for wireless communication, cryptography, and radar*. Cambridge University Press, 2005. [Online]. Available: https://books.google.co.uk/books?id=DhYXL4miZj4C

[113] J. G. Proakis and M. Salehi, *Digital Communications*, ser. McGraw-Hill International Edition. McGraw-Hill, 2008. [Online]. Available: https://books.google.co.uk/books?id=ksh0GgAACAAJ

[114] L.-L. Yang and L. Hanzo, "A recursive algorithm for the error probability evaluation of m-QAM," vol. 4, no. 10, pp. 304–306, 2000. [Online]. Available: http://ieeexplore.ieee.org/stamp/stamp.jsp?arnumber=880816

[115] John R. Barry and Edwared A. Lee and David G. Messerschmitt, *Digital Communication*, 3rd ed. Springer, 2004.

[116] G. M. Goodfellow, "Development of an acoustic communication link for micro underwater vehicles," Ph.D. dissertation, University of Newcastle Upon Tyne, 2014.

[117] M. Johnson, L. Freitag, and M. Stojanovic, "Improved doppler tracking and correction for underwater acoustic communications," in *Acoustics, Speech, and Signal Processing, 1997. ICASSP-97., 1997 IEEE International Conference on*, vol. 1. IEEE, 1997, pp. 575–578.

[118] A. Berni and W. Gregg, "On the utility of chirp modulation for digital signaling," *IEEE Transactions on Communications*, vol. 21, no. 6, pp. 748–751, 1973.

[119] H. S. Dol, P. Casari, T. van der Zwan, and R. Otnes, "Software-defined underwater acoustic modems: Historical review and the nilus approach," *IEEE Journal of Oceanic Engineering*, vol. PP, no. 99, pp. 1–16, 2016.

[120] E. Demirors, B. G. Shankar, G. E. Santagati, and T. Melodia, "Seanet: A software-defined acoustic networking framework for reconfigurable underwater networking," in *Proceedings of the 10th International Conference on Underwater Networks & Systems*. ACM, 2015, p. 11.

[121] E. Demirors, G. Sklivanitis, T. Melodia, S. N. Batalama, and D. A. Pados, "Software-defined underwater acoustic networks: toward a high-rate real-time reconfigurable modem," *IEEE Communications Magazine*, vol. 53, no. 11, pp. 64–71, Nov. 2015.

[122] H. Lee, T. H. Kim, J. W. Choi, and S. Choi, "Chirp signal-based aerial acoustic communication for smart devices," in *Computer Communications (INFOCOM), 2015 IEEE Conference on*, 2015, pp. 2407–2415. [Online]. Available: http://ieeexplore.ieee.org/stamp/stamp.jsp?arnumber=7218629

[123] I. S. Reed and G. Solomon, "Polynomial codes over certain finite fields," *Journal of the society for industrial and applied mathematics*, vol. 8, no. 2, pp. 300–304, 1960.

[124] "Tutorial on reed-solomon error correction coding," *Technical Support Package NASA Tech Briefs MSC-21834*, 1998.

[125] C. Clarke, "Reed-solomon error correction," *BBC Research & Development, White Paper WHP*, vol. 31, 2002.

[126] R. Gallager, “Low-density parity-check codes,” *IRE Transactions on information theory*, vol. 8, no. 1, pp. 21–28, 1962.

[127] D. MacKay and R. Neal, “Good codes based on very sparse matrices,” *Cryptography and Coding*, pp. 100–111, 1995.

[128] M. C. Davey and D. MacKay, “Low-density parity check codes over gf (q),” *IEEE Communications Letters*, vol. 2, no. 6, pp. 165–167, 1998.

[129] V. Ganepola, R. Carrasco, I. Wassell, and S. Le Goff, “Performance study of non-binary LDPC codes over GF(q),” in *Communication Systems, Networks and Digital Signal Processing, 2008. CNSDSP 2008. 6th International Symposium on*, 2008, pp. 585–589. [Online]. Available: http://ieeexplore.ieee.org/stamp/stamp.jsp?arnumber=4610743

[130] J. Huang, S. Zhou, and P. Willett, “Nonbinary ldpc coding for multicarrier underwater acoustic communication,” *IEEE Journal on Selected Areas in Communications*, vol. 26, no. 9, 2008.

[131] B. Zhou, L. Zhang, J. Kang, Q. Huang, Y. Y. Tai, S. Lin, and M. Xu, “Non-binary ldpc codes vs. reed-solomon codes,” in *Information Theory and Applications Workshop, 2008*. IEEE, 2008, pp. 175–184.

[132] M. Johnston, B. S. Sharif, C. C. Tsimenidis, and L. Chen, “Sum-product algorithm utilizing soft distances on additive impulsive noise channels,” *IEEE Transactions on Communications*, vol. 61, no. 6, pp. 2113–2116, 2013.

[133] G. J. Byers and F. Takawira, “Fourier transform decoding of non-binary ldpc codes,” in *Proceedings Southern African Telecommunication Networks and Applications Conference (SATNAC). Spier Wine Estate, Western Cape, South Africa*, 2004.

[134] R. A. Carrasco and M. Johnston, *Non-binary error control coding for wireless communication and data storage*. John Wiley & Sons, 2008.